Synthesis, Characterization, and Reactivity of Thiolate-Supported Metalloradicals

Thesis by

Nina Xiao Gu

In Partial Fulfillment of the Requirements for

the degree of

Doctor of Philosophy

CALIFORNIA INSTITUTE OF TECHNOLOGY

Pasadena, California

2020

(Defended March 9, 2020)

Nina Xiao Gu
ORCID: 0000-0002-4637-8418

ACKNOWLEDGEMENTS

My time at Caltech has been a challenging yet enriching experience, and I am lucky to have had many fantastic mentors and co-workers who have helped me reach the finish line. First and foremost, I thank Jonas for his mentorship and support during my graduate studies. His feedback has challenged me to grow as a scientist and to think more critically about my science, for which I am grateful. I'm also appreciative of the freedom that Jonas has allowed me to pursue chemistry that sparked my interest. Although at times it can feel like nothing is working, it has also been a lot of fun to see if reactions that I dream up actually pan out in the lab. I would additionally like to thank the rest of my committee, Theo Agapie, Linda Hsieh-Wilson, and Greg Fu, for their constructive feedback and advice during our meetings.

I am fortunate to have had wonderful undergraduate research experiences, which sowed my interest in chemistry and motivated me to pursue graduate studies in the first place. Ted Betley is thanked for his encouragement and his dedication to mentoring undergraduate students. During my time in his lab, I also had the privilege to learn from two talented graduate students, Tamara Powers and Benji Lin, who each taught me a great deal about synthesis. Additionally, I would like to thank Cliff Kubiak for his mentorship during my first stint in a research lab, and my postdoc mentor, Kyle Grice, for his guidance and patience with a very green undergraduate.

The staff who run the facilities at Caltech are truly outstanding, and I owe them a big thank you for their help over these years. I've been fortunate to work on several projects with Paul Oyala, who has been a great person to talk to for all things EPR-related. Mike Takase and Larry Henling are thanked for their help with my crystals, as well as their patience and good humor with the many, many amorphous samples that I've brought them. Dave VanderVelde, Nathan Dalleska, Mona Shahgholi are additionally acknowledged for sharing their expertise in NMR, GC, and mass spectrometry, respectively.

I'm grateful to all the individuals that I've overlapped with during my time in Jonas' lab. In particular, I'd like to thank Gaël Ung for helping me get on my feet during my first year and for being a great role model. Meaghan Deegan is an exceptionally hard-working and rigorous scientist, and I am grateful for the helpful suggestions and friendship over these years. In addition to their wise words and support, I also thank Kumiko Yamamoto and Gerri Roberts for tasty food outings and Trixia Buscagan for much-needed coffee breaks! I am also appreciative of the people that I've shared an

office bay with, most recently Cooper Citek, Heejun Lee, Dirk Schild, and Christian Johansen (honorary member), for the interesting scientific discussions and entertaining, not-quite-so-scientific ones as well.

Lastly, I'd like to thank Kareem, Olivia, and my parents for their unwavering support (I'm the luckiest!). None of this would have been possible without the hard work and sacrifices of my parents – this thesis is dedicated to them.

ABSTRACT

Reactive metalloradical intermediates have been implicated in both biological and synthetic catalyst systems for small molecule activation processes, including proton reduction and ammonia oxidation. Towards a greater mechanistic understanding of such transformations on well-defined model complexes, this thesis explores relevant H–H and N–N bond-forming reactions mediated by trivalent Fe, Ni species, as well as catalytic N–N bond cleavage mediated by an open-shell VFe bimetallic complex. First, a pair of thiolate-supported, S = ½ iron and nickel hydrides are synthesized and spectroscopically characterized at low temperatures (Chapters 2, 3). Paramagnetic iron and nickel hydrides have been proposed as catalytic intermediates of [NiFe] hydrogenase and nitrogenase, but characterization of such molecular species are limited. For both the Fe and Ni hydride complexes described herein, spin delocalization onto the thiolate ligand is proposed to stabilize the formal 3+ metal oxidation state. Furthermore, both the Fe^{III}–H and Ni^{III}–H species are demonstrated to undergo the bimolecular reductive elimination of dihydrogen upon warming, albeit with distinct activation parameters consistent with different proposed pathways for H–H bond formation. Chapter 4 expands upon the H–H bond forming chemistry demonstrated on the Ni system to demonstrate related N–N bond formation proposed from an analogous Ni^{III}–NH_2 species, resulting in the formation of a $Ni^{II}_2(N_2H_4)$ complex. Given the diverse mechanistic possibilities for the overall $6e^-/6H^+$ transformation to oxidize ammonia to dinitrogen, identification of the active $M(NH_x)$ intermediate and pathway for N–N bond formation is a central mechanistic question. While the homocoupling of M–NH_2 species to form hydrazine has been hypothesized as the key N–N bond forming step in ammonia oxidation systems, stoichiometric examples of this transformation from M–NH_2 complexes are rare. Lastly, Chapter 5 details the synthesis of a heterobimetallic VFe complex featuring a bridging thiolate, inspired by the structure of the VFe nitrogenase cofactor. This VFe species is demonstrated to be an active catalyst for the disproportionation of hydrazine to dinitrogen and ammonia. Notably, the heterobimetallic complex is appreciably more active than monometallic analogues of the individual V and Fe sites, suggesting that bimetallic cooperativity may facilitate the observed catalysis.

PUBLISHED CONTENT AND CONTRIBUTIONS

(1) Gu, N. X.; Oyala, P. H.; Peters, J. C. An $S = ½$ Iron Complex Featuring N_2, Thiolate, and Hydride Ligands: Reductive Elimination of H_2 and Relevant Thermochemical Fe–H Parameters. *J. Am. Chem. Soc.* **2018**, *140*, 6374-6382. DOI: 10.1021/jacs.8b02603.

N.X.G. synthesized all of the compounds, collected characterization data, performed computational studies, and prepared the manuscript.

(2) Gu, N. X.; Ung, G.; Peters, J. C. Catalytic hydrazine disproportionation mediated by a thiolate-bridged VFe complex. *Chem. Commun.* **2019**, *55*, 5363-5366. DOI: 10.1039/C9CC00345B.

N.X.G. synthesized the metallated complexes, performed all catalytic reactions and kinetic studies, and prepared the manuscript.

(3) Gu, N. X.; Oyala, P. H.; Peters, J. C. H_2 Evolution from a Thiolate-Bound Ni(III) Hydride. *J. Am. Chem. Soc.* **2020**, accepted. DOI: 10.1021/jacs.0c00712.

N.X.G. synthesized all of the compounds, collected characterization data, performed computational studies, and prepared the manuscript.

TABLE OF CONTENTS

Acknowledgments iii
Abstract v
Published Content and Contributions vi
Table of Contents vii
List of Illustrations and/or Tables ix
Nomenclature xi
Chapter I: Introduction 1
1.1 Motivation 1
1.2 Proton Reduction to Dihydrogen 1
1.3 Ammonia Oxidation to Dinitrogen 7
1.4 Redox Non-Innocence of Thiolate Ligands 9
1.5 Chapter Summaries 11
1.6 References 12
Chapter II: An $S = ½$ Iron Complex Featuring N_2, Thiolate and Hydride Ligands: Reductive Elimination of H_2 and Relevant Thermochemical Fe–H Parameters 15
2.1 Introduction 15
2.2 Results and Discussion 17
2.3 Conclusion 31
2.4 Experimental Section 32
2.5 References 42
Chapter III: H_2 Evolution from a Thiolate-Bound Ni(III) Hydride 49
3.1 Introduction 49
3.2 Results and Discussion 50
3.3 Conclusion 62
3.4 Experimental Section 63
3.5 References 74

Chapter IV: $H_2N–NH_2$ Bond Formation from a $Ni^{III}–NH_2$ Species:
Mechanistic Insights into Ni-Mediated Ammonia Oxidation 81
4.1 Introduction 81
4.2 Results and Discussion 84
4.3 Conclusion 87
4.4 Experimental Section 88
4.5 References 96
Chapter V: Catalytic Hydrazine Disproportionation Mediated by a
Thiolate-Bridged VFe Complex 99
5.1 Introduction 99
5.2 Results and Discussion 100
5.3 Conclusion 106
5.4 Experimental Section 106
5.5 References 112
Appendix A: Supplementary Information for Chapter 2 116
Appendix B: Supplementary Information for Chapter 3 156
Appendix C: Supplementary Information for Chapter 4 215
Appendix D: Supplementary Information for Chapter 5 240

LIST OF ILLUSTRATIONS AND TABLES

Chapter 1 *Page*

Figure 1.1. Hydride-bound hydrogenase intermediates and proposed mechanism of [NiFe] hydrogenase 3

Figure 1.2. Proposed mechanism for biological nitrogen fixation 4

Figure 1.3. Homolytic and heterolytic pathways for molecular HER 5

Figure 1.4. Examples of paramagnetic Fe and Ni hydrides 6

Figure 1.5. Examples of molecular catalysts for ammonia oxidation 8

Figure 1.6. Pathways for O–O and N–N bond formation 9

Figure 1.7. Resonance structures of thiolate-bound metal complexes 10

Chapter 2

Scheme 2.1. Synthesis of $HSiP_2S^{iPr}$ and metallated Fe complexes 18

Figure 2.1. X-ray structures of $(SiP_2S)Fe$ complexes 19

Table 2.1. Select bond metrics and angles of $(SiP_2S)Fe$ complexes 19

Figure 2.2. Characterization data on $(SiP_2S)FeHN_2$ 21

Figure 2.3. Calculated spin density map for $(SiP_2S)FeHN_2$ 23

Figure 2.4. ENDOR and CW EPR data on $(SiP_2S)FeHN_2$ and $(SiP_2S)FeDN_2$ 24

Figure 2.5. Spectroscopic and kinetic data on H_2 evolution from $(SiP_2S)FeHN_2$ 25

Figure 2.6. Proposed mechanism for H_2 evolution from $(SiP_2S)FeHN_2$ 27

Scheme 2.2. Synthesis of $(SiP_2S)FeN_2^{-/2-}$ and hydride transfer from $(SiP_2S)FeHN_2^-$ 28

Figure 2.7. Thermochemical scheme relating H^+, $H^\bullet$, and H^- transfers from $(SiP_2S)FeHN_2^{0/-}$ 30

Table 2.2. Oxidation potentials and thermochemical parameters of pertaining to Fe–H cleavage from $(SiP_2S)FeHN_2^{0/-}$ 31

Chapter 3

Figure 3.1. Proposed biological Ni^{III} hydride intermediates and pathways for H_2 evolution from $(SiP_2S)NiH$ 50

Scheme 3.1. Synthesis of (SiP_2S)Ni complexes 51
Figure 3.2. X-ray structures of (SiP_2S)Ni complexes 52
Table 3.1. Select bond lengths of (SiP_2S)Ni complexes 53
Figure 3.3. CW EPR and ENDOR data on (SiP_2S)NiH 55
Figure 3.4. Synthesis, X-ray structure, and CW EPR data of (SiP_2S)NiMe 57
Table 3.2. Bond lengths of (SiP_2S)NiH (DFT) and (SiP_2S)NiMe (XRD) 57
Figure 3.5. Calculated Mulliken spin densities of the Ni-C hydrogenase state and (SiP_2S)NiH 59
Figure 3.6. UV-vis spectra monitoring the decay of (SiP_2S)NiH 60
Scheme 3.2. Comparison of H_2 evolution mechanisms from (SiP_2S)NiH and (SiP_2S)$FeHN_2$ 61

Chapter 4

Figure 4.1. Pathways for O–O bond formation in water oxidation and Ni-mediated amide coupling 81
Scheme 4.1. Synthesis of (SiP_2S)$Ni_x(N_yH_z)$ complexes 83
Figure 4.2. X-ray structure of (SiP_2S)$Ni_x(N_yH_z)$ complexes 84
Figure 4.3. NMR spectra of $[(SiP_2S)Ni]_2(N_2H_4)$ and isotopologues 85
Scheme 4.2. Comparison of H–H and N–N bond formation from (SiP_2S)$Ni^{III}X$ 86
Scheme 4.3. Summary of (SiP_2S)Ni-mediated ammonia oxidation 87

Chapter 5

Figure 5.1. Thiolate-bridged FeFe and VFe bimetallic scaffolds 100
Scheme 5.1. Synthesis of thiolate-bridged VFe complex 101
Figure 5.2. X-ray structure of thiolate-bridged VFe complex 102
Figure 5.3. Monometallic Fe and V complexes 103
Table 5.1. Catalytic hydrazine disproportionation mediated by the VFe catalyst 104
Table 5.2. Hydrazine disproportionation mediated by V and Fe complexes 105
Figure 5.4. Proposed general pathway for catalyzed hydrazine disproportionation 106

NOMENCLATURE

Å. Angstrom
μ_B. Bohr Magneton
μ_{eff}. Effective magnetic moment
12-c-4. 12-crown-4
2-MeTHF. 2-methyltetrahydrofuran
$[BAr^F{}_4]^-$. Tetrakis(3,5-bis(trifluoromethyl)phenyl)borate
ca. Circa
Cat. Catalyst
Cp. Cyclopentadienyl
CV. Cyclic voltammetry
CW. Continuous wave
DFT. Density functional theory
DME. 1,2-dimethoxyethane
EPR. Electron paramagnetic resonance
ENDOR. Electron nuclear double resonance
Equiv. Equivalents
Fc. Ferrocene
g. Electron g-factor.
G. Gibbs free energy
GC. Gas chromatography
Gt. Gigatonne
H. Enthalpy
HER. Hydrogen evolution reaction
HYSCORE. Hyperfine sublevel correlation.
IR. Infrared
NMR. Nuclear magnetic resonance
MeCN. Acetonitrile
S. Entropy
S. Spin quantum number
TEMPO. 2,2,6,6-Tetramethyl-1-piperidinyloxy
UV-vis. Ultraviolet-visible
PPN. Bis(triphenylphosphine)iminium

Chapter 1

INTRODUCTION

1.1 Motivation

Given the environmental impacts of carbon-based fuels and finite fossil fuel reserves, largescale adoption of a carbon-neutral energy economy is central to global sustainability.[1] Thus, the development of active, efficient, and Earth-abundant catalysts for relevant transformations are critical. A unifying theme of this thesis is the study of first-row transition metal complexes that mediate small molecule activation chemistry pertinent to renewable energy processes, serving as model systems to understand these bond-breaking and -making reactions on a molecular level. Model systems are uniquely well-suited for spectroscopic studies and probing structure-function relationships, which may in turn aid the understanding of more complex catalyst systems, as well as uncover new reactivity modes for a ground-up approach to catalyst design. Specifically, the characterization of model species allow for the identification of spectroscopic handles to support reliable characterization of transient catalytic intermediates, and the reactivity of these model species can inform mechanistic hypotheses involving such motifs in complex enzymatic or synthetic systems. Furthermore, the molecular understanding of these elementary transformations may aid the rational design of new catalysts for processes relevant to sustainable energy. These general principles motivate the study of the model complexes described in this thesis.

1.2 Proton Reduction to Dihydrogen

1.2.1 Dihydrogen as a Fuel

Molecular hydrogen is a promising alternative fuel given its high gravimetric density and because it is clean burning, generating water as a byproduct of combustion.[2] However, one challenge to adopting a largescale hydrogen fuel economy is the carbon footprint associated with current hydrogen production methods; industrial steam reforming processes

convert methane and water into carbon dioxide and dihydrogen and account for greater than 90% of H_2 produced in the United States today.[3] An attractive alternative method to generate hydrogen is through direct proton reduction ($H^+ + e^- \rightarrow ½ H_2$), as such a process would circumvent the reliance on, and generation of, carbon-based compounds. Ideally, water would serve the source of protons, and solar photovoltaic cells would generate the necessary energy.[1] Platinum electrodes are highly efficient catalysts for the hydrogen evolution reaction (HER), but the high cost and limit supply of platinum are prohibitive toward large-scale use. It would thus be highly desirable to replicate this efficient activity with base metal catalysts, which is currently an unmet challenge and an active area of research.[4] As a demonstration of the viability of such a goal, Nature employs hydrogenase enzymes containing active sites comprised of Ni and Fe centers to mediate proton reduction with high turnover frequency and low overpotentials, exhibiting efficiencies comparable to that of platinum electrodes.[5]

1.2.2 Biological Proton Reduction

1.2.2.1 Hydrogenase Enzymes

Hydrogenase enzymes catalyze the reversible reduction of protons to H_2, which allow for a broad range of microorganisms to employ H_2 as fuel and regulate intracellular redox properties.[6] Exhibiting turnover frequencies of up to *ca.* 10^4 s^{-1}, hydrogenases catalyze water-derived proton reduction under ambient temperatures and pressures at low overpotentials.[7] It is estimated that hydrogenase enzymes consume and produce a total of *ca.* 0.3 Gt H_2 per year,[8] making them a key player in the global hydrogen cycle.[9] These enzymes can be categorized as [NiFe], [FeFe], or [Fe] hydrogenases based on the metal composition in the active sites.[7,10] [NiFe] hydrogenase is the most abundant variant, and the proposed pathway for reversible H_2 evolution catalyzed by [NiFe] hydrogenase is depicted in Fig. 1.1.

Considering the case of proton reduction, introduction of $1e^-/1H^+$ to the diamagnetic Ni-SI_a state is believed to protonate a cysteine ligand to yield the S = ½ Ni-L state. Isomerization of the Ni-L state results in the S = ½ Ni-C intermediate, which is assigned as bearing a hydride bridging the Ni^{III} and Fe^{II} centers through pulse EPR and computational studies.[11] Introduction of another electron and proton results in cysteine protonation (Ni-R

state), and finally a heterolytic H–H bond formation yields dihydrogen to regenerate the Ni-SI_a state. Catalysis is hypothesized to be Ni-centered rather than Fe-centered; under turnover conditions, the iron center persists in the divalent state, whereas the Ni center accesses formal 1+, 2+, and 3+ oxidation states.[12] Accordingly, Ni-substituted rubredoxin is studied as a functional model enzyme for [NiFe] hydrogenase and bears an active site comprised of single Ni center bound to four cysteines.[13,14] Proton reduction catalysis mediated by Ni-substituted rubredoxin is believed to proceed via an analogous pathway as that of [NiFe] hydrogenase, including accessing a terminally bound Ni^{III}-H species akin to the Ni-C intermediate.

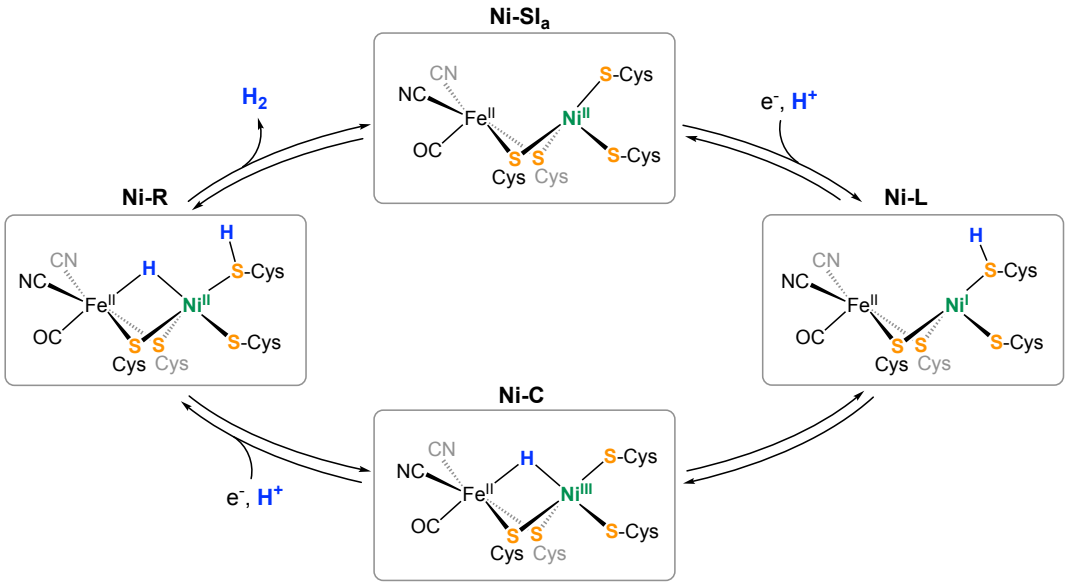

Figure 1.1. Proposed mechanism for reversible proton reduction mediated by [NiFe] hydrogenase

1.2.2.2 Nitrogenase Enzymes

Nitrogenase enzymes catalyze the conversion of dinitrogen to ammonia and play a crucial role in the global nitrogen cycle, generating around half of the bioavailable nitrogen on the planet.[15] Three nitrogenase variants are known, MoFe, VFe and Fe-only nitrogenases, which are categorized by the metal composition of the active sites.[16] Research on nitrogenase is generally motivated by its ability to fix dinitrogen, but a curious aspect of this reductive

process is the concomitant generation of at least one equivalent of H_2 per fixed N_2.[17] Given the tandem occurrence of biological N_2 and H^+ reduction, H_2 evolution has been proposed as an obligate step in the pathway for nitrogenase-catalyzed N_2 reduction.

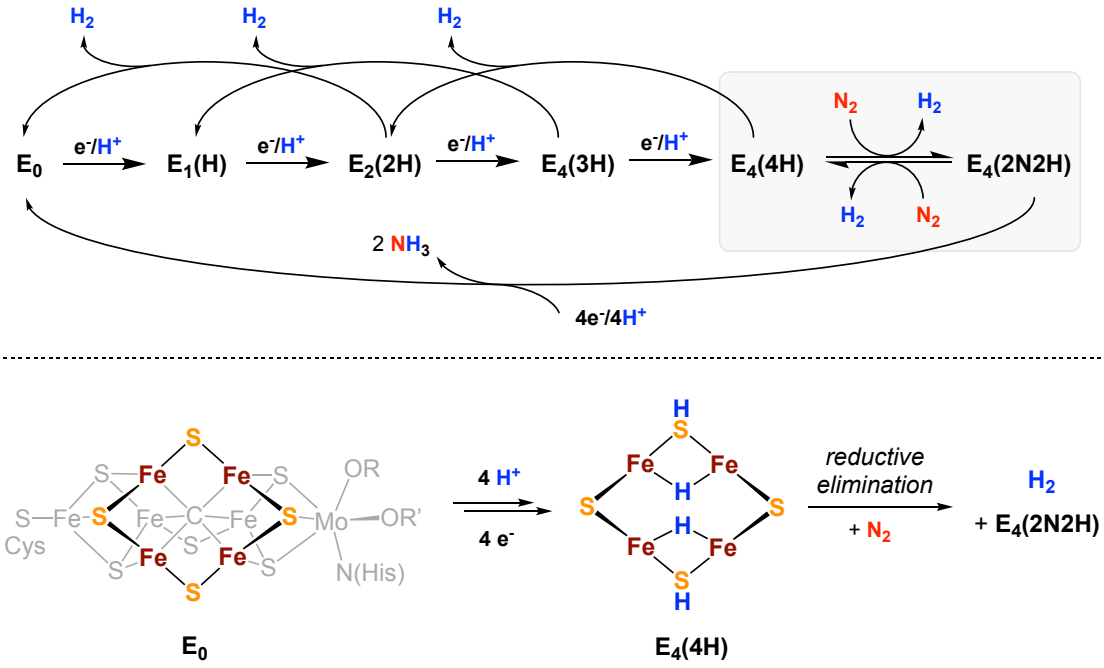

Figure 1.2. (top) Simplified Lowe-Thorneley model for biological nitrogen fixation; (bottom) Structure of the resting E_0 state of the FeMo cofactor and a depiction of bridging hydrides proposed in the $E_4(4H)$ state

The Lowe-Thorneley kinetic model describes the biological nitrogen fixation cycle as a function of electron loading, and a simplified model is illustrated in Figure 1.2.[18] Generated after introduction of 4 $e^-/4H^+$ to the resting E_0 state, the $S = ½$ $E_4(4H)$ state is a key intermediate where N_2 binding can occur and nitrogen fixation can proceed, or alternatively, evolution of two equivalents of dihydrogen can regenerate the resting E_0 state.[19] Pulse EPR studies on the purported $E_4(4H)$ state reveal two D_2O-exchangeable hydrogen nuclei assigned as bridging hydride (Fe–*H*–Fe) motifs.[19] In the productive pathway for ammonia generation, it is hypothesized that reductive elimination of dihydrogen from the two bridging hydrides precedes dinitrogen binding at E_4 state, and the formal 2 e^- reduction

upon dihydrogen evolution promotes dinitrogen activation at iron (Fig. 1.2).[20] Such a mechanism has been suggested to be universally operative for the MoFe, VFe, and Fe-only nitrogenases at different efficiencies.[21]

1.2.3 Molecular Proton Reduction Catalysis

1.2.3.1 Pathways for Molecular H−H Bond Formation

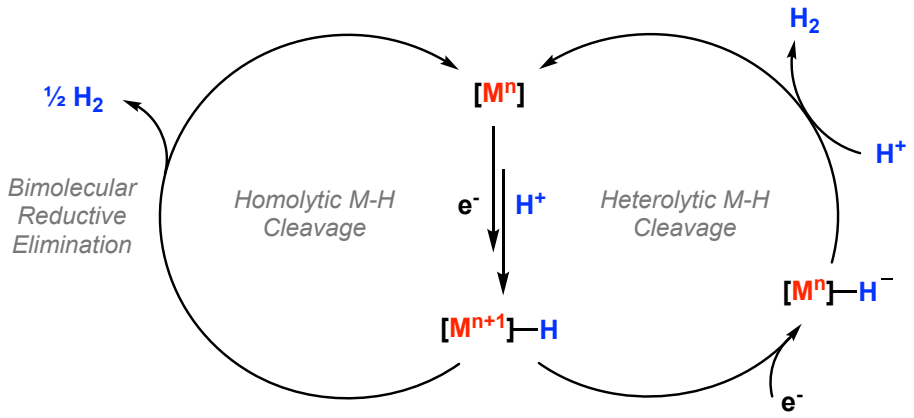

Figure 1.3. General pathways for proton reduction featuring the intermediacy of metal hydrides that may proceed through a homolytic and/or heterolytic pathway for H_2 evolution.

Molecular HER electrocatalysts containing Earth-abundant transition metals such as Mo, Fe, Co, and Ni have been developed,[21,22] and metal hydride intermediates are often implicated in HER schemes, akin to the biological HER pathways described above. The general mechanism for molecular HER catalysts involves protonation of the metal center to yield a metal hydride intermediate, and subsequent H–H bond formation may proceed either through a heterolytic or homolytic pathway for M–H bond cleavage (Fig. 1.3). The heterolytic pathway invokes metal hydride protonation to release H_2, whereas the homolytic pathway proceeds via bimolecular reductive elimination of H_2 from a metal hydride intermediate. Multiple pathways may be operative under turnover conditions. The stoichiometric protonation of metal hydrides to release H_2 is a commonly demonstrated transformation.[22] Considering the case of a solvated proton in MeCN, the hydricity (ΔG_{H^-}) of the metal hydride needs to be < 76 kcal/mol for protonation to be thermodynamically

favorable.[23] However, examples of bimolecular reductive elimination of dihydrogen from a well-defined metal hydride are limited. For metal hydrides with a M–H bond dissociation free energy less than *ca.* 52 kcal/mol, release of H_2 is thermodynamically favorable.[24] However, the demonstration of such reactivity from an observable metal hydride species is limited given the comparatively weak M–H bond and propensity for self-reaction.

1.2.3.2 Paramagnetic Metal Hydride Complexes

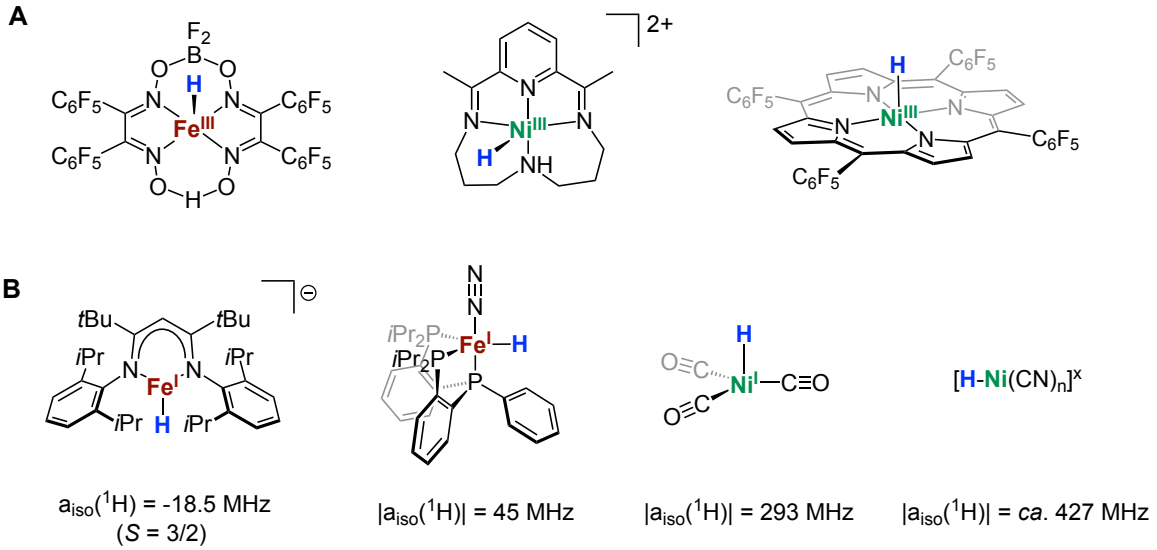

Figure 1.4. (A) Proposed paramagnetic iron and nickel hydride intermediates in electrochemical proton reduction. (B) Examples of terminally bound, paramagnetic hydrides with measured $a_{iso}(^1H)$ values. Spin states for these complexes are $S = ½$ unless otherwise noted.

In addition to being implicated in biological systems, the intermediacy of paramagnetic metal hydrides has been implicated in proton reduction catalyzed by synthetic electrocatalysts (Fig. 1.4A),[25–27] but such species are difficult to observe and study due to general instability, especially under turnover conditions.[28] Thermochemical studies reported by Tilset demonstrate considerable M–H bond weakening upon oxidation of several diamagnetic metal hydrides to the radical cation analogues.[29] Accordingly, spectroscopic data on such paramagnetic species in general are limited, and the study of model

paramagnetic metal hydride species can serve to canvass accessible pathways for H_2 evolution and be utilized to obtain relevant spectroscopic handles.

Particularly given that pulse EPR techniques have been employed to characterize enzymatic hydride-bound intermediates, the study of molecular metal hydrides through such techniques may aid the reliable assignment of these motifs in both biological and synthetic systems. Figure 1.4B depicts several examples of paramagnetic, terminal M–H species with measured hyperfine coupling values determined through EPR spectroscopy.[30–33] The hyperfine coupling tensor ($\mathbf{A} = [A_x, A_y, A_z]$) to an EPR-active nucleus can be parsed into the isotropic hyperfine constant ($a_{iso} = (A_x + A_y + A_z)/3$) and the dipolar tensor ($\mathbf{T}$; $\mathbf{A} = a_{iso} + \mathbf{T}$).[34] These parameters can be utilized to estimate spin density and probe local geometry; the isotropic hyperfine constant is a measure of the Fermi contact interaction, and the dipolar tensor reports on dipolar interactions. In general, spin density in atomic *s* orbitals contribute to the isotropic hyperfine constant for that nucleus, and spin density in *p* or *d* orbitals contribute to the dipolar tensor due to orbital nodes at the nucleus. Since hydrogen comprises of only the 1*s* orbital, the $a_{iso}(^1H)$ value can be directly used to estimate spin density on the hydride by scaling by the $a_{iso}(^1H)$ of a free hydrogen atom (1420 MHz; $a_{iso}(^1H)/1420 = \rho(^1H)$).[35] Furthermore, point-dipole models for metal hydrides suggest that terminally bound hydrides (M–H) are anticipated to exhibit approximately axial dipolar tensors ($\mathbf{T} \approx [t, t, -2t]$), whereas approximately symmetric bridging paramagnetic hydrides (M–H–M) are predicted to exhibit rhombic dipolar tensors ($\mathbf{T} \approx [t, -t, 0]$).[36]

1.3 Ammonia Oxidation to Dinitrogen

1.3.1 Ammonia as a Hydrogen Carrier and Fuel

In addition to the aforementioned carbon footprint associated with hydrogen production, another challenge to adopting a hydrogen fuel economy is the low volumetric energy density of hydrogen, which makes it challenging to transport and store.[37] The volumetric energy density of hydrogen at 700 bar is 5.6 MJ/L, compared to 32 MJ/L for gasoline at atmospheric pressure.[2] One solution is to use hydrogen carriers for more efficient transportation, which can then be converted to H_2 on site when power is required. Ammonia

is a promising candidate given its higher volumetric energy density (13.6 MJ/L at 10 bar), its relative ease of condensation, and the existing infrastructure and technology to distribute and store large quantities of ammonia.[38] Furthermore, research is also ongoing to utilize ammonia directly in fuel cells.[39] For example, the anodic reaction would be the oxidation of ammonia to dinitrogen ($2\ NH_3 \rightarrow N_2 + 6\ H^+ + 6\ e^-$), which could be coupled to dioxygen reduction to water at the cathode ($O_2 + 4\ H^+ + 4\ e^- \rightarrow 2\ H_2O$). Thus, for both hydrogen carrier and fuel cell applications, the development of efficient catalysts for the overall $6e^-/6H^+$ oxidation of ammonia to dinitrogen is essential.

1.3.2 Ammonia Oxidation Catalysts and Mechanistic Analogy to Water Oxidation

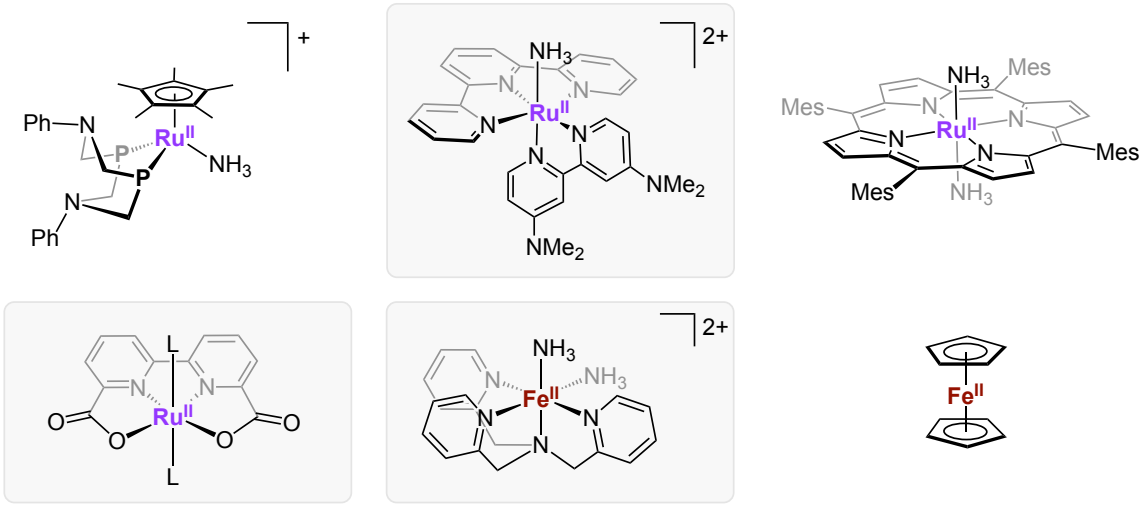

Figure 1.5. Reported homogenous catalysts for ammonia oxidation to dinitrogen. Complexes highlighted in gray are also demonstrated to catalyze water oxidation to dioxygen. **P** = P*t*Bu, Mes = mesityl

Early examples of stoichiometric ammonia oxidation include reports from the Taube, Meyer, and Collman groups using Os[40–43] and Ru[44–47] complexes, and there has been a recent renewed interest in this transformation. The first demonstration of catalytic ammonia oxidation was demonstrated last year from a polypyridyl Ru electrocatalyst,[48] and since then, several Ru[49–51] and Fe[52,53] catalysts for ammonia oxidation to dinitrogen have been reported, either under electrochemical or chemical reaction conditions (Fig. 1.5). Notably, several of

these systems for ammonia oxidation are also known to be water oxidation catalysts.[54–57] For the catalysts can mediate both water and ammonia oxidation, do these two transformations operate through analogous pathways? If so, is this mechanistic analogy more generally true for all complexes that mediate ammonia oxidation?

For water oxidation catalysts, metal oxo species are widely proposed intermediates, and the key O–O bond forming step is generally believed to be either nucleophilic attack by an exogenous equivalent of water/hydroxide or bimolecular coupling of two oxo fragments (Fig. 1.6A).[58] In the related case of ammonia oxidation to dinitrogen, analogous intermediates featuring metal-ligand multiple bonding have been proposed, namely metal imide and metal nitride species, which have been suggested to form N–N bonds either through nucleophilic attack by exogenous NH_3 or bimolecular coupling (Fig. 1.6B).[48,51] In contrast, while the N–N coupling of metal amides to yield hydrazine has been proposed as the N–N coupling step in ammonia oxidation catalyzed by ferrocene[53] and (tetramesitylporphyrin)Ru(NH_3),[50] there are no reported examples of such reactivity from a characterized M–NH_2 species.

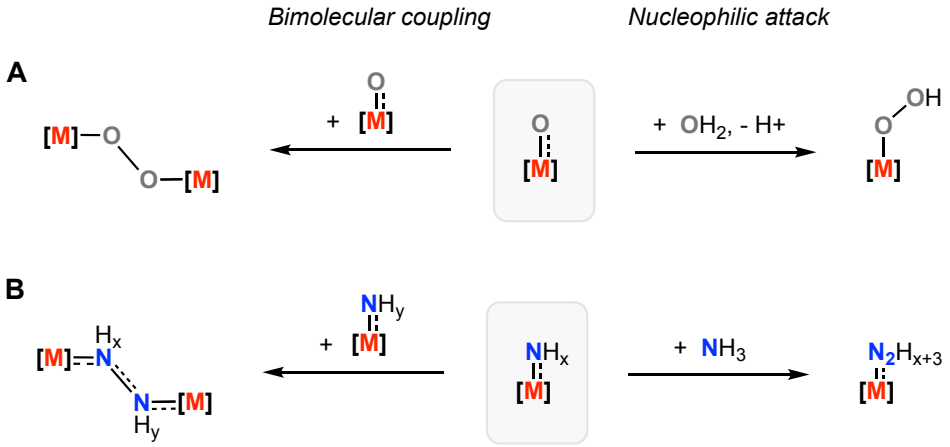

Figure 1.6. Possible pathways for (A) O−O bond formation in water oxidation and (B) N−N bond formation in ammonia oxidation

1.4 Redox Non-Innocence of Thiolate Ligands

Cysteine ligation is commonly found in metalloenzyme active sites, and the redox noninnocence of such motifs has been suggested to be a stabilizing factor in accessing formal

high-valent metal states under biological conditions.[59,60] The redox noninnocence of thiolate ligands is also observed in synthetic complexes, and in fact, dithiolene ligands were the first recognized example of redox non-innocent ligands in coordination compounds.[61] More generally, thiolate ligands have been spectroscopically demonstrated to bear significant spin density upon oxidation, which arises from the high degree of covalency in the M–S bond. For example, oxidation state formalism assigns the complexes depicted in Fig. 1.7 as Ni^{3+}/V^{5+}, whereas a purely ligand-based oxidation to generate a thiyl radical would yield no change in metal oxidation state. However, in both cases, the authors suggest that the "true oxidation state" of the metal center is somewhere in between the two resonance structures based on spectroscopic and computational data. In other words, the one-electron oxidation of the starting Ni^{2+}/V^{4+} complexes is borne out to a significant degree on both the metal center and supporting thiolate ligand(s), which stabilizes the oxidized species of high formal oxidation state. Thiolate-supported transition metal complexes are thus a suitable platform to pursue the spectroscopic characterization and reactivity of oxidized, formally high-valent complexes.

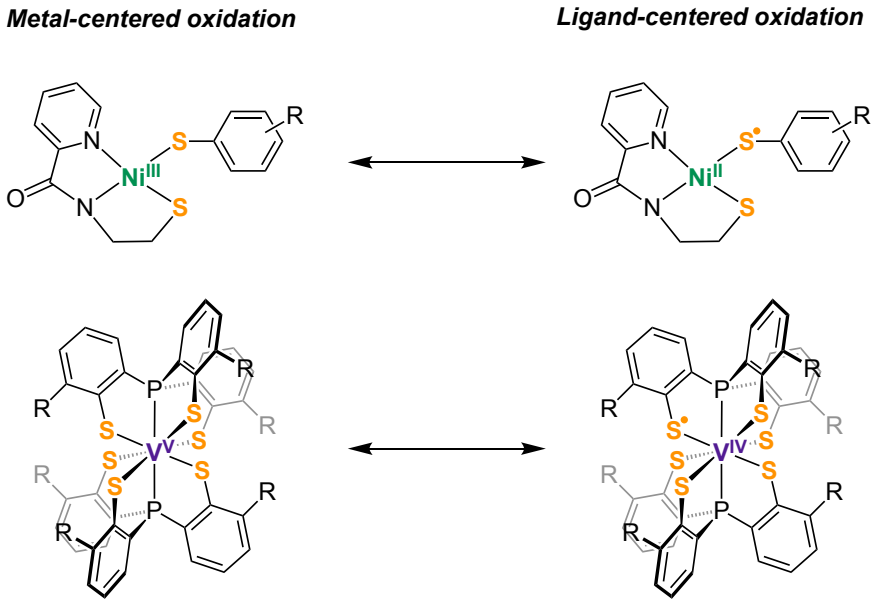

Figure 1.7. Resonance structures for thiolate-supported Ni and V complexes, illustrating the limiting metal-centered and ligand-centered oxidation descriptors.

1.5 Chapter Summaries

Chapter 2 describes the synthesis and characterization of a thiolate-supported $Fe^{III}(H)(N_2)$ species. Based on DFT calculations, there is significant spin delocalization onto the thiolate ligand, which likely stabilizes this $S = ½$ species at low temperatures to allow for characterization by methods including pulse EPR spectroscopy and X-ray diffraction. Upon warming, this ferric hydride is demonstrated to release H_2, and thermochemical and kinetic data support bimolecular reductive elimination as the mechanism for H_2 evolution. Notably, a positive entropic activation term is measured for this transformation, which is postulated to arise from dinitrogen dissociation prior to the rate-determining H–H bond forming step.

Chapter 3 details the synthesis of an $S = ½$ Ni^{III}–H species supported by the tetradentate ligand introduced in Chapter 2. Akin to the ferric hydride analogue, this Ni^{III}–H is observed to undergo bimolecular reductive elimination of dihydrogen upon warming, albeit with a measured negative entropic activation parameter. Spectroscopic characterization of the Ni^{III}–H species was carried out at low temperatures, and an isotropic hyperfine coupling value to the hydride is measured ($|a_{iso}(^1H)| = 11.7$ MHz). This measured $a_{iso}(^1H)$ is comparable to that measured for the bridging hydride in the Ni-C hydrogenase state, demonstrating that hydrides covalently bound to a paramagnetic nickel center can bear $a_{iso}(^1H)$ values on this order of magnitude; previous work on matrix-trapped Ni–H species exhibited $a_{iso}(^1H)$ values on an order of magnitude larger.

Chapter 4 demonstrates stoichiometric ammonia oxidation mediated by the Ni platform introduced in Chapter 3. This work demonstrates that the H–H homocoupling chemistry observed from the Ni^{III}–H species can be extended to other X-type ligands; the key N–N bond forming step is believed to be the coupling of two Ni^{III}–NH_2 species to yield a $Ni_2(N_2H_4)$ complex. Subsequent oxidation of the hydrazine fragment can be carried out to ultimately generate ammonia-derived dinitrogen, and several Ni-bound N_xH_y intermediates are synthesized and characterized.

In Chapter 5, a bimetallic VFe complex featuring a thiolate bridge is prepared, inspired by the V–S–Fe linkage of VFe nitrogenase. This VFe complex is demonstrated to be a highly active catalyst for the disproportionation of hydrazine to ammonia and dinitrogen.

The catalytic activity of the heterobimetallic VFe complex is greater than the sum of the activity of representative monometallic V and Fe analogues, suggesting a possible role for bimetallic cooperativity in the hydrazine disproportionation activity.

1.6 References

(1) Gray, H. B. *Nat. Chem.* **2009**, *1*, 7.
(2) Møller, K. T.; Jensen, T. R.; Akiba, E.; Li, H. *Prog. Nat. Sci*. **2017**, *27*, 34-40.
(3) Ogden, J. M. *Annu. Rev. Energy. Environ.* **1999**, *24*, 227-279.
(4) Roger, I.; Shipman, M. A.; Symes, M. D. *Nat. Rev. Chem.* **2017**, *1*, 3.
(5) Jones, A. K.; Sillery, E.; Albracht, S. P. J.; Armstrong, F. A. *Chem. Commun.* **2002**, *8*, 866-867.
(6) Vignais, P. M.; Billoud, B. *Chem. Rev.* **2007**, *107*, 4206–4272.
(7) Lubitz, W.; Ogata, H.; Rüdiger, O.; Reijerse, E. *Chem. Rev.* **2014**, *114*, 4081–4148.
(8) Thauer, R. K. *Eur. J. Inorg. Chem.* **2011**, *2011*, 919-921.
(9) Greening, C.; Constant, P.; Hards, K.; Morales, S. E.; Oakeshott, J. G.; Russell, R. J.; Taylor, M. C.; Berney, M.; Conrad, R.; Cook, G. M. *Appl. Environ. Microbiol.* **2015**, *81*, 1190-1199.
(10) Schilter, D.; Camara, J. M.; Huynh, M. T.; Hammes-Schiffer, S.; Rauchfuss, T. B. *Chem. Rev.* **2016**, *116*, 8693-8749.
(11) Brecht, M.; van Gastel, M.; Buhrke, T.; Friedrich, B.; Lubitz, W. *J. Am. Chem. Soc.* **2003**, *125*, 13075-13083.
(12) Brazzolotto, D.; Gennari, M.; Queyriaux, N.; Simmons, T. R.; Pécaut, J.; Demeshko, S.; Meyer, F.; Orio, M.; Artero, V.; Duboc, C. *Nat. Chem.* **2016**, *8*, 1054-1060.
(13) Slater, J. W.; Marguet, S. C.; Cirino, S. L.; Maugeri, P. T.; Shafaat, H. S. *Inorg. Chem.* **2017**, *56*, 3926-3938.
(14) Slater, J. W.; Marguet, S. C.; Monaco, H. A.; Shafaat, H. S. *J. Am. Chem. Soc.* **2018**, *140*, 10250-10262.
(15) Buscagan, T. M.; Rees, D. C. *Joule* **2019**, *3*, 2662-2678.
(16) Eady, R. R. *Chem. Rev.* **1996**, *96*, 3013-3030.
(17) Simpson, F.; Burris, R. *Science* **1984**, *224*, 1095-1097.
(18) Lowe, D. J.; Thorneley, R. N. *Biochem. J.* **1984**, *224*, 877-886.
(19) Hoeke, V.; Tociu, L.; Case, D. A.; Seefeldt, L. C.; Raugei, S.; Hoffman, B. M. *J. Am. Chem. Soc.* **2019**, *141*, 11984-11996.
(20) Hoffman, B. M.; Lukoyanov, D.; Yang, Z.-Y.; Dean, D. R.; Seefeldt, L. C. *Chem. Rev.* **2014**, *114*, 4041-4062.
(21) Harris, D. F.; Lukoyanov, D. A.; Kallas, H.; Trncik, C.; Yang, Z.-Y.; Compton, P.; Kelleher, N.; Einsle, O.; Dean, D. R.; Hoffman, B. M.; et al. *Biochemistry* **2019**, *58*, 3293-3301.
(22) Besora, M.; Lledós, A.; Maseras, F. *Chem. Soc. Rev.* **2009**, *38*, 957.
(23) Wiedner, E. S.; Chambers, M. B.; Pitman, C. L.; Bullock, R. M.; Miller, A. J. M.; Appel, A. M. *Chem. Rev.* **2016**, *116*, 8655-8692.

(24) Warren, J. J.; Tronic, T. A.; Mayer, J. M. *Chem. Rev.* **2010**, *110*, 6961-7001.
(25) Rose, M. J.; Gray, H. B.; Winkler, J. R. *J. Am. Chem. Soc.* **2012**, *134*, 8310-8313.
(26) Efros, L. L.; Thorp, H. H.; Brudvig, G. W.; Crabtree, R. H. *Inorg. Chem.* **1992**, *31*, 1722-1724.
(27) Han, Y.; Fang, H.; Jing, H.; Sun, H.; Lei, H.; Lai, W.; Cao, R. *Angew. Chem. Int. Ed.* **2016**, *55*, 5457-5462.
(28) Hu, Y.; Shaw, A. P.; Estes, D. P.; Norton, J. R. *Chem. Rev.* **2016**, *116*, 8427-8462.
(29) Tilset, M. *J. Am. Chem. Soc.* **1992**, *114*, 2740-2741.
(30) Chiang, K. P.; Scarborough, C. C.; Horitani, M.; Lees, N. S.; Ding, K.; Dugan, T. R.; Brennessel, W. W.; Bill, E.; Hoffman, B. M.; Holland, P. L. *Angew. Chem. Int. Ed.* **2012**, *51*, 3658-3662.
(31) Buscagan, T. M.; Oyala, P. H.; Peters, J. C. *Angew. Chem. Int. Ed.* **2017**, *56*, 6921-6926.
(32) Morton, J. R.; Preston, K. F. *J. Chem. Phys.* **1984**, *81*, 5775-5778.
(33) Symons, M. C. R.; Aly, M. M.; West, D. X. *J. Chem. Soc., Chem. Commun.* **1979**, *2*, 51-52.
(34) Roessler, M. M.; Salvadori, E. *Chem. Soc. Rev.* **2018**, *47*, 2534-2553.
(35) Wittke, J. P.; Dicke, R. H. *Phys. Rev.* **1956**, *103*, 620-631.
(36) Kinney, R. A.; Saouma, C. T.; Peters, J. C.; Hoffman, B. M. *J. Am. Chem. Soc.* **2012**, *134*, 12637-12647.
(37) Léon, A., Ed., Hydrogen Technology. Springer Berlin Heidelberg: Berlin, Heidelberg, 2008.
(38) Zamfirescu, C.; Dincer, I. *J. Power Sources* **2008**, *185*, 459-465.
(39) Lan, R.; Tao, S. *Front. Energy Res.* **2014**, *2*.
(40) Buhr, J. D.; Taube, H. *Inorg. Chem.* **1979**, *18*, 2208-2212.
(41) Coia, G. M.; Devenney, M.; White, P. S.; Meyer, T. J.; Wink, D. A. *Inorg. Chem.* **1997**, *36*, 2341-2351.
(42) Pipes, D. W.; Bakir, M.; Vitols, S. E.; Hodgson, D. J.; Meyer, T. J. *J. Am. Chem. Soc.* **1990**, *112*, 5507-5514.
(43) Demadis, K. D.; Meyer, T. J.; White, P. S. *Inorg. Chem.* **1997**, *36*, 5678-5679.
(44) Ishitani, O.; White, P. S.; Meyer, T. J. *Inorg. Chem.* **1996**, *35*, 2167-2168.
(45) Ishitani, O.; Ando, E.; Meyer, T. J. *Inorg. Chem.* **2003**, *42*, 1707-1710.
(46) Collman, J. P.; Hutchison, J. E.; Lopez, M. A.; Guilard, R.; Reed, R. A. *J. Am. Chem. Soc.* **1991**, *113*, 2794-2796.
(47) Collman, J. P.; Hutchison, J. E.; Ennis, M. S.; Lopez, M. A.; Guilard, R. *J. Am. Chem. Soc.* **1992**, *114*, 8074-8080.
(48) Habibzadeh, F.; Miller, S. L.; Hamann, T. W.; Smith, M. R. *Proc. Natl. Acad. Sci.* **2019**, *116*, 2849-2853.
(49) Bhattacharya, P.; Heiden, Z. M.; Chambers, G. M.; Johnson, S. I.; Bullock, R. M.; Mock, M. T. *Angew. Chem. Int. Ed.* **2019**, *58*, 11618-11624.
(50) Dunn, P. L.; Johnson, S. I.; Kaminsky, W.; Bullock, R. M. *J. Am. Chem. Soc.* **2020**, *142*, 3361-3365.
(51) Nakajima, K.; Toda, H.; Sakata, K.; Nishibayashi, Y. *Nat. Chem.* **2019**, *11*, 702-709.

(52) Zott, M. D.; Garrido-Barros, P.; Peters, J. C. *ACS Catal.* **2019**, *9*, 10101-10108.
(53) Raghibi Boroujeni, M.; Greene, C.; Bertke, J. A.; Warren, T. H. *preprint*, **2019**, D OI: 10.26434/chemrxiv.9729635.v1
(54) Duan, L.; Bozoglian, F.; Mandal, S.; Stewart, B.; Privalov, T.; Llobet, A.; Sun, L. *Nat. Chem.* **2012**, *4*, 418-423.
(55) Fillol, J. L.; Codolà, Z.; Garcia-Bosch, I.; Gómez, L.; Pla, J. J.; Costas, M. *Nat. Chem* **2011**, *3*, 807-813.
(56) Concepcion, J. J.; Jurss, J. W.; Templeton, J. L.; Meyer, T. J. *J. Am. Chem. Soc.* **2008**, *130*, 16462-16463.
(57) Concepcion, J. J.; Jurss, J. W.; Norris, M. R.; Chen, Z.; Templeton, J. L.; Meyer, T. J. *Inorg. Chem.* **2010**, *49*, 1277-1279.
(58) Blakemore, J. D.; Crabtree, R. H.; Brudvig, G. W. *Chem. Rev.* **2015**, *115*, 12974–13005.
(59) Hausinger, R. P. Biochemistry of Nickel. Springer US: Boston, MA, 1993.
(60) Das, P. K.; Samanta, S.; McQuarters, A. B.; Lehnert, N.; Dey, A. *Proc. Natl. Acad. Sci.* **2016**, *113*, 6611-6616.
(61) Eisenberg, R.; Gray, H. B. *Inorg. Chem.* **2011**, *50*, 9741-9751.

Chapter 2

AN $S = ½$ IRON COMPLEX FEATURING N_2, THIOLATE, AND HYDRIDE LIGANDS: REDUCTIVE ELIMINATION OF H_2 AND RELEVANT THERMOCHEMICAL FE–H PARAMETERS

2.1 Introduction

Despite a wealth of recent progress towards functional models of biological N_2-to-NH_3 conversion,[1,2] many questions remain as to how the active site cofactors of nitrogenase enzymes, as in the iron-molybdenum cofactor (FeMoco) of MoFe-nitrogenase,[3] manage N_2 binding and the subsequent bond-breaking and making steps en route to NH_3 formation. While the community has primarily focused on iron as the most likely site/s of N_2 binding in recent years,[4] a particular conundrum concerns the presence of relatively weak-field sulfide (S^{2-}) ligands around the candidate iron sites,[5] as yet unknown ligands in Fe–N_2 model chemistry, and the related requirement that N_2 binding must occur at a biologically accessible redox potential.[6]

One plausible scenario to help account for N_2 binding at iron at the FeMoco is that redox leveling of successive electron transfer steps may be achieved by concomitant proton transfers[7] to generate, for example, protonated sulfides (e.g., SH^-)[8] and/or iron hydrides (e.g. Fe–H, Fe–(μ-H)–Fe).[9] Such a scenario would not only alleviate local charge build-up, thereby buffering redox potential, but would also install comparatively strong-field hydrides that are compatible with, and might even facilitate, Fe–N_2 bound states.[4,10] Hence, there is substantial motivation to prepare synthetic model complexes featuring Fe–N_2 with a combination of thioether[11,12]/thiolate[13,14] and hydride ligands within the immediate iron coordination sphere.[15]

Relatedly, spin-active model complexes of these types, and $S = ½$ systems especially, may provide needed spectroscopic parameters to help guide reliable assignments of

intermediate states within the biological systems. Accordingly, various EPR techniques have proven effective for observing $S = ½$ intermediate states during nitrogenase turnover (e.g., hydride- and N_xH_y-bound states),[4,9,16] and an EPR-active, hydride-bound nitrogenase state, where the hydride ligands have been assigned as iron-ligated, has been proposed to undergo H_2 elimination concurrent with nitrogen uptake and subsequent reduction.[9,17]

H_2 elimination steps from metal-bound hydride states are also presumed to be relevant to iron-rich hydrogenase enzymes,[18,19] and often in synthetic molecular catalysts for the hydrogen evolution reaction (HER),[19,20] including examples featuring Fe, Co, and Ni.[20bc,21,22] When considering the key H–H bond formation step from metal hydride complexes, there are a number of pathways one might consider, including bond formation via direct protonation of the hydride ligand,[23] ligand-facilitated protonation of metal hydrides,[20b,24] and reductive elimination from a metal polyhydride species.[25] In particular, although bimolecular reductive elimination of H_2 from metal hydride species has been demonstrated to play a role in electrocatalytic systems for proton reduction,[22] examples of such reactivity from well-defined terminal metal hydride complexes are limited.[26] There is thus substantial motivation to map the reactivity patterns and fundamental thermochemical parameters of Fe–H (and other M–H) species in the presence of thiolate and N_2 ligands, particularly in systems where H_2 evolution is viable.

In this study, we report the synthesis and characterization of structurally unusual Fe(H)(N_2)(thiolate) complexes in two redox states, $S = 0$ Fe^{II}(H)(N_2)(thiolate) and $S = ½$ Fe^{III}(H)(N_2)(thiolate), which have each been characterized by numerous techniques, including by XRD analysis and pulse electron-nuclear double resonance (ENDOR) spectroscopy for the $S = ½$ state. EPR data for terminally bound and open-shell Fe–H species, regardless of the other ligands in the coordination sphere, is highly limited.[2,27,28] Furthermore, prior to this report, Fe–N_2 complexes have, to our knowledge, only been characterized in oxidation states of 2+ and lower;[29] our finding that Fe(III) binds a weakly activated N_2 ligand in the presence of thiolate and hydride ligands is hence noteworthy.

The Fe^{III}(H)(N_2)(thiolate) species persists at low temperatures in solution but undergoes bimolecular conversion to a diiron Fe^{II}–N_2–Fe^{II} product upon warming, along

with associated loss of H_2. Such reactivity has strong precedence for second- and third-row transition metal hydrides,[26] but is still unusual among first-row metal hydrides,[30,31,32,33,34] and among paramagnetic hydrides in general.[26ab,27] Thus, the present Fe^{II}/Fe^{III} hydride system offers an opportunity to map kinetic parameters for H_2 evolution and fundamental Fe–H thermochemical (H^+, $H^\bullet$, H^-) parameters of broad current interest in the context of HER and small molecule reduction catalysis.[35]

2.2 Results and Discussion

2.2.1 Synthesis and Characterization of $Fe^{II}(H)(N_2)$(thiolate), 2.7-H and $Fe^{III}(H)(N_2)$(thiolate), 2.8-H

To template a thiolate-supported iron(N_2) complex, we envisioned the incorporation of a thiolate group within a polyphosphino silyl framework, a motif our lab has previously utilized to gain entry into Fe(N_2) chemistry (Scheme 2.1).[36] Alkylation of 2-phenylbenzenethiol (**2.1**)[37] followed by directed ortho lithiation provides the aryl lithium salt (**2.3**) as a TMEDA adduct (88%). Treatment of bis(*o*-diisopropylphosphino-phenyl)-chlorosilane (**2.4**)[12] with **2.3** affords the ligand $HSiP_2S$ (**2.5**) (Scheme 2.1a; 66%). A singlet corresponding to the two phosphines is observed by ^{31}P NMR spectroscopy at 1.10 ppm, and IR spectroscopy reveals an Si–H stretch at 2228 cm^{-1}. Complexation of **2.5** using $FeCl_2$ and subsequent addition of excess MeMgCl promotes cleavage of the Si–H and S–*i*Pr bonds to afford the thiolate-bound, yellow-brown complex $[(SiP_2S)Fe]_2(\mu\text{-}N_2)$ (**2.6**) in moderate yield (Scheme 2.1b). The two previous reports of thiolate-coordinated Fe(N_2) species exhibit terminally bound N_2 ligands.[13,14]

Compound **2.6** exhibits a bridging N_2 ligand coordinated end-on to each iron center. This is confirmed by X-ray crystallography, which elucidates two similar but crystallographically distinct iron centers in the solid state with a bridging N≡N bond length of 1.138(2) Å (Fig. 2.1a, Table 2.1). A weak N_2 stretch at 1888 cm^{-1} is observed in the solid-state by IR spectroscopy, consistent with the absence of a rigorous inversion center. The 80 K ^{57}Fe Mössbauer spectrum of **2.6** can be fit to one unique iron center (δ = 0.447 mm/s, ΔE_Q = 1.776 mm/s) with an isomer shift similar to other five-coordinate, $S = 1$ iron species ligated

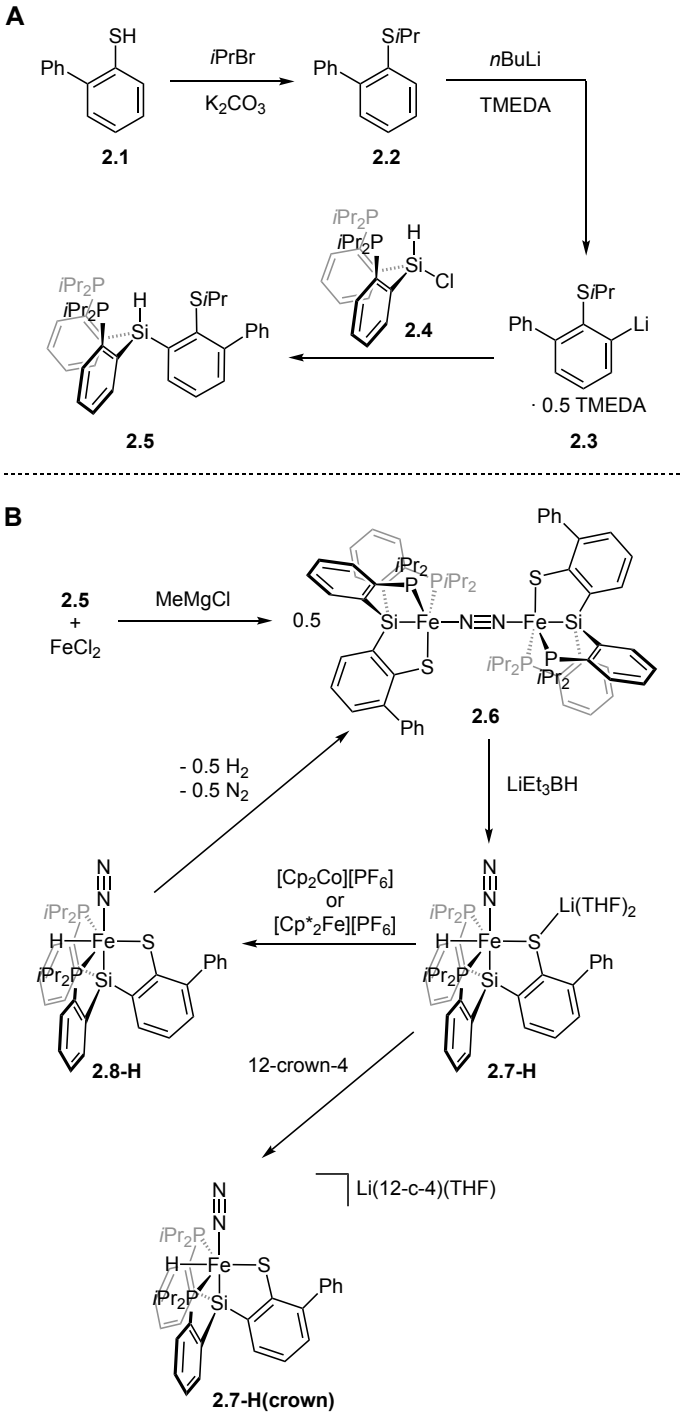

Scheme 2.1. (A) Synthesis of ligand precursor **2.5**. (B) Metallation procedure of **2.5** to yield diiron **2.6**, and the synthesis of species **2.7-H**, **2.7-H(crown)** and **2.8-H**.

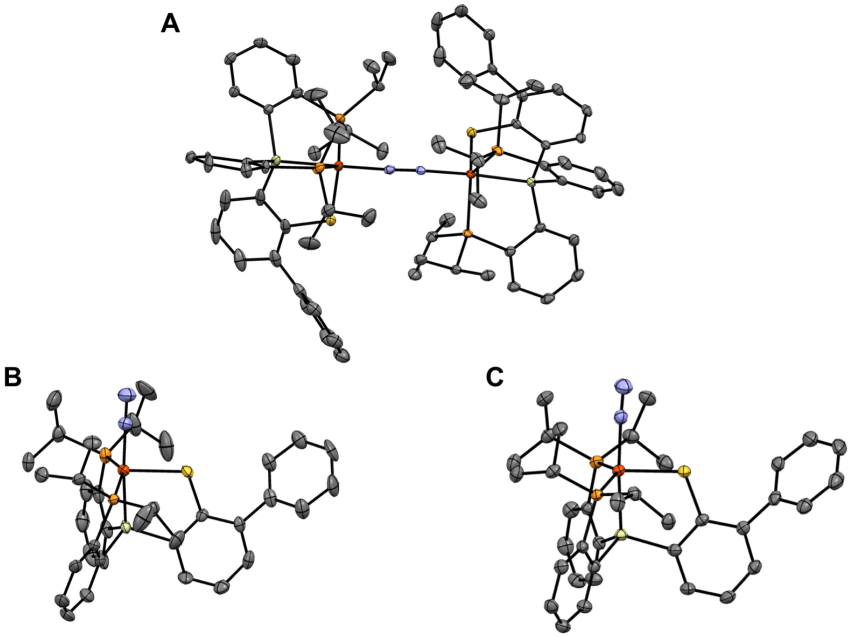

Figure 2.1. X-ray structures of (A) **2.6** (B) **2.7-H(crown)** (C) **2.8-H**. C-*H* hydrogen atoms, solvent molecules, and the counterion of **2.7-H(crown)** are omitted for clarity. Ellipsoids are depicted at 50% occupancy.

Table 2.1. Select bond metrics and angles of complexes **2.6**, **2.7-H(crown)**, and **2.8a**[a]

	***d*(Fe–N)**	***d*(N–N)**	***d*(Fe–P)**	***d*(Fe–S)**	**∠(P–Fe–P)**	**∠(P–Fe–S)**
2.6	1.871(1)	1.138(2)	2.3059(6) 2.3132(7)	2.2314(5)	130.72(2)	110.53(2) 112.59(2)
	1.865(1)	-	2.3444(6) 2.3189(5)	2.2323(6)	131.34(2)	110.75(2) 111.98(2)
2.7-H(crown)	1.810(4)	1.117(6)	2.16(1) 2.180(2)	2.339(2)	146.5(3)	104.21(6) 106.3(3)
2.8-H	1.822(3)	1.077(4)	2.2541(8) 2.2422(8)	2.2185(7)	138.70(3)	106.98(3) 111.19(3)

[a] Bond distances listed in Å and bond angles listed in degrees

by related polyphosphine ligands.[38] The room temperature solution-state magnetic moment of compound **2.6** ($\mu_{eff} = 4.8\mu_B$) suggests an overall $S = 2$ species, and magnetic susceptibility data collected between 25 ˚C and −75 ˚C obey the Curie-Weiss law. These data are consistent

with a description for **2.6** featuring two $S = 1$ centers with strong ferromagnetic exchange. Strong ferromagnetic coupling has been observed in an $S = 3/2$, dinitrogen-bridged Fe(I)/Fe(II) species,[12] and weak ferromagnetic exchange in an $S = 3$ Fe(I)/Fe(I) species,[39] both previously described by our lab. Alternatively, Fe–N≡N–Fe species are known to exhibit antiferromagnetic coupling between iron centers,[2] or bear iron centers antiferromagnetically coupled to an $S = 1$ dinitrogen (N_2^{2-}) unit.[40]

To install the desired hydride ligand on iron, we found that treatment of diiron **2.6** with lithium triethylborohydride affords red, diamagnetic $[(SiP_2S)Fe^{II}(H)(N_2)]Li(THF)_2$ (**2.7-H**). X-ray diffraction data confirms the assignment of **2.7-H** and reveals a coordinated dinitrogen with an N–N bond length of 1.128(9) Å. Although the hydride ligand could not be resolved from the XRD analysis of **2.7-H**, a wide P–Fe–P angle of 145.24(7)° is consistent with the presence of a hydride located between the two phosphine groups. Furthermore, a hydridic resonance coupled to the two ^{31}P nuclei is observed by ^1H NMR spectroscopy at −19.32 ppm (t, $^3J_{H,\ P}$ = 71.3 Hz), absent in the ^1H NMR spectrum of $[(SiP_2S)Fe^{II}(D)(N_2)]Li(THF)_2$ (**2.7-D**); the latter species is obtained in an analogous fashion to **2.7-H** with lithium triethylborodeuteride. IR spectroscopy of compound **2.7-H** reveals three N_2 stretches (2020, 1976, 1935 cm^{-1}) that presumably arise from distinct coordination modes of the lithium cation, and an Fe–H stretch at 1864 cm^{-1} that is absent in the IR spectrum of **2.7-D**. Treatment of **2.7-H** with 12-crown-4 affords $[(SiP_2S)Fe^{II}(H)(N_2)][Li(12\text{-crown-4})(THF)]$ (**2.7-H(crown)**), which is isolated as a red solid. IR spectroscopy of **2.7-H(crown)** shows a single N_2 stretch at 1971 cm^{-1} (ν(Fe–H) at 1886 cm^{-1}), and XRD analysis of **2.7-H(crown)** confirms its relation to **2.7-H** (Fig. 2.1b, Table 1).

Room temperature cyclic voltammetry measurements of **2.7-H** in THF reveal a reversible oxidation event at −1.63 V vs. Fc/Fc^+, corresponding to the $Fe^{III/II}$ couple (Fig. 2.2a). Chemical oxidation of the Fe(II) precursor **2.7-H** with $[Cp_2Co][PF_6]$ affords a dark blue solution that persists for several hours at room temperature, enabling the characterization of the title complex $(SiP_2S)Fe^{III}(H)(N_2)$ (**2.8-H**). Neutral **2.8-H** co-crystallizes with crystals of the cobaltocene byproduct; despite repeated attempts, **2.8-H** and

Cp_2Co could not be separated, owing to very similar solubility. Nevertheless, high quality X-ray data confirms the solid-state structure of **2.8-H** (Fig. 2.1, Table 2.1).

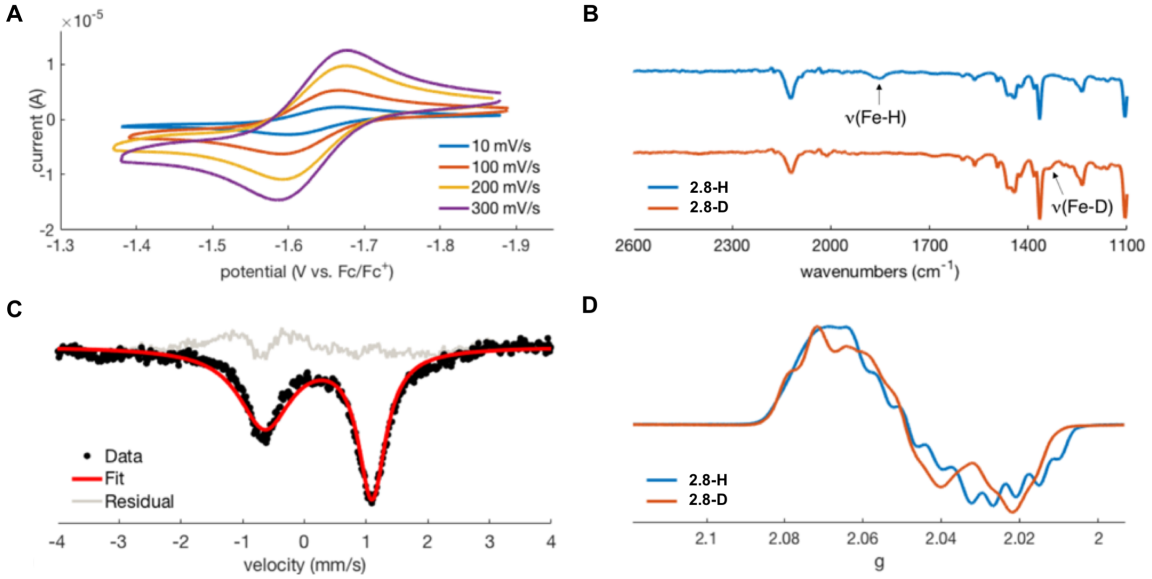

Figure 2.2. (A) Cyclic voltammetry of **2.7-H** at various scan rates depicting the $Fe^{III/II}$ couple at −1.63 V vs. Fc/Fc^+ (0.4 M $[NBu_4][PF_6]$ in THF). (B) Thin-film IR spectra of isotopologues **2.8-H** and **2.8-D**. (C) ^{57}Fe Mössbauer spectrum of **2.8-H** collected at 80 K with a 50 mT applied parallel field. (D) 77 K CW X-band EPR spectra of isotopologues **2.8-H** and **2.8-D** in 2-MeTHF.

Compared to the crystallographic data for **2.7-H(crown)**, the structure of **2.8-H** reveals elongation of the *Fe–N*≡N bond (from 1.810(4) Å to 1.882(3) Å) and contraction of the N≡N bond (1.117(6) Å to 1.077(4) Å) upon oxidation, consistent with poorer π-donicity from the more oxidized iron center. The crystallographically determined N≡N bond length of **2.8-H** of 1.077(4) Å suggests that the dinitrogen fragment is only weakly activated (1.0975 Å in free N_2).[41] Furthermore, the Fe–P bond lengths elongate upon conversion of diamagnetic **2.7-H(crown)** to doublet **2.8-H**, consistent with the observed correlation between spin state and Fe–P bond length noted on related polyphosphino Fe complexes.[42] The hydride ligand can be located in the difference map of **2.8-H** and freely refined to an Fe–H bond length of 1.54(4) Å, comparable to the crystallographically determined Fe–H bond lengths of other paramagnetic, terminal iron hydride species.[28a,b] The isotopologue $(SiP_2S)Fe^{III}(D)(N_2)$ (**2.8-D**) is prepared in an analogous fashion to **2.8-H** via oxidation of **2.7-D**. Spectroscopic

characterization of charge-neutral **2.8-H** and **2.8-D** is carried out on samples generated *in situ* at −78 °C. Furthermore, manipulations with **2.8-H** and **2.8-D** are carried out at low temperature due to their thermal instability (*vide infra*).

The IR spectrum of **2.8-H** reveals N_2 and Fe–H stretches at 2123 cm^{-1} and 1852 cm^{-1}, respectively (Fig. 2.2b). Compared to **2.7-H(crown)**, there is a 152 cm^{-1} shift in the N_2 stretching frequency upon oxidation, consistent with a metal-centered oxidation. The observed Fe–D IR stretch of **2.8-D** is in good agreement with the values predicted by the simple harmonic oscillator model (calculated: 1321 cm^{-1}; observed: 1333 cm^{-1}). Additionally, the ^{57}Fe Mössbauer spectrum of **2.8-H** is consistent with a single iron-containing species (δ = 0.227 mm/s, ΔE_Q = 1.734 mm/s); these parameters correspond to an approximate fit due to asymmetric line broadening of the spectrum (Fig. 2.2c).[43] Broad, paramagnetically shifted peaks are observed by ^{1}H NMR spectroscopy of **2.8-H** at −78 °C, and the S = ½ spin state is corroborated by continuous-wave (CW) EPR spectroscopy (Fig. 2.2d, *vide infra*).[44]

In addition to the coordination of a strong field hydride ligand, the ferric Fe–N_2 species **2.8-H** is additionally stabilized by partial spin delocalization onto the aryl thiolate ligand;[45] this attenuates the perturbation to Fe–N_2 and Fe–H bonding upon oxidation. There is significant contraction in the Fe–S bond of the more oxidized **2.8-H** (2.2185(7) Å) compared to **2.7-H(crown)** (2.339(2) Å), which contrasts with the observed elongation of the Fe–P bonds in the ferric analogue (Fe–P_{avg}: 2.17 Å in **2.7-H(crown)**, 2.25 Å in **2.8-H**).

The spin density map of the gas-phase optimized **2.8-H** structure (M06-L: def2tzvp (Fe), def2svp (all other atoms)) indeed reveals partial spin leakage onto the sulfur atom, with lesser delocalization onto the other coordinated fragments (Fig. 2.3). However, the calculated distribution of unpaired spin suggests that the oxidation is predominantly metal based, which is consistent with the significant shift in N_2 stretching frequency observed between **2.7-H(crown)** and **2.8-H**. There is a calculated spin density of 0.92 e^- (58%) localized at Fe and 0.18 e^- (11%) at sulfur. Additionally, the calculated −0.029 e^- (2%) localized on the hydride fragment is consistent with the experimentally observed hyperfine coupling obtained via EPR and ENDOR spectroscopies (*vide infra*).

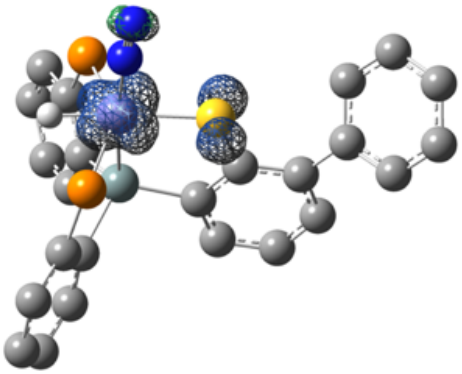

Figure 2.3. Spin density map of gas-phase optimized structure of compound **2.8-H** (Isovalue: 0.005 $e^{-}/Å^3$; M06-L functional: def2tzvp (Fe), def2svp (all other atoms)). Atom colors: Fe (purple), S (yellow), H (white), P (orange), C (gray), N (blue), Si (light blue).

2.2.2 EPR and ENDOR Characterization of 2.8-H

The 77 K X-band CW EPR spectrum of **2.8-H** (Fig. 2.2d) shows a rhombic signal, which is simulated with slight g anisotropy (**g** = [2.07, 2.0475, 2.02]). Q-band Davies ENDOR spectra collected at 18.5 K on **2.8-H** across the EPR envelope are simulated well (Fig. 2.4a) with coupling to the hydridic ^{1}H nucleus (**A**(^{1}H) = ±[15, 56, 58] MHz) with a small Euler rotation β = 25° of the ^{1}H **A** tensor relative to the g-tensor, and two similar but inequivalent ^{31}P nuclei (**A**(^{31}Pα) = ±[31, 36, 27] MHz; **A**(^{31}Pβ) = ±[28, 25, 23] MHz). Additional coupling to a ^{1}H nucleus is also observable (**A**(^{1}H') = ±[6.8, 10, 6.8] MHz), likely arising from coupling to hydrogen atom(s) of the ligand; this coupling is also present in the spectra of **2.8-D**. ENDOR data on **2.8-D** are additionally simulated (Fig. 2.4b) with coupling to two ^{31}P nuclei with identical parameters as that of **2.8-H** and a ^{2}H nucleus; almost complete disappearance of the ^{1}H hydride signal is also evident. The ^{2}H signal can be suitably simulated by scaling **A**(^{1}H) by the ratio of the ^{2}H/^{1}H gyromagnetic ratios, (**A**(^{2}H) = ±[2.3, 8.6, 8.9] MHz), and the X-band CW EPR spectra of both **2.8-H** and **2.8-D** are simulated well by using the hyperfine coupling constants obtained via ENDOR spectroscopy (Fig. 2.4c,d).

Pulse EPR data on an S = ½ freeze-trapped state of MoFe nitrogenase, which has been observed during FeMoco-catalyzed proton reduction[9] and nitrogen fixation,[46] are consistent with the accumulation of hydride intermediates at the cofactor under turnover conditions. Two ^{1}H nuclei (H_1: a_{iso} = 24.3 MHz, **T** = [−13.3, 0.7, 12.7] MHz; H_2: a_{iso} = 22.3

MHz, **T** = [10.7, −12.3, 1.7] MHz) are assigned as Fe–(μ-H)–Fe moieties.[9a] The ^{1}H signals are believed to arise from bridging hydrides, as opposed to terminal, due to the approximate rhombic symmetry of the dipolar tensor; a point-dipole model predicts a dipolar tensor of approximate axial symmetry for a terminally bound hydride.[47]

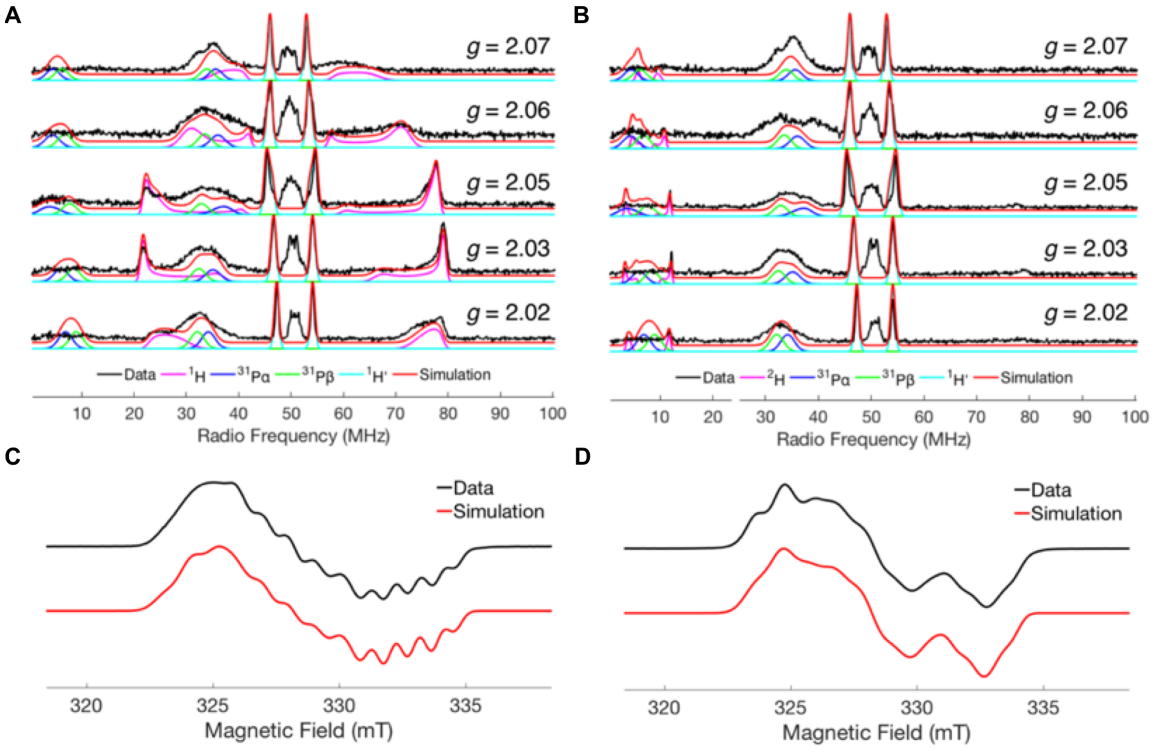

Figure 2.4. Field-dependent Q-band Davies ENDOR of (a) **2.8-H** and (b) **2.8-D** in 2-MeTHF with simulations. Simulation parameters: **g** = [2.07, 2.0475, 2.02]; **A**(^{31}Pα) = ±[31, 36, 27] MHz; **A**(^{31}Pβ) = ±[28, 25, 23] MHz; **A**(^{1}H') = ±[6.8, 10, 6.8] MHz. Fig. 2.4a was simulated with additional coupling to Fe–*H* (**A**(^{1}H) = ±[15, 56, 58] MHz), whereas Fig. 2.4b was simulated with additional coupling to Fe–*D* (**A**(^{2}H) = ±[2.3, 8.6, 8.9] MHz). Summation of individual component ENDOR simulations is displayed in red. Experimental conditions: microwave frequency = 33.674 GHz; MW π pulse length = 40 ns; interpulse delay τ = 300 ns; π_{RF} pulse length = 15 μs; TRF delay = 1 μs; shot repetition time (srt) = 5 ms; temperature = 18.5 K; RF frequency randomly sampled. 77 K X-band CW EPR spectra of (c) **2.8-H** and (d) **2.8-D** in 2-MeTHF with simulations. The CW EPR spectra were simulated with the same parameters as the corresponding ENDOR spectra.

Decomposition of the hydridic ^{1}H coupling constants of **2.8-H** to the isotropic and dipolar contributions yields an isotropic value of $a_{iso} = \pm 43$ MHz and an approximately axial dipolar tensor of $\mathbf{T} = \pm [-28, 13, 15]$ MHz, in good agreement with the predicted tensor symmetry for a terminal hydride. Notably, this experimental a_{iso} value indicates that ± 0.030 e^- is localized at the hydride ligand,[48] which is consistent with the DFT-calculated value of –0.029 e^-. The greater a_{iso} value observed for **2.8-H** compared to that of the hydride-bound form of FeMoco correlates with greater spin density localized at the hydrogen atom of **2.8-H**, presumably due to a greater degree of spin delocalization within the cofactor.

2.2.3 Bimolecular H_2 Elimination from 2.8-H.

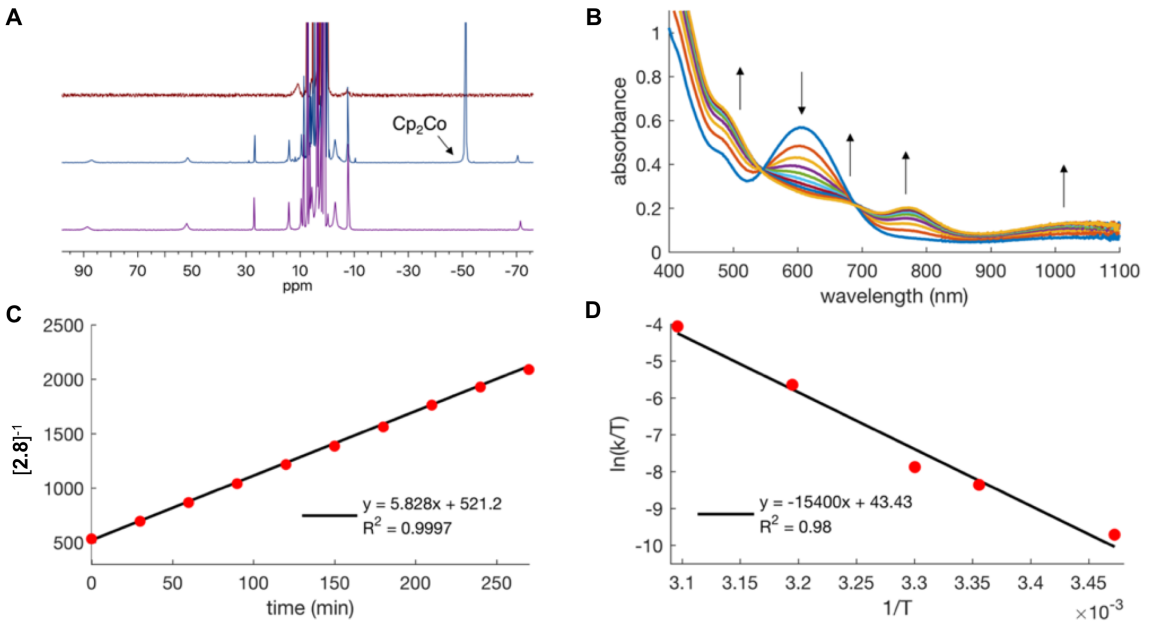

Figure 2.5. (A) ^{1}H NMR spectra of **2.8-H** in THF-d_8 collected at −78 °C (top) and after stirring at 25 °C overnight (middle), with ^{1}H NMR spectrum of **2.6** in THF-d_8 (bottom). (B) UV-vis spectra showing the decay of **2.8-H** and the growth of **2.6** at 50 °C. Spectra were collected every 30 min. (C) Plot of $[\mathbf{2.8\text{-}H}]^{-1}$ (M^{-1}) versus time, using the UV-vis data shown in Fig. 2.5b. (D) Eyring plot of the conversion of **2.8-H** to **2.6**. (T in K, k in $M^{-1}\cdot min^{-1}$).

Although $Fe^{III}(H)(N_2)$(thiolate) **2.8-H** could be spectroscopically characterized, it is thermally unstable in solution and liberates H_2. Monitoring a THF-d_8 solution of **2.8-H** at room temperature by ^{1}H NMR spectroscopy reveals the near quantitative conversion of dark blue **2.8-H** to yellow-brown **2.6** overnight, which corresponds to formal loss of an $H^{\bullet}$ and

half an N_2 molecule per Fe (Fig. 2.5a). H_2 liberation was confirmed by GC analysis of the headspace.

Monitoring the decay of **2.8-H** at 50 °C by UV-vis spectroscopy shows that **2.8-H**, with an absorption at 607 nm, decays in concert with the growth of **2.6** (Fig. 2.5b). The decay of **2.8-H** follows second-order kinetics (Fig. 2.5c), consistent with a bimolecular H_2 reductive elimination pathway to all-ferrous diiron **2.6**. The UV-vis timecourse data display isosbestic behavior, and the absence of observable intermediates indicates that transformations prior to the rate determining step are both endergonic and reversible. At 25 °C, the conversion of **2.8-H** to **2.6** proceeds with a second-order rate constant of $k = 0.068\ M^{-1}\cdot min^{-1}$. Monitoring the decay of **2.8-D** reveals a kinetic isotope effect of 1.7 at 25 °C, suggesting a role for the hydride ligand in the transition state of the rate determining step. An early transition state featuring substantial Fe–H character in a bimolecular reductive elimination step is consistent with these data.[49]

Eyring plot analysis of the conversion of **2.8-H** to diiron **2.6** provides the following activation parameters: $\Delta H^{\ddagger} = 31(4)$ kcal/mol; $\Delta S^{\ddagger} = 39(13)$ cal/(mol·K); $\Delta G^{\ddagger} = 19$ kcal/mol (25 °C) (Fig. 2.5d). The large and positive $\Delta S^{\ddagger}$ value is surprising as the transition state of two iron centers interacting in an ordered manner is likely to incur high entropic cost. For comparison, Wayland's classic study of Rh(II)-porphyrin metalloradical M–H/M–R species shows that bimolecular release of R–H provides negative entropies of activation correlated with highly ordered, tertiary transition states (e.g., $\{[Rh]–H\cdots R–[Rh]\}^{\ddagger}$).[50]

For the present iron system, we suggest that the large and positive $\Delta S^{\ddagger}$ value may be rationalized if a requisite N_2-dissociation step precedes the rate determining step via pre-equilibration of an N_2-bound and an N_2-dissociated state. A plausible mechanism consistent with this scenario and the data in hand is depicted in Fig. 2.6. Accordingly, an N_2 ligand of **2.8-H** first dissociates, giving rise to free N_2 and an unobserved, reactive hydride intermediate, $(SiP_2S)Fe^{III}H$. This Fe–H intermediate is intercepted by **2.8-H**, present at much higher concentration, via a transition state containing one N_2 ligand and two Fe–H subunits, then decaying to H_2 and the final product, diiron **2.6**. While in principle it may also be

possible for two molecules of $(SiP_2S)FeH$ to react directly to form H_2 without a coordinated N_2 ligand in the transition state, we favor the scenario shown in Fig. 2.6.

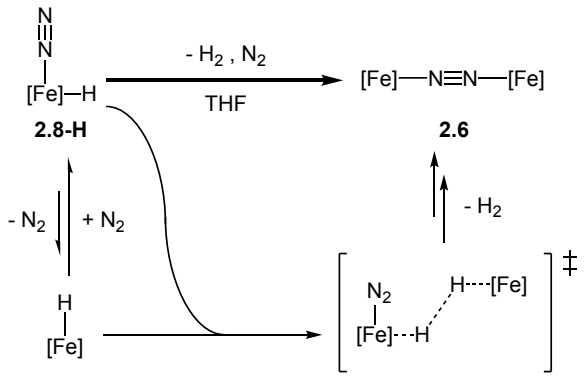

Figure 2.6. Proposed mechanism for the conversion of **2.8-H** to **2.6**, where [Fe] = $(SiP_2S)Fe$.

2.2.4 Thermochemical Parameters for the Fe–H Subunit in 2.7-H(crown) and 2.8-H

The bimolecular elimination of H_2 from **2.8-H** is indicative of an Fe–H bond with a relatively low homolytic bond strength, consistent with spin density localized on the hydride ligand as evidenced by the large coupling constants to the hydridic ^1H nucleus.[27,28] Hence, our use of the term "hydride" masks radical $H^{\bullet}$ character present in the Fe–H subunit. We therefore sought to explore this idea in greater detail.

The immediate product of $H^{\bullet}$ loss from **2.8-H** is the iron(II) species $(SiP_2S)Fe(N_2)$, but this species is not experimentally observed, presumably because the formation of diiron **2.6** is too facile. However, we have been able to generate and spectroscopically characterize the one- and two-electron reduced relatives of this species, $(SiP_2S)Fe(N_2)^{n-}$ (n = 1, 2, Scheme 2.2a). Under an N_2 atmosphere, reduction of **2.6** with excess Na(Hg) in THF followed by addition of 12-crown-4 affords the $S = ½$ iron(I) species $[(SiP_2S)Fe(N_2)][Na(12\text{-crown-}4)_2]$ (**2.9**) as a dark red solid ($\nu(N_2) = 1963\ cm^{-1}$). The gas-phase optimized structure of **2.9** (M06-L: def2tzvp (Fe), def2svp (all other atoms)) indicates less unpaired spin density localized at the sulfur atom (0.02 e^-, 1% overall spin density) than for **2.8-H** (0.18 e^-, 11% overall spin density). Alternatively, treatment of **2.6** with excess potassium metal in THF under N_2

provides the dianionic and diamagnetic iron(0) complex $[(SiP_2S)Fe(N_2)][K(THF)_x]_2$ (**10**) as a dark brown species ($\nu(N_2)$ = 1805 cm^{-1}). The availability of **2.9** and **2.10** provides access to additional data needed to assess the thermochemical properties of the hydride ligand in **2.8-H**.

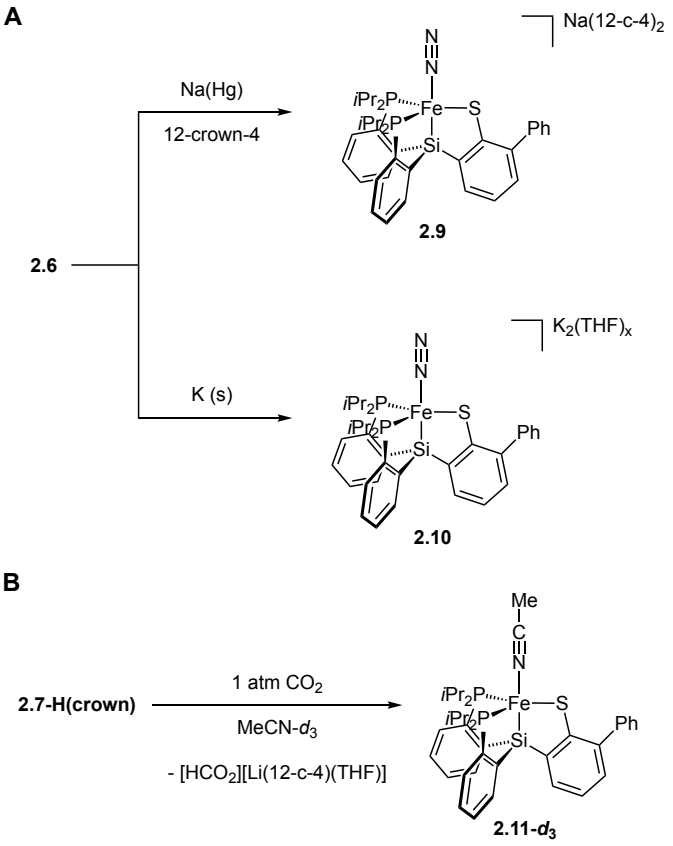

Scheme 2.2. (A) Synthesis of **2.9** and **2.10** via reduction of **2.6**. (B) Hydride transfer upon treatment of **2.7-H(crown)** with CO_2.

Complex **2.9** shows a reversible $Fe^{II/I}$ redox couple in THF at −1.75 V vs. Fc/Fc^+, but data collection in MeCN reveals instead an irreversible oxidation event at −1.71 V vs. Fc/Fc^+, presumably due to rapid solvent substitution for the N_2 ligand upon oxidation to produce $(SiP_2S)Fe(MeCN)$, **2.11** (see below). Additionally, a reversible reductive couple ($Fe^{I/0}$) is observed at −2.94 V vs. Fc/Fc^+ in MeCN, corresponding to the conversion of $[(SiP_2S)Fe(N_2)]^-$ to $[(SiP_2S)Fe(N_2)]^{2-}$.

Cyclic voltammograms of the $Fe^{II}(H)(N_2)$(thiolate) **2.7-H(crown)** derivative in MeCN shows an irreversible oxidative feature at −0.58 V vs. Fc/Fc^+. This feature is significantly shifted from the reversible oxidative $Fe^{III/II}$ couple that is recorded in THF (−1.63 V vs. Fc/Fc^+). The irreversibility and extreme solvent dependence of the oxidation potential of **2.7-H(crown)** indicates that a process that is more complex than outer-sphere electron transfer may be occurring in MeCN. Thus, for the thermochemical calculations presented below, we have utilized −1.63 V vs. Fc/Fc^+ as the value for the **2.7-H(crown)**/ **2.8-H** couple, because it is a well-defined, reversible feature as obtained in THF.

Exposing a degassed MeCN-d_3 solution of **2.7-H(crown)** to an atmosphere of CO_2 results in complete hydride transfer to yield the formate salt [Li(12-crown-4)][HCO_2] and the solvent complex (SiP_2S)Fe(CD_3CN) (**2.11-*d*$_3$**, Scheme 2.2b); the hydricity of **2.7-H(crown)** in MeCN must therefore be close to, or less than, the hydricity of formate (ΔG_H- = 44 kcal/mol in MeCN).[35b] Loss of H^- from **2.7-H(crown)** should generate (SiP_2S)Fe(N_2), which is not observed due to facile ligand substitution by MeCN to produce the MeCN adduct **2.11-*d*$_3$** instead. Thus, the hydricity of **2.7-H(crown)** can be estimated to have an upper bound of ~44 kcal/mol in MeCN.[51] There are two previous reports of the hydricity of terminally-bound Fe–H species.[52,53] A study by our lab of a related five-coordinate iron(II) hydride complex, (SiP_3)Fe(H)(H_2), estimated a hydricity of 54.3 ± 0.9 kcal/mol in MeCN,[52] significantly less hydridic than **2.7-H(crown)**, likely in part reflective of the different charges.

Utilizing available thermodynamic values that relate H^+, $H^\bullet$, and H^- in MeCN (eq. 2.1, 2.2),[35b] the upper bounds for the free energies of $H^+/H^\bullet/H^-$ transfer from **2.7-H(crown)** and $H^+/H^\bullet$ transfer from **2.8-H** can be related (Fig. 2.7, eq. 2.3-2.6). The approximated upper bounds for homolytic and heterolytic values of Fe–H bond cleavage from **2.7-H(crown)** and **2.8-H** are shown in Table 2.2. Although absolute free energy values for the $H^+/H^\bullet/H^-$ transfers (ΔG) are not established, the difference between any two such free energies ($\Delta\Delta G$) can be determined from eq. 2.1-2.6. The Fe–H bond of **2.7-H(crown)** is estimated to have a bond dissociation free energy (BDFE) of < 57 kcal/mol and a pK_a of < 53. Compared to the

Fe–H bond of **2.7-H(crown)**, the Fe–H bond of **2.8-H** is considerably more acidic, by more than 22 pK_a units, with an estimated upper bound of $pK_a < 30$.

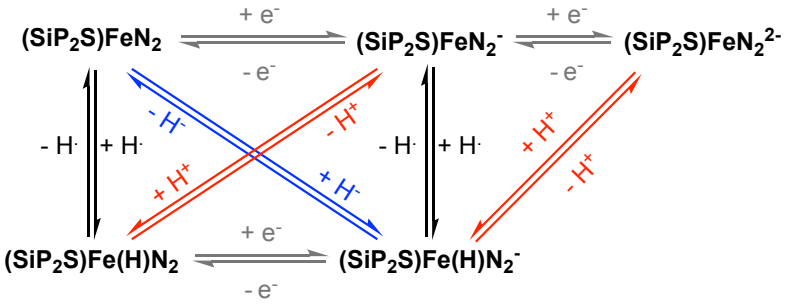

Figure 2.7. Thermochemical scheme relating H^+, $H^\bullet$, and H^- transfers from **2.7-H(crown)** and **2.8-H**.

$$H^\bullet \rightarrow H^+ + e^- \quad (\Delta G = -53.6 \text{ kcal/mol}) \tag{2.1}$$

$$H^- \rightarrow H^\bullet + e^- \quad (\Delta G = -26.0 \text{ kcal/mol}) \tag{2.2}$$

$$\Delta G(\textbf{2.7-H(crown)})_{H+} = \Delta G(\textbf{2.7-H(crown)})_{H\cdot} - 23.06(E_{ox}(\textbf{2.10})) - 53.6 \tag{2.3}$$

$$\Delta G(\textbf{2.7-H(crown)})_{H-} = 23.06(E_{ox}(\textbf{2.7-H(crown)}) + \Delta G(\textbf{2.8-H})_{H\cdot} + 26.0 \tag{2.4}$$

$$\Delta G(\textbf{2.8-H})_{H+} = \Delta G(\textbf{2.8-H})_{H\cdot} - 23.06(E_{ox}(\textbf{2.9})) - 53.6 \tag{2.5}$$

$$\Delta G(\textbf{2.7-H(crown)})_{H\cdot} = \Delta G(\textbf{2.8-H})_{H\cdot} + 23.06(E_{ox}(\textbf{2.7-H(crown)}) - E_{ox}(\textbf{2.9})) \tag{2.6}$$

The estimated upper bound for the BDFE of the Fe–H bond in $Fe^{III}(H)(N_2)$(thiolate) **2.8-H** of 56 kcal/mol is in close agreement with the DFT-predicted value of 55.6 kcal/mol (M06-L; def2tzvp (Fe), def2svp (all other atoms) in MeCN solvation). It has been previously suggested that M–H bonds with bond dissociation enthalpies of < 56 kcal/mol[54] are competent to release H_2 at room temperature (BDFE(H_2) in MeCN = 102.3 kcal/mol).[55] Interestingly, eq. 2.6 indicates that the Fe–H BDFE of Fe(II) **2.7-H(crown)** is only 2.8 kcal/mol greater than that of Fe(III) **2.8-H** in THF, but **2.7-H(crown)** is observed to be stable in solution at room temperature, whereas **2.8-H** undergoes clean conversion to **2.6** with release of H_2.

Table 2.2. Oxidation potentials and thermochemical parameters pertaining to Fe–H bond cleavage of **2.7-H(crown)** and **2.8-H**

Compound	Hydricity[a]	BDFE[a]	pKa	E_{ox}[b]
2.7-H(crown)	< 44	< 57	< 53	−1.63
2.8-H	-	< 56	< 30	-
2.9	-	-	-	−1.71
2.10	-	-	-	−2.94

[a] values in kcal/mol [b] potentials reported in V vs. Fc/Fc^+

Although there is only a small difference in BDFE between the ferrous and ferric hydrides, the K_{eq} for homolytic Fe–H bond cleavage is thus about 100 times greater at room temperature for **2.8-H** than **2.7-H(crown)**; this is further biased by the thermodynamic stability afforded by the formation of **2.6** rather than $(SiP_2S)FeN_2$, the direct product of Fe–H bond homolysis from **2.8-H**. Additionally, electrostatic penalties associated with a biomolecular reaction between two anionic species may be a kinetic impediment to H_2 release. Finally, assuming N_2 dissociation would need to precede an H_2 evolution in **2.7-H(crown)**, as we have suggested is likely for **2.8-H** (Fig. 2.6), the stability of **2.7-H(crown)** may be correlated to a greater kinetic barrier to N_2 dissociation from **2.7-H(crown)**, which features a more strongly coordinated N_2 ligand.

2.3 Conclusion

The synthesis of a trivalent, thiolate-$Fe^{III}(H)(N_2)$ complex has been accomplished and serves as an unusual Fe–N_2 species from the perspective of both oxidation state and the presence of both hydride and thiolate ligands. This is the first example of a ferric dinitrogen complex, and it is sufficiently persistent at low temperature to be amenable to characterization by X-ray crystallography and various spectroscopic techniques, including CW EPR and ENDOR spectroscopies. Additionally, we have demonstrated, via kinetic measurements, that this ferric Fe–H complex undergoes bimolecular reductive elimination to liberate H_2 with a primary kinetic deuterium isotope effect. To the best of our knowledge,

this is the first example of a well-defined, bimolecular H_2 elimination process from a terminal Fe–H species. Surprisingly, the entropy of activation for H_2 elimination is positive ($\Delta S^{\ddagger}$ = 39(13) cal/(mol·K)), whereas a large and negative value would be anticipated based solely on the prediction of a highly ordered transition state ([Fe–H···H–Fe]‡). Pre-dissociation of N_2 from thiolate–$Fe^{III}(H)(N_2)$ to afford thiolate–$Fe^{III}(H)$, which is then captured by thiolate-$Fe^{III}(H)(N_2)$ to proceed to an H–H bond-forming transition state, is invoked to accommodate the collective data. Finally, synthetic access to thiolate–$Fe^{II}(H)(N_2)$ and thiolate–$Fe^{III}(H)(N_2)$ species, in addition to the reduced derivatives thiolate–$Fe^{I}(N_2)^{-}$ and thiolate–$Fe^{0}(N_2)^{2-}$, has provided access to the physical detail needed to estimate important thermochemical H^+, $H^{\bullet}$, and H^- parameters of broad current interest and within an S = ½ Fe system that evolves H_2.

2.4 Experimental Section

2.4.1 Experimental Details

2.4.1.1 General Considerations

All syntheses and measurements, unless otherwise stated, were carried out under an inert atmosphere (N_2) in a glovebox or using standard Schlenk techniques, and solvents were dried and degassed by thoroughly sparging with N_2 and then passing through an activated alumina column in a solvent purification system supplied by SG Water, LLC. Deuterated solvents were purchased from Cambridge Isotope Laboratories, Inc., degassed, and dried over activated 3 Å molecular sieves before use. 2-phenylbenzenethiol,[56] bis(*o*-diisopropylphosphino-phenyl)-chlorosilane (**2.4**),[57] lithium triethylborodeuteride[58] were prepared according to literature procedures. All other reagents were purchased from commercial vendors and used without further purification unless otherwise stated.

2.4.1.2 Physical Methods

Electrochemical measurements were carried out in a glovebox under an N_2 atmosphere in a one-compartment cell using a CH Instruments 600B electrochemical analyzer. A glassy carbon electrode was used as the working electrode and a platinum wire was used as the auxiliary electrode. A silver pseudoreference electrode was used with the

ferrocene couple (Fc/Fc^+) as an internal reference, unless otherwise noted. Solutions of electrolyte (0.4 M $[NBu_4][PF_6]$ in THF) and analyte were also prepared under an N_2 atmosphere. NMR spectra (^1H, ^{13}C, ^{31}P) were collected on Varian 300, 400, or 500 MHz spectrometers (25 °C unless otherwise specified). ^1H and ^{13}C chemical shifts are reported in ppm, relative to tetramethylsilane using residual proton and ^{13}C resonances from solvent as internal standards. ^{31}P chemical shifts are reported in ppm relative to 85% aqueous H_3PO_4. Thin film IR spectra were obtained using a Bruker Alpha Platinum ATR spectrometer with OPUS software in a glovebox under an N_2 atmosphere. Optical spectroscopy measurements were taken on a Cary 50 UV-Vis spectrophotometer using a 1-cm quartz cell, unless otherwise noted. Temperature regulation for UV-Vis measurements was carried out with a Unisoku cryostat. Time-course UV-Vis spectra were collected with the Scanning Kinetics application of the Cary WinUV software and fit to Gaussian lineshapes with the Curve Fitting tool of Matlab. H_2 was analyzed on an Agilent 7890A gas chromatograph (HP-PLOT U, 30 m, 0.32 mm ID; 30 °C isothermal; nitrogen carrier gas) using a thermal conductivity detector. Combustion analyses were carried out by either Midwest Microlabs (Indianapolis) or the Beckman Institute Crystallography Facility (Caltech).

2.4.1.3 X-ray Crystallography

X-ray diffraction measurements were carried out in the Beckman Institute Crystallography Facility. XRD measurements were collected using a dual source Bruker D8 Venture, four-circle diffractometer with a PHOTON CMOS detector. Structures were solved using SHELXT and refined against F^2 on all data by full-matrix least squares with SHELXL. The crystals were mounted on a glass fiber under Paratone N oil.

2.4.1.4 DFT Calculations

Optimization and frequency calculations were performed using the Gaussian 09 program.[59] Structures of **2.8-H** and **2.9** were optimized using the crystal structure coordinates as the input. Structures utilized for thermochemical estimations were optimized with MeCN solvation. The M06-L functional[60] with the def2-TZVP[61] basis set was used on Fe, and the

def2-SVP basis set was used on all other atoms. DFT-estimated free energies of H• transfer in MeCN are referenced to H• dissociation from TEMPO in MeCN (BDFE of TEMPO-H = 66.5 kcal/mol).[62]

2.4.1.5 ^{57}Fe Mössbauer Spectroscopy

Mössbauer spectra were recorded on a spectrometer from SEE Co. (Edina, MN) operating in the constant acceleration mode in a transmission geometry. The sample was kept in an SVT-400 cryostat from Janis (Wilmington, MA). The quoted isomer shifts are relative to the centroid of the spectrum of a metallic foil of α-Fe at room temperature. Solid samples were prepared by grinding polycrystalline material into a fine powder and then mounted in a Delrin cup fitted with a screwcap as a boron nitride pellet. Frozen solution samples were prepared by freezing the sample in a Delrin cup. All samples were prepared within a glovebox with rapid transfer to a liquid nitrogen bath before mounting in the cryostat. Data analysis was performed using the program WMOSS (www.wmoss.org) and quadrupole doublets were fit to Lorentzian lineshapes.

2.4.1.6 CW EPR Spectroscopy

77 K X-band EPR spectra were obtained on a Bruker EMX spectrometer on solutions prepared as frozen glasses in 2-MeTHF. Spectra were simulated using the EasySpin[63] suite of programs with Matlab.

2.4.1.7 Pulse EPR Spectroscopy

All pulse Q-band (≈ 33.7 GHz) EPR and electron nuclear double resonance (ENDOR) experiments were aquired using a Bruker (Billerica, MA) ELEXSYS E580 pulse EPR spectrometer equipped with a Bruker D2 resonator. Temperature control was achieved using an ER 4118HV-CF5-L Flexline Cryogen-Free VT cryostat manufactured by ColdEdge (Allentown, PA) equipped with an Oxford Instruments Mercury ITC.

Pulse Q-band ENDOR was acquired using the Davies pulse sequence ($\pi - T_{RF} - \pi_{RF} - T_{RF} - \pi/2 - \tau - \pi -$ echo), where T_{RF} is the delay between mw pulses and RF pulses,

π_{RF} is the length of the RF pulse and the RF frequency is randomly sampled during each pulse sequence.

In general, the ENDOR spectrum for a given nucleus with spin I= ½ (^{1}H, ^{31}P) coupled to the S = ½ electron spin exhibits a doublet at frequencies

$$\nu_{\pm} = \left|\frac{A}{2} \pm \nu_N\right| \tag{2.7}$$

where ν_N is the nuclear Larmor frequency and A is the hyperfine coupling. For nuclei with $I \geq 1$ (^{2}H), an additonal splitting of the $\nu_{\pm}$ manifolds is produced by the nuclear quadrupole interaction (P)

$$\nu_{\pm,m_I} = \left|\nu_N \pm \frac{3P(2m_I - 1)}{2}\right| \tag{2.8}$$

Simulations of all pulse EPR data were achieved using the EasySpin[63] simulation toolbox (release 5.1.8) with Matlab 2016 using the following Hamiltonian:

$$\hat{H} = \mu_B \vec{B}_0 g \hat{S} + \mu_N g_N \vec{B}_0 \hat{I} + h\hat{S} \cdot \boldsymbol{A} \cdot \hat{I} + h\hat{I} \cdot \boldsymbol{P} \cdot \hat{I} \tag{2.9}$$

In this expression, the first term corresponds to the electron Zeeman interaction term where μ_B is the Bohr magneton, g is the electron spin g-value matrix with principle components g = [g_{xx} g_{yy} g_{zz}], and $\hat{S}$ is the electron spin operator; the second term corresponds to the nuclear Zeeman interaction term where μ_N is the nuclear magneton, g_N is the characteristic nuclear g-value for each nucleus (e.g. ^{1}H, ^{2}H, ^{31}P) and $\hat{I}$ is the nuclear spin operator; the third term corresponds to the electron-nuclear hyperfine term, where $\boldsymbol{A}$ is the hyperfine coupling tensor with principle components $\boldsymbol{A}$ = [A_{xx} A_{yy} A_{zz}]; and for nuclei with $I \geq 1$, the final term corresponds to the nuclear quadrupole (NQI) term which arises from the interaction of the nuclear quadrupole moment with the local electric field gradient (efg) at the nucleus, where $\boldsymbol{P}$ is the quadrupole coupling tensor. In the principle axis system (PAS), $\boldsymbol{P}$ is traceless and

parametrized by the quadrupole coupling constant e^2Qq/h and the asymmetry parameter η such that:

$$\boldsymbol{P} = \begin{pmatrix} P_{xx} & 0 & 0 \\ 0 & P_{yy} & 0 \\ 0 & 0 & P_{zz} \end{pmatrix} = \frac{e^2Qq/h}{4I(2I-1)} \begin{pmatrix} -(1-\eta) & 0 & 0 \\ 0 & -(1+\eta) & 0 \\ 0 & 0 & 2 \end{pmatrix} \quad (2.10)$$

where $\frac{e^2Qq}{h} = 2I(2I-1)P_{zz}$ and $\eta = \frac{P_{xx}-P_{yy}}{P_{zz}}$. The asymmetry parameter may have values between 0 and 1, with 0 corresponding to an electric field gradient with axial symmetry and 1 corresponding to a fully rhombic efg.

The orientations between the hyperfine and NQI tensor principle axis systems and the g-matrix reference frame are defined by the Euler angles (α, β, γ).

2.4.2 Synthetic Details

2.4.2.1 Synthesis of 2-(isopropylthio)biphenyl (2.2)

A mixture of 2-phenylbenzenethiol (26.5 g, 0.142 mol), 2-bromopropane (17.5 g, 0.142 mol) and K_2CO_3 (29.4 g, 0.213 mol) in acetone (500 mL) was allowed to reflux for 5 h. The reaction was cooled to room temperature and filtered through Celite. The filtrate was concentrated to an oil and purified *via* vacuum distillation to yield the title compound as a pale yellow oil (26.0 g, 80%). ^{1}H NMR ($CDCl_3$, 400 MHz, 298 K, δ): 7.49 – 7.22 (m, 9H), 3.20 (hept, J = 6.7 Hz, 1H), 1.19 (d, J = 6.9 Hz, 6H). ^{13}C NMR ($CDCl_3$, 101 MHz, 298 K) δ 143.5 (s), 141.1 (s), 134.7 (s), 130.7 (s), 130.5 (s), 129.6 (s), 127.9 (s), 127.7 (s), 127.3 (s), 126.1 (s), 37.3 (s), 23.0 (s).

2.4.2.2 Synthesis of (2-(isopropylthio)-[1,1'-biphenyl]-3-yl)lithium · 0.5 TMEDA (2.3)

Neat tetramethylethylenediamine (4.0 mL, 26.7 mmol) and *n*BuLi (16.4 mL, 1.6 M in hexanes) were sequentially added dropwise to a stirring solution of compound **2.2** (6.0 g, 26.3 mmol) in pentane (100 mL) at 0 °C. The yellow reaction mixture was stirred at 23 °C overnight, which yielded ample white precipitate. The solids were collected by filtration and

washed with pentane (3 x 10 mL) to yield the title compound as an off-white solid. (6.75 g, 88%) ^{1}H NMR (C_6D_6, 400 MHz, 298 K, δ): 8.05 (bs, 1H), 7.79 (d, *J* = 6.0 Hz, 2H), 7.41 – 7.31 (m, 3H), 7.21 – 7.17 (m, 2H), 2.98 (bs, 1H), 1.91 (s, 6H, TMEDA), 1.75 (s, 2H, TMEDA), 1.06 (bs, 6H).

2.4.2.3 Synthesis of $HSiP_2S$ (2.5)

A suspension of compound **2.3** (4.54 g, 15.5 mmol) in toluene (20 mL) was added to a stirring solution of bis(*o*-diisopropylphosphino-phenyl)-chlorosilane (**2.4**) (5.84 g, 12.9 mmol) in toluene (30 mL) at –78 °C. The reaction mixture was stirred for 12 h, with gradual warming from –78 °C to 23 °C. The resulting orange reaction mixture was filtered through Celite and concentrated. The resulting orange oil was triturated with pentane (20 mL) to yield the title compound as an off-white solid, which was isolated by filtration and washed with cold pentane (–78 °C, 40 mL). The filtrate was concentrated to 10 mL and stored at –33 °C overnight, which yielded additional product. (5.47 g, 66%) ^{1}H NMR (C_6D_6, 400 MHz, 298 K, δ): 7.55 (d, *J* = 7.3 Hz, 2H), 7.44 (d, *J* = 8.0 Hz, 2H), 7.40 (d, *J* = 7.5 Hz, 2H), 7.29 – 7.26 (m, 3H), 7.23 – 7.16 (m, 3H), 7.11 – 7.01 (m, 4H), 2.99 (hept, *J* = 6.3 Hz, 1H), 2.14 – 1.98 (m, 4H), 1.15 (m, 12H), 1.04 – 0.97 (m, 18H). ^{31}P NMR (C_6D_6, 162 MHz, 298 K, δ): 1.10 (s). IR (solid, cm^{-1}): 2228 (Si–H). ESI-MS (positive ion, amu): Calcd. 643.3 ($[M+H]^+$); Found. 643.2.

2.4.2.4 Synthesis of $[(SiP_2S)Fe]_2(\mu\text{-}N_2)$ (2.6)

A solution of **2.5** (1.0 g, 1.6 mmol) in THF (15 mL) was added to solid $FeCl_2$ (0.28 g, 1.6 mmol) and stirred for 9 h. The reaction mixture was cooled to −78 °C, and MeMgCl (3.0 M in THF, 1.6 mL) was added dropwise to the stirring solution. The reaction mixture was stirred overnight with gradual warming from –78 °C to 23 °C and stirred at 23 °C for an additional day. The reaction mixture was filtered through Celite and concentrated to dryness. The resulting brown solids were washed with pentane (20 mL), extracted with C_6H_6 (50 mL) and lyophilized. The brown material was redissolved in C_6H_6 (20 mL) and filtered through Celite. The filtrate was lyophilized to yield the title compound as a dark brown solid. (crude yield: 1.09 g, 52%) Smaller portions of the crude product were recrystallized prior to use: Pentane

(10 mL) was layered over a benzene (5 mL) solution of **2.4** (160.0 mg, 0.1 mmol) and allowed to stand at 23 °C, which yielded the product as dark brown blocks (62 mg, 39% yield from recrystallization). Dark brown crystals suitable for XRD were grown from slow evaporation of a Et_2O solution at 23 °C. ^{1}H NMR (C_6D_6, 300 MHz, 298 K, δ): 83.0, 52.6, 27.0, 13.7, 9.9, 8.7, 7.2, 6.4, 6.0, 4.9, 4.0, 3.6, 3.3, −2.5, −7.7, −70.3. μ_{eff} ($C_6D_5CD_3$, Evans method, 298 K): 4.8μ_B. IR (solid, cm^{-1}): 1888 (N≡N). UV-Visible (THF, 298 K, nm {$M^{-1}cm^{-1}$}): 495 {4478}, 678 {1273}, 773 {1250}, 1019 {1210}. Anal. Calcd. for $[(SiP_2S)Fe]_2(N_2)\cdot(C_6H_6)_{0.5}$ ($C_{75}H_{141}Fe_2N_2P_4S_2Si_2$): C, 65.45; H, 6.66; N, 2.04. Found: C, 65.51; H, 7.03; N, 2.16.

2.4.2.5 Synthesis of $[(SiP_2S)Fe(H)(N_2)]Li(THF)_2$ (2.7-H)

To a stirring solution of **2.6** (0.100 g, 0.074 mmol) in THF (5 mL), $LiEt_3BH$ (1.0 M in THF, 0.16 mL) was added dropwise at –78 °C. The reaction mixture was stirred at 23 °C for 30 min. The reaction mixture was subsequently chilled to –78 °C, and a second portion of $LiEt_3BH$ (1.0 M in THF, 0.16 mL) was added. The dark red reaction mixture was stirred at 23 °C for 30 min, and the volatiles were then removed *in vacuo*. The resulting red residue was washed with 2:1 pentane/Et_2O (3 mL) and pentane (10 mL) then extracted with THF (10 mL) to yield compound **2.7-H** as a red solid. (97 mg, 78%) Dark red crystals suitable for XRD were grown from slow evaporation of a Et_2O solution into HMDSO at 23 °C. ^{1}H NMR (C_6D_6, 400 MHz, 298 K, δ): 8.58 (d, J = 7.4 Hz, 2H), 8.10 (d, J = 7.4 Hz, 1H), 7.71 (d, J = 7.5 Hz, 2H), 7.52 (d, J = 7.3 Hz, 2H), 7.39 (t, J = 7.3 Hz, 2H), 7.22 (t, J = 7.4 Hz, 2H), 7.10 (t, J = 7.6 Hz, 2H), 6.97 (q, J = 10.3, 9.0 Hz, 2H), 6.88 (d, J = 7.2 Hz, 1H), 3.30 (bs, 8H, THF), 2.78 (bs, 2H), 2.51 (bs, 2H), 1.64 (q, J = 6.9 Hz, 8H, THF), 1.36 – 1.28 (m, 12H), 1.10 – 1.00 (m 12H), −19.32 (t, J = 71.3 Hz, 1H). ^{31}P NMR (C_6D_6, 162 MHz, 298 K, δ): 96.8 (s), 96.4 (s). IR (solid, cm^{-1}): 2020 (N≡N), 1976 (N≡N), 1935 (N≡N), 1864 (Fe–H); the inequivalent N_2 stretches arise from distinct coordination modes of the Li cation. UV-Visible (THF, 298 K, nm {$M^{-1}cm^{-1}$}): 336 {6903}, 379 {4263}, 437 {3194}, 535 {1471}. Anal. Calcd. for $C_{44}H_{61}FeLiN_2O_2P_2SSi$: C, 63.30; H, 7.37; N, 3.36. Found: C, 63.32; H, 7.59; N, 3.23.

2.4.2.6 Synthesis of [(SiP$_2$S)Fe(D)(N$_2$)]Li(THF)$_2$ (2.7-D)

Prepared in an analogous fashion to **2.7-H** but employing LiEt$_3$BD (1.0 M in THF). Except for the absence of the hydridic proton resonance at −19.32 ppm, spectroscopic features in the ^{1}H NMR spectrum of **2.7-D** were identical to that of **2.7-H**. ^{31}P NMR (C$_6$D$_6$, 162 MHz, 298 K, δ): 96.85 (t, J = 9.3 Hz). ^{31}P{^{2}H} NMR (C$_6$D$_6$, 162 MHz, 298 K, δ): 96.85 (s). IR (solid, cm^{-1}): 2016 (N≡N), 1975 (N≡N), 1924 (N≡N); the inequivalent N$_2$ stretches arise from distinct coordination modes of the Li cation.

2.4.2.7 Synthesis of [(SiP$_2$S)Fe(H)(N$_2$)][Li(12-crown-4)(THF)] (2.7-H(crown))

Neat 12-crown-4 (5.8 μL, 36 μmol) was added in one portion to a homogeneous stirring solution of **2.7-H** (30 mg, 36 μmol) in Et$_2$O (10 mL) at 23 °C. Red solids immediately precipitated from solution upon addition of 12-crown-4. The reaction mixture was stirred at 23 °C for 5 min. The resulting solids were isolated by filtration, washed with Et$_2$O (5 mL) and pentane (5 mL), then extracted with THF (5 mL) to yield the title compound as a red solid. (26 mg, 76%) Dark red crystals suitable for XRD were grown from slow diffusion of pentane into a concentrated THF solution at 23 °C. ^{1}H NMR (THF-d_8, 400 MHz, 298 K, δ): 8.25 (d, J = 6.9 Hz, 2H), 7.60 (d, J = 7.5 Hz, 2H), 7.36 (bs, 3H), 7.19 – 7.11 (m, 4H), 7.01 (t, J = 7.2 Hz, 3H), 3.62 (bs, 16H, 12-crown-4), 2.60 (bs, 2H), 2.40 (bs, 2H), 1.41 (q, J = 6.8 Hz, 6H), 1.32 (q, J = 6.9 Hz, 6H), 0.78 (q, J = 6.3 Hz, 6H), 0.71 (q, J = 6.4 Hz, 6H), −19.39 (t, J = 69.6 Hz, 1H). ^{31}P NMR (THF-d_8, 162 MHz, 298 K, δ): 101.20 (s), 100.87 (s). IR (solid, cm^{-1}): 1971 (N≡N), 1886 (Fe–H). UV-Visible (THF, 298 K, nm {M^{-1}cm^{-1}}): 333 {8713}, 421 {4674}, 532 {1906}, 885 {280}. Anal. Calcd. for C$_{48}$H$_{69}$FeLiN$_2$O$_5$P$_2$SSi: C, 61.40; H, 7.41; N, 2.98. Found: C, 61.26; H, 7.71; N, 2.67.

2.4.2.8 Synthesis of (SiP$_2$S)Fe(H)(N$_2$) (8-H)

^{1}H NMR (THF-d_8, 500 MHz, 195 K, δ): 11.0, 5.8, 5.4, 4.7, 3.6, 1.3, 0.9, -7.5. IR (solid, cm-1): 2123 (N≡N), 1852 (Fe–H). UV-Visible (THF, 298 K, nm {M^{-1}cm^{-1}}): 607 {2830}. *Note: The thermal instability of **2.8-H** precluded characterization by combustion analysis.

2.4.2.8.1 EPR and ENDOR Spectroscopies

Solid [Cp*$_2$Fe][PF$_6$] (1.4 mg, 3.0 μmol) was added in one portion to a solution of **2.7-H** (4.8 mg, 5.7 μmol) in 2-MeTHF (0.5 mL, –78 °C). The reaction was allowed to stir at –78 °C for 1 h and the resulting dark blue solution was filtered through a pre-chilled pipette filter (pipette/glass fiber) to remove excess [Cp*$_2$Fe][PF$_6$]. The filtered solution was analyzed directly. *Note: 77 K X-band EPR spectra of **2.7-H** generated via oxidation with [Cp$_2$Co][PF$_6$] and [Cp*$_2$Fe][PF$_6$] were identical, see Figure S41.

2.4.2.8.2 Representative Sample Preparation for all other Spectroscopies

Solid [Cp$_2$Co][PF$_6$] (2.2 mg, 6.6 μmol) was added in one portion to a solution of **2.7-H** (5.0 mg) in THF (0.5 mL, −78 °C). The reaction was allowed to stir at –78 °C for 1 h and the resulting dark blue solution was filtered through a pre-chilled pipette filter (pipette/glass fiber) to remove excess [Cp$_2$Co][PF$_6$]. This filtered solution was analyzed via the procedures detailed below.

2.4.2.9 Synthesis of (SiP$_2$S)Fe(D)(N$_2$) (2.8-D)

Prepared *in situ* in an analogous fashion to **8-H** but employing **7-D**. IR (solid, cm^{-1}): 2121 (N≡N), 1333 (Fe–D).

2.4.2.10 Synthesis of [(SiP$_2$S)Fe(N$_2$)][Na(12-crown-4)$_2$] (2.9)

A solution of **2.6** (50 mg, 0.037 mmol) in THF (2 mL) was added to Na(Hg) (12 mg Na, 0.52 mmol; 2 g Hg) and stirred vigorously for 5 h at 23 °C. The resulting red solution was decanted, and neat 12-crown-4 (24 μL) was added in one portion to the reaction mixture. The reaction was stirred at 23 °C for 1 h and subsequently layered with pentane (2 mL). The mixture was allowed to stand at –33 °C overnight, resulting in the precipitation of dark red solids. The solids were collected by vacuum filtration, washed with Et$_2$O (2 mL x 2) and pentane (2 mL x 2), then extracted with THF (5 mL) to yield the title compound as a red solid. (61.0 mg, 77%). Dark red crystals suitable for XRD were grown from slow diffusion of pentane into a concentrated THF solution at 23 °C. ^{1}H NMR (THF-d_8, 400 MHz, 298 K,

δ) 11.6, 8.90, 7.6, 6.6, 6.2, 5.7, 3.6, 0.1, −3.3. μ_{eff} (THF-d_8, Evans method, 298 K): 1.8μ_B. IR (solid, cm^{-1}): 1963 (N≡N). UV-Visible (THF, 298 K, nm {$M^{-1}cm^{-1}$}): 547 {2020}, 826 {499}. Anal. Calcd. for $[(SiP_2S)Fe(N_2)][Na(12\text{-crown-}4)_2]\cdot THF_{0.5}$ ($C_{54}H_{80}FeN_2NaO_{8.5}P_2SSi$): C, 59.28; H, 7.37; N, 2.56. Found: C, 58.98; H, 7.66; N, 2.40.

2.4.2.11 Synthesis of $[(SiP_2S)Fe(N_2)][K(THF)_x]$ (2.10)

A solution of **2.6** (30 mg, 0.022 mmol) in THF (5 mL) was stirred with potassium metal (25 mg, 0.64 mmol) at 23 °C for 15 min. The resulting dark brown solution was filtered and concentrated to dryness to yield the title complex as a dark brown solid. (37 mg) *Note: The broad signals in the room temperature ^{1}H NMR spectrum hindered reliable peak integration. ^{1}H NMR (THF-d_8, 300 MHz, 298 K, δ) 7.92 (bs), 7.63 (bs), 7.23 (bs), 7.02 (t, J = 7.0, 2.2 Hz), 6.79 (bs), 6.43 (bs), 2.41 (bs), 1.09 (bs), 0.78 (bs). ^{31}P NMR (THF-d_8, 121 MHz, 298 K, δ): 93.6 (bs). IR (solid, cm^{-1}): 1805 cm^{-1}.

2.4.2.12 Synthesis of $(SiP_2S)Fe(NCMe)$ (2.11)

MeCN (0.5 mL) was added to a solution of **2.6** (50 mg, 0.037 mmol) in C_6H_6 (3 mL) at 23 °C, and the resulting dark red solution was stirred at 23 °C for 15 min. The reaction mixture was concentrated to dryness, and the red solids were washed with pentane (3 mL x 2) and extracted with C_6H_6 (5 mL). The volatiles were removed *in vacuo*, and the title complex was isolated as a red solid. (48 mg, 92%) Dark red crystals suitable for XRD were grown from slow diffusion of pentane into a concentrated THF solution 23 °C. ^{1}H NMR (400 MHz, C_6D_6) δ 96.1, 80.5, 51.3, 15.9, 8.9, 8.5, 7.3, 7.2, 6.1, 5.8, 4.2, 2.4, −1.0, −2.8, −4.1, −43.6. μ_{eff} (C_6D_6, Evans method, 298 K): 2.9μ_B. UV-Visible (THF, 298 K, nm {$M^{-1}cm^{-1}$}): 485 {2405}, 680 {325}, 1029 {639}. Anal. Calcd. for $C_{38}H_{47}FeNP_2SSi$: C, 65.60; H, 6.81; N, 2.01. Found: C, 65.72; H, 6.85; N, 1.91

2.4.3 Quantification of H_2 from the Conversion of 2.8-H to 2.6

A representative sample preparation: A filtered solution of **2.8-H**, which was generated in situ in THF at −78 °C from **2.7-H** and $[Cp_2Co][PF_6]$, (800 μL, 35.5 mM) was transferred into a Schlenk tube and sealed. The solution was allowed to stir at 23 °C for a minimum of

2 d. An aliquot of the headspace was sampled and analyzed for H_2 by GC. Yield of H_2: 99% (± 11%)

2.4.4 Reaction of 2.7-H(crown) with CO_2 to Form 2.11

A J. Young NMR tube containing a solution of **2.7-H(crown)** (4.9 mg, 5.7μmol) in MeCN-d_3 (0.5 mL) was degassed via three freeze-pump-thaw cycles and exposed to 1 atm of CO_2 at 23 °C. The red solution of **2.7-H(crown)** turned a darker red color upon addition of CO_2. The tube was rotated at 23 °C for 1 h. ^{1}H NMR data collected an hour after CO_2 addition reveals full consumption of **2.7-H(crown)** and generation of **2.11**. Thin-film IR spectrum of the reaction mixture contains a broad stretch at 1605 cm^{-1}, consistent with the formation of HCO_2^-.

2.5 References

(1) For select examples see: (a) Yandulov, D. V.; Schrock, R. R. *Science*, **2003**, *301*, 76-78. (b) Arashiba, K.; Miyake, Y.; Nishibayashi, Y. *Nat. Chem.* **2011**, *3*, 120-125. (c) Anderson, J. S.; Rittle, J.; Peters, J. C. *Nature* **2013**, *501*, 84-87. (d) Tuczek, F.; Stucke, N.; Floeser, B.; Weyrich, T. *Eur. J. Inorg. Chem.* **2018**, *12*, 1337-1355.

(2) Buscagan, T. M.; Oyala, P. H.; Peters, J. C. *Angew. Chemie. Int. Ed.* **2017**, *56*, 6921-6926.

(3) Rees, D. C.; Howard, J. B. *Curr. Opin. Chem. Biol.* **2000**, *4*, 559-566.

(4) Hoffman, B. M; Lukoyanov, D.; Yang, Z.-Y.; Dean, D. R.; Seefeldt, L. C. *Chem. Rev.* **2014**, *114*, 4041-4062.

(5) Einsle, O.; Tezcan, F. A.; Andrade, S. L. A.; Schmid, B.; Yoshida, M.; Howard, J. B.; Rees, D. C. *Science* **2002**, *297*, 1696-1700.

(6) Lough, S.; Burns, A.; Watt, G. D. *Biochemistry* **1983**, *22*, 4062-4066.

(7) Doan, P. E.; Telser, J.; Barney, B. M.; Igarashi, R. Y.; Dean, D. R.; Seefeldt, L. C.; Hoffman, B. M. *J. Am. Chem. Soc*. **2011**, *133*, 17329-17340.

(8) Morrison, C. N.; Spatzal, T.; Rees, D. C. *J. Am. Chem. Soc.* **2017**, *139*, 10856-10862.

(9) (a) Igarashi, R. Y.; Laryukhin, M.; Dos Santos, P. C.; Lee, H.-I.; Dean, D. R.; Seefeldt, L. C.; Hoffman, B. M. *J. Am. Chem. Soc.* **2005**, *127*, 6231-6241. (b) Lukoyanov, D. A.; Khadka, N.; Yang, Z.-Y.; Dean, D. R.; Seefeldt, L. C.; Hoffman, B. M. *Inorg. Chem.* **2018**, *57*, 6847-6852.

(10) Rittle, J.; McCrory, C. C. L.; Peters, J. C. *J. Am. Chem. Soc.* **2014**, *136*, 13853-13862.

(11) Bart, S. C.; Lobkovsky, E.; Bill, E.; Wieghardt, K.; Chirik, P. J. *Inorg. Chem.* **2007**, *46*, 7055-7063.

(12) Takaoka, A.; Mankad, N. P.; Peters, J. C. *J. Am. Chem. Soc.* **2011**, *133*, 8440-8443.

(13) Creutz, S. E.; Peters, J. C. *J. Am. Chem. Soc.* **2015**, *137*, 7310-7313.

(14) Čorić, I.; Mercado, B. Q.; Bill, E.; Vinyard, D. J.; Holland, P. L. *Nature* **2015**, *526*, 96-99.

(15) (a) Čorić, I.; Holland, P. L. *J. Am. Chem. Soc.* **2016**, *138*, 7200-7211. (b) Speelman, A. L.; Holland, P. L. In Nitrogen Fixation; Nishibayashi, Y., Ed.; Springer International Publishing: Cham, 2017; pp 197-213.

(16) Lukoyanov, D.; Barney, B. M.; Dean, D. R.; Seefeldt, L. C.; Hoffman, B. M. *Proc. Natl. Acad. Sci.* **2007**, *104*, 1451-1455.

(17) Simpson, F. B.; Burris, R. H. *Science* **1984**, *224*, 1095-1097.

(18) Lubitz, W.; Ogata, H.; Rüdiger, O.; Reijerse, E. *Chem. Rev.* **2014**, *114*, 4081-4148.

(19) Schilter, D.; Camara, J. M.; Huynh, M. T.; Hammes-Schiffer, S.; Rauchfuss, T. B. *Chem. Rev.* **2016**, *116*, 8693-8749.

(20) (a) Kaeffer, N.; Chavarot-Kerlidou, M; Artero, V. *Acc. Chem. Res.* **2015**, *48*, 1286-1295. (b) DuBois, D. L.; Bullock, M. R. *Eur. J. Inorg. Chem.* **2011**, *7*, 1017-1027. (c) Dempsey, J. L.; Brunschwig, B. S.; Winkler, J. R.; Gray, H. B. *Acc. Chem. Res.* **2009**, *42*, 1995-2004.

(21) Du, P.; Eisenberg, R. *Energy Environ. Sci.* **2012**, *5*, 6012-6021.

(22) (a) Hu, X.; Brunschwig, B. S.; Peters, J. C. *J. Am. Chem. Soc.* **2007**, *129*, 8988-8998. (b) Marinsescu, S. C.; Winkler, J. R.; Gray, H. B. *Proc. Natl. Acad. Sci.* **2012**, *109*, 15127-15131. (c) Rose, M. J.; Gray, H. B.; Winkler, J. R. *J. Am. Chem. Soc.* **2012**, *134*, 8310-8313.

(23) Besora, M.; Lledós, A.; Maseras, F. *Chem. Soc. Rev.* **2009**, *38*, 957-966.

(24) Bullock, R. M.; Appel, A. M.; Helm, M. L. *Chem. Commun.* **2014**, *50*, 3125-3143.

(25) (a) Packett, D. L.; Trogler, W. C. *Inorg. Chem.* **1988**, *27*, 1768-1755. (b) Chirik, P. J.; Henling, L. M.; Bercaw, J. E. *Organometallics* **2001**, *20*, 534-544. (c) Kaesz, H. D.; Saillant, R. B. *Chem. Rev.* **1972**, *72*, 231-281. (d) Daida, E. J.; Peters, J. C. *Inorg. Chem.* **2004**, *43*, 7474-7485. (e) Deutsch, P. P.; Eisenberg, R. *Organometallics* **1990**, *9*, 709-718.

(26) (a) Collman, J. P.; Wagenknecht, P. S.; Lewis, N. S. *J. Am. Chem. Soc.* **1992**, *114*, 5665-5673. (b) Collman, J. P.; Hutchison, J. E.; Wagenknecht, P. S.; Lewis, N. S.; Angel Lopez, M.; Guilard, R. *J. Am. Chem. Soc.* **1990**, *112*, 8206-8208. (c) Norton, J. R. *Acc. Chem. Res.* **1979**, *12*, 139-145. (d) Evans, J.; Norton, J. R. *J. Am. Chem. Soc.* **1974**, *96*, 7577-7578. (e) Inoki, D.; Matsumoto, T.; Nakai, H.; Ogo, S. *Organometallics* **2012**, *31*, 2996-3001.

(27) (a) Hu, Y.; Shaw, A. P.; Estes, D. P.; Norton, J. R. *Chem. Rev.* **2016**, *116*, 8427-8462. (b) Poli, R., Paramagnetic Mono-and Polyhydrides of the Transition Metals. In Recent Advances in Hydride Chemistry; Poli, R., Peruzzini, M., Eds. Elsevier B. V. 2001; pp 139-188.

(28) (a) Chiang, K. P.; Scarborough, C. C.; Horitani, M.; Lees, N. S.; Ding, K.; Dugan, T. R.; Brennessel, W. W.; Bill, E.; Hoffman, B. M.; Holland, P. L. *Angew. Chemie. Int. Ed.* **2012**, *51*, 3658-3662. (b) Hamon, P.; Toupet, L.; Hamon, J.-R.; Lapinte, C. *Organometallics*. **1992**, *11*, 1429-1431. (c) Hamon, P.; Hamon, J.-R.; Lapinte, C. *J. Chem. Soc., Chem. Commun.* **1992**, 1602-1603

(29) Crossland, J. L.; Tyler, D. R. *Chem. Rev.* **2010**, *254*, 1883-1894.

(30) For studies of heterobimetallic bimolecular HER, see: (a) Mazzacano, T. J.; Mankad, N. P. *J. Am. Chem. Soc.* **2013**, *135*, 17258-17261. (b) Parmelee, S. R.; Mazzacano, T. J.; Zhu, Y.; Mankad, N. P.; Keith, J. A. *ACS Catal.* **2015**, *5*, 3689-3699.

(31) Koelle, U.; Ohst, S. *Inorg. Chem.* **1986**, *25*, 2689-2694.

(32) For related examples of unimolecular reductive elimination from multimetallic, first-row transition metal hydride complexes, see: (a) Vollhardt, K. P. C.; Cammack, J. K.; Matzger, A. J.; Bauer, A.; Capps, K. B.; Hoff, C. D. *Inorg. Chem.* **1999**, *38*, 2624-2631. (b) Lee, Y.; Anderton, K. J.; Sloane, F. T.; Ermert, D. M.; Abboud, K. A.; García-Serres, R.; Murray, L. J. *J. Am. Chem. Soc.* **2015**, *137*, 10610-10617. (c) Manz, D.-H.; Duan, P.-C.;

Dechert, S.; Demeshko, S.; Oswald, R.; John, M.; Mata, R. A.; Meyer, F. *J. Am. Chem. Soc.* **2017**, *139*, 16720-16731. (d) Bellows, S. M.; Arnet, N. A.; Gurubasavaraj, P. M.; Brennessel, W. W.; Eckhard, B.; Cundari, T. R.; Holland, P. L. *J. Am. Chem. Soc.* **2016**, *138*, 12112-12123. (e) Yu, Y.; Sadique, A. R.; Smith, J. R.; Dugan, T. R.; Cowley, R. E.; Brennessel, W. W.; Flaschenriem, C. J.; Bill, E.; Cundari, T. R.; Holland, P. L. *J. Am. Chem. Soc.* **2008**, *130*, 6624-6638. (f) Ding, K.; Brennessel, W. W.; Holland, P. L. *J. Am. Chem. Soc.* **2009**, *131*(31), 10804-10805.

(33) The elimination of H_2 from two M–H species (2 M–H $\rightarrow$ H_2 + M_2) may also occur through a M–M bonded species, whereby the intermediate prior to reductive elimination is a dinuclear M_2H_2 species, see: (a) Halpern, J.; Pribaníc, M.; *Inorg. Chem.* **1970**, *9*, 2616-2618. (b) Ungváry, F.; Markó, L. *J. Organomet. Chem.* **1969**, *20*, 205-209. (c) Trinquier, G.; Hoffmann, R. *Organometallics* **1984**, *3*, 370-380.

(34) It has been reported that $CpFe(CO)_2H$ (FpH) undergoes reductive elimination of H_2 to yield $\{CpFe(CO)_2\}_2$. See: Green, M. L. H.; Street, C. N.; Wilkinson, G. *Z. Naturforschg.* **1959**, *14*, 738. However, subsequent studies provided evidence to suggest that the H_2 evolution was catalyzed by the presence of a trace oxidant. See: Shackleton, T. A.; Mackie, S. C.; Fergusson, S. B.; Johnston, L. J.; Baird, M. C. *Organometallics* **1990**, *9*, 2248-2253. The reverse bimolecular oxidative addition of H_2 ($Fp_2 + H_2 \rightarrow 2$ FpH) is known to occur at high pressures of H_2 ($Fp_2 + H_2 \rightarrow 2$ FpH). See: Chang, B.-H.; Coil, P. C.; Brown, M. J.; Barnett, K. W. *J. Organomet. Chem.* **1984**, *270*, C23-C25.

(35) (a) Waldie, K. M.; Ostericher, A. L.; Reineke, M. H.; Sasayama, A. F.; Kubiak, C. P. *ACS Catal.* **2018**, *8*, 1313-1324. (b) Wiedner, E. S.; Chambers, M. B.; Pitman, C. L.; Bullock, R. M.; Miller, A. J. M.; Appel, A. M. *Chem. Rev.* **2016**, *116*, 8655-8692. (c) Pearson, R. G. *Chem. Rev.* **1985**, *85*, 41-49.

(36) (a) Whited, M. T.; Mankad, N. P.; Lee, Y.; Oblad, P. F.; Peters, J. C. *Inorg. Chem.* **2009**, *48*, 2507-2517. (b) Lee, Y.; Mankad, N. P.; Peters, J. C. *Nat. Chem.* **2010**, *2*, 558-565.

(37) McGinley, P. L.; Koh, J. T. *J. Am. Chem. Soc.* **2007**, *129*, 3822-3823.

(38) Del Castillo, T. J.; Thompson, N. B.; Peters, J. C. *J. Am. Chem. Soc.* **2016**, *138*, 5341-5350.

(39) Hendrich, M. P.; Gunderson, W.; Behan, R. K.; Green, M. T.; Mehn, M. P.; Betley, T. A.; Lu, C. C.; Peters, J. C. *Proc. Natl. Acad. Sci. U.S.A.* **2006**, *103*, 17107-17112.

(40) Stoian, S. A.; Vela, J.; Smith, J. M.; Sadique, A. R.; Holland, P. L.; Münck, E.; Bominaar, E. L. *J. Am. Chem. Soc.* **2006**, *128*, 10181-10192.

(41) M. D. Fryzuk and S. A. Johnson *Coord. Chem. Rev.* **2000**, *200*, 379.

(42) (a) Jenkins, D. M.; Peters, J. C. *J. Am. Chem. Soc.* **2005**, *127*, 7148-7165. (b) Creutz, S. E.; Peters, J. C. *Inorg. Chem.* **2016**, *55*, 3894-3906.

(43) An asymmetric ^{57}Fe Mössbauer spectrum has been similarly observed for (a) [Fe(Cp*)(dppe)(CO)(H)]PF_6, an S = ½ Fe(III) hydride. See Ref. 28c; (b) polyphosphine-bound iron complexes studied by previously by our lab. See, for example: Rittle, J.; Peters, J. C. *J. Am. Chem. Soc.* **2016**, *138*, 4243-4248.

(44) Unless otherwise noted, [Cp*$_2$Fe][PF_6] was utilized as the oxidant to prepare EPR and ENDOR samples of **2.8-H** and **2.8-D**. Decamethylferrocenium was favored over cobaltocenium because the resultant Cp*$_2$Fe byproduct is diamagnetic. However, the 77 K X-band EPR spectrum obtained *via* oxidation with [Cp_2Co][PF_6] was indiscernible from that obtained utilizing [Cp*$_2$Fe][PF_6] as the oxidant (see Appendix A for complete details).

(45) a) Chang, Y.-H.; Su, C.-L.; Wu, R.-R.; Liao, J.-H.; Liu, Y.-H.; Hsu, H.-F. *J. Am. Chem. Soc.* **2011**, *133*, 5708-5711. (b) Broering, E. P.; Dillon, S.; Gale, E. M.; Steiner, R. A.; Telser, J.; Brunold, T. C.; Harrop, T. C. *Inorg. Chem.* **2015**, *54*, 3815-3828.

(46) Lukoyanov, D.; Khadka, N.; Yang, Z.-Y.; Dean, D. R.; Seefeldt, L. C.; Hoffman, B. M. *J. Am. Chem. Soc.* **2016**, *138*, 10674-10683.

(47) Kinney, R. A.; Saouma, C. T.; Peters, J. C.; Hoffman, B. M. *J. Am. Chem. Soc.* **2012**, *134*, 12637-12647.

(48) The spin density at the hydride ligand is calculated using the a_{iso} value for a free hydrogen atom of 1420 MHz, see: Wittke, J. P.; Dicke, R. H. Dicke *Phys. Rev.* **1956**, *103*, 620-631.

(49) Gómez-Gallego, M.; Sierra, M. A. *Chem. Rev.* **2011**, *111*, 4857-4963.

(50) Wayland, B. B.; Ba, S.; Sherry, A. E. *J. Am. Chem. Soc.* **1991**, *113*, 5305-5311.

(51) Following the reaction of **2.7-H(crown)** with CO_2 by ^1H NMR reveals direct conversion of **2.7-H(crown)** to **2.11**; a N_2-bound intermediate is not observed in the reaction mixture. It may be possible that the thermodynamic stability afforded by MeCN coordination drives the hydride transfer reaction forward, even if the hydricity of **2.7-H(crown)** is slightly greater than 44 kcal/mol. Thus, 44 kcal/mol is determined to be an approximate upper bound for the hydricity of **2.7-H(crown)**.

(52) Fong, H.; Peters, J. C. *Inorg. Chem.* **2015**, *54*, 5124-5135.

(53) Estes, D. P.; Vannucci, A. K.; Hall, A. R.; Lichtenberger, D. L.; Norton, J. R. *Organometallics* **2011**, *30*, 3444-3447.

(54) Kiss, G.; Zhang, K.; Mukerjee, S. L.; Hoff, C. D. *J. Am. Chem. Soc.* **1990**, *112*, 5657-5658.

(55) Warren, J. J.; Tronic, T. A.; Mayer, J. M. *Chem. Rev.* **2010**, *110*, 6961-7001.

(56) McGinley, P. L.; Koh, J. T. *J. Am. Chem. Soc.* **2007**, *129*, 3822-3823.

(57) Takaoka, A.; Mankad, N. P.; Peters, J. C. *J. Am. Chem. Soc.* **2011**, *133*, 8440-8443.

(58) Bhattacharyya, K. X.; Dreyfuss, S.; Saffon-Merceron, N.; Mézailles, N. *Chem. Commun.* **2016**, *52*, 5179-5182.

(59) Gaussian 09, Revision B.01, M.J. Frisch, G. W. Trucks, H. B. Schlegel, G. E. Scuseria, M. A. Robb, J. R. Cheeseman, G. Scalmani, V. Barone, B. Mennucci, G. A. Petersson, H. Nakatsuji, M. Caricato, X. Li, H. P. Hratchian, A. F. Izmaylov, J. Bloino, G. Zheng, J. L. Sonnenberg, M. Hada, M. Ehara, K. Toyota, R. Fukuda, J. Hasegawa, M. Ishida, T. Nakajima, Y. Honda, O. Kitao, H. Nakai, T. Vreven, J. A. Montgomery Jr., J. E. Peralta, F. Ogliaro, M. Bearpark, J. J. Heyd, E. Brothers, K. N. Kudin, V. N. Staroverov, R. Kobayashi, J. Normand, K. Raghavachari, A. Rendell, J. C. Burant, S. S. Iyengar, J. Tomasi, M. Cossi, N. Rega, J. M. Millam, M. Klene, J. E. Knox, J. B. Cross, V. Bakken, C. Adamo, J. Jaramillo, R. Gomperts, R. E. Stratmann, O. Yazyev, A. J. Austin, R. Cammi, C. Pomelli, J. W. Ochterski, R. L. Martin, K. Morokuma, V. G. Zakrzewski, G. A. Voth, P. Salvador, J. J. Dannenberg, S. Dapprich, A. D. Daniels, Ö. Farkas, J. B. Foresman, J. V. Ortiz, J. Cioslowski, D. J. Fox, Gaussian, Inc., Wallingford CT, 2009.

(60) Zhao, Y.; Truhlar, D. G. *J. Chem, Phys.* **2006**, *125*, 1-18.

(61) Weigend, F.; Ahlrichs, R. *Phys. Chem. Chem. Phys.* **2005**, *7*, 3297-3305.

(62) Warren, J. J.; Tronic, T. A.; Mayer, J. M. *Chem. Rev.* **2010**, *110*, 6961-7001.

(63) Stoll, S.; Schweiger, A. *J. Magn. Reson*. **2006**, *178*, 42-55.

Chapter 3

H_2 ELIMINATION FROM A THIOLATE-BOUND NI(III) HYDRIDE

3.1 Introduction

Hydrogen is a promising alternative to carbon-based fuel, and homogenous electrocatalysts for the H_2 evolution reaction (HER) have been scrutinized for possible practical applications and especially as well-defined systems for mechanistic studies.[1] Although metal hydrides may not be required intermediates of HER,[2] for HER catalysts featuring nickel, terminally bound Ni^{III} hydride intermediates have been implicated in both stoichiometric[3] and catalytic[4] proton reduction.[5] Additionally, paramagnetic Ni^{III} hydride intermediates have been proposed in enzymatic H_2 evolution (Fig. 3.1, top). A bridging hydride has been identified in the S = ½ [NiFe] hydrogenase intermediate (Ni^{III}–H–Fe^{II}) assigned as the Ni-C state,[6] and computational data suggest that the hydride is bound more tightly to Ni than to Fe (Ni–H: 1.61 Å, Fe–H: 1.72 Å).[7,8] Additionally, EPR data support an estimated Ni–H bond length of ~1.6 Å.[6a] The possible role of a [NiFe] hydrogenase state featuring a terminal Ni^{III}–H has also been computationally investigated for the related case of H_2 oxidation.[9] Furthermore, studies on Ni-substituted rubredoxin, a model enzyme for [NiFe] hydrogenase bearing a single Ni center in the active site, support the intermediacy of a terminal Ni^{III}–H species in proton reduction catalysis.[10]

Owing to their posited role as intermediates in HER catalysis, well-characterized paramagnetic nickel hydride model complexes are needed for detailed study, but examples are lacking, whereas examples of related terminally bound $Ni^{I/III}$–Me species are available.[11] For hydride cases, such species largely feature bridging hydrides bound to two metal centers (Ni–H–Ni),[12] three metal centers (Ni_3–(H)),[12d,13] or as borohydride adducts (Ni–H–BR_3).[14] Characterization data for *terminally* bound $Ni^{I/III}$ hydride complexes are scant. In previous work, irradiation of a matrix-isolated sample containing $Ni(CO)_4$ and HI yielded several EPR-active compounds, including a species assigned as H–$Ni^{I}(CO)_4$.[15] Related solid-state

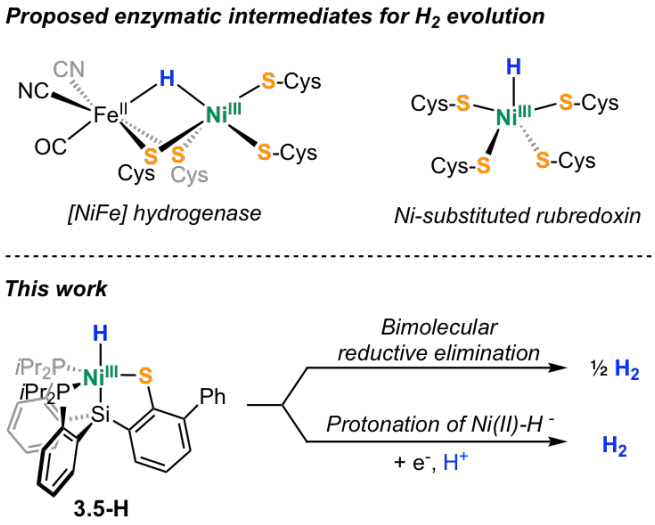

Figure 3.1. (top) Proposed hydrogenase intermediates featuring a Ni^{III} hydride motif (bottom) Accessible pathways for H_2 evolution from the Ni hydride complexes described in this work.

experiments employing $Ni(CN)_4^{2-}$ generated a $[H–Ni(CN)_n]^x$ species as one of the EPR-active products.[16] Additionally, the Ni^{III} hydride $[(PS_3)Ni^{III}H][PPN]$ has been reported in solution by treatment of the analogous Ni^{III}–OPh complex with pinacolborane.[17,18] Characterization data for this species was limited; in particular, the inferred hydride ligand was not confirmed by spectroscopic analysis (*vide infra*).

Herein, we generate and spectroscopically characterize a thiolate-supported, terminally-bound Ni^{III}–H species at low temperature. Direct identification of the terminal hydride ligand is confirmed by both vibrational and pulse EPR data. Of note, bimolecular reductive elimination of H_2 proceeds upon warming this Ni^{III}–H species, followed with N_2 binding to quantitatively generate a Ni^{II}–N_2 product. Stoichiometric reactivity studies from the Ni^{II}–H^- and Ni^{III}–H species featured herein demonstrate the viability of both a heterolytic and homolytic pathway for H_2 evolution.

3.2 Results and Discussion

3.2.1 Synthesis and Characterization of Ni precursors

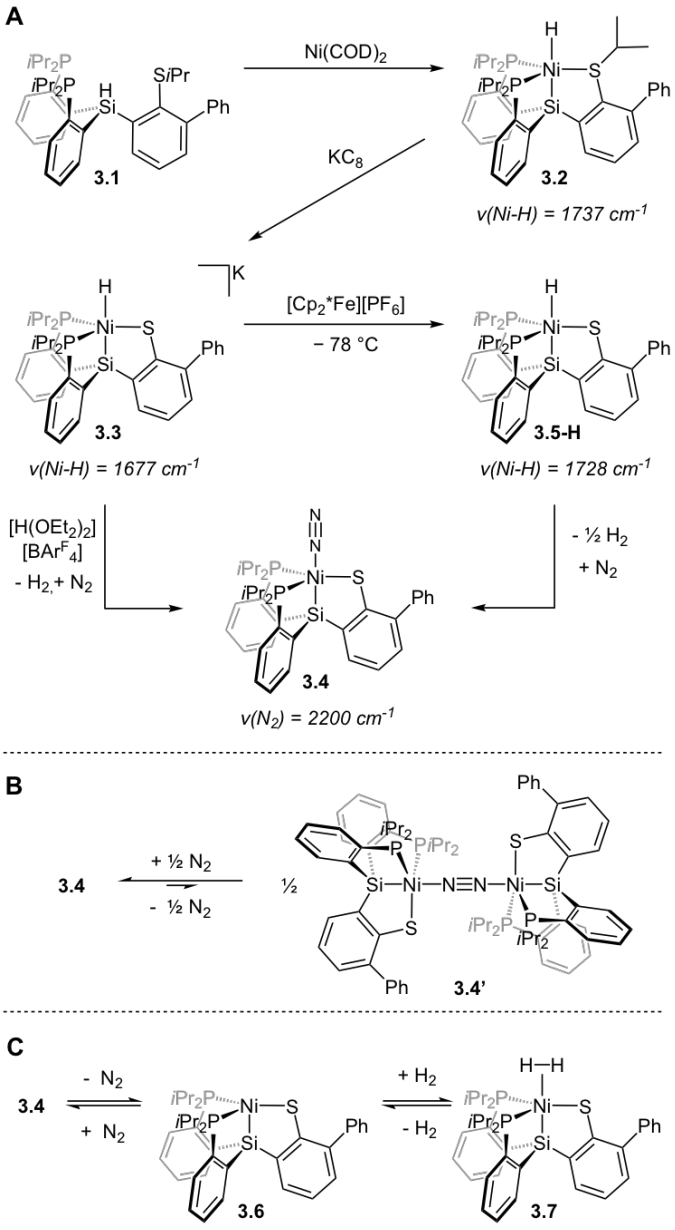

Scheme 3.1. Synthesis and numbering scheme of compounds discussed herein.

Following a recent study of a ferric Fe(H)(N_2) species featuring a tetradentate bis(phosphine)(silyl)(thiolate) ligand (Scheme 3.1),[19] we targeted the generation of a trivalent Ni–H species supported by this ligand framework. Treatment of $HSiP_2S^{iPr}$ (**3.1**)[19] with Ni(COD)$_2$ (COD = 1,5-cyclooctadiene) yields a thioether-bound Ni(II) hydride, (SiP_2S^{iPr})$Ni^{II}H$ (**3.2**, Scheme 3.1a; see Fig. 3.2A for solid-state structure) with a Ni–H stretch

at 1737 cm^{-1} and a ^1H NMR hydride signal at −6.90 ppm (t, $^3J_{H,P}$ = 46.3 Hz, in C_6D_6). Addition of KC_8 to **3.2** results in the reductive cleavage of the S–*i*Pr bond to furnish a thiolate-bound Ni(II) hydride, [(SiP_2S)$Ni^{II}H$]K (**3.3**, see Fig. 3.2B for solid-state structure; ν(Ni–H) at 1677 cm^{-1}; hydridic resonance at −8.10 ppm (t, $^3J_{H,P}$ = 43.0 Hz) in C_6D_6).

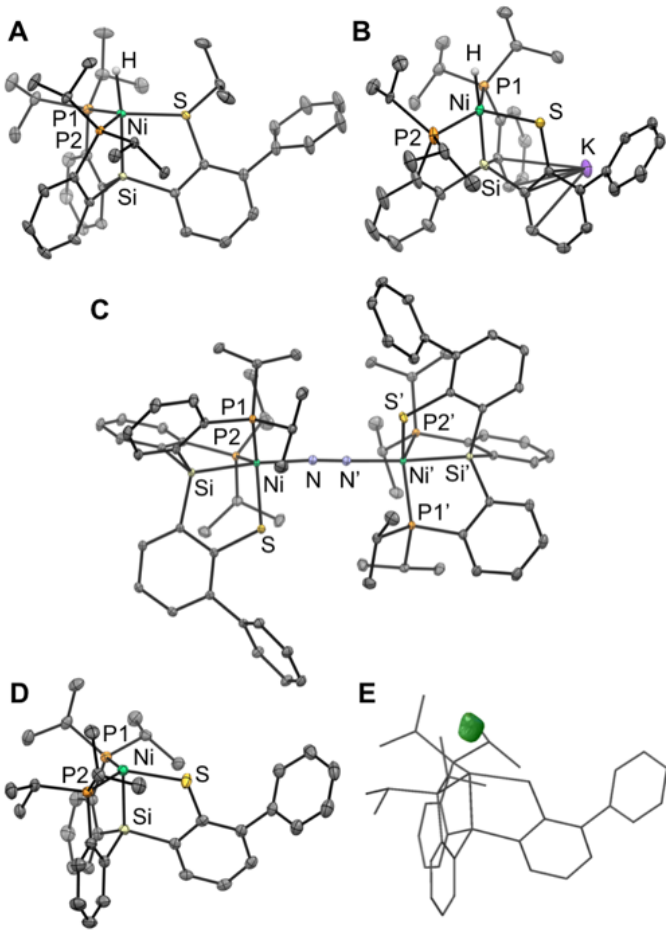

Figure 3.2. X-ray structures of **3.2** (A), **3.3** (B), **3.4'** (C), **3.7** (D), and the residual positive electron density plot of **3.7** (isovalue: 0.78) (E). C–*H* hydrogen atoms and solvent molecules are omitted for clarity. Ellipsoids are depicted at 50% probability.

Protonation of hydride **3.3** with [$H(OEt_2)_2$][$BAr^F{}_4$] under an N_2 atmosphere affords a nickel(II) complex, (SiP_2S)$Ni^{II}(N_2)$ (**3.4**), which crystallizes as the dimeric, dinitrogen-bridged species, [(SiP_2S)Ni^{II}]$_2(N_2)$ (**3.4'**) (Scheme 3.1B). XRD data confirms the structure

of **3.4'** (Fig. 3.2C; Table 3.1) and reveals an N–N bond length of 1.115(2) Å. Solid-state IR data of crystals of **3.4'** do not show an N_2 stretch, consistent with the inversion center gleaned in the solid-state structure. However, an intense N_2 stretch at 2200 cm^{-1} is observed in solution under an N_2 atmosphere, indicating that **3.4'** dissociates to monomeric **3.4** in solution. Notably, a solid thin-film produced by concentration of a solution of **3.4** under an N_2 stream does not exhibit the N_2 stretch at 2200 cm^{-1}, demonstrating that **3.4'** predominates upon concentration and is consistent with an equilibrium between **3.4** and **3.4'**.

Table 3.1. Bond lengths of **3.4'** and **3.7**.

	***d*(Ni–S)**	***d*(Ni–P)**	**∠(P–Ni–P)**	**∠(P–Ni–S)**
3.4	2.3320(6)	2.2405(5)	129.82(3)	109.69(2)
		2.2627(6)		116.49(2)
3.7	2.3089(9)	2.208(1)	129.12(4)	108.62(4)
		2.2246(6)		119.77(4)

A degassed solution of diamagnetic **3.4** bears NMR features distinct from those acquired under an N_2 atmosphere, intimating the loss of N_2 to generate a diamagnetic four-coordinate Ni species, $(SiP_2S)Ni^{II}$ (**3.6**), under vacuum (Scheme 3.1C). Exposure of **3.6** to an atmosphere of H_2 yields the five-coordinate Ni^{II}–H_2 complex, $(SiP_2S)Ni^{II}(H_2)$ (**3.7**). XRD data obtained on crystals grown under an atmosphere of H_2 are consistent with the assignment of **3.7**; while the H_2 unit could not be reliably identified from the XRD data, positive residual electron density located trans to the silyl group is consistent with a bound H_2 (Fig. 3.2d,e).[20] Notably, the structural similarity between **3.7** and **3.4'** suggests that **3.7** bears an intact H–H fragment in the solid state, as opposed to a $Ni(H)_2$ or NiH(SH) species (Table 3.1). Additionally, the HD analogue, $(SiP_2S)Ni^{II}(HD)$, exhibits a $^1J_{HD}$ of 35 Hz (toluene-d_8, −80 °C), indicative of an intact dihydrogen unit in solution.[21] Examples of $Ni(H_2)$ complexes are rare,[22,23] and **3.7** is distinct by virtue of the thiolate donor ligand; H_2 activation across a Ni–thiolate bonds has been invoked elsewhere.[24]

3.2.2 Generation and Characterization of a Ni^{III}–H

The cyclic voltammogram of **3.4** in THF reveals a reduction event at −2.33 V vs. Cp_2Fe/Cp_2Fe^+, and **3.4** slowly catalyzes HER in the presence of PhOH as a weak acid source at a strongly cathodic potential (see Appendix B for details).[25] Treatment of the Ni^{II}–H^- **3.3** with PhOH in THF results in quantitative generation of H_2 and $(SiP_2S)NiOPh^-$, demonstrating a heterolytic pathway for H–H bond formation within the system. For comparison, we also explored the viability of a homolytic pathway for H_2 generation from the corresponding Ni^{III}–H species. Examples of $M^{n/n+1}$ hydride pairs that can access H_2 evolution via a homolytic pathway from one oxidation state and a heterolytic pathway from another are rare.[27e,28a] Whereas protonation of a metal hydride complex to release H_2 is commonly observed,[1,26] examples of bimolecular reductive elimination of H_2 from two well-defined M–H units is less precedented,[19,27,28,29] although such a pathway has been proposed in a number of HER electrocatalysts.[1,4f,27e,30]

The cyclic voltammogram of the Ni^{II}–H^- species **3.3** exhibits a reversible feature at −1.26 V vs. Cp_2Fe/Cp_2Fe^+ in THF that corresponds to the formal $Ni^{II/III}$ couple, and chemical oxidation using $[Cp^*_2Fe][PF_6]$ at −78 °C in THF yields a dark blue-green solution of the desired $(SiP_2S)Ni^{III}H$ (**3.5-H**) species. Solutions of **3.5-H** are thermally sensitive (*vide infra*) and were therefore handled at low temperatures to obtain spectroscopic data. As expected for a Kramer's doublet species, **3.5-H** exhibits paramagnetically shifted peaks in its ^1H NMR spectrum (THF-d_8, −40 °C). A characteristic terminal Ni–H stretch is observed in the IR spectrum at 1728 cm^{-1} (THF solution, −78 °C) that vanishes upon deuteration via the analogue $(SiP_2S)Ni^{III}D$ (**3.5-D**).[31] This Ni–H stretch is in good agreement with the DFT-predicted gas-phase value of 1720 cm^{-1}.[32]

The 77 K X-band CW EPR spectrum of **3.5-H** confirms the expected $S = ½$ spin state (Fig. 3.3) and is simulated with a rhombic g tensor of $\mathbf{g} = [2.166, 2.056, 2.039]$ and hyperfine coupling to two equivalent ^{31}P nuclei ($\mathbf{A}(^{31}P\alpha) = \mathbf{A}(^{31}P\beta) = \pm[200, 210, 260]$ MHz) and a Ni–*H* nucleus ($\mathbf{A}(^1H) = \pm[1.63, 1.63, 31.9]$ MHz; for **3.5-D**, $\mathbf{A}(^2H) = \pm[0.25, 0.25, 4.9]$ MHz). These simulation parameters are consistent with Q-band ^1H, ^{31}P Davies ENDOR and ^2H HYSCORE data for **3.5-H** and **3.5-D** (see Appendix B). Notably, the ^1H dipolar tensor (**T**)

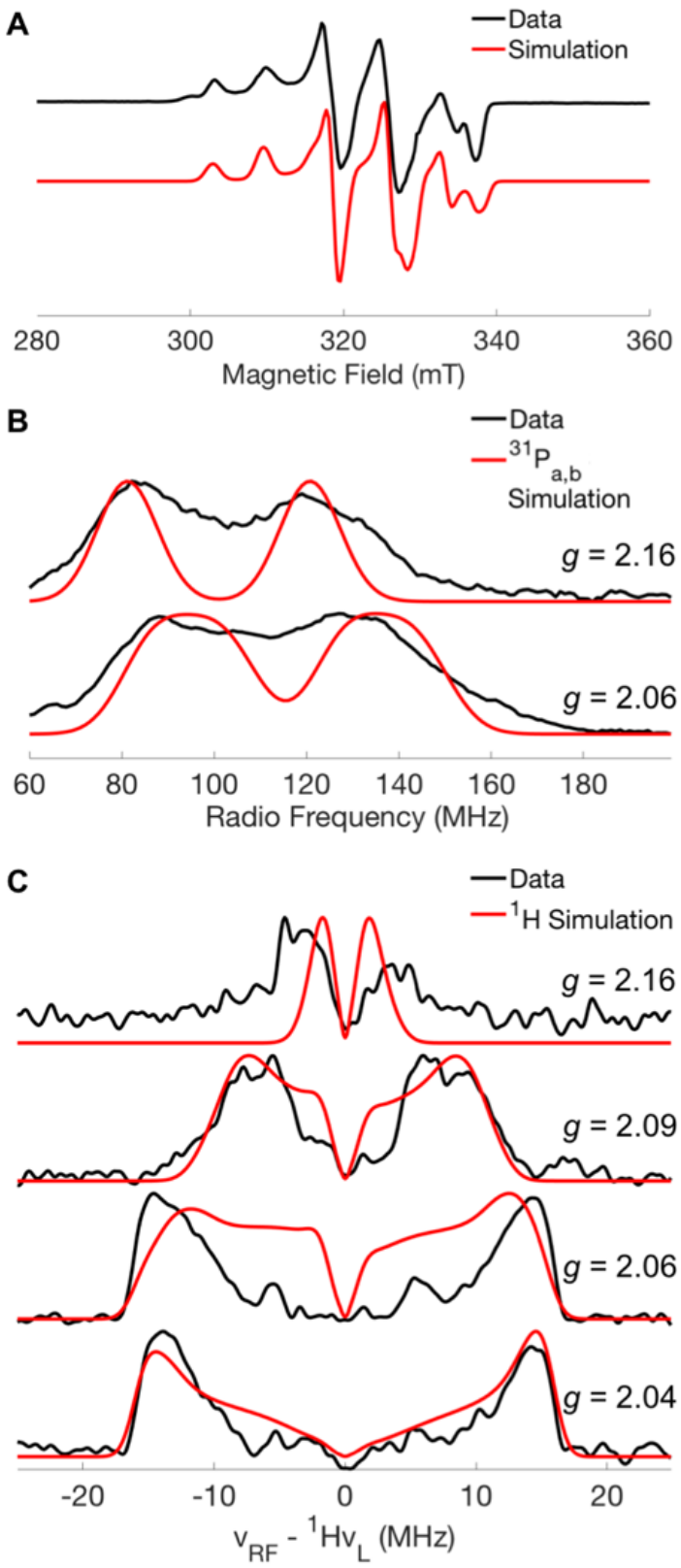
A
Data
Simulation
280
300
320
340
360
Magnetic Field (mT)
B
Data
$^{31}P_{a,b}$ Simulation
g = 2.16
g = 2.06
60
80
100
120
140
160
180
Radio Frequency (MHz)
C
Data
^{1}H Simulation
g = 2.16
g = 2.09
g = 2.06
g = 2.04
-20
-10
0
10
20
$\nu_{RF} - {}^{1}H\nu_{L}$ (MHz)

Figure 3.3. (A) 77 K X-band CW EPR spectrum of **3.5-H** in 2-MeTHF with simulation. Simulation parameters: g = [2.166, 2.056, 2.039]; **A**(^{31}Pα) = **A**(^{31}Pβ) = [200, 210, 260] MHz); A(^{1}H) = [1.6, 1.6, 31.9] MHz. (B) Field-dependent ^{31}P Q-band Davies ENDOR spectra of **3.5-D**. (C) Field-dependent Q-band Davies ENDOR ^{1}H minus ^{2}H difference spectra of **3.5-H** and **3.5-D**; difference spectra were smoothed using a 5-point Savitzky-Golay filter. ENDOR samples were prepared in 2-MeTHF, and spectra are simulated with the same g-values and hyperfine coupling as Fig. 3.3A. Experimental conditions for Fig. 3.3B, 3.3C: microwave frequency = 34.040 GHz; MW π pulse length = 80 ns; interpulse delay τ = 400 ns; πRF pulse length = 15 μs; TRF delay = 2 μs; shot repetition time (srt) = 2 ms; temperature = 12 K.

of **3.5-H** is axially symmetric (**A**(^{1}H) = a_{iso} + **T**; **T** = ±[−10.1, −10.1, 20.2] MHz), as can be anticipated for a terminally bound metal hydride (M−H), whereas a rhombic dipolar tensor would instead be expected for an approximately symmetric bridging hydride (M−H−M).[33] By scaling the isotropic component of the ^{1}H hyperfine coupling tensor ($|a_{iso}(^{1}H)|$ = 11.7 MHz) by the a_{iso} value for a hydrogen atom (1420 MHz),[34] spin density localized at the hydride is estimated as ±0.008 e^{-}. The DFT-optimized structure in the gas phase for **3.5-H** (M06l) predicts a Mulliken spin density of −0.005 e^{-} on the hydride, consistent with the experimental data.

Complex **3.5-H** could not be obtained in solid-state form due to its highly reactive nature. However, an analogous and more stable Ni^{III}-Me species could be prepared, isolated, and crystallographically characterized. Accordingly, treatment of **3.4** with methyl lithium yields diamagnetic [(SiP_2S)Ni^{II}Me]Li (**3.8**), and its oxidation by [Cp*$_2$Fe][PF_6] at −78 °C affords a dark blue-green solution of (SiP_2S)Ni^{III}Me (**3.9**, Fig. 3.4).[35] Structural parameters for **3.9** compare favorably to the gas-phase, DFT-optimized parameters for **3.5-H** (Table 3.2). The 77 K X-band CW EPR spectrum exhibits a rhombic *g* tensor (**g** = [2.255, 2.073, 2.037]) and hyperfine coupling to two similar but distinct ^{31}P nuclei (**A**(^{31}Pα) = ±[170, 133, 330] MHz; **A**(^{31}Pβ) = ±[260, 257, 130] MHz). Compared to that of **3.5-H**, the EPR spectrum of **9** exhibits slightly greater *g*-anisotropy and comparable $|a_{iso}(^{31}P)|$ values (**3.5-H**: $|a_{iso}(^{31}P\alpha)| = |a_{iso}(^{31}P\beta)|$ = 223 MHz; **3.9**: $|a_{iso}(^{31}P\alpha)|$ = 211 MHz, $|a_{iso}(^{31}P\beta)|$ = 216 MHz).

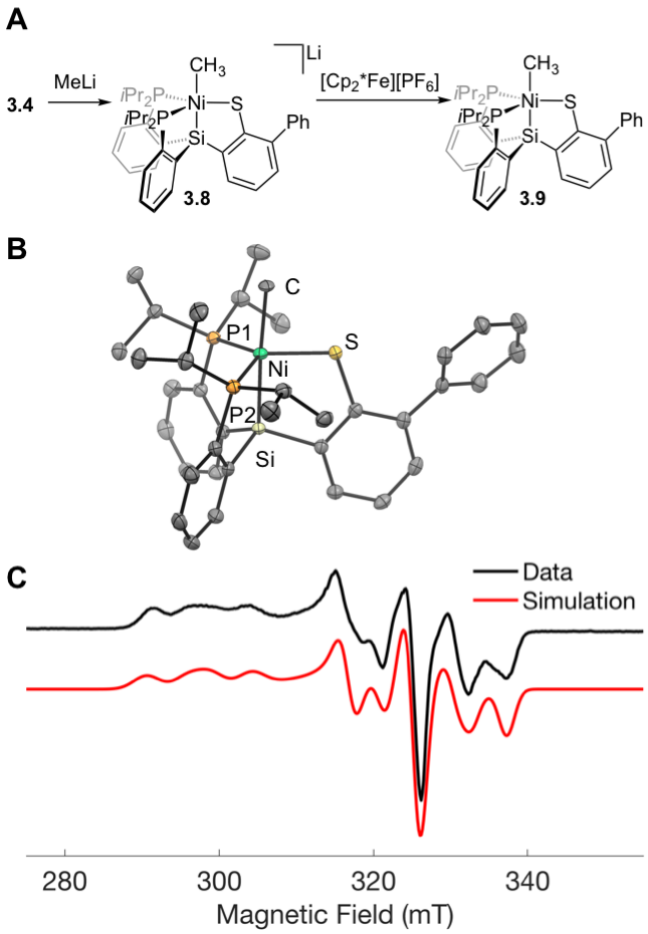

Figure 3.4. (A) Synthetic route to access compound **3.9**. (B) X-ray structure of **3.9**. Hydrogen atoms and disordered components are omitted for clarity. Ellipsoids are depicted at 50% probability. (C) 77 K X-band CW EPR spectrum of **3.9** in 2-MeTHF with simulation. Simulation parameters: **g** = [2.255, 2.073, 2.037]; **A**(^{31}Pα) = [170, 133, 330] MHz; **A**(^{31}Pβ) = [260, 257, 130] MHz.

Table 3.2. Bond lengths of **3.5-H** (DFT) and **3.9** (XRD)

	***d*(Ni–X)**	***d*(Ni–S)**	***d*(Ni–P)$_{avg}$**	***d*(Ni–Si)**
3.5-H	1.55	2.22	2.25	2.25
3.9	2.047(5)	2.1972(6)	2.2428(6)	2.2541(6)

X = H (**3.5-H**), CH_3 (**3.9**)

3.2.3 EPR characterization of [(PS$_3$)NiH][PPN]

Given the potential value for EPR data of model Ni^{III}–H species to guide reliable assignments of such intermediates in Ni-containing hydrogenases, we also undertook the generation of the previously reported [(PS$_3$)NiH][PPN] species[17] and the analogous nickel deuteride for related characterization by EPR techniques. As noted above, previously reported vibrational and EPR data did not locate the presence of the terminal hydride moiety, though its chemical reactivity was consistent with such a formulation.

Through X-band HYSCORE experiments, the ^{2}H hyperfine coupling for [(PS$_3$)NiD][PPN] could be detected: **A**(^{2}H) = ±[1.6, 9.3, 9.3] MHz (See Appendix B for more details). Scaling **A**(^{2}H) by the ratio of the ^{1}H/^{2}H gyromagnetic ratios (^{1}Hγ/^{2}Hγ = 6.514) approximates a ^{1}H hyperfine coupling of **A**(^{1}H) = ±[10.4, 60.6, 60.6] MHz in [(PS$_3$)NiH][PPN], with $|a_{iso}(^1H)|$ = 43.9 MHz and **T** = ±[−33.5, 16.7, 16.7] MHz. The $|a_{iso}(^1H)|$ value corresponds to approximately ±0.03 e$^-$ of spin density localized on the hydride of [(PS$_3$)NiH][PPN], in agreement with a DFT-estimated value of −0.05 e$^-$ (gas phase, M06l; see Appendix B). There hence appears to be greater spin delocalization onto the hydride ligand of [(PS$_3$)NiH][PPN] compared to **3.5-H**. This difference presumably arises from an increased metal-ligand covalency in **3.5-H**; a Mulliken spin density of 0.73 e$^-$ is calculated on Ni in [(PS$_3$)NiH][PPN], compared to 0.60 e$^-$ in **3.5-H**.

3.2.4 Comparison of Ni^{III}–H Species with the Ni-C Hydrogenase State

In both systems, spin delocalization onto the ligand framework likely stabilizes the Ni^{III}–H species. Consistent with this idea, DFT-calculated Mulliken spin densities (M06-L functional: def2tzvp [Ni] and def2svp [all other atoms] basis sets) suggests that there is considerable spin leakage onto the supporting thiolate ligands of **3.5-H** (0.22 e$^-$) and [(PS$_3$)NiH][PPN] (0.07, 0.07, 0.16 e$^-$). For comparison, in the case of the Ni-C hydrogenase state, DFT calculations suggest the presence of significant spin delocalization onto one of the bridging cysteine groups (Fig. 3.5, BP86 functional),[36] with the majority of spin localized on Ni (0.72 e$^-$) rather than Fe (0.01 e$^-$). Additionally, a spin density of −0.01 e$^-$ is calculated on the hydride bridging the Ni and Fe centers; experimental data support $|a_{iso}(^1H)|$ = *ca.* 11

MHz for the hydride ligand in *D. gigas* hydrogenase,[6c] and a value of $|a_{iso}(^1H)| = 3.5$ MHz is measured for both *Ralstonia eutropha*[6a] and *D. vulgaris* Miyazaki F hydrogenases.[6d]

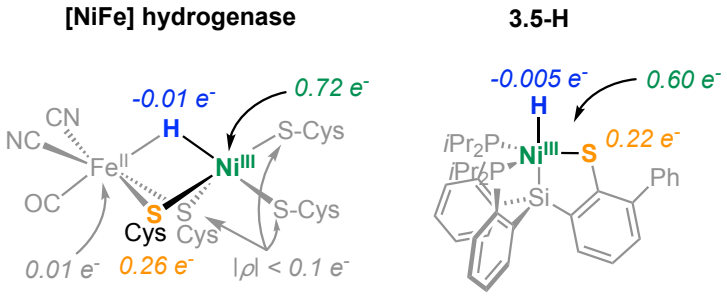

Figure 3.5. Calculated Mulliken spin densities of the Ni-C hydrogenase state and **3.5-H**.

It has been noted that the $|a_{iso}(^1H)|$ value for the hydride of the Ni-C hydrogenase state is significantly smaller than that anticipiated for a hydride covalently bound to Ni,[6a,b,c] given that $|a_{iso}(^1H)|$ for $H–Ni^I(CO)_3$ was reported to be 293 MHz,[15,37] and that of $[H–Ni(CN)_n]^x$ was estimated to be *ca*. 427 MHz.[16] Assuming these assignments are reliable, one suggested explanation for the discrepancy is the presence of a proximal iron center in the Ni-C state, which may in turn perturb the spin distribution.[6a] However, it has been observed that the spin density on Fe is very low in the Ni-C state,[38] corroborated by DFT calculations.[36] In this context, it is therefore significant that **3.5-H** and $[(PS_3)NiH][PPN]$ are measured to have $|a_{iso}(^1H)|$ values quite comparable to that of the Ni-C hydride. The data presented here demonstrates that hydrides covalently bound to a paramagnetic Ni center can exhibit comparatively small $|a_{iso}(^1H)|$ values. We attribute the small $|a_{iso}(^1H)|$ of these complexes in part to the significant spin delocalization onto the thiolate ligands of **3.5-H** and $[(PS_3)NiH][PPN]$, and by extension suggest that the bridging cysteine in the Ni-C state mitigates the magnitude of $|a_{iso}(^1H)|$ in the Ni-C state hydride, and likely more so than the proximal Fe center.[39] Furthermore, although DFT-calculated EPR parameters for the hydrogenase structure featuring a bridging hydride between Ni^{III} and Fe^{II} provide a satisfactory fit to experimental data for the Ni-C state,[6f,g] the present study demonstrates that

terminally bound Ni^{III} hydrides can bear $|a_{iso}(^1H)|$ values comparable to that measured for the Ni-C state.

3.2.2 Bimolecular H_2 Release from Thiolate–Ni^{III}–H and Comparison with H_2 Release from Thiolate–Fe^{III}–H

Our ability to generate and reliably characterize the Ni^{III}–H species **3.5-H** enabled us to evaluate its propensity to undergo a bimolecular homocoupling process to generate H_2.[40] Accordingly, dark blue-green solutions of **3.5-H** prepared *in situ* at −78 °C quantitatively convert to orange solutions of **3.4** upon warming to 25 °C under N_2. H_2 production was confirmed by GC analysis (98%). The decay of **3.5-H** to **3.4** monitored by UV-Vis spectroscopy exhibits isosbestic behavior and is second-order with respect to **3.5-H** (Fig. 3.6, k = 20 $M^{-1}\cdot min^{-1}$ at 25 °C). A kinetic isotope effect is observed (k_H/k_D = 1.6 at 25 °C), suggesting that the hydride ligand is present in the rate-determining transition state, and Eyring analysis reveals activation parameters of $\Delta S^{\ddagger}$ = −30(7) cal/(mol·K) and $\Delta H^{\ddagger}$ = 9(2) kcal/mol. The large and negative entropic activation term is consistent with an ordered rate-determining transition state, and these data support the bimolecular reductive elimination of H_2 between two Ni^{III}–H fragments.

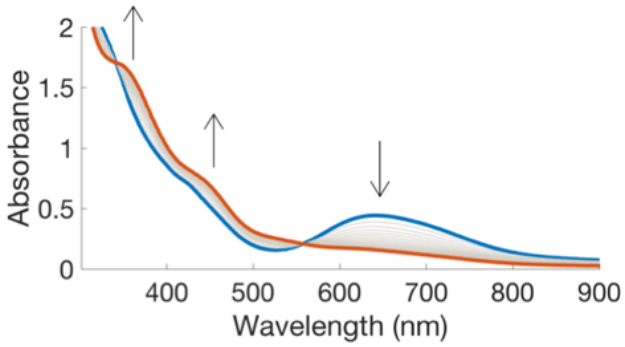

Figure 3.6. UV-vis spectra depicting the decay of **3.5-H** to **3.4** at 25 °C in THF. Spectra collected in 20 min intervals.

Metal hydrides with BDFE(M–H) less than half the BDFE of H_2 (BDFE(M–H) < *ca.* 52 kcal/mol in MeCN)[41] are thermodynamically favored to undergo bimolecular reductive elimination of H_2 (2 M–H → 2 M + H_2). Under vacuum, a THF solution of **3.5-H** reacts to

form the vacant species **3.6**, suggesting that the Ni–H BDFE is < *ca.* 52 kcal/mol. This is in approximate agreement with the DFT-estimated Ni–H gas-phase BDFE of 57 kcal/mol (**3.5-H** → H• + **3.6**).

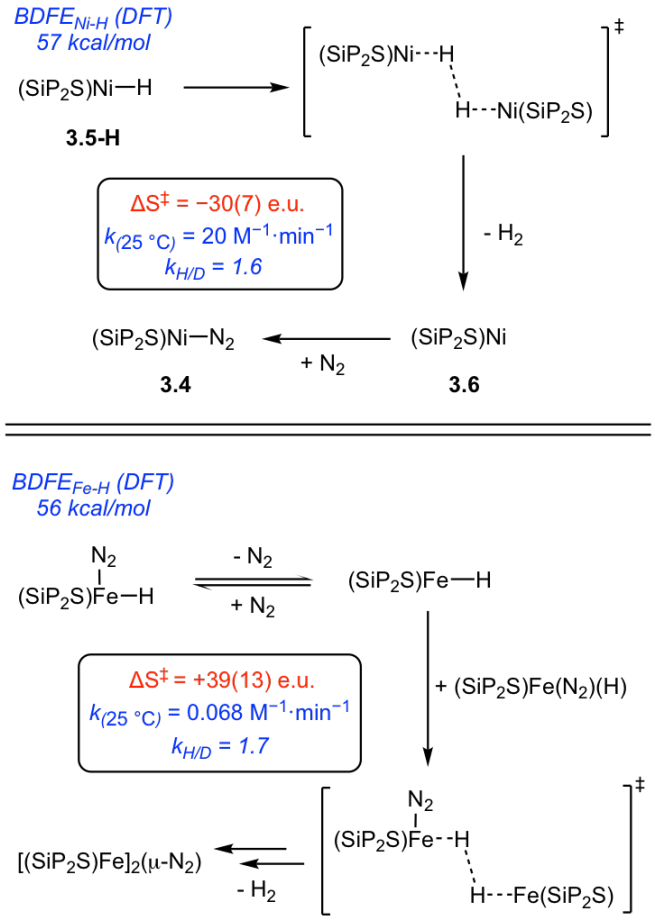

Scheme 3.2. Comparison of **3.5-H** and **(SiP$_2$S)Fe(H)(N$_2$)**, which both undergo bimolecular reductive elimination of H_2 upon warming but with different rates and activation parameters in accord with the presented pathways. Gas-phase BDFEs were calculated with the M06-L functional (def2tzvp [Fe or Ni], def2svp [all other atoms]).

A related S = ½ ferric hydride, (SiP$_2$S)Fe^{III}(H)(N$_2$), that we have previously reported,[19] has a DFT-estimated gas phase Fe–H BDFE of 56 kcal/mol ((SiP$_2$S)Fe(H)(N$_2$) → H• + (SiP$_2$S)Fe(N$_2$)) and also undergoes bimolecular reductive elimination of H_2 upon warming to yield the N_2-bridged species [(SiP$_2$S)Fe^{II}]$_2$(N$_2$). Compared to the Ni system, there is a greater degree of spin delocalization onto the hydride ligand in the Fe system, evidenced

by a greater $|a_{iso}(^1H)|$ value of 43 MHz. However, HER from the ferric hydride proceeds with a significantly smaller second-order rate constant at 25 °C compared to the Ni system ([Fe]: $k = 0.068\ M^{-1}\cdot min^{-1}$, Scheme 3.2). Additionally, the bimolecular transformation of the ferric hydride bears a large and positive $\Delta S^{\ddagger}$ of 39(13) cal/(mol·K) that we hypothesized to arise from N_2 dissociation prior to H–H bond formation (e.g. $\{N_2\ (g) + [Fe^{III}]–H\cdots H–[Fe^{III}(N_2)]\}^{\ddagger}$). Such a scenario contrasts with the negative $\Delta S^{\ddagger}$ determined for the present Ni system, which is consistent with an ordered rate-determining transition state (e.g. $\{[Ni^{III}]–H\cdots H–[Ni^{III}]\}^{\ddagger}$).

The unobserved, N_2-dissociated ferric hydride $(SiP_2S)Fe^{III}(H)$ would be an electron-deficient 15 $e^–$ species, favoring N_2 binding to yield a 17 $e^–$ species $(SiP_2S)Fe^{III}(H)(N_2)$. In contrast, the Ni(III) hydride **3.5-H** is a 17 $e^–$ species, and N_2 binding to form the 19 $e^–$ species $(SiP_2S)Ni^{III}(H)(N_2)$ is thus disfavored. Pre-dissociation of N_2 hence does not play a role in the H_2 evolution chemistry of the Ni system, whereas it does in the Fe system. This is likely a significant factor in the dramatically enhanced rate of H_2 formation in the Ni system compared to Fe. Additionally, because the terminal product is an N_2-bound species, thermodynamic stabilization afforded by N_2 binding may also contribute to the relative rates of H_2 elimination.

3.3 Conclusion

In closing, we have reported the synthesis and spectroscopic characterization of an unusual $S = ½$, terminal Ni^{III}–H species, **3.5-H**, and its propensity to undergo homolytic bimolecular H–H coupling to release H_2. Heterolytic H_2 evolution via protonation of its 1-electron reduced state, Ni^{II}–$H^–$, has also been demonstrated. For the Ni^{III}–H of most interest, the sulfur donor bears a considerable amount of spin density (0.22 $e^–$) based on DFT calculations, stabilizing the system and allowing, for the first time, direct measurement of salient spectroscopic parameters, including a terminal Ni–H vibration (1728 cm^{-1} in THF), and hyperfine coupling to the terminal hydride ligand ($|a_{iso}(^1H)|$ = 11.7 MHz) as detected via pulse EPR studies. Importantly, this isotropic hyperfine coupling value is similar to that of the hydride ligand in the Ni-C hydrogenase state,[6a,c,d] whereas significantly larger $|a_{iso}(^1H)|$

values, on the order of 10^2 MHz, were reported for H–$Ni^{I}(CO)_4$[15] and [H–$Ni(CN)_n$]^{x} [16] (via generation and detection in a solid matrix), the only previous examples of Ni–H species with reported $|a_{iso}(^1H)|$ values.

The discrepancy between the significantly smaller $|a_{iso}(^1H)|$ measured for the assigned Ni–*H*–Fe moiety of the Ni-C hydrogenase state, compared to the previously reported paramagnetic nickel hydride species, has been highlighted previously.[6a,b,c] The EPR data for the well-defined Ni^{III}–H species featured herein demonstrates that smaller $|a_{iso}(^1H)|$ values are in fact compatible with a nickel hydride ligand assignment, especially when covalently bound to a spin active nickel center with one (or more) sulfur donors, as is suggested for the Ni-C hydrogenase state. Thus, the Ni^{III}–H species reported here, and related structures in future studies, can provide valuable platforms for constraining spectroscopic assignments in enzymatic systems, and specific reactivity patterns including H–H bond formation to generation H_2.

3.4 Experimental Section

3.4.1 Experimental Details

3.4.1.1 General Considerations

All syntheses and measurements, unless otherwise stated, were carried out under an inert atmosphere (N_2) in a glovebox or using standard Schlenk techniques, and solvents were dried and degassed by thoroughly sparging with N_2 and then passing through an activated alumina column in a solvent purification system supplied by SG Water, LLC. Deuterated solvents were purchased from Cambridge Isotope Laboratories, Inc., degassed, and dried over activated 3 Å molecular sieves before use. **3.1**,[19] [Cp^*_2Fe][PF_6],[42] KC_8,[43] [$H(OEt_2)_2$][BAr^F_4],[44] PPh_3PCH_2,[45] lithium triethylborodeuteride,[46] [(PS_3)NiOPh][PPN],[47] [(PS_3)NiH][PPN],[17] and DBPin[48] were prepared according to literature procedures. All other reagents were purchased from commercial vendors and used without further purification unless otherwise stated.

3.4.1.2 Physical Methods

Electrochemical measurements were carried out in a glovebox under an N_2 atmosphere in a one compartment cell using a CH Instruments 600B electrochemical analyzer. A glassy carbon electrode was used as the working electrode and a platinum wire was used as the auxiliary electrode. A Ag/AgOTf reference electrode was used with the ferrocene couple (Fc/Fc^+) as an external reference, unless otherwise noted. Solutions of electrolyte (0.4 M $[NBu_4][PF_6]$ in THF) and analyte were also prepared under an N_2 atmosphere. NMR spectra (^1H, ^{31}P) were collected on Varian 300, 400, or 500 MHz spectrometers (25 °C unless otherwise specified). ^1H chemical shifts are reported in ppm, relative to tetramethylsilane using residual proton resonances from solvent as internal standards. ^{31}P chemical shifts are reported in ppm relative to 85% aqueous H_3PO_4. IR spectra were obtained using a Bruker Alpha Platinum ATR spectrometer with OPUS software in a glovebox under an N_2 atmosphere. Optical spectroscopy measurements were taken on a Cary 50 UV−Vis spectrophotometer using a 1-cm quartz cell, unless otherwise noted. Temperature regulation for UV-Vis measurements was carried out with a Unisoku cryostat. Time-course UV-Vis spectra were collected with the Scanning Kinetics application of the Cary WinUV software. H_2 was analyzed on an Agilent 7890A gas chromatograph (HP-PLOT U, 30 m, 0.32 mm ID; 30 °C isothermal; nitrogen carrier gas) using a thermal conductivity detector. Combustion analyses were carried out by the Beckman Institute Crystallography Facility (Caltech).

3.4.1.3 X-Ray Crystallography

X-ray diffraction measurements were carried out in the Beckman Institute Crystallography Facility. XRD measurements were collected using a dual source Bruker D8 Venture, four-circle diffractometer with a PHOTON CMOS detector. Structures were solved using SHELXT and refined against F^2 on all data by full-matrix least squares with SHELXL. The crystals were mounted on a glass fiber under Paratone N oil.

3.4.1.4 DFT Calculations

Optimization and frequency calculations were performed using the Gaussian 09 program.[49] Structures utilized for thermochemical estimations were optimized in the gas phase. The M06-L functional[50] with the def2-TZVP[51] basis set was used on Ni, and the def2-SVP basis set was used on all other atoms. DFT-estimated free energies of H• transfer are referenced to H• dissociation from TEMPOH.[52]

3.4.1.5 CW EPR Spectroscopy

77 K X-band EPR spectra were obtained on a Bruker EMX spectrometer on solutions prepared as frozen glasses in 2-MeTHF, unless otherwise noted.

3.4.1.6 Pulse EPR Spectroscopy

All pulse Q-band ($\nu \approx 34$ GHz) EPR and electron nuclear double resonance (ENDOR) experiments were aquired using a Bruker (Billerica, MA) ELEXSYS E580 pulse EPR spectrometer equipped with a Bruker D2 resonator. Temperature control was achieved using an ER 4118HV-CF5-L Flexline Cryogen-Free VT cryostat manufactured by ColdEdge (Allentown, PA) equipped with an Oxford Instruments Mercury ITC.

Pulse Q-band ENDOR was acquired using the Davies pulse sequence ($\pi - T_{RF} - \pi_{RF} - T_{RF} - \pi/2 - \tau - \pi -$ echo), where T_{RF} is the delay between mw pulses and RF pulses, π_{RF} is the length of the RF pulse, and the RF frequency is randomly sampled during each pulse sequence.

Q-band HYSCORE spectra were acquired using the 4-pulse sequence ($\pi/2 - \tau - \pi/2 - t_1 - \pi - t_2 - \pi/2 -$ echo), where τ is a fixed delay, while t_1 and t_2 are independently incremented by Δt_1 and Δt_2, respectively. The time domain data was baseline-corrected (third-order polynomial) to eliminate the exponential decay in the echo intensity, apodized with a Hamming window function, zero-filled to eight-fold points, and fast Fourier-transformed to yield the 2-dimensional frequency domain. For ^{2}H-^{1}H difference spectra, the time domain of the HYSCORE spectrum of the ^{1}H sample was subtracted from that of the

^{2}H sample, and the same data processing procedure detailed above was used to generate the frequency spectrum.

In general, the ENDOR spectrum for a given nucleus with spin $I = ½$ (^{1}H, ^{31}P) coupled to the $S = ½$ electron spin exhibits a doublet at frequencies

$$\nu_{\pm} = \left|\frac{A}{2} \pm \nu_N\right| \tag{3.1}$$

where ν_N is the nuclear Larmor frequency and A is the hyperfine coupling. For nuclei with $I \geq 1$ (^{2}H), an additonal splitting of the $\nu_{\pm}$ manifolds is produced by the nuclear quadrupole interaction (P)

$$\nu_{\pm,m_I} = \left|\nu_N \pm \frac{3P(2m_I - 1)}{2}\right| \tag{3.2}$$

In HYSCORE spectra, these signals manifest as cross-peaks or ridges in the 2-D frequency spectrum which are generally symmetric about the diagonal of a given quadrant. This technique allows hyperfine levels corresponding to the same electron-nuclear submanifold to be differentiated, as well as separating features from hyperfine couplings in the weak-coupling regime ($|A| < 2|\nu_I|$) in the (+,+) quadrant from those in the strong coupling regime ($|A| > 2|\nu_I|$) in the (−,+) quadrant. The (−,−) and (+,−) quadrants of these frequency spectra are symmetric to the (+,+) and (−,+) quadrants, thus typically only two of the quadrants are typically displayed in literature.

For systems with appreciable hyperfine anisotropy in frozen solutions or solids, HYSCORE spectra typically do not exhibit sharp cross peaks, but show ridges that represent the sum of cross peaks from selected orientations within the excitation bandwidth of the MW pulses at the magnetic field position at which the spectrum is collected. The length and curvature of these correlation ridges can allow for the separation and estimation of the magnitude of the isotropic and dipolar components of the hyperfine tensor, as shown in Fig. 3.7.

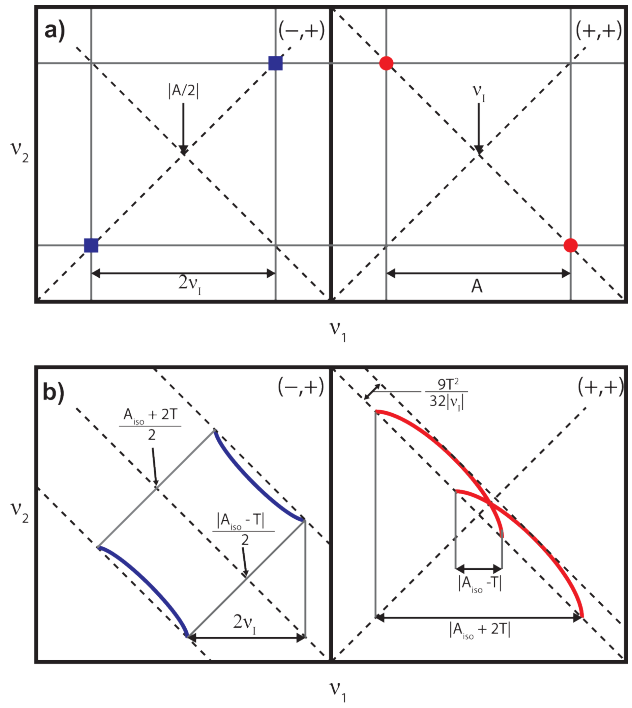

Figure 3.7. a) HYSCORE powder patterns for an $S = ½$, $I = ½$ spin system with an isotropic hyperfine tensor A. b) HYSCORE powder patterns for an $S = ½$, $I = ½$ spin system with an isotropic hyperfine tensor which contains isotropic (a_{iso}) and dipolar (T) contributions. Blue correlation ridges represent the strong coupling case; red correlation ridges represent the weak coupling case.

3.4.1.7 EPR Simulations

Simulations of all CW and pulse EPR data were achieved using the EasySpin[53] simulation toolbox (release 5.2.21) with Matlab 2018b using the following Hamiltonian:

$$\hat{H} = \mu_B \vec{B}_0 g \hat{S} + \mu_N g_N \vec{B}_0 \hat{I} + h\hat{S} \cdot \boldsymbol{A} \cdot \hat{I} + h\hat{I} \cdot \boldsymbol{P} \cdot \hat{I} \qquad (3.3)$$

In this expression, the first term corresponds to the electron Zeeman interaction term where μ_B is the Bohr magneton, g is the electron spin g-value matrix with principle components g = [g_{xx} g_{yy} g_{zz}], and $\hat{S}$ is the electron spin operator; the second term corresponds to the nuclear Zeeman interaction term where μ_N is the nuclear magneton, g_N is the characteristic nuclear g-value for each nucleus (e.g. ^{1}H, ^{2}H, ^{31}P), and $\hat{I}$ is the nuclear spin operator; the third term

corresponds to the electron-nuclear hyperfine term, where $\boldsymbol{A}$ is the hyperfine coupling tensor with principle components $\boldsymbol{A}$ = [A_{xx}, A_{yy}, A_{zz}]; and for nuclei with $I \geq 1$, the final term corresponds to the nuclear quadrupole (NQI) term which arises from the interaction of the nuclear quadrupole moment with the local electric field gradient (efg) at the nucleus, where $\boldsymbol{P}$ is the quadrupole coupling tensor. In the principle axis system (PAS), $\boldsymbol{P}$ is traceless and parametrized by the quadrupole coupling constant e^2Qq/h and the asymmetry parameter η such that:

$$\boldsymbol{P} = \begin{pmatrix} P_{xx} & 0 & 0 \\ 0 & P_{yy} & 0 \\ 0 & 0 & P_{zz} \end{pmatrix} = \frac{e^2Qq/h}{4I(2I-1)} \begin{pmatrix} -(1-\eta) & 0 & 0 \\ 0 & -(1+\eta) & 0 \\ 0 & 0 & 2 \end{pmatrix} \tag{3.4}$$

where $\frac{e^2Qq}{h} = 2I(2I-1)P_{zz}$ and $\eta = \frac{P_{xx}-P_{yy}}{P_{zz}}$. The asymmetry parameter may have values between 0 and 1, with 0 corresponding to an electric field gradient with axial symmetry and 1 corresponding to a fully rhombic efg. The orientations between the hyperfine and NQI tensor principle axis systems and the g-matrix reference frame are defined by the Euler angles (α, β, γ).

3.4.2 Synthetic Details

3.4.2.1 Synthesis of (SiP_2S^{iPr})NiH (3.2)

A solution of **3.1** (1.83 g, 2.8 mmol) in Et_2O (20 mL) was added to solid $Ni(COD)_2$ (0.82 g, 3.0 mmol), and the mixture was stirred at 23 °C for 1 d. The yellow-brown reaction was concentrated to dryness. The resulting yellow-brown material was extracted with C_6H_6 (10 mL), and the solution was filtered through Celite. The filtrate was lyophilized and dissolved in Et_2O (25 mL). The solution was filtered through Celite, and the product was crystallized at 23 °C via slow concentration of the filtrate. The yellow crystals were isolated by filtration and washed with pentane (10 mL) to afford the title complex (1.14 g, 57%). Yellow crystals suitable for XRD were grown from slow concentration of an Et_2O solution at 23 °C. ^{1}H NMR (C_6D_6, 300 MHz, 298 K, δ): 8.22 (d, J = 7.2 Hz, 2H), 8.13 (dd, J = 7.1, 1.4 Hz, 1H), 7.39 –

6.98 (m, 13H), 2.64 (hept, J = 6.6 Hz, 1H), 2.29 (m, 4H), 1.13 – 0.85 (m, 30H), −6.90 (t, J = 46.3 Hz, 1H). ^{31}P NMR (C_6D_6, 121 MHz, 298 K, δ): 73.8. IR (solid, cm^{-1}): 1737 (Ni–H). Anal. Calcd. For $C_{39}H_{52}NiP_2SSi$: C, 66.76; H, 7.47; N, 0.00. Found: C, 67.19; H, 7.48; N, 0.03.

3.4.2.2 Synthesis of [(SiP$_2$S)NiH]K (3.3-H)

A suspension of KC_8 (0.26 g, 1.9 mmol) in THF (3 mL) was added dropwise to a stirring solution of **3.2** (0.64 g, 0.9 mmol) in THF (3 mL) at 78 °C. The reaction mixture was stirred at −78 °C for 30 min and then stirred at 23 °C for 1 h. The dark yellow reaction was filtered through Celite, and the filtrate was concentrated to dryness. The resulting solids were washed with pentane (3 x 5 mL) to afford the title complex as a yellow solid. (0.58 g, 91%). Yellow crystals suitable for XRD were grown from slow concentration of an Et_2O solution at 23 °C. ^{1}H NMR (THF-d_8, 300 MHz, 298 K, δ): 8.18 (dd, J = 7.3, 1.3 Hz, 2H), 7.57 (dd, J = 5.3, 3.2 Hz, 1H), 7.55 – 7.49 (m, 2H), 7.44 (d, J = 7.4 Hz, 2H), 7.35 – 7.22 (m, 2H), 7.21 – 6.96 (m, 5H), 6.61 (d, J = 2.1 Hz, 1H), 6.59 (s, 1H), 2.33 – 2.07 (m, 4H), 1.05 (q, J = 7.0 Hz, 6H), 1.00 – 0.89 (m, 12H), 0.74 (q, J = 6.8 Hz, 6H), −7.83 (t, J = 44.3 Hz, 1H). ^{31}P NMR (THF-d_8, 121 MHz, 298 K, δ): 77.47. IR (solid, cm^{-1}): 1677 (Ni–H). Anal. Calcd. For $C_{36}H_{45}KNiP_2SSi$: C, 61.98; H, 6.50; N, 0.00. Found: C, 61.73; H, 6.73; N, 0.03.

3.4.2.3 Synthesis of [(SiP$_2$S)Ni]$_2$(N$_2$) (3.4')

A solution of $[H(OEt_2)_2][BAr^F{}_4]$ (0.73 g, 0.72 mmol) in Et_2O (3 mL) was added dropwise to a stirring solution of **3.3-H** (0.50 g, 0.72 mmol) in Et_2O (3 mL) at –78 °C. The stirring reaction mixture was slowly warmed from –78 °C to 23 °C overnight, and the resulting dark red solution was concentrated to dryness. The crude material was extracted with 2:1 C_6H_6/pentane (10 mL) and filtered through Celite. The volatiles were removed *in vacuo*, and the resulting solid was recrystallized from slow evaporation of an Et_2O solution at 23 °C to yield the title complex as a red solid (0.24 g, 50%). Red crystals suitable for XRD were grown from slow concentration of an Et_2O solution at 23 °C. Anal. Calcd. For $C_{72}H_{88}N_2Ni_2P_4S_2Si_2$: C, 64.39; H, 6.60; N, 2.09. Found: C, 63.83; H, 6.61; N, 1.84. In

solution under an N_2 atmosphere, **3.4'** is in equilibrium with the monomeric form $(SiP_2S)NiN_2$ (**3.4**) and has the following spectroscopic parameters: ^{1}H NMR (THF-d_8, 400 MHz, 298 K, δ): 7.75 – 7.66 (m, 8H), 7.64-7.60 (m, 16H), 7.33 – 7.27 (m, 16H), 7.22 (t, J = 7.6 Hz, 8H), 7.17 – 7.08 (m, 4H), 6.90 (ddd, J = 19.3, 7.2, 1.4 Hz, 8H), 6.73 (t, J = 7.2 Hz, 4H), 2.60 (m, 4H), 2.38 (m, 4H), 1.22 (q, J = 7.1 Hz, 12H), 1.16 (q, J = 7.0 Hz, 12H), 1.07 (q, J = 7.4 Hz, H), 0.99 (q, J = 6.9 Hz, 6H). ^{31}P NMR (THF-d_8, 162 MHz, 298 K, δ): 45.50. IR (C_6H_6 solution): 2200 (N_2). UV-Visible (THF, 298 K, nm {$M^{-1}mm^{-1}$}): 354 {1400}, 446 {560}, 531 {320}.

3.4.2.4 Synthesis of [(SiP$_2$S)NiD]Li (3.3-D)

A solution of $LiBEt_3D$ (66 µL, 1.0 M in THF) was added in one portion to a stirring THF solution of **3.4** (0.040 g, 0.040 mmol) at –78 °C. The reaction mixture was stirred at 23 °C for 30 min, and the resulting yellow solution was concentrated to dryness. The resulting yellow solids were washed with 3:1 pentane/Et_2O (5 mL) and extracted with THF (5 mL). The filtrate was filtered through Celite and concentrated to afford the title complex as a yellow solid (0.036 g, 90%). ^{1}H NMR (C_6D_6, 400 MHz, 298 K, δ): 8.16 (d, J = 7.2 Hz, 2H), 7.73 (dd, J = 6.9, 1.6 Hz, 1H), 7.67 – 7.60 (m, 2H), 7.44 (d, J = 7.6 Hz, 3H), 7.27 (t, J = 7.3 Hz, 2H), 7.19 (s, 1H), 7.08 (td, J = 7.3, 4.3 Hz, 3H), 7.00 (dd, J = 8.3, 6.5 Hz, 1H), 6.90 (d, J = 7.6 Hz, 1H), 2.30 – 2.07 (m, 2H), 1.15 (t, J = 7.1 Hz, H), 1.14 (q, J = 7.1 Hz, 4H), 0.94 (q, J = 6.6 Hz, 3H), 0.79 (q, J = 7.1 Hz, 3H). ^{31}P NMR (C_6D_6, 162 MHz, 298 K, δ): 69.68. ^{2}H NMR (C_6H_6, 61 MHz, 298 K, δ): −8.38.

3.4.2.5 Generation of (SiP$_2$S)NiH (3.5-H) *in situ*

A representative sample preparation: Solid [Cp*$_2$Fe][PF_6] (7 mg, 16 µmol) was added in one portion to a THF solution of **3.3-H** (10 mg, 14 µmol, 1 mL) at –78 °C. The resulting dark blue-green solution was stirred at –78 °C and then filtered through a pre-chilled glass fiber pipette filter. The dark blue-green filtrate was analyzed directly. ^{1}H NMR (THF-d_8, 500 MHz, −40 °C, δ) δ 16.0, 13.7, 10.7, 6.3, 4.5, −1.2. IR (THF solution, −78 °C): 1728 (Ni–H). UV-Visible (THF, 298 K, nm {$M^{-1}cm^{-1}$}): 395 {3900}, 632 {1400}.

3.4.2.6 Generation of (SiP_2S)NiD (3.5-D) *in situ*

The title compound was generated *in situ* in an analogous manner as **3.5-H** employing **3.3-D**. ^{1}H NMR (THF-d_8, 500 MHz, −40 °C, δ) 16.3, 13.8, 10.8, 6.2, 4.4, −1.3. *Note: Based on the simple harmonic oscillator model, the estimated Ni–D stretch for **3.5-D** is 1232 cm^{-1}, given that **3.5-H** exhibits a Ni–H stretch at 1728 cm^{-1}. However, this falls in a region that is dominated by intense IR stretches from THF, so the Ni–D stretch could not be resolved in the solution IR spectrum collected in THF at −78 °C. Nonetheless, the broad, intense stretch at 1728 cm^{-1} observed in **3.5-H** was not observed in the IR spectrum of **3.5-D**, which supports the assignment as a Ni–H stretch (See Figs. B.2.8, B.2.9)

3.4.2.7 Generation of (SiP_2S)Ni (3.6) *in situ*

A solution of **3.4** in THF was degassed via freeze-pump-thaw cycles (x 3) to generate a red solution of the title complex, which is quantitative by NMR spectroscopy. ^{1}H NMR (THF-d_8, 400 MHz, 298 K, δ): 7.72 – 7.63 (m, 4H), 7.61 (dt, J = 6.0, 2.1 Hz, 2H), 7.30 – 7.24 (m, 4H), 7.22 (t, J = 7.7 Hz, 2H), 7.14 – 7.04 (m, 1H), 6.93 – 6.85 (m, 2H), 6.72 (t, J = 7.2 Hz, 1H), 2.62 (m, 1H), 2.35 (m, 1H), 1.24 (q, J = 7.2 Hz, 3H), 1.22 (q, J = 7.2 Hz, 3H), 1.10 (q, J = 7.1 Hz, 3H), 0.98 (q, J = 6.8 Hz, 3H). ^{31}P NMR (THF-d_8, 162 MHz, 298 K, δ): 41.27. UV-Visible (THF, 298 K, nm {M^{-1}mm^{-1}}): 340 {700}, 535 {130}. Combustion analysis was not obtained on compound **3.6** due to conversion to **3.4** in the presence of N_2.

3.4.2.8 Generation of (SiP_2S)Ni(H_2) (3.7) *in situ*

A solution of **3.4** in THF-d_8 was degassed via freeze-pump-thaw cycles (x 3), and the solution was exposed to 1 atm of H_2 at 23 °C, which immediately yielded an orange solution of the title complex and was quantitative by NMR spectroscopy. Orange crystals were grown from a concentrated Et_2O solution of **3.7** at −35 °C under an atmosphere of H_2. ^{1}H NMR (THF-d_8, 400 MHz, 298 K, δ): 7.88 – 7.71 (m, 2H), 7.74 – 7.50 (m, 4H), 7.31 (dd, J = 6.8, 3.3 Hz, 4H), 7.20 (t, J = 7.5 Hz, 2H), 7.09 (t, J = 7.4 Hz, 1H), 6.99 (d, J = 7.1 Hz, 1H), 6.86 (d, J = 7.3 Hz, 1H), 6.73 (t, J = 7.2 Hz, 1H), 2.61 – 2.42 (m, 1H), 2.50 (m, 1H), 2.34 (m, 1H), 1.18 (dq, J = 18.1, 7.2 Hz, 6H), 0.95 (dq, J = 14.7, 6.8 Hz, 6H), −1.68 (s, 2H). (Note: At 23 °C,

bound H_2 and free H_2 are in exchange, so the peak at −1.68 ppm may shift depending on sample conditions. At −80 °C in toluene-d_8, a distinct peak for free H_2 is observed, and the ^{1}H NMR shift corresponding to bound H_2 is observed at −2.89 ppm). ^{31}P NMR (THF-d_8, 162 MHz, 298 K, δ): 50.93. UV-Visible (THF, 298 K, nm {$M^{-1}mm^{-1}$}): 360 {600}, 535 {200}. Combustion analysis was not obtained on compound **3.7** due to conversion to **3.4** in the presence of N_2.

3.4.2.9 Synthesis of [(SiP$_2$S)Ni(CH$_3$)]Li(solv)$_x$ (3.8)

A solution of methyl lithium (3.6 mg, 0.16 mmol) in Et_2O (3 mL) was added to a stirring solution of **3.4** (0.100 g, 0.075 mmol) in Et_2O (3 mL) at −78 °C. The stirring reaction mixture was stirred at −78 °C for 1 h and then stirred at 23 °C for 30 min, resulting in a yellow-orange solution. The reaction mixture was concentrated to dryness, and the resulting solid was washed with pentane (5 mL, −78 °C) to afford the title compound as a yellow-orange solid (0.073 g, 72%). Yellow-orange crystals suitable for XRD were grown from slow concentration of a pentane solution at −35 °C. ^{1}H NMR (C_6D_6, 300 MHz, 298 K, δ): 8.08 (dd, J = 7.1, 1.4 Hz, 2H), 7.72 (d, J = 7.5 Hz, 2H), 7.63 (dd, J = 6.9, 1.5 Hz, 1H), 7.41 (d, J = 7.6 Hz, 2H), 7.30 – 7.17 (m, 5H), 7.08 (t, J = 7.2 Hz, 3H), 7.03 – 6.90 (m, 1H), 2.61 – 2.25 (m, 4H), 1.19 (q, J = 6.9, 6.6 Hz, 6H), 1.13 (q, J = 7.0 Hz, 6H), 1.00 (q, J = 6.7, 6.2 Hz, 6H), 0.89 (q, J = 6.9 Hz, 6H), −0.57 (t, J = 7.1 Hz, 3H). ^{31}P NMR (C_6D_6, 121 MHz, 298 K, δ): 47.22. UV-Visible (C_6H_6, 298 K, nm {$M^{-1}cm^{-1}$}): 360 {4100}, 432 {2600}. Anal. Calcd. For $C_{37}H_{47}LiNiP_2SSi$: C, 65.40; H, 6.97; N, 0.00. Found: C, 64.25 ; H, 6.87 ; N, 0.05.

3.4.2.10 Synthesis of (SiP$_2$S)Ni(CH$_3$) (3.9)

Solid [Cp*$_2$Fe][PF_6] (0.035 g, 0.074 mmol) was added in one portion to a stirring Et_2O solution of **3.8** (0.046 g, 0.068 mmol, 1 mL) at −78 °C. The resulting dark green solution was stirred at −78 °C for 30 min then concentrated to dryness at 25 °C. The resulting solid was washed with chilled pentane (5 mL, −78 °C) and Et_2O (1 mL, −78 °C), then extracted with THF (0.5 mL, −78 °C) and filtered. The dark blue-green filtrate was layered with chilled pentane (3 mL, −78 °C) and stored at −78 °C, which yielded a dark blue-green precipitate.

The solids were isolated by vacuum filtration, then washed with pentane (3 mL, −78 °C) and dried under vacuum to yield the title complex as a dark blue-green solid (0.014 g, 31%). ^{1}H NMR (400 MHz, THF-d_8) δ 73.4, 59.3, 25.2, 22.2, 13.9, 10.7, 9.2, 8.0, 7.3, 5.8, 5.4, −0.1, −0.8, −50.7. μ_{eff} (C_6D_6, Evans method, 298 K): 1.70μ_B. UV-Visible (THF, 298 K, nm {$M^{-1}cm^{-1}$}): 641 {2300}, 937 {620}. Satisfactory combustion analysis was not obtained on compound **3.9**, likely due to relatively facile Ni–CH_3 bond homolysis.

3.4.3. H_2 Quantification from the Decay of 3.5-H to 3.4

A solution of **3.3-H** (0.030 g, 0.045 mmol) in THF (1 mL) was added to a Schlenk tube and frozen. Subsequently, a thawing solution of [Cp^*_2Fe][PF_6] (0.022 g, 0.047 mmol) in THF (1 mL) was added to the tube and frozen. The tube was stirred at −78 °C for 30 min to generate **3.5-H** as a dark blue-green solution, then warmed to 23 °C and stirred for 1 h. During this period, the solution changed from blue-green to red. An aliquot of the headspace was sampled and analyzed for H_2 by GC. Yield of H_2: 98%

3.4.4. H_2 quantification from the protonation of 3.3-H with [$H(OEt_2)_2$][BAr^F_4]

Solid **3.3-H** (0.020 g, 0.029 mmol) and [$H(OEt_2)_2$][BAr^F_4] (0.029 g, 0.029) were added to a round bottom, and the flask was sealed with a septum. Chilled Et_2O (1 mL, −78 °C) was added to the round bottom via syringe, and the flask was stirred at 23 °C for 10 min. An aliquot of the headspace was sampled and analyzed for H_2 by GC. Yield of H_2: 99%

3.4.5. H_2 Quantification from the Protonation of 3.3-H with PhOH

A THF solution of **3.3-H** (0.030 g, 0.045 mmol, 1 mL) was added to a round bottom and frozen. To the chilled round bottom, a THF solution of PhOH (4.2 mg, 0.045 mmol, 1 mL) was added and frozen. The flask was sealed, and the sample was warmed to 23 °C and stirred at 23 °C for 30 min. During this period, the solution changed color from yellow-orange to dark red. An aliquot of the headspace was sampled and analyzed for H_2 by GC. Yield of H_2: 97%.

NMR analysis of the protonation reaction of **3.3-H** with PhOH in THF-d_8 reveals quantitative conversion to [(SiP$_2$S)NiOPh]K (See Figs. B.1.30, B.1.31) : ^{1}H NMR (THF-d_8, 400 MHz, 298 K, δ): 7.76 (d, J = 7.0 Hz, 2H), 7.60 (d, J = 7.6 Hz, 2H), 7.47 (d, J = 7.3 Hz, 2H), 7.21 – 7.01 (m, 8H), 6.75 (t, J = 7.6 Hz, 2H), 6.69 (d, J = 7.3 Hz, 1H), 6.60 (d, J = 7.5 Hz, 3H), 5.99 (t, J = 7.0 Hz, 1H), 2.55 (bs, 4H), 1.12 (dd, J = 15.6, 8.4 Hz, 6H), 1.06 (q, J = 6.5 Hz, 12H), 0.74 (q, J = 7.1 Hz, 6H). ^{31}P NMR (THF-d_8, 162 MHz, 298 K, δ): 36.74

3.4.6. Bulk Electrolysis Experiments for Proton Reduction Catalyzed by 3.4

Controlled-potential electrolysis experiments were conducted in a sealed two-chambered H cell equipped with a glassy carbon plate working electrode (5.5 cm × 1 cm × 2 mm) and a Ag/AgOTf reference electrode in the working chamber and a glassy carbon plate counter electrode in the auxiliary chamber. The two chambers were separated by a fine-porosity glass frit, and the cell was sealed under a N_2 atmosphere. Bulk electrolysis runs were performed at 23 °C in THF containing 0.4 M [NBu$_4$][PF$_6$] as the electrolyte, with a controlled potential at −2.7 V vs. Cp_2Fe/Cp_2Fe^+. In a standard run, the working chamber contained 0.5 mM complex **3.4** and 50 mM PhOH. Following the electrolysis period of 4 h, H_2 was quantified by sampling the headspace volume and analyzing by gas chromatography.

3.5 References

(1) (a) McKone, J. R.; Marinescu, S. C.; Brunschwig, B. S.; Winkler, J. R.; Gray, H. B. *Chem. Sci.* **2014**, *5*, 865-878. (b) Bullock, R. M.; Appel, A. M.; Helm, M. L. *Chem. Commun.* **2014**, *50*, 3125-3143. (c) Tong, L.; Duan, L.; Zhou, A.; Thummel, R. P. *Coord. Chem. Rev.* **2020**, *402*, 213097. (d) Artero, V.; Chavarot-Kerlidou, M.; Fontecave, M. *Angew. Chem. Int. Ed.* **2011**, *50*, 7238-7266.

(2) (a) Haddad, A. Z.; Garabato, B. D.; Kozlowski, P. M.; Buchanan, R. M.; Grapperhaus, C. A. *J. Am. Chem. Soc.* **2016**, *138*, 7844-7847. (b) Thompson, E. J.; Berben, L. A. *Angew. Chemie. Int. Ed.* **2015**, *54*, 11642-11646.

(3) (a) James, T. L.; Cai, L.; Muetterties, M. C.; Holm, R. C. *Inorg. Chem.* **1996**, *35*, 4148-4161. (b) Lahiri, G. K.; Schussel, L. J.; Stolzenberg, A. M. *Inorg. Chem.* **1992**, *31*, 4991-5000.

(4) (a) Efros, L. L.; Thorp, H. H.; Brudvig, G. W.; Crabtree, R. H. *Inorg. Chem.* **1992**, *31*, 1722-1724. (b) Beley, M.; Collin, J.-P.; Ruppert, R.; Sauvage, J.-P. *J. Am. Chem. Soc.* **1986**, *108*, 7461-7467. (c) Collin, J.-P.; Jouaiti, A.; Sauvage, J.-P. *Inorg. Chem.* **1988**, *27*, 1986-1990. (d) Kaur-Ghumaan, S.; Hasche, P.; Spannenberg, A.; Beweries, T. *Dalton Trans.* **2019**, *48*, 16322-16329. (e) Luca, O. R.; Blakemore, J. D.; Konezny, S. J.; Praetorius, J. M.; Schmeier, T. J.; Hunsinger, G. B.; Batista, V. S.; Brudvig, G. W.; Hazari, N.; Crabtree, R. H. *Inorg. Chem.* **2012**, *51*, 8704-8709. (f) Han, Y.; Fang, H.; Jing, H.; Sun, H.; Lei, H.; Lai, W.; Cao, R. *Angew. Chem. Int. Ed.* **2016**, *55*, 5457-5462.

(5) Additionally, paramagnetic $Ni^{I/III}$ hydrides have been proposed as intermediates in catalytic organometallic transformations, see: (a) Kuang, Y.; Anthony, D.; Katigbak, J.; Marrucci, F.; Humagain, S.; Diao, T. *Chem* **2017**, *3*, 268-280. (b) Zarate, C.; Yang, H.; Bezdek, M. J.; Hesk, D.; Chirik, P. J. *J. Am. Chem. Soc.* **2019**, *141*, 5034-5044.

(6) (a) Brecht, M.; van Gastel, M.; Buhrke, T.; Friedrich, B.; Lubitz, W. *J. Am. Chem. Soc.* **2003**, *125*, 13075-13083. (b) Whitehead, J. P.; Gurbiel, R. J.; Bagyinka, C.; Hoffman, B. M.; Maroney, M. J. *J. Am. Chem. Soc.* **1993**, *115*, 5629-5635. (c) Fan, C.; Teixeira, M.; Moura, J.; Moura, I.; Hanh, H. B.; Le Gall, J.; Peck, H. D.; Hoffman, B. M. *J. Am. Chem. Soc.* **1991**, *113*, 20-24. (d) Foerster, S; van Gastel, M.; Brecht, M.; Lubtiz, W. *J. Biol. Inorg. Chem.* **2005**, *10*, 51-62. (e) Lubitz, W.; Ogata, H.; Rüdiger, O.; Reijerse, E. *Chem. Rev.* **2014**, *114*, 4081-4148. (f) Foerster, S.; Stein, M.; Brecht, M.; Ogata, H.; Higuchi, Y.; Lubitz, W. *J. Am. Chem. Soc.* **2003**, *125*, 83-93. (g) Stein, M.; van Lenthe, E.; Jan Baerends, E.; Lubitz, W. *J. Am. Chem. Soc.* **2001**, *123*, 5839-5840.

(7) Stein, M.; Lubitz, W. *Phys. Chem. Chem. Phys.* **2001**, *3*, 5115-5120.

(8) In the EPR-silent Ni-R state (Ni^{II}–H–Fe^{II}), XRD and NRVS data suggest that the hydride is also bound more tightly to Ni than Fe. See: (a) Ogata, H.; Nishikawa, K.. Lubitz, W. *Nature* **2015**, *520*, 571-574. (b) Ogata, H.; Krämer, T.; Wang, H.; Schilter, D.; Pelmenschikov, V.;

van Gastel, M.; Neese, F.; Rauchfuss, T. B.; Gee, L. B.; Scott, A. D.; Yoda, Y.; Tanaka, Y.; Lubitz, W.; Cramer, S. P. *Nat. Commun.* **2015**, *6*, 7890.

(9) Nilsson Lill, S. O.; Siegbahn, P. E. M. *Biochemistry* **2009**, *48*, 1056-1066.

(10) (a) Slater, J. W.; Marguet, S. C.; Monaco, H. A.; Shafaat, H. S. *J. Am. Chem. Soc.* **2018**, *140*, 10250-10262. (b) Slater, J. W.; Marguet, S. C.; Cirino, S. L.; Maugeri, P. T.; Shafaat, H. S. *Inorg. Chem.* **2017**, *56*, 3926-3938.

(11) (a) Lee, C.-M.; Chen, C.-H.; Liao, F.-X.; Hu, C.-H.; Lee, G.-H. *J. Am. Chem. Soc.* **2010**, *132*, 9256-9258. (b) Zheng, B.; Tang, F.; Luo, J.; Schultz, J. W.; Rath, N. P.; Mirica, L. M. *J. Am. Chem. Soc.* **2014**, *136*, 6499-6504. (c) Lipschutz, M. I.; Yang, X.; Chatterjee, R.; Tilley, T. D. *J. Am. Chem. Soc.* **2013**, *135*, 15298-15301. (d) Schultz, J. W.; Fuchigami, K.; Zheng, B.; Rath, N. P.; Mirica, L. M. *J. Am. Chem. Soc.* **2016**, *138*, 12928-12934. (e) Diccianni, J. B.; Hu, C. T.; Diao, T. *Angew. Chem. Int. Ed.* **2019**, *58*, 13865-13868.

(12) (a) Dong, Q.; Zhao, Y.; Su, Y.; Su, J.-H.; Wu, B.; Yang, X.-J. *Inorg. Chem.* **2012**, *51*, 13162-13170. (b) Kriley, C. E.; Woolley, C. J.; Krepps, M. K.; Popa, E. M.; Fanwick, P. E.; Rothwell, I. P. *Inorg. Chim. Acta.* **2000**, *300-302*, 200-205. (c) Pfirrmann, S.; Limberg, C.; Herwig, C.; Knispel, C.; Braun, B.; Bill, E.; Stösser, R. *J. Am. Chem. Soc.* **2010**, *132*, 13684-13691. (d) Beck, R.; Shoshani, M.; Johnson, S. A. *Angew. Chemie. Int. Ed.* **2012**, *51*, 11753-11756. (e) Gehring, H.; Metzinger, R.; Herwig, C.; Intemann, J.; Harder, S.; Limberg, C. *Chem. Eur. J.* **2013**, *19*, 1629-1636. (f) Yao, S. A.; Corcos, A. R.; Infante, I.; Hillard, E. A.; Clérac, R.; Berry, J. F. *J. Am. Chem. Soc.* **2014**, *136*, 13538-13541. (g) Ogo, S.; Kabe, R.; Uehara, K.; Kure, B.; Nishimura, T.; Menon, S. C.; Harada, R.; Fukuzumi, S.; Higuchi, Y.; Ohhara, T.; Tamada, T.; Kuroki, R. *Science* **2007**, *316*, 585-587.

(13) (a) Müller, J.; Dorner, H.; Huttner, G.; Lorenz, H. *Angew. Chemie. Int. Ed.* **1973**, *12*, 1005-1006. (b) Smith, M. E.; Andersen, R. A. *Organometallics* **1996**, *15,* 2680-2682.

(14) (a) Kandiah, M.; McGrady, G. S.; Decken, A.; Sirsch, P. *Inorg. Chem.* **2005**, *44*, 8650-8652. (b) Journaux, Y.; Lozan, V.; Klingele, J.; Kersting, B. *Chem. Commun.* **2006**, 83-84. (c) MacMillan, S. N. Ph.D. Dissertation, Massachusetts Institute of Technology, Cambridge, MA, 2013.

(15) The authors favor the assignment as a trigonal pyramidal H–Ni(CO)$_3$ species, but also note that H–Ni(CO)$_x$ ($x \geq 2$) could not be experimentally ruled out as possible assignments, see: Morton, J. R.; Preston, K. F. *J. Chem. Phys.* **1984**, *81*, 5775-5778.

(16) Irradiation of Ni(CN)$_4^{2-}$ in the presence of water results in the generation of several EPR-active species. One of the species exhibits a large $|a_{iso}(^1H)|$ value of *ca*. 427 MHz and an axial g tensor (**g** = [2.00, 2.05, 2.05]), which was initially attributed to H–Ni^{III}(CN)$_4^{2-}$ (See: Symons, M. C. R.; Aly, M. M.; West, D. X. *J. Chem. Soc., Chem. Commun.* **1979**, 51-52). However, the subsequent study of H–Ni^{I}(CO)$_3$ revealed similar EPR parameters to that of the putative H–Ni^{III}(CN)$_4^{2-}$ complex, and the authors suggest that H–Ni^{I}(CN)$_3^{3-}$ is also a plausible assignment given the available data (See Ref. 15).

(17) Lai, K.-T.; Ho, W.-C.; Chiou, T.-W.; Liaw, W.-F. *Inorg. Chem.* **2013**, *52*, 4151-4153.

(18) In Ref. 17, it is noted that H_2 and [Ni$_2^{II}$(P(C$_6$H$_3$-3-SiMe$_3$-2-S)$_3$)$_2$]$^{2-}$ are detected upon warming a solution of [(PS$_3$)NiH][PPN]. However, because the yields of either product are not included, it is not clear whether H_2 loss is a major reaction pathway.

(19) Gu, N. X.; Oyala, P. H.; Peters, J. C. *J. Am. Chem. Soc.* **2018,** *140*, 6374-6382.

(20) Suess, D. L. M.; Tsay, C.; Peters, J. C. *J. Am. Chem. Soc.* **2012**, *134*, 14158-14164.

(21) Crabtree, R. H. *Chem. Rev.* **2016**, *116*, 8750-8769.

(22) (a) Tsay, C.; Peters, J. C. *Chem. Sci*. **2012**, *3*, 1313-1318. (b) Connelly, S. J.; Zimmerman, A. C.; Kaminsky, W.; Heinekey, D. M. *Chem. Eur. J.* **2012**, *18*, 15932-15934. (c) He, T.; Tsvetkov, N. P.; Andino, J. G.; Gao, X.; Fullmer, B. C.; Caulton, K. G. *J. Am. Chem. Soc.* **2010**, *132*, 910-911. (d) Sweany, R. L.; Polito, M. A.; Moroz, A. *Organometallics* **1989**, *8*, 2305-2308.

(23) For examples of d^{10} Ni(H_2) complexes supported by group 13 Z-type ligands, see: (a) Cammarota, R. C.; Lu, C. C. *J. Am. Chem. Soc.* **2015**, *137*, 12486-12489. (b) Harman, W. H.; Lin, T.-P.; Peters, J. C. *Angew. Chemie. Int. Ed.* **2014**, *53*, 1081-1086.

(24) (a) Olechnowicz, F.; Hillhouse, G. L.; Cundari, T. R.; Jordan, R. F. *Inorg. Chem*. **2017**, *56*, 9922-9930. (b) Sellmann, D.; Geipel, F.; Moll, M. *Angew. Chem. Int. Ed.* **2000**, *39*, 561-563.

(25) Bulk electrolysis experiments confirmed the generation of 5.8 ± 0.6 equivalents of H_2 per Ni center (106 ± 5% FE) over 4 hours in THF at a controlled potential of −2.7 V vs. Cp_2Fe/Cp_2Fe^+. The yield of H_2 is the average of two independent runs. Only trace H_2 is detected in the absence of PhOH. In the absence of **3.4**, there is a small but measurable background HER process accounting for 0.6 equiv H_2, corrected for in the yield of the Ni-catalyzed process. Rinse test experiments were consistent with a molecular catalyst but do not reliably rule out a heterogeneous component.

(26) Besora, M.; Lledos, A.; Maseras, F. *Chem. Soc. Rev.* **2009**, *38*, 957−966.

(27) For examples of bimolecular HER from first-row transition metal hydrides, see: (a) Halpern, J.; Pribanić *Inorg. Chem*. **1970**, *9*, 2616-2618. (b) Ungváry, F.; Markó, L. *J. Organomet. Chem.* **1969**, *20*, 205-209. (c) Prokopchuk, D. E.; Chambers, G. M.; Walter, E. D.; Mock, M. T.; Bullock, R. M. *J. Am. Chem. Soc.* **2019**, *141*, 1871-1876. (d) Rettenmeier, C.; Wadepohl, H.; Gade, L. H. *Chem. Eur. J.* **2014**, *20*, 9657-9665. (e) Marinescu, S. C.; Winkler, J. R.; Gray, H. B. *Proc. Natl. Acad. Sci.* **2012**, *109*, 15127-15131.

(28) For examples of bimolecular HER from 2nd and 3rd row transition metal hydrides, see: (a) Collman, J. P.; Wagenknecht, P. S.; Lewis, N. S. *J. Am. Chem. Soc.* **1992**, *114*, 5665−5673. (b) Collman, J. P.; Hutchison, J. E.; Wagenknecht, P. S.; Lewis, N. S.; Lopez, M. A.; Guilard, R. *J. Am. Chem. Soc.* **1990**, *112*, 8206−8208. (c) Norton, J. R. *Acc. Chem. Res.* **1979**, *12*, 139−145. (d) Evans, J.; Norton, J. R. *J. Am. Chem. Soc.* **1974**, *96*, 7577−7578. (e) Inoki, D.; Matsumoto, T.; Nakai, H.; Ogo, S. *Organometallics* **2012**, *31*, 2996−3001.

(29) For an example of unimolecular H_2 evolution from a dinickel(II) dihydride species, see: Manz, D.-H.; Duan, P.-C.; Dechert, S.; Demeshko, S.; Oswald, R.; John, M.; Mata, R. A.; Meyer, F. *J. Am. Chem. Soc.* **2017**, *139*, 16720-16731.

(30) (a) Hu, X.; Brunschwig, B. S.; Peters, J. C. *J. Am. Chem. Soc.* **2007**, *129*, 8988-8998. (b) Rose, M. J.; Gray, H. B.; Winkler, J. R. *J. Am. Chem. Soc.* **2012**, *134*, 8310-8313.

(31) Based on the harmonic oscillator model, the Ni–D stretch of **3.5-D** is estimated to be 1232 cm^{-1}. This falls in a region that is dominated by intense IR stretches from THF, and the Ni–D stretch could not be resolved in the solution IR spectrum collected in THF at −78 °C. (See Figs. B.2.8, B.2.9).

(32) The gas-phase DFT calculated Ni–H stretches for **3.2** (calc: 1742 cm^{-1}, expt: 1737 cm^{-1}) and **3.3** (calc: 1689 cm^{-1}, expt: 1677 cm^{-1}) are also in good agreement with the experimental solid-state IR stretches. (M06-L functional: def2tzvp [Ni], def2svp [all other atoms])

(33) (a) Kinney, R. A.; Saouma, C. T.; Peters, J. C.; Hoffman, B. M. *J. Am. Chem. Soc.* **2012**, 134, 12637-12647. (b) Hoeke, V.; Tociu, L.; Case, D. A.; Seefeldt, L. C.; Raugei, S.; Hoffman, B. M. *J. Am. Chem. Soc.* **2019**, *141*, 11984-11996.

(34) Wittke, J. P.; Dicke, R. H. *Phys. Rev.* **1956**, *103*, 620-631.

(35) The apical ligand of compound **3.9** is modeled with 87% occupancy as Ni–CH_3 and 13% occupancy as Ni–N_2. The presence of the disordered component results from the slow decomposition of **3.9** in solution at −35 °C.

(36) Kampa, M.; Lubitz, W.; van Gastel, M.; Neese, F. *J. Biol. Inorg. Chem.* **2012**, *17*, 1269-1281.

(37) Stein, M.; van Lenthe, E.; Baerends, E. J.; Lubitz, W. *J. Phys. Chem. A.* **2001**, *105*, 416-425.

(38) Huyett, J. E.; Carepo, M.; Pamplona, A.; Franco, R.; Moura, I.; Moura, J. J. G.; Hoffman, B. M. *J. Am. Chem. Soc.* **1997**, *119*, 9291-9292.

(39) Another proposed cause for the small ^{1}H hyperfine coupling of the Ni-C state is that the hydride resides close to the equatorial plane (near the nodal surface) of the singly-populated Ni(d_z^2) orbital of a distorted square pyramidal Ni center, where three cysteines and the hydride lie approximately along the xy-plane (See Refs. 6a,d,e and 37). For comparison, the DFT-optimized structure of **3.5-H** is best described as a distorted trigonal bipyramid. Nonetheless, a $S = ½$, d^7 configuration for a trigonal bipyramidal complex would place the unpaired electron largely in xy-plane (defining the z-axis along the C_3-axis). The combination of significant spin delocalization onto the thiolate and limited spatial overlap with the singly-occupied Ni *d* orbital in the xy-plane likely both contribute to the small $a_{iso}(^1H)$ value for **3.5-H**. These are analogous factors to what is hypothesized for the Ni-C hydrogenase state, which is measured to have a hydride $|a_{iso}(^1H)|$ value of comparable magnitude as **3.5-H**.

(40) Related H• transfer from a Ni(II)–H species has been previously demonstrated, see: (a) Ref. 27d (b) Yao, C.; Wang, S.; Norton, J. R.; Hammond, M. DOI: 10.1021/jacs.9b13757

(41) Warren, J. J.; Tronic, T. A.; Mayer, J. M. *Chem. Rev.* **2010**, *110*, 6961-7001.

(42) Hess, C. R.; Weyhermüller, T.; Bill, E.; Wieghardt, K. *Inorg. Chem.* **2010**, *49*, 5686-5700.

(43) Weitz, I. S.; Rabinovitz, M. *J. Chem. Soc. Perkin Trans.* **1993**, *1*, 117-120.

(44) Brookhart, M.; Grant, B.; Volpe, A. F. *Organometallics* **1992**, *11*, 3920-3922.

(45) Vedejs, E.; Meier, G. P.; Snoble, K. A. J. *J. Am. Chem. Soc.* **1981**, *103*, 2823-2831.

(46) Bhattacharyya, K. X.; Dreyfuss, S.; Saffon-Merceron, N.; Mézailles, N. *Chem. Commun.* **2016**, *52*, 5179-5182.

(47) Chiou, T.-W.; Liaw, W.-F. *Inorg. Chem.* **2008**, *47*, 7908-7913.

(48) Smith, S. M.; Takacs, J. M. *Org. Lett.* **2010**, *12*, 4612-4615.

(49) Gaussian 09, Revision B.01, M.J. Frisch, G. W. Trucks, H. B. Schlegel, G. E. Scuseria, M. A. Robb, J. R. Cheeseman, G. Scalmani, V. Barone, B. Mennucci, G. A. Petersson, H. Nakatsuji, M. Caricato, X. Li, H. P. Hratchian, A. F. Izmaylov, J. Bloino, G. Zheng, J. L. Sonnenberg, M. Hada, M. Ehara, K. Toyota, R. Fukuda, J. Hasegawa, M. Ishida, T. Nakajima, Y. Honda, O. Kitao, H. Nakai, T. Vreven, J. A. Montgomery Jr., J. E. Peralta, F. Ogliaro, M. Bearpark, J. J. Heyd, E. Brothers, K. N. Kudin, V. N. Staroverov, R. Kobayashi, J. Normand, K. Raghavachari, A. Rendell, J. C. Burant, S. S. Iyengar, J. Tomasi, M. Cossi, N. Rega, J. M. Millam, M. Klene, J. E. Knox, J. B. Cross, V. Bakken, C. Adamo, J. Jaramillo, R. Gomperts, R. E. Stratmann, O. Yazyev, A. J. Austin, R. Cammi, C. Pomelli, J. W. Ochterski, R. L. Martin, K. Morokuma, V. G. Zakrzewski, G. A. Voth, P. Salvador, J. J. Dannenberg, S. Dapprich, A. D. Daniels, Ö. Farkas, J. B. Foresman, J. V. Ortiz, J. Cioslowski, D. J. Fox, Gaussian, Inc., Wallingford CT, 2009.

(50) Zhao, Y.; Truhlar, D. G. *J. Chem, Phys.* **2006**, *125*, 194101: 1-18.

(51) Weigend, F.; Ahlrichs, R. *Phys. Chem. Chem. Phys.* **2005**, *7*, 3297–3305.

(52) Warren, J. J.; Tronic, T. A.; Mayer, J. M. *Chem. Rev.* **2010**, *110*, 6961-7001.

(53) Stoll, S.; Schweiger, A. *J. Magn. Reson*. **2006**, *178*, 42-55.

Chapter 4

$H_2N–NH_2$ BOND FORMATION FROM A NI–NH_2 COMPLEX: MECHANISTIC INSIGHTS INTO NI-MEDIATED AMMONIA OXIDATION TO DINITROGEN

4.1 Introduction

Intermediates featuring metal-ligand multiple bonding are often implicated in the mechanism of water oxidation to O_2, as well as in the related oxidation of ammonia to N_2. For water oxidation catalysts, O–O bond formation is generally proposed to occur either via bimolecular oxo coupling or nucleophilic attack of a metal oxo intermediate by water (Fig. 4.1),[1] and the ability to stabilize oxo ligands has been suggested to be a design requirement for water oxidation catalysts.[1a] The related $6e^-/6H^+$ process of ammonia oxidation to N_2 has been studied stoichiometrically on Mo,[2] Mn,[3] Os,[4] and Ru[5,6] complexes, and molecular Ru[7] and Fe[8] species have been recently demonstrated to mediate the transformation catalytically. In analogy to the mechanisms of water oxidation catalysts, several systems have invoked the role of metal nitride and imido intermediates in N–N bond formation.[2,3abd,4,5ab,7ac] Furthermore, bimolecular nitride[3ab,4b,9] or imide[10] coupling and the nucleophilic attack of amines on M=NR[4d,11] species has been implicated in N–N bond forming reactions.

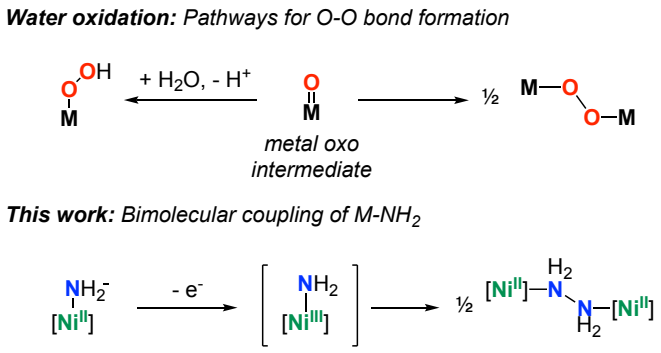

Figure 4.1 General mechanisms for O−O coupling proposed for water oxidation catalysts, and the N−N coupling mechanism described in this work

In contrast, although N–N bond formation from a M–NH_2 intermediate has been hypothesized as the N–N coupling step in the catalytic ammonia oxidation mediated by ferrocene[8b] and (tetramesitylporphyrin) $Ru(NH_3)_2$,[7d] stoichiometric examples of such reactivity from a M–NH_2 complex are rare.[12] Collman and coworkers reported that treatment of a cofacial diporphyrin $Ru_2(NH_3)_2$ complex with either *t*BuOOH or a combination of oxidant and base yields a mixture of $Ru_2(N_2H_4)$, $Ru_2(N_2H_2)$, and $Ru_2(N_2)$ species, and it has been hypothesized that the hydrazine formation occurs through the coupling of two Ru–NH_2 fragments.[5c,d] Relatedly, Sellmann and coworkers detected trace amounts of $CpMn(CO)_2N_2H_4$ in electrochemical bulk oxidation experiments of $CpMn(CO)_2NH_3$.[3c] Generation of N–N coupled product was hypothesized to proceed through a similar pathway as the Ru diporphyrin system.[5d] Stoichiometric examples of H_2N–NH_2 reductive elimination are limited likely due to the relatively weak bond that is generated. The N–N bond dissociation enthalpy of free hydrazine is 66 kcal/mol,[13] although the coordination of hydrazine to a metal center influences the N–N bond strength. In this work, we demonstrate the stepwise oxidation of NH_3 facilitated by a Ni complex, the first example of ammonia oxidation mediated by a molecular late transition metal system. We propose that the key N–N bond formation step occurs via the bimolecular H_2N–NH_2 reductive elimination from a transient Ni^{III}–NH_2 species.

4.2 Results and Discussion

Our group has previously reported the synthesis of the tetradentate ligand framework $HSiP_2S$[14] and metalation procedures to yield $[(SiP_2S)Ni]_2(N_2)$ (**4.1**).[15,16] Treatment of **4.1** with a THF solution of ammonia yields $(SiP_2S)Ni^{II}(NH_3)$ (**4.2**), and deprotonation of the coordinated NH_3 with *n*BuLi gives quantitative conversion to $[(SiP_2S)Ni^{II}(NH_2)]Li$ (**4.3**), which can also be prepared by treatment of **4.1** with $LiNH_2$ in THF (Scheme 4.1A, Fig. 4.2A). ^1H NMR data of **4.3** in C_6D_6 support the coordination of three THF molecules to the lithium cation,[17] and recrystallization in benzene allows structural characterization of the solvent-free dimer, $[(SiP_2S)Ni^{II}NH_2]_2Li_2$ (Scheme 4.1A, Fig. 4.2B). The cyclic voltammogram of **4.3** in 0.4 M $[NBu_4][PF_6]$ in THF reveals an oxidation event at −0.72 V

vs. Cp_2Fe/Cp_2Fe^+, corresponding to the formal Ni^{II}/Ni^{III} couple. Our group has previously demonstrated that oxidation of a related $Fe^{II}–NH_2$ complex leads to the generation of the $Fe^{II}–NH_3$ species, likely due to hydrogen atom abstraction from solvent by the transient $Fe^{III}–NH_2$ species.[18] In contrast, the chemical oxidation reaction of **4.3** with one equivalent of $[Cp_2Fe][BAr^F{}_4]$ ($BAr^F{}_4$ = B(3,5-$(CF_3)_2C_6H_3)_4$) at −78 ºC in 1,2-dimethoxyethane (DME) generates both **4.2** (60(4)%) and the N–N coupled product, $[(SiP_2S)Ni^{II}]_2(N_2H_4)$ (**4.4**) (41(3)%). Complex **4.4** can be independently generated via treatment of **4.1** with half an equivalent of hydrazine. XRD data of compound **4.4** reveal an N–N bond length of 1.488(4) Å, which is slightly elongated compared to free hydrazine (1.449 Å, Scheme 4.1A, Fig. 4.2C).[19]

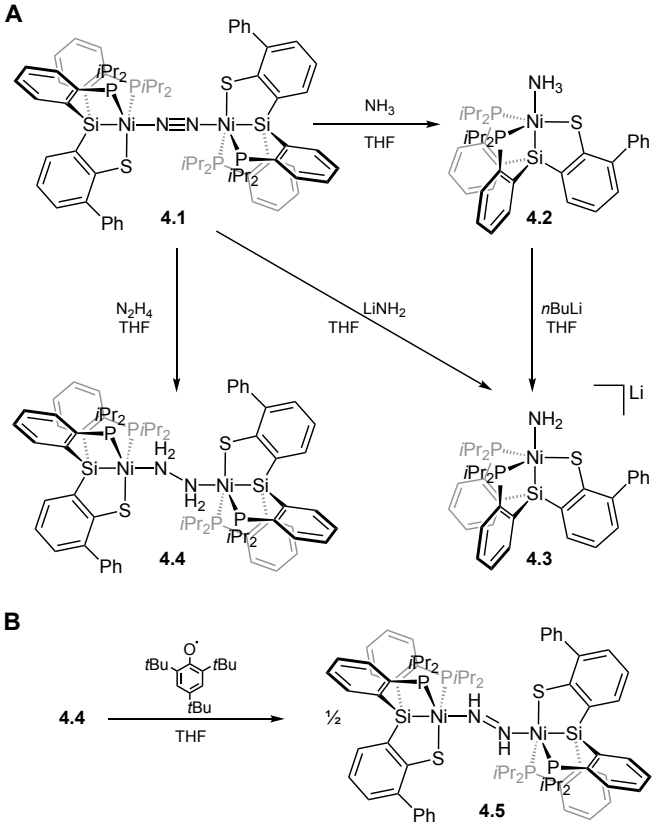

Scheme 4.1 (A) Synthesis of compounds **4.2**, **4.3**, and **4.4**. (B) Hydrogen atom abstraction from **4.4** to generate **4.5**

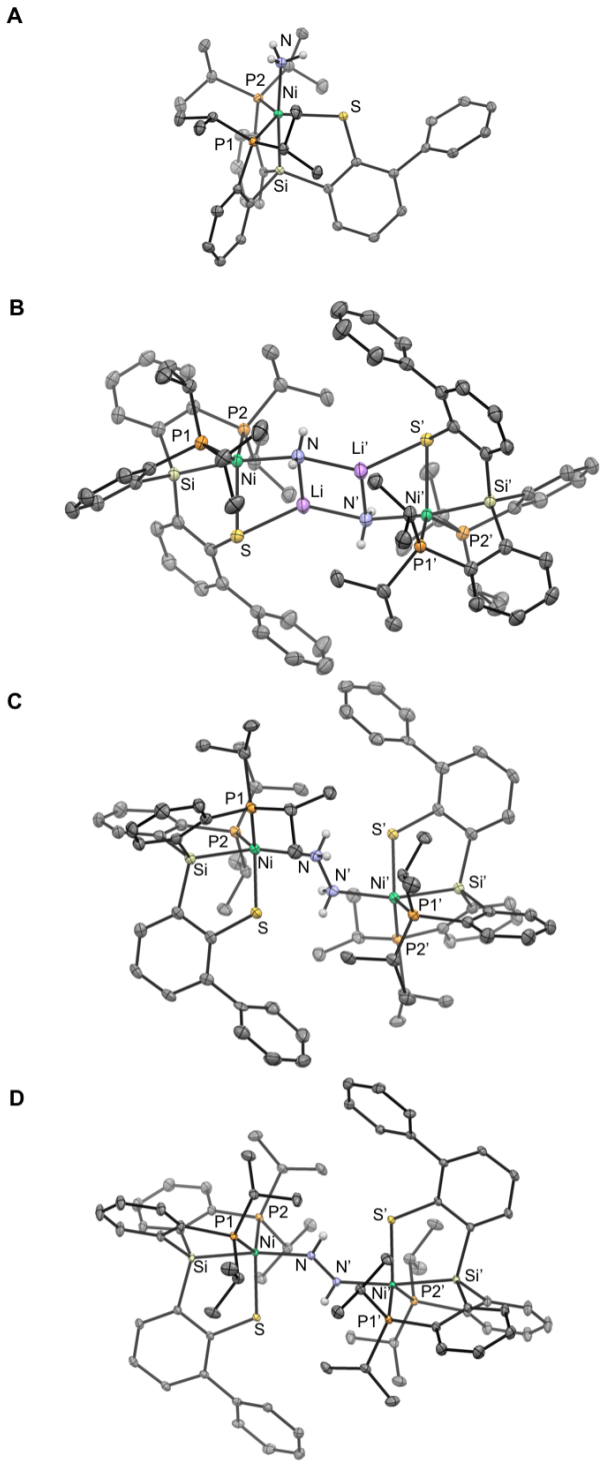

Figure 4.2. Crystal structures of compounds (A) **4.2**, (B) **4.3**, (C) **4.4**, and (D) **4.6**. Solvent molecules, disordered components, and C–*H* hydrogens omitted for clarity. Ellipsoids shown at 50% probability.

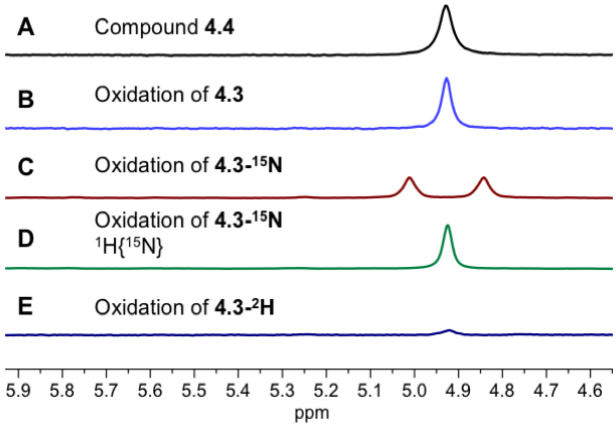

Figure 4.3. Partial ^{1}H NMR spectra of (A) compound **4.4** generated by treatment of **4.1** with N_2H_4 and (B-E) reaction mixtures generated by oxidation of isotopologues of **4.3** in DME, showing the N–*H* resonance at 4.93 ppm (C_6D_6, 400 MHz, 298 K)

Oxidation of the ^{15}N-labeled amide, $[(SiP_2S)Ni^{II}(^{15}NH_2)]Li$, and deuterated amide, $[(SiP_2S)Ni^{II}(ND_2)]Li$, yields $[(SiP_2S)Ni^{II}]_2(^{15}N_2H_4)$ and $[(SiP_2S)Ni^{II}]_2(N_2D_4)$ respectively, as the N–N coupled products, confirming that the coordinated hydrazine fragment is exclusively amide-derived (Fig. 4.3).[20] Of note, H_2 is not detected in the headspace, and NH_3 is absent in the volatiles of the oxidation reaction of **4.3**. Considering that N–N coupling follows addition of two equivalents of oxidant, it is possible that N–N bond formation occurs between two molecules of $(SiP_2S)Ni^{III}(NH_2)$ or alternatively between $(SiP_2S)Ni^{III}(NH_2)$ and **4.3**, followed by one-electron oxidation. However, treatment of **4.3** with 0.5 equivalents of $[Cp_2Fe][BAr^F{}_4]$ in DME at −78 ºC generated no EPR-active species, yielding no evidence to support the intermediacy of $[(SiP_2S)Ni]_2(N_2H_4)^{-}$. This one-electron reduced congener of **4.4** would be a mixed-valent Ni^{I}/Ni^{II} species with the Ni^{I} center bearing 19 e^{-}, and thus likely to be a high energy intermediate. Thus, we favor the mechanism of N−N coupling between two Ni^{III}-NH_2 units to directly generate **4.4**. The concurrent generation of **4.2** in the oxidation reaction of **4.3** likely arises from H-atom abstraction from solvent by $(SiP_2S)Ni^{III}(NH_2)$. Previous work from our lab has demonstrated that the SiP_2S ligand framework can support a formal Ni^{III}–H species competent for the bimolecular release of H_2. H_2 evolution is posited to occur via a transition state featuring the direct H–H coupling between two Ni^{III}–H

fragments, which is analogous to the proposed N–N coupling pathway discussed in this work (Scheme 4.2).

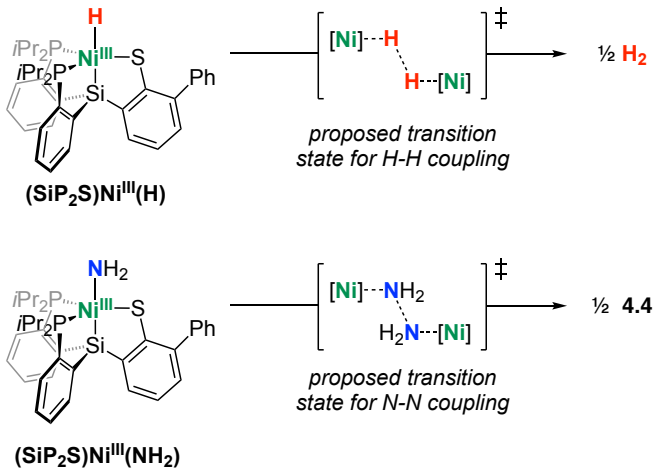

Scheme 4.2. Comparison of H–H and N–N bond formation by $(SiP_2S)Ni^{III}X$ species (X = H, NH_2)

The coordinated hydrazine in complex **4.4** can be further oxidized to the diazene-bridged dinickel species, $[(SiP_2S)Ni]_2$(*trans*-N_2H_2) (**4.5**), by treatment with two equivalents of 2,4,6-tri-*tert*-butylphenoxyl radical and generating two equivalents of 2,4,6-tri-*tert*-butylphenol as byproducts (Scheme 4.1B; Fig. 4.2D). Additionally, in the absence of a radical abstractor, complex **4.4** slowly undergoes disproportionation in solution at 25 ºC to yield **4.2** and **4.5** in a 1:1 molar ratio, where a formal H_2 equivalence is transferred from between two molecules of **4.4**.[21] To the best of our knowledge, there is only one example of a nickel complex featuring a coordinated N_2H_2 unit, which is bound side-on to a single Ni center.[22] The reported crystal structure features an N–N bond length of 1.351(3) Å, and the authors suggest that it is best described as a $(HN–NH)^{2-}$ ligand. XRD data confirm the assignment of **4.5** and reveal a contracted N–N bond length of 1.277(2) Å compared to that of **4.4** (1.488(4) Å). Given that free diazene bears an N–N bond length of 1.252(2) Å,[23] we believe that compound **4.5** is best described as a N=N doubly bonded species. A related Cu^{I}_2(*trans*-N_2H_2) species has been structurally characterized, but the determination of reliable bond metrics of the N_2H_2 fragment was hindered by crystal disorder.[24] However, the

methylated Cu^{I}_2(*trans*-$N_2(CH_3)_2$) species exhibited an N=N bond length of 1.27(2) Å, which is comparable to that of **4.5**.

Treatment of the diazene-bridged species **4.5** with excess NH_3 in THF results in the quantitative displacement of the diazene ligand with NH_3 to yield the ammonia-bound species **4.2**, as determined by ^{31}P NMR spectroscopy. Free diazene is unstable toward disproportionation to N_2 and N_2H_4,[25] thereby liberating ammonia-derived N_2 upon displacement (Scheme 4.3). Liberation of N_2 from **4.5** closes the ammonia oxidation cycle, and regenerates compound **4.2**. In this stoichiometric cycle, the conversion of two NH_3 molecules to ½ N_2 and ½ N_2H_4 is an overall $4e^-/4H^+$ process, but under potential turnover conditions, the N_2H_4 generated upon diazene disproportionation could undergo further iterative oxidation via compounds **4.4** and **4.5** to achieve the full $6e^-/6H^+$ conversion of 2 NH_3 to N_2.

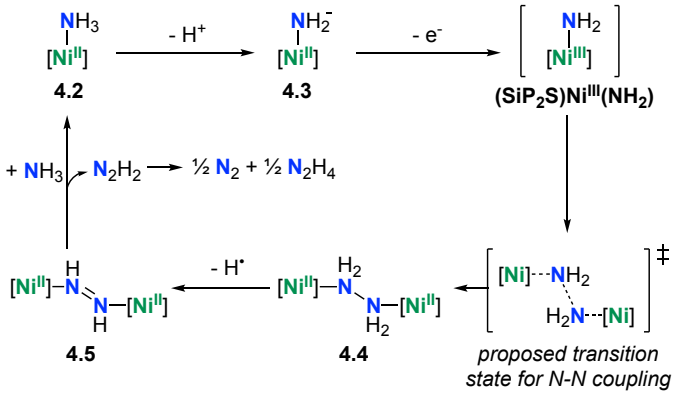

Scheme 4.3. Oxidation of NH_3 to N_2 mediated by (SiP_2S)Ni complexes

4.3 Conclusion

In this work, we report the first example of Ni-mediated oxidation of ammonia, where the key N–N bond formation step is believed to be the homocoupling of a Ni^{III}–NH_2 species to generate a hydrazine-bridged dinickel complex. The reductive elimination of an N–N single bond has been proposed in several ammonia oxidation systems, but stoichiometric observation of such reactivity is limited. This homocoupling pathway from a M–NH_2 species is in contrast to mechanisms for water oxidation catalysts, which commonly invoke high

valent metal oxo intermediates prior to O–O bond formation. Compared to the oxidation of water to O_2, catalysts for the analogous oxidative conversion of ammonia to dinitrogen may traverse an even greater oxidation state change during turnover (e.g. $M^n + NH_3 \rightarrow\rightarrow M^{n+3}\equiv N$). It is thus notable that the ammonia oxidation cycle described herein is carried out exclusively in the Ni^{II}/Ni^{III} oxidation states. This is attributable to the fact that the N−N bond forming step is from a M–NH_2 species (rather than a metal-ligand multiply bonded intermediate), and the redox load is distributed between two metal centers (e.g. H_2N–NH_2 reductive elimination from a mononuclear $M(NH_2)_2$ species would be a $2e^-$ process). Carrying out multielectron oxidation processes at a single redox couple (M^n/M^{n+1}) could potentially bypass the need to access high valent intermediates at highly oxidizing potentials, and incorporating these two components in the design of novel ammonia or water oxidation systems may facilitate catalysis at lower overpotentials.

4.4 Experimental Section

4.4.1 Experimental Details

4.4.1.1 General Considerations

All syntheses and measurements, unless otherwise stated, were carried out under an inert atmosphere (N_2) in a glovebox or using standard Schlenk techniques, and solvents were dried and degassed by thoroughly sparging with N_2 and then passing through an activated alumina column in a solvent purification system supplied by SG Water, LLC. Deuterated solvents were purchased from Cambridge Isotope Laboratories, Inc., degassed, and dried over activated 3 Å molecular sieves before use. Complex **4.1**,[15] ferrocenium tetrakis[3,5-bis(trifluoromethyl)phenyl]borate ($[Cp_2Fe][BAr^F_4]$),[26] $LiNH_2$,[27] and 2,4,6-tri-*tert*-butylphenoxyl radical[28] were prepared according to literature procedures. All other reagents were purchased from commercial vendors and used without further purification unless otherwise stated.

4.4.1.2 Physical Methods

Electrochemical measurements were carried out in a glovebox under an N_2 atmosphere in a one-compartment cell using a CH Instruments 600B electrochemical analyzer. A glassy carbon electrode was used as the working electrode and a platinum wire was used as the auxiliary electrode. A Ag/AgOTf reference electrode was used with the ferrocene couple (Cp_2Fe/Cp_2Fe^+) as an external reference, unless otherwise noted. Solutions of electrolyte (0.4 M $[NBu_4][PF_6]$ in THF) and analyte were also prepared under an N_2 atmosphere. NMR spectra (^1H, ^{31}P) were collected on Varian 300, 400, or 500 MHz spectrometers (25 °C unless otherwise specified). ^1H chemical shifts are reported in ppm, relative to tetramethylsilane using residual proton resonances from solvent as internal standards. ^{31}P chemical shifts are reported in ppm relative to 85% aqueous H_3PO_4. IR spectra were obtained using a Bruker Alpha Platinum ATR spectrometer with OPUS software in a glovebox under an N_2 atmosphere. Optical spectroscopy measurements were taken on a Cary 50 UV-Vis spectrophotometer using a 1-cm quartz cell, unless otherwise noted. H_2 was analyzed on an Agilent 7890A gas chromatograph (HP-PLOT U, 30 m, 0.32 mm ID; 30 °C isothermal; nitrogen carrier gas) using a thermal conductivity detector. Combustion analyses were carried out by the Beckman Institute Crystallography Facility (Caltech).

4.4.1.3 X-Ray Crystallography

X-ray diffraction measurements were carried out in the Beckman Institute Crystallography Facility. XRD measurements were collected using a dual source Bruker D8 Venture, four-circle diffractometer with a PHOTON CMOS detector. Structures were solved using SHELXT and refined against F^2 on all data by full-matrix least squares with SHELXL. The crystals were mounted on a glass fiber under Paratone N oil.

4.4.2 Synthetic Details

4.4.2.1 Synthesis of $(SiP_2S)Ni(NH_3)$ (4.2)

A THF solution of NH_3 (0.4 M, 1.5 mL) was added at 25 ºC to a stirring red solution of **4.1** (0.20 g, 0.15 mmol) in 10 mL THF, resulting in a yellow-orange solution. The reaction

mixture was stirred at 25 ºC for 1 h and then concentrated to dryness. The orange solids were washed with pentane (5 mL), then extracted with C_6H_6 (10 mL) and filtered through Celite. The filtrate was lyophilized to yield the title complex as an orange solid (0.18 g, 89%). Orange crystals suitable for XRD were grown at −35 ºC by layering pentane over a concentrated THF solution. ^{1}H NMR (C_6D_6, 400 MHz, 298 K, δ): 8.02 (d, *J* = 7.8 Hz, 2H), 7.94 (d, *J* = 7.2 Hz, 2H), 7.42 (d, *J* = 7.2 Hz, 1H), 7.33 (t, *J* = 7.5 Hz, 2H), 7.31 – 7.23 (m, 3H), 7.20 – 7.17 (m, 3H), 7.11 (t, *J* = 7.4 Hz, 2H), 7.04 (t, *J* = 7.2 Hz, 1H), 2.14 (m, 4H), 1.13 (q, *J* = 6.9 Hz, 6H), 1.01 (q, *J* = 7.0 Hz, 6H), 0.82 (q, *J* = 6.7 Hz, 6H), 0.77 (s, 3H), 0.67 (q, *J* = 7.0 Hz, 6H). ^{31}P NMR (C_6D_6, 162 MHz, 298 K, δ): 42.18. UV-Visible (THF, 298 K, nm {$M^{-1}cm^{-1}$}): 363 {6200}, 469 {3000}. Anal. Calcd. For $C_{36}H_{47}NNiP_2SSi$: C, 64.10; H, 7.02; N, 2.08. Found: C, 64.46; H, 6.74; N, 1.70.

4.4.2.1 Synthesis of (SiP$_2$S)Ni(^{15}NH$_3$) (4.2-^{15}N)

A solution of *n*BuLi (1.6 M in hexanes, 0.45 mmol) was added to a suspension of $^{15}NH_4Cl$ (0.024 g, 0.44 mmol) in THF (5 mL) at 25 ºC, and the reaction mixture was stirred at 50 ºC for 2 h. The volatiles were subsequently vacuum transferred to a frozen solution of **4.1** (0.100 g, 0.07 mmol) in THF (5 mL). The frozen reaction mixture was thawed and stirred at 25 ºC for 3 h, then the orange reaction mixture was concentrated to dryness. The resulting orange solids were washed with pentane (10 mL), then extracted with C_6H_6 (5 mL) and filtered through Celite. The filtrate was lyophilized to yield the title complex as an orange solid (0.078 g, 77%). ^{1}H NMR (C_6D_6, 400 MHz, 298 K, δ): 8.01 (d, *J* = 7.6 Hz, 2H), 7.93 (d, *J* = 7.2 Hz, 2H), 7.42 (d, *J* = 7.1 Hz, 1H), 7.32 (t, *J* = 7.5 Hz, 2H), 7.29 – 7.26 (m, 3H), 7.19 – 7.17 (m, 3H), 7.11 (t, *J* = 7.3 Hz, 2H), 7.04 (t, *J* = 7.2 Hz, 1H), 2.14 (m, 4H), 1.13 (q, *J* = 6.9 Hz, 6H), 1.01 (q, *J* = 7.0 Hz, 6H), 0.82 (q, *J* = 6.8 Hz, 6H), 0.69 (s, 3H), 0.66 (q, *J* = 7.0 Hz, 6H). ^{31}P NMR (C_6D_6, 162 MHz, 298 K, δ): 42.17. ^{15}N NMR (C_6D_6, 41 MHz, 298 K, δ): −24.41

4.4.2.1 Synthesis of $(SiP_2S)Ni(ND_3)$ (4.2-^{2}H)

Prepared in an analogous manner as **4.2-^{15}N** but employing ND_4Cl. ^{1}H NMR (C_6D_6, 400 MHz, 298 K, δ): 8.02 (d, *J* = 7.9 Hz, 2H), 7.94 (d, *J* = 7.2 Hz, 2H), 7.42 (d, *J* = 7.1 Hz, 1H), 7.33 (t, *J* = 7.7 Hz, 2H), 7.30 – 7.24 (m, 3H), 7.19 – 7.09 (m, 5H), 7.04 (t, *J* = 7.3 Hz, 1H), 2.13 (m, 4H), 1.13 (q, *J* = 6.9 Hz, 6H), 1.01 (q, *J* = 7.0 Hz, 6H), 0.81 (q, *J* = 6.7 Hz, 6H), 0.66 (q, *J* = 7.0 Hz, 6H). ^{31}P NMR (C_6D_6, 162 MHz, 298 K, δ): 42.27. ^{2}H NMR (C_6H_6, 61 MHz, 298 K, δ): 0.70.

4.4.2.1 Synthesis of $[(SiP_2S)Ni(NH_2)]Li$ (4.3)

Method A: A solution of **4.1** (0.029 g, 0.022 mmol) in THF (1 mL) was added to a suspension of $LiNH_2$ (0.002 g, 0.087) in THF (1 mL) at −78 ºC. The reaction mixture was stirred at −78 ºC for 1 h and then stirred at 25 ºC for 1 h. The red-orange reaction mixture was filtered through Celite and concentrated to dryness to yield the title complex as a red-orange solid (0.035 g, 90%).

Method B: A solution of *n*BuLi (1.6 M in hexanes, 0.071 mmol) was added in one portion at −78 ºC to a stirring solution of **4.2** (0.040 g, 0.059 mmol) in THF (3 mL). The reaction mixture was stirred at −78 ºC for 30 min and then stirred at 25 ºC for 30 min. The red-orange reaction mixture was filtered and concentrated to dryness. The resulting red-orange solid was dissolved in minimal benzene (~0.5 mL) and allowed to stand at 25 ºC, resulting in the formation of red-orange crystals. The red-orange crystals were isolated by filtration and washed with 1:1 C_6H_6/pentane (3 mL) and dried under vacuum (0.035 g, 87%). Note: Unlike with Method A, material prepared via Method B does not contain THF molecules coordinated the lithium cation. Instead, $[(SiP_2S)Ni(NH_2)]Li$ is crystallized in benzene as a dimer with no solvent molecules bound to lithium. Prior to recrystallization, the crude material generated by deprotonation of **4.2** in THF also bears three coordinated THF molecules, as determined by ^{1}H NMR spectroscopy in C_6D_6 (See Figs. C.1.30, C.1.31).

Red-orange crystals suitable for XRD were grown from a benzene solution at 25 ºC. ^{1}H NMR (C_6D_6, 300 MHz, 298 K, δ): 7.92 – 7.85 (m, 2H), 7.67 (d, *J* = 7.5 Hz, 2H), 7.42 (dd, *J* = 7.1, 1.6 Hz, 1H), 7.34 (dt, *J* = 6.0, 2.1 Hz, 2H), 7.24 – 6.95 (m, 9H), 2.40 (m, 2H), 3.51 (m, THF, 12H), 2.27 (bs, 2H), 1.38 (m, THF, 12H), 1.19 (dd, *J* = 13.7, 6.9 Hz, 6H), 1.15 (dd, *J* = 13.4, 6.9 Hz, 6H), 1.04 (q, *J* = 6.7 Hz, 4H), 0.83 (q, *J* = 7.2 Hz, 6H), −1.98 (t, *J* = 4.9 Hz, 2H). ^{31}P NMR (C_6D_6, 121 MHz, 298 K, δ): 40.94. ^{1}H NMR (1:5 THF-d_8/C_6D_6, 400 MHz, 298 K, δ): 7.97 (d, *J* = 7.0 Hz, 2H), 7.71 (d, *J* = 7.4 Hz, 2H), 7.46 – 7.42 (m, 3H), 7.21 – 7.08 (m, 7H), 7.03 – 6.94 (m, 2H), 2.50 (bs, 2H), 2.42 (bs, 2H), 1.24 (q, *J* = 6.5 Hz, 6H), 1.16 (q, *J* = 6.9 Hz, 6H), 1.05 (q, *J* = 6.4 Hz, 6H), 1.00 (q, *J* = 6.7 Hz, 6H), −2.31 (t, *J* = 6.2 Hz, 2H). ^{1}H NMR (1:5 THF-d_8/C_6D_6, 400 MHz, 298 K, δ): 40.69. UV-Visible (THF, 298 K, nm {$M^{-1}cm^{-1}$}): 365 {5000}, 471 {2300}. Anal. Calcd. For $C_{36}H_{46}LiNNiP_2SSi\cdot(C_6H_6)$: C, 66.49; H, 6.91; N, 1.85; Found: C, 66.81; H, 7.00; N, 1.91.

4.4.2.1 Synthesis of [(SiP$_2$S)Ni(^{15}NH$_2$)]Li (4.3-^{15}N)

A solution of *n*BuLi (1.6 M in hexanes, 0.048 mmol) was added in one portion to a stirring solution of **4.2-^{15}N** (0.030 g, 0.044 mmol) in THF at −78 ºC. The reaction mixture was stirred at −78 ºC for 30 min and then stirred at 25 ºC for 30 min. The red-orange reaction mixture was filtered and concentrated to dryness. The resulting red-orange solid was dissolved in minimal benzene (~ 0.5 mL) and allowed to stand at 25 ºC, resulting in the formation of red-orange crystals. The crystals were isolated by filtration and washed with 1:1 C_6H_6/pentane (3 mL) and dried under vacuum (0.020 g, 65%). ^{1}H NMR (1:5 THF-d_8/C_6D_6, 400 MHz, 298 K, δ): 7.96 (d, *J* = 7.1 Hz, 2H), 7.71 (d, *J* = 7.5 Hz, 2H), 7.46 – 7.42 (m, 3H), 7.21 – 7.08 (m, 7H), 7.02 – 6.93 (m, 2H), 2.50 (bs, 2H), 2.42 (bs, 2H), 1.24 (q, *J* = 6.6 Hz, 6H), 1.16 (q, *J* = 6.9 Hz, 6H), 1.05 (q, *J* = 6.4 Hz, 6H), 1.00 (q, *J* = 7.0 Hz, 6H), −2.31 (dt, *J* = 55.6, 5.9 Hz, 2H). ^{31}P NMR (1:5 THF-d_8/C_6D_6, 162 MHz, 298 K, δ): 40.69. ^{15}N NMR (1:5 THF-d_8/C_6D_6, 41 MHz, 298 K, δ): −62.07

4.4.2.1 Synthesis of [(SiP$_2$S)Ni(ND$_2$)]Li (4.3-^{2}H)

Prepared in an analogous manner as **4.3-^{15}N** but employing **4.2-^{2}H**. ^{1}H NMR (1:5 THF-d_8/C_6D_6, 400 MHz, 298 K, δ): 7.97 (d, J = 6.6 Hz, 2H), 7.71 (d, J = 8.1 Hz, 2H), 7.47 – 7.42 (m, 3H), 7.21 – 7.08 (m, 7H), 7.03 – 6.94 (m, 2H), 2.50 (bs, 2H), 2.42 (bs, 2H), 1.24 (q, J = 6.6 Hz, 6H), 1.16 (q, J = 7.0 Hz, 6H), 1.05 (q, J = 6.3 Hz, 6H), 1.00 (q, J = 7.0 Hz, 6H). ^{31}P NMR (1:5 THF-d_8/C_6D_6, 162 MHz, 298 K, δ): 40.86. ^{2}H NMR (1:5 THF-H_8/C_6H_6, 61 MHz, 298 K, δ): −2.3.

4.4.2.1 Synthesis of (SiP$_2$S)Ni(NH$_2$)Na(THF)$_3$

A mixture of $NaNH_2$ (0.004 g, 0.10 mmol) in THF (1 mL) was added to a stirring solution of **4.1** (0.060 g, 0.045 mmol) in THF (1 mL) at −78 ºC. The reaction mixture was stirred at −78 ºC for 1 h and then stirred at 25 ºC for 1 h. The orange mixture was filtered and concentrated to dryness to yield the title complex as an orange solid (0.045 g, 55%) Red crystals suitable for XRD were grown by layering pentane onto a concentrated THF solution at −35 ºC. ^{1}H NMR (C_6D_6, 400 MHz, 298 K, δ): 8.04 (d, J = 7.2 Hz, 2H), 7.77 – 7.52 (m, 1H), 7.42 (dd, J = 22.5, 7.3 Hz, 4H), 7.21 (t, J = 7.3 Hz, 2H), 7.15 – 6.94 (m, 6H), 6.79 (t, J = 6.8 Hz, 1H), 3.57 (m, THF, 12H), 2.56 (bs, 4H), 1.41 (m, THF, 12H), 1.29 (q, J = 6.4 Hz, 6H), 1.18 (bs, 12H), 1.05 (q, J = 6.8 Hz, 6H), −2.22 (bs, 2H). ^{31}P NMR (C_6D_6, 162 MHz, 298 K, δ): 42.76. ^{1}H NMR (1:5 THF-d_8/C_6D_6, 400 MHz, 298 K, δ): 8.02 (d, J = 7.2 Hz, 2H), 7.81 (d, J = 7.5 Hz, 2H), 7.50 (d, J = 7.0 Hz, 1H), 7.42 (d, J = 7.8 Hz, 2H), 7.27 – 7.09 (m, 7H), 7.04 (t, J = 7.3 Hz, 1H), 6.95 (t, J = 7.2 Hz, 1H), 2.48 (bs, 2H), 2.35 (bs, 2H), 1.25-1.05 (m, 18H), 1.01 (q, J = 6.6 Hz, 6H), −2.21 (bs, 2H).^{31}P NMR (1:5 THF-d_8/C_6D_6, 162 MHz, 298 K, δ): 41.40

4.4.2.1 Synthesis of [(SiP$_2$S)Ni]$_2$(N$_2$H$_4$) (4.4)

Neat hydrazine (0.0012 g, 0.037 mmol) was added in one portion to a stirring solution of **4.1** in THF (1 mL) at −78 ºC. The dark orange solution was stirred at 25 ºC for 10 min, then concentrated to dryness. The resulting orange material was washed with pentane (1 mL) and Et_2O (2 mL), then extracted with THF (5 mL) and filtered through Celite. The filtrate was

then layered with pentane (5 mL) and stored at −35 ºC. The title complex crystallized as dark red crystals suitable for XRD (0.020 g, 39%). ^{1}H NMR (C_6D_6, 400 MHz, 298 K, δ): 7.83 (d, *J* = 7.1 Hz, 4H), 7.63 (d, *J* = 7.7 Hz, 4H), 7.34 (d, *J* = 7.3 Hz, 2H), 7.32 – 7.17 (m, 8H), 7.17 – 7.10 (m, 14H), 4.86 (s, 4H), 2.33 (s, 4H), 2.24 (hept, *J* = 7.2 Hz, 4H), 1.16 (q, *J* = 6.3 Hz, 12H), 1.00 (q, *J* = 7.3 Hz, 12H), 0.87 (t, *J* = 6.6 Hz, 12H), 0.72 (q, *J* = 7.5 Hz, 12H). ^{31}P NMR (C_7D_8, 162 MHz, 298 K, δ): 40.79. UV-Visible (THF, 298 K, nm {$M^{-1}cm^{-1}$}): 355 {9600}, 472 {3500}. Anal. Calcd. For $C_{72}H_{92}N_2Ni_2P_4S_2Si_2$: C, 64.20; H, 6.88; N, 2.08. Found: C, 64.55; H, 7.19; N, 1.80.

4.4.2.1 Synthesis of [(SiP$_2$S)Ni]$_2$(N$_2$H$_2$) (4.5)

A solution of 2,4,6-tri-*tert*-butylphenoxyl radical (0.047 g, 0.18 mmol) in THF (3 mL) was added dropwise to a stirring solution of **4.4** (0.117 g, 0.085 mmol) in THF (3 mL) at −78 ºC, which resulted in a green solution. The reaction mixture was stirred at 25 ºC for 1 h and then concentrated to dryness. The resulting material was washed with pentane (20 mL) and Et_2O (10 mL), then extracted with THF (20 mL) and filtered through Celite. The green filtrate was concentrated to dryness to yield the title complex as a green solid (0.088 g, 75%). Dark green-brown crystals suitable for XRD were grown at −35 ºC by layering pentane over a concentrated THF solution. ^{1}H NMR (C_7D_8, 400 MHz, 298 K, δ): 15.62 (s, 2H), 7.87 (d, *J* = 7.2 Hz, 4H), 7.67 (d, *J* = 7.6 Hz, 4H), 7.36 (d, *J* = 7.1 Hz, 2H), 7.29 – 7.23 (m, 11 H), 7.17 – 6.97 (m, 11H), 2.36 (bs, 4H), 2.20 (hept, *J* = 7.2 Hz, 4H), 1.02 – 0.93 (m, 24H), 0.86 (q, *J* = 7.2, 6.8 Hz, 12H), 0.66 (q, *J* = 7.3, 6.5 Hz, 12H). ^{31}P NMR (C_6D_6, 162 MHz, 298 K, δ): 49.54. UV-Visible (THF, 298 K, nm {$M^{-1}cm^{-1}$}): 349 {13000}, 444 {13000}, 789 {6000}. Anal. Calcd. For $C_{72}H_{90}N_2Ni_2P_4S_2Si_2$: C, 64.29; H, 6.74; N, 2.08. Found: C, 64.42; H, 6.84; N, 1.97.

4.4.3 Deprotonation of 4.2 with *n*BuLi to generate 4.3

A solution of *n*BuLi (0.025 mL, 1.6 M in hexanes) was added to a stirring solution of **4.2** (0.025 g, 0.019 mmol) in THF (1 mL) at −78 ºC. The orange reaction mixture was stirred at −78 ºC for 30 min, then stirred at 25 ºC for 30 min and concentrated to dryness. ^{1}H, ^{31}P NMR

spectra of the crude reaction mixture reveal quantitative conversion of **4.2** to **4.3** (See Figs. C.1.30, C.1.31).

4.4.2.1 Hydrogen Atom Abstraction from 4.4 to Generate 4.5

A solution of 2,4,6-tri-*tert*-butylphenoxyl radical (2.4 mg, 9.2 μmol) in THF (1 mL) was added to a stirring solution of **4.4** (5.0 mg, 3.6 μmol) in THF (1 mL) at −78 ºC, resulting in a green solution. The reaction mixture was stirred at −78 ºC for 1 h, then stirred at 25 ºC for 30 min and concentrated to dryness. The crude material was analyzed by ^{1}H, ^{31}P NMR spectroscopy to reveal quantitative conversion of **4.4** to **4.5** (See Figs. C.1.37, C.1.38).

4.4.2.1 Conversion of 4.5 to 4.2 in 0.4 M NH_3 in THF

A solution of NH_3 in THF (0.4 M, 1 mL) was added to solid **4.5** (0.005 g, 0.0036 mmol) at 25 ºC. The reaction mixture was transferred to a J. Young NMR tube, and *ca*. 50 μL C_6D_6 was added to the tube and sealed. The dark green solution was stirred at 25 ºC for 3 h, which resulted in a color change to an orange solution. ^{31}P NMR data of the reaction mixture reveals the quantitative formation of **4.2** (See Figs. C.1.41, C.1.42).

4.4.2.1 Detection of H_2 and free NH_3 in the oxidation of 4.3

Solid **4.3** (0.008 g, 0.010 mmol) and solid $[Cp_2Fe][BAr^F_4]$ (0.010 g, 0.010 mmol) were added to a septum-sealed Schlenk tube. Cold dimethoxyethane (0.5 mL, −78 ºC) was added by syringe, and the reaction mixture stirred at −78 ºC for 30 min. An aliquot of the headspace was sampled and analyzed for H_2. Subsequently, the reaction volatiles were vacuum transferred into a vessel containing 2M HCl in Et_2O (3 mL) and analyzed for ammonia (in the form of $[NH_4][Cl]$) by the indophenol method.[29] No H_2 or ammonia was detected in the reaction mixture.

4.4.2.1 Oxidation of 4.3 to yield 4.2 and 4.4

Cold solutions of **4.3** (0.008 g, 0.01 mmol) in DME (0.25 mL) and $[Cp_2Fe][BAr^F_4]$ (0.010 g, 0.01 mmol) in DME (0.25 mL) were mixed in a glovebox coldwell cooled with an external dry ice/acetone bath (−78 ºC). The reaction mixture was green immediately upon addition,

and then changed color within a few seconds to orange, which persisted for the duration of the reaction. The reaction mixture was stirred at −78 ºC for 30 min, then the volatiles were removed under vacuum. The remaining orange solids were dissolved in C_6D_6 (0.5 mL), then filtered through a glass fiber filter pipette and analyzed by NMR spectroscopy. Yield of **4.4**: 41 ± 3%; yield of **4.2**: 60 ± 4%

4.5 References

(1) (a) Kärkäs, M. D.; Verho, O.; Johnston, E. V.; Åkermark, B. *Chem. Rev.* **2014**, *114*, 11863-12001. (b) Blakemore, J. D.; Crabtree, R. H.; Brudvig, G. W. *Chem. Rev.* **2015**, *23*, 12974-13005.

(2) Johnson, S. I.; Heins, S. P.; Klug, C. M.; Wiedner, E. S.; Bullock, R. M.; Raugei, S. *Chem. Commun.* **2019**, *55*, 5083-5086.

(3) (a) Clarke, R. M.; Storr, T. *J. Am. Chem. Soc.* **2016**, *138*, 15299-15302. (b) Keener, M.; Peterson, M.; Hernández Sánchez, R.; Oswald, V. F.; Wu, G.; Ménard, G. *Chem. Eur. J.* **2017**, *23*, 11479-11484. (c) Würminghausen, T.; Sellmann, D. *J. Organomet. Chem.* **1980**, *1999*, 77-85. (d) Chantarojsiri, T.; Reath, A. H.; Yang, J. Y. *Angew. Chem. Int. Ed.* **2018**, *57*, 14037-14042.

(4) (a) Pipes, D. W.; Bakir, M.; Vitols, S. E.; Hodgson, D. J.; Meyer, T. J. *J. Am. Chem. Soc.* **1990**, *112*, 5507-5514. (b) Demadis, K. D.; Meyer, T. J.; White, P. S. *Inorg. Chem.* **1997**, *36*, 5678-5679. (c) Buhr, J. D.; Taube, H. *Inorg. Chem.* **1979**, *18*, 2208-2212. (d) Coia, G. M.; Devenney, M.; White, P. S.; Meyer, T. J.; Wink, D. A. *Inorg. Chem.* **1997**, *36*, 2341-2351.

(5) (a) Ishitani, O.; White, P. S.; Meyer, T. J. *Inorg. Chem.* **1996**, *35*, 2167-2168. (b) Ishitani, O.; Ando, E.; Meyer, T. J. *Inorg. Chem.* **2003**, *42*, 1707-1710. (c) Collman, J. P.; Hutchison, J. E.; Lopez, M. A.; Guilard, R.; Reed, R. A. *J. Am. Chem. Soc.* **1991**, *113*, 2794-2796. (d) Collman, J. P.; Hutchison, J. E.; Ennis, M. S.; Lopez, M. A.; Guilard, R. *J. Am. Chem. Soc.* **1992**, *114*, 8074-8080.

(6) For a related example of Ru-catalyzed ammonia oxidation to nitrite/nitrate, see: Thompson, M. S.; Meyer, T. J. *J. Am. Chem. Soc.* **1981**, *103*, 5577-5579.

(7) (a) Habibzadeh, F.; Miller, S. L.; Hamann, T. W.; Smith III, M. R. *Proc. Natl. Acad. Sci.* **2019**, *116*, 2849-2853. (b) Bhattacharya, P.; Heiden, Z. M.; Chambers, G. M.; Johnson, S. I.; Bullock, R. M.; Mock, M. T. *Angew. Chemie. Int. Ed.* **2019**, *58*, 11618-11624. (c) Nakajima, K.; Toda, H.; Sakata, K.; Nishibayashi, Y. *Nat. Chem.* **2019**, *11*, 702-709. (d) Dunn, P.; Johnson, S. I.; Kaminsky, W.; Bullock, R. M. *J. Am. Chem. Soc.* **2020**, DOI: 10.1021/jacs.9b13706.

(8) (a) Zott, M. D.; Garrido-Barros, P.; Peters, J. C. *ACS Catal.* **2019**, *9*, 10101-10108. (b) Raghibi Boroujeni, M.; Greene, C.; Bertke, J. A.; Warren, T. H. *ChemRxiv* **2019**, DOI: 10.26434/chemrxiv. 9729635.v1.

(9) Betley, T. A.; Peters, J. C. *J. Am. Chem. Soc.* **2004**, *126*, 6252-6254.

(10) (a) Mankad, N. P.; Müller, P.; Peters, J. C. *J. Am. Chem. Soc.* **2010**, *132*, 4083-4085. (b) Powers, I. G.; Andjaba, J. M.; Luo, X.; Mei, J.; Uyeda, C. *J. Am. Chem. Soc.* **2018**, *140*, 4110-4118. (c) Yiu, S.-M.; Lam, W. W. Y.; Ho, C.-M.; Lau, T.-C. *J. Am. Chem. Soc.* **2007**, *129*, 803-809.

(11) Coia, G. M.; White, P. S.; Meyer, T. J.; Wink, D. A.; Keefer, L. K.; Davis, W. M. *J. Am. Chem. Soc.* **1994**, *116*, 3649-3650.

(12) The related reductive elimination of an N−N single bond between nitrogen-based heterocyclic ligands has been demonstrated on a dinuclear Ni system, see: Diccianni, J. B.; Hu, C.; Diao, T. *Angew. Chemie. Int. Ed.* **2016**, *55*, 7534-7538. Additionally, homocoupling reactions have been proposed between putative $Cu^{II}(NR_2)$ species to yield N−N coupled products, see: (a) Gephart III, R. T.; Huang, D. L; Aguila, M. J. B.; Schmidt, G.; Shahu, A.; Warren, T. H. *Angew. Chem. Int. Ed.* **2012**, *51*, 6488-6492. (b) Kinoshita, K. *Bull. Chem. Soc. Jpn.* **1959**, *32*, 780-783. (c) Ryan, M. C.; Kim, Y. J.; Gerken, J. B.; Wang, F.; Aristov, M. M.; Martinelli, J. R.; Stahl, S. S. *Chem. Sci.* **2020**, *11*, 1170-1175.

(13) Warren, J. J.; Tronic, T. A.; Mayer, J. M. *Chem. Rev.* **2010**, *110*, 6961-7001.

(14) Gu, N. X.; Oyala, P. H.; Peters, J. C. *J. Am. Chem. Soc.* **2018**, *140*, 6374-6382.

(15) Gu, N. X.; Oyala, P. H.; Peters, J. C. *J. Am. Chem. Soc.* **2020**, DOI: 10.1021/jacs.0c00712.

(16) Complex **4.1** is isolated as a dinickel species featuring a bridging N_2 unit, but is in equilibrium with the monomeric $(SiP_2S)NiN_2$ in solution under an N_2 atmosphere.

(17) Crystals of the sodium analogue, $[(SiP_2S)Ni^{II}(NH_2)]Na(THF)_3$, can be grown from THF/pentane mixtures, and XRD data reveal the coordination of three THF molecules to the sodium ion. ^{1}H NMR data of $[(SiP_2S)Ni^{II}(NH_2)]Na(THF)_3$ in C_6D_6 also corroborate the presence of three THF molecules. See Appendix C for more information.

(18) Creutz, S. E.; Peters, J. C. *Chem. Sci.* **2017**, *8*, 2321-2328.

(19) Kohata, K.; Fukuyama, T.; Kuchitsu, K. *J. Phys. Chem.* **1982**, *86*, 602-606.

(20) The ^{1}H NMR spectrum of the oxidation reaction of $[(SiP_2S)Ni^{II}(ND_2)]Li$ bears a minor component of $[(SiP_2S)Ni]_2(N_2H_4)$ due to incomplete deuteration of the starting ^{2}H-labeled amide.

(21) For an example of this disproportionation reaction mediated by a Ru system, see: Sellmann, D.; Hille, A.; Rösler, A.; Heinemann, F. W.; Moll, M.; Brehm, G.; Schneider, S.; Reiher, M.; Hess, B. A.; Bauer, W. *Chem. Eur. J.* **2004**, *10*, 819-830.

(22) Köthe, C.; Braun, B.; Herwig, C.; Limberg, C. *Eur. J. Inorg. Chem.* **2014**, 5296-5303.

(23) Carlotti, M.; Johns, J. W. C.; Trombetti, A. *Can. J. Phys.* **1974**, *52*, 340-344.

(24) Fujisawa, K.; Lehnert, H.; Ishikawa, Y.; Okamoto, K. *Angew. Chemie. Int. Ed.* **2004**, *43*, 4944-4947.

(25) Stanbury, D. M. *Inorg. Chem.* **1991**, *30*, 1293-1296.

(26) Chávez, I.; Alvarez-Carena, A.; Molins, E.; Roig, A.; Maniukiewicz, W.; Arancibia, A.; Arancibia, V.; Brand, H.; Manríquez, J. M. *J. Organomet. Chem.* **2000**, *601*, 126-132.

(27) Baldissin, G.; Boag, N. M.; Tang, C. C.; Bull, D. J. *Eur. J. Inorg. Chem.* **2013**, 1993-1996.

(28) Manner, V. W.; Markle, T. F.; Freudenthal, J. H.; Roth, J. P.; Mayer, J. M. *Chem. Commun.* **2008**, 256-258.

(29) Weatherburn, M. W. *Anal. Chem.* **1967**, *39*, 971-974.

Chapter 5

CATALYTIC HYDRAZINE DISPORPORTIONATION MEDIATED BY A THIOLATE-BRIDGED VFE COMPLEX

5.1 Introduction

Despite structural similarities between the MoFe and VFe nitrogenase cofactors,[1] these variants demonstrate variable efficiencies for nitrogen fixation,[2] and it is unknown how the distinct metal compositions of the cofactors influence catalytic performance, and the mechanistic pathways that are viable. Similarly, questions remain regarding which metal site(s) are active toward nitrogen fixation at the VFe cofactor,[3] and whether bimetallic cooperativity between V and Fe sites may play a role. Synthetic V[4] and Fe[5] complexes are now known that catalyse molecular N_2 reduction to NH_3 (or hydrazine). It remains of interest to study the reactivity of bimetallic MFe (M= Mo, V, Fe) complexes toward N_2 and other nitrogenous substrates to canvas accessible chemistry on such systems.

N_2 binding to heterobimetallic VFe complexes has not been previously demonstrated, and relatedly, there are as yet no examples of heterobimetallic VFe-based molecular N_2 fixation catalysts. However, VFe complexes are known to generate ammonia via reduction of hydrazine ($N_2H_4 + 2\ H^+ + 2\ e^- \rightarrow 2\ NH_3$),[6] which is both a detectable product of biological nitrogen fixation,[7] as well as a substrate for some nitrogenases.[8] Alternatively, the 2 H^+/2 e^- employed in the reduction of hydrazine may be derived from hydrazine itself via a disproportionation pathway, coupling the reduction of N_2H_4 to NH_3 to the oxidation of N_2H_4 to N_2 ($3\ N_2H_4 \rightarrow 4\ NH_3 + N_2$).[9,10] Whether N_2H_4 is an essential intermediate of biological nitrogen fixation is not known. Nonetheless, one possible pathway to catalyse nitrogen fixation to ammonia is the selective reduction N_2 to N_2H_4, which has been demonstrated both stoichiometrically[11] and catalytically in molecular Fe systems,[5d] followed by subsequent hydrazine disproportionation.

Herein, we synthesize a thiolate-supported vanadium-iron complex, with N_2 and hydride ligands bound to the Fe centre, and demonstrate that it is an active catalyst for the disproportionation of hydrazine under ambient conditions, achieving yields of up to 1073 equivalents of NH_3 per VFe complex. In comparison to the bimetallic complex, monometallic analogues of the individual V and Fe centres display attenuated catalytic activity, which suggests a cooperative bimetallic mechanism may be operative in the disproportionation reaction.

5.2 Results and Discussion

To template the target VFe complex, we modified the binucleating ligand used to support the thiolate-bridged diiron complex N_2Fe-(μ-SAr)-FeN_2 (**5.1**), previously reported by our lab (Fig. 5.1),[10] to incorporate a (polythiolate)phosphine fragment to coordinate V.[12] Treatment of the thioether-substituted aryllithium **5.2**[13] with dichloro(diethylamino) phosphine (0.5 equivalent), followed by addition of HCl, yields the thioether-substituted diaryl(chloro)phosphine (**5.3**, Scheme 5.1a). Lithium-halogen exchange of (diphosphino)thioether-functionalized triarylsilane **5.4** and subsequent treatment with **5.3** yields the thioether-protected ligand precursor **5.5**. Reductive cleavage of the S-*i*Pr groups with excess KC_8 and subsequent protonation yields the thiol-functionalized ligand **5.6**.

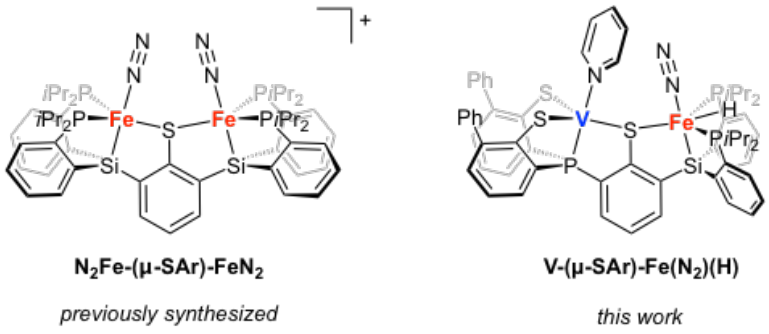

Figure 5.1. Thiolate-bridged bimetallic complexes N_2Fe–(μ-SAr)–$Fe(N_2)$ (**5.1**) and V–(μ-SAr)–$Fe(N_2)(H)$ (**5.8**)

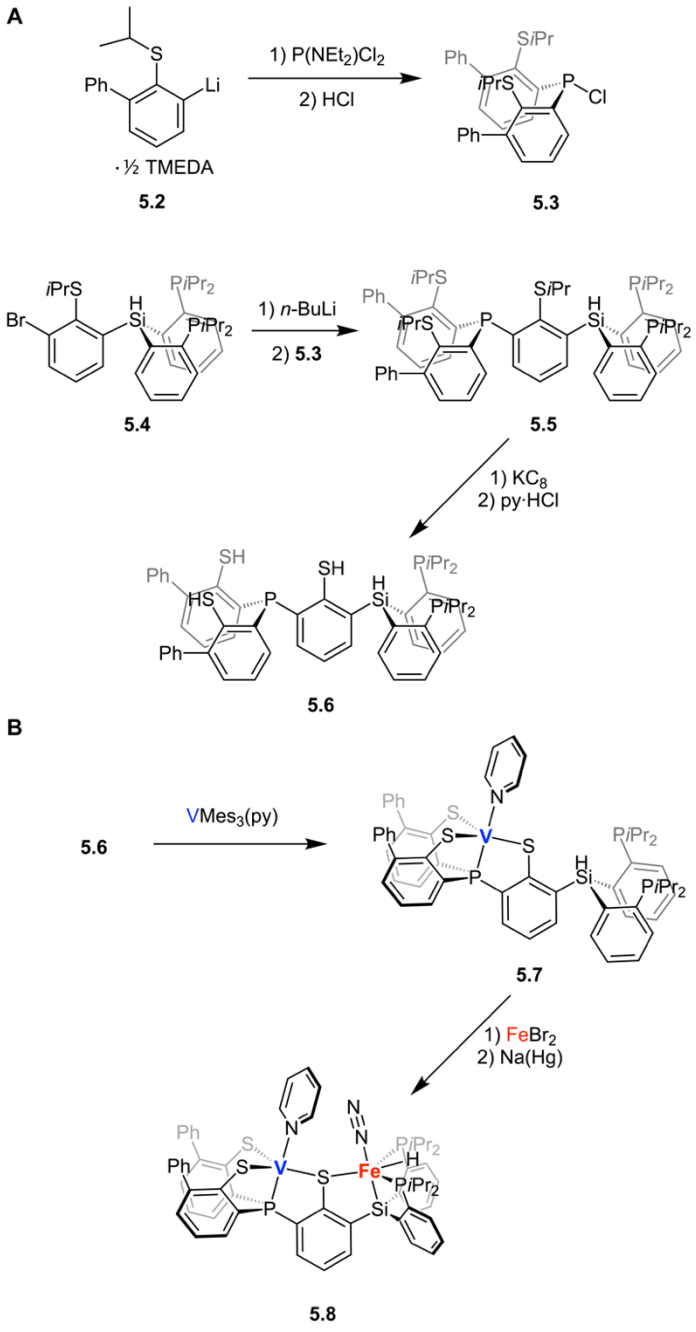

Scheme 5.1. (A) Synthesis of ligand **5.6** and (B) metalation of complexes **5.7** and **5.8**.

Treatment of **5.6** with $VMes_3(py)$ (Mes = 2,4,6-$Me_3C_6H_2$, py = NC_5H_5) generates V-(SAr) (**5.7**, Scheme 5.1b). Compound **5.7** is a yellow-orange solid and has a spin state of S = 1 at 25 °C. Stirring **5.7** with iron dibromide, followed by reduction with Na(Hg) amalgam

(2.1 equiv. Na) under an N_2 atmosphere yields V–(μ-SAr)–Fe(N_2)(H) (**5.8**) in moderate yields, whereby reduction promotes the Fe-centred Si–H bond cleavage and N_2 coordination. Compound **5.8** has a solution magnetic moment of 3.1 μ_B (25 °C), consistent with an overall $S = 1$ species.

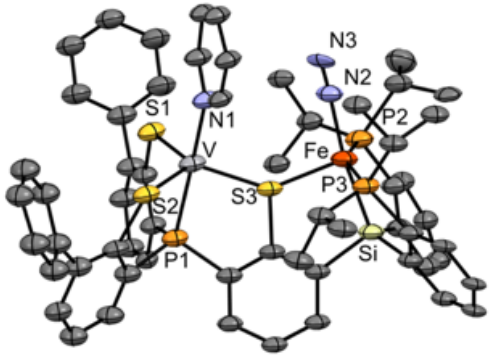

Figure 5.2. X-ray structure of **5.8**. Hydrogen atoms and solvent molecules are omitted for clarity. Ellipsoids are depicted at 50% probability.

Despite repeated attempts, only moderate-quality crystallographic data could be obtained on compound **5.8**. Nonetheless, the XRD data support the structural assignment of **5.8** (Fig. 5.2). The Fe-bound hydride could not be located in the XRD data of **5.8**, but the large ∠P–Fe–P angle (153.0(6)°) suggests it is positioned trans to the thiolate. The IR spectrum of **5.8** reveals an Fe–H stretch at 1898 cm^{-1}, which corroborates the presence of the hydride ligand. Additionally, treatment of **5.8** with one equivalent of [H(OEt_2)][$BAr^F{}_4$] results in the protonation of the hydride ligand to form H_2. The N_2 stretch is observed at 2054 cm^{-1}, similar to that of a structurally related diamagnetic ferrous species, (SiP_2S^{Ad})Fe(H)(N_2) (**5.9**, 2055 cm^{-1}, Fig. 5.3).[14] This comparison is consistent with a description for **5.8** as a V(III)/Fe(II) species. In an alternate oxidation state assignment, if the bridging thiolate is described as an L-type ligand to V and an X-type ligand to Fe, compound **5.8** can instead be considered a V(II)/Fe(III) species. However, the IR spectrum of a related ferric hydride, (SiP_2S)Fe(H)(N_2) (**5.10**),[13] exhibits a significantly less activated N_2 stretch of 2123 cm^{-1}.[15] Thus, we favour the description of **5.8** as bearing an $S = 1$ V(III) centre and an $S = 0$ Fe(II)

centre. Of note, a related thiolate-bound V(III) species (**5.11**) has a spin state of $S = 1$ at 25 °C.

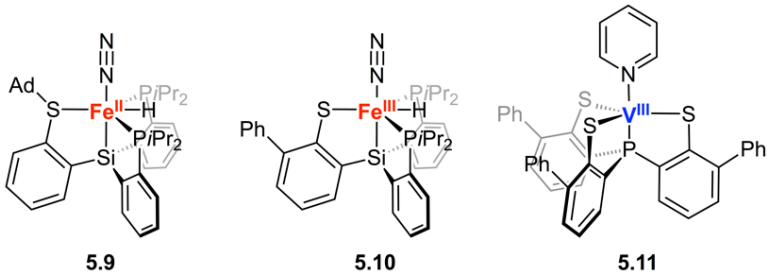

Figure 5.3. Monometallic complexes **5.9**-**5.11**. Ad = adamantyl

Complex **5.8** is an active catalyst for the disproportionation of hydrazine (3 $N_2H_4 \rightarrow$ 4 $NH_3 + N_2$).[16] Treatment of **5.8** with 50 equivalents of hydrazine results in the detection of NH_3 after 2 hours (Table 5.1), with higher yields of ammonia using Et_2O (10 equiv. NH_3/**5.8**, 16%, entry a) as a solvent as compared to THF (5 equiv. NH_3/**5.8**, 7%, entry b). Employing Et_2O as the solvent, 46 equivalents of NH_3 per VFe complex were detected after 12 hours of reaction time (69%, entry c), and 60 equivalents of NH_3 were produced after 24 hours of reaction time (89%, entry d). At higher substrate loading (100 equiv. N_2H_4/**5.8**), 89 equivalents of NH_3 were produced after 24 h (67%, entry e), and 113 equivalents after 48 h (85%, entry f). Addition of elemental Hg or PPh_3 did not affect catalysis.[17]

There are no previously reported examples of vanadium complexes that facilitate the catalytic disproportionation of N_2H_4, although V complexes have been demonstrated to catalyse hydrazine reduction[12d] and the disproportionation of substituted hydrazines.[18] When considering Fe-only catalysts, diiron **5.1** bears the highest previously reported turnover number; in the presence of one equivalent of co-acid, treatment of **5.1** with 50 equivalents N_2H_4 yields 29 equivalents of NH_3 (44% yield).[10] To the best of our knowledge, the most active molecular hydrazine disproportionation catalyst with respect to turnover number is a dimolybdenum complex, which generated 1232 equivalents of NH_3 per complex (1440 equivalents of N_2H_4, 64% yield) over 17 days.[9g,h] For direct comparison, treatment of **5.8** with 1440 equivalents of N_2H_4 yielded 1073 equivalents of ammonia (56%) over the same time period (Table 5.1, entry g), demonstrating their similar activities.

Table 5.1. N_2H_4 disproportionation catalysed by compound **5.8**

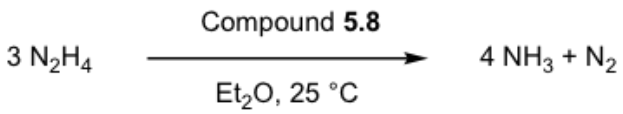

Entry	Time	N_2H_4 (equiv./5.8)	NH_3 (equiv./5.8)	NH_3 (%)
a	2 h	50	10(1)	16
b[1]	2 h	50	5(1)	7
c	12 h	50	46(7)	69
d	24 h	50	60(4)	89
e	24 h	100	89(12)	67
f	48 h	100	113(16)	85
g	17 d	1440	1073(84)	56

Catalytic runs are performed at catalyst concentrations of 1 mM unless otherwise noted. Yields are an average of 2 runs; the spread between the two runs is shown in parentheses as a std deviation for N = 2, and values for all individual runs are presented in Appendix D. [1]Entry b was carried out with THF as the solvent. [2]Entry g was carried out with a catalyst concentration of 0.1 mM.

The catalytic activities of the monometallic Fe and V analogues (**5.9** and **5.11**) were assayed to compare their respective activities with that of bimetallic **5.8**. Upon treatment of 50 equiv of hydrazine in THF (Table 5.2),[19] complexes **5.9** (0.4 equiv/**5.9**, entry h) and **5.11** (0.2 equiv/**5.11**, entry i) yielded far less NH_3 than **5.8** (5 equiv/**5.8**, Table 5.1, entry b) after 2 hours. Additionally, an equimolar mixture of **5.9** and **5.11** yielded 1.0 equiv of NH_3/**5.9** after 2 hours (Table 5.2, entry j), which is comparable to the sum of their independent yields in entries h and i. While we do not know all the factors at play, the poorer activity of the equimolar mixture of **5.9** and **5.11** compared to that of **5.8** suggests that arrangement of the Fe and V centres in a binucleating scaffold may enhance the activity for ammonia formation.

Employing the method of initial rates, a pseudo-zero order dependence on N_2H_4 is observed at high substrate loadings (*ca*. 50 equiv. N_2H_4) in THF,[20] which is due to saturation kinetics and is relevant to the catalysis at early timepoints. Probing kinetics at lower substrate

Table 5.2. N_2H_4 disproportionation catalysed by compounds **5.9** and **5.11**

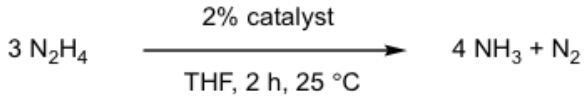

Entry	Catalyst	NH_3 (equiv./cat.)
h	**5.9**	0.4(0.2)
i	**5.11**	0.2(0.1)
j[1]	**5.9** + **5.11**	1.0(0.2)

Catalytic runs are performed at catalyst concentrations of 1 mM unless otherwise noted. Yields are an average of 2 runs; the spread between the two runs is shown in parentheses as a std deviation for N = 2, and values for all individual runs are presented in the Appendix D. [1][**5.9**] = [**5.11**] = 1 mM.

loadings (*ca*. 10 equiv. of N_2H_4), a first order dependence on N_2H_4 is determined, which is the regime that the catalyst operates under at late timepoints when most of the substrate has been consumed. Additionally, a first order dependence on **5.8** is measured, which is consistent with a unimolecular pathway with respect to the VFe catalyst, as depicted in Figure 5.4. However, an on-path step involving two VFe species cannot be ruled out. Here, a formal dihydrogen transfer between two hydrazine species yields two equivalents of ammonia and one equivalent of diazene, which can undergo thermal decomposition upon release,[21] followed by N_2H_4 binding to close the catalytic cycle. The dominant decomposition pathway for diazene yields half an equivalent of dinitrogen and half an equivalent hydrazine. Additionally, it has been proposed as an intermediate in other hydrazine disproportionation systems.[9e,i]

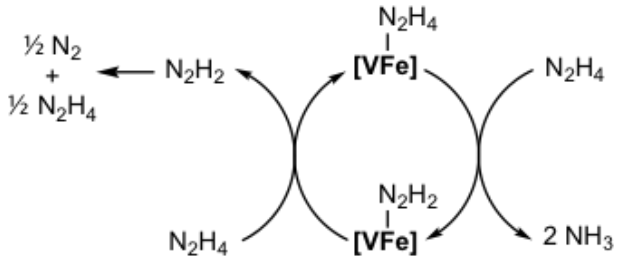

Figure 5.4. Proposed catalytic cycle for hydrazine disproportionation catalysed by **5.8**.

5.3 Conclusion

Drawing inspiration from the VFe cofactor, we have synthesized an N_2-bound VFe complex with supporting thiolate, phosphine, and silyl donors, and demonstrated that it is a highly active catalyst for hydrazine disproportionation with respect to turnover number, as active as any known. Whereas there are no known V catalysts for N_2H_4 disproportionation, there are several less active Fe complexes that also catalyse this transformation.[9 dfi,10] It is unclear whether both metal centres are synergistically participating in the key bond-breaking and -forming steps, but assuming that the monometallic complexes **5.9** and **5.11** are representative models for the catalytic activities of the Fe and V centres of **5.8**, the much poorer activity of the vanadium and iron monometallic species compared to the activity of **5.8** indicates that arranging the two metal centres within the bimetallic scaffold described promotes hydrazine disproportionation catalysis.

5.4 Experimental Section

5.4.1 Experimental Details

5.4.1.1 General Considerations

All syntheses and measurements, unless otherwise stated, were carried out under an inert atmosphere (N_2) in a glovebox or using standard Schlenk techniques, and solvents were dried and degassed by thoroughly sparging with N_2 and then passing through an activated alumina column in a solvent purification system supplied by SG Water, LLC. 2-phenylbenzenethiol,[22] $VMes_3(py)$,[23] $VMes_3(THF)$,[24] $^{Ph}PS_3H_3$[25] , **5.2**,[13] **5.4**,[10] and **5.9**[14] were prepared according to

literature procedures. All other reagents were purchased from commercial vendors and used without further purification unless otherwise stated.

5.4.1.2 Physical Methods

NMR spectra (^{1}H, ^{31}P) were collected on Varian 300 or 400 MHz spectrometers (25 °C unless otherwise specified). ^{1}H chemical shifts are reported in ppm, relative to tetramethylsilane using residual proton and ^{31}P chemical shifts are reported in ppm relative to 85% aqueous H_3PO_4. Thin film IR spectra were obtained using a Bruker Alpha Platinum ATR spectrometer with OPUS software in a glovebox under an N_2 atmosphere. Optical spectroscopy measurements were taken on a Cary 50 UV-Vis spectrophotometer using a 1 cm quartz cell, unless otherwise noted. Combustion analysis was carried out by either Midwest Microlabs (Indianapolis) or the Beckman Institute Crystallography Facility (Caltech). H_2 was analyzed on an Agilent 7890A gas chromatograph (HP-PLOT U, 30 m, 0.32 mm ID; 30 °C isothermal; nitrogen carrier gas) using a thermal conductivity detector. Mass spectroscopy data for **5.5** and **5.6** were obtained using a Thermo LCQ ion trap mass spectrometer. High-resolution mass spectroscopy data for **5.7** was collected by direct infusion electrospray ionization in the positive ion mode using an LCT Premier XE time-of-flight mass spectrometer (Waters).

5.4.1.3 X-Ray Crystallography

X-ray diffraction (XRD) measurements were carried out in the Beckman Institute Crystallography Facility. XRD measurements were collected using a dual source Bruker D8 Venture, four-circle diffractometer with a PHOTON CMOS detector. Structures were solved using SHELXT and refined against F^2 on all data by full-matrix least squares with SHELXL. The crystals were mounted on a glass fiber under Paratone N oil.

5.4.2 Synthetic Details

5.4.2.1 Synthesis of Chlorobis(2-(isopropylthio)-[1,1'-biphenyl]-3-yl)phosphine (5.3)

Neat $P(NEt_2)Cl_2$ (1.3 g, 7.1 mmol) was added dropwise to a stirring suspension of **5.2** (5.0 g, 14.3 mmol) in Et_2O (100 mL) at −78 °C. The reaction was stirred overnight with slow warming to 25 °C. The volatiles were subsequently removed under reduced pressure, and the resulting solids were extracted with pentane (3 x 25 mL), then dried and redissolved in Et_2O (100 mL). HCl (2 M in Et_2O, 28.5 mL) was added dropwise to the stirring reaction mixture at 0 °C, and the reaction was allowed to stir at 25 °C for 1 h. The reaction volatiles were subsequently removed under reduced pressure, and the crude product was extracted from the mixture with pentane (3 x 50 mL). The pentane solution was concentrated to 15 mL and chilled to −78 °C to precipitate the product. The title compound was isolated by filtration as a white solid. The filtrate was collected, concentrated, and cooled to −78 °C to yield additional material (1.94 g, 26%). ^{1}H NMR (C_6D_6, 400 MHz, 298 K, δ): 7.81 (d, J = 7.5 Hz, 2H), 7.40 (d, J = 7.2 Hz 2H), 7.12 – 7.03 (m, 16H), 2.84 (hept, J = 7.0 Hz, 1H), 1.00 (d, J = 6.7 Hz, 6H), 0.84 (d, J = 6.8 Hz, 6H). ^{31}P NMR (C_6D_6, 300 MHz, 298 K, δ): 49.81 (s).

5.4.2.2 Synthesis of (((3-(bis(2-(isopropylthio)-[1,1'-biphenyl]-3-yl) phosphino)-2-(isopropylthio)phenyl)silanediyl)bis(2,1-phenylene))bis(diisopropylphosphine) (5.5)

N-BuLi (1.6 M in hexane, 0.9 mL, 1.4 mmol) was added dropwise to a stirring solution of **5.4** (0.82 g, 1.3 mmol) in Et_2O (20 mL) at −78 °C. The reaction was allowed to stir at −78 °C for 1 h and subsequently allowed to stir at 25 °C for 1 h. The volatiles were removed under reduced pressure, and the resulting off-white solid was redissolved in toluene (20 mL). A cold solution of **5.3** (0.66 g, 1.3 mmol) in toluene (20 mL) was added dropwise to the stirring reaction, and the reaction mixture was stirred overnight with slow warming to 25 °C. The volatiles were subsequently removed *in vacuo.* The resulting residue was redissolved in Et_2O (20 mL) and filtered through Celite. The filtrate was concentrated to yield the title compound as an off-white solid (1.10 g, 82%). The title compound can be recrystallized from a concentrated pentane solution at 25 °C. ^{1}H NMR (C_6D_6, 400 MHz, 298 K, δ): 7.52 (dd, J = 17.5, 7.4 Hz, 4H), 7.41 (t, J = 8.6 Hz, 2H), 7.36 – 7.02 (m, 20H), 6.96 (t, J = 7.4 Hz, 1H),

4.59 (bs, 1H), 3.31 (hept, 1H), 3.10 (hept, 1H), 2.20 – 1.89 (m, 4H), 1.52 (d, J = 6.8 Hz, 6H), 1.36 – 1.25 (m, 3H), 1.25 – 0.94 (m, 21H), 0.90 – 0.79 (m, 12H). ^{31}P NMR (C_6D_6, 300 MHz, 298 K, δ): 2.12 (s), 1.84 (s), −17.00 (s). ESI-MS (positive ion, amu): Calcd. 1089.4 ([M-Na]$^+$); Found. 1089.2.

5.4.2.3 Synthesis of 3,3''-((3-(bis(2-(diisopropylphosphino)phenyl)silyl)-2-mercaptophenyl)phosphinediyl)bis(([1,1'-biphenyl]-2-thiol)) (5.6)

A suspension of KC_8 (0.470 g, 3.5 mmol) in THF (15 mL) was added dropwise to a stirring solution of **5.5** (1.108 g, 1.05 mmol) in THF (50 mL) at −78 °C. The reaction was stirred at 25 °C for 1 h to yield a deep red solution. The reaction mixture was filtered to remove graphite, and solid pyridinium chloride (0.670 g, 5.8 mmol) was added at 25 °C to the stirring solution. The color of the reaction mixture changed from deep red to pale yellow during the addition of acid. The reaction was stirred at 25 °C for 1 h, and the volatiles were subsequently removed *in vacuo*. The product was extracted from the remaining white solid with pentane (3 x 25 mL), and the volatiles were removed under reduced pressure to afford the title compound as an off-white solid and used as is (0.803 g, 82%). ^{1}H NMR (C_6D_6, 300 MHz, 298 K, δ): 7.43 – 7.01 (m, 19 H), 6.91 (t, J = 7.6 Hz, 5H), 6.83 (t, J = 7.4 Hz, 3H), 4.72 (d, J = 3.7 Hz, 2H), 4.65 (bs, 1H), 2.06-1.88 (m, 4H), 1.09 (ddd, J = 14.4, 9.4, 6.9 Hz, 12H), 0.93 (dd, J = 12.0, 7.1 Hz, 6H), 0.86 (dd, J = 11.7, 7.2 Hz, 6H). ^{31}P NMR (C_6D_6, 162 MHz, 298 K, δ): 0.95 (s), −24.15 (s). ESI-MS (positive ion, amu): Calcd. 925.3 ([M-H]$^+$); Found. 925.0.

5.4.2.4 Synthesis of V-(SAr) (5.7)

A solution of $VMes_3$(py) (0.218 g, 0.45 mmol) and pyridine (0.1 mL) in THF (10 mL) was added dropwise to a stirring solution of **5.6** (0.376 g, 0.41 mmol) in THF at 25 °C. The reaction mixture was stirred for 5 h at 25 °C, and the volatiles were subsequently removed *in vacuo* to yield a dark yellow-brown residue. The resulting solids were washed with THF (3 x 5 mL) to yield the title compound as a yellow-orange solid. The filtrate was concentrated and pentane was allowed to slowly diffuse onto the solution to precipitate additional material (0.125 g, 29%). Yellow-orange crystals suitable for XRD were grown from slow diffusion of pentane into a concentrated THF solution at 25 °C. ^{1}H and ^{31}P NMR in C_6D_6 at 25 °C were

silent. μ_{eff} (THF, Evans method, 298 K): 3.3μ_B. Anal. Calcd. for $C_{59}H_{61}NP_3S_3SiV$: C, 67.34; H, 5.84; N, 1.33. Found: C, 66.52, H, 6.00; N, 1.23. UV-Vis (THF, 298 K, nm {cm^{-1} M^{-1}}): 462 {3600}. ESI-MS (positive ion, amu): Calc (M^+): 1051.2388, Found: 1051.2361.

5.4.2.5 Synthesis of V-(μ-SAr)-Fe(N_2)(H) (5.8)

A solution of **5.7** (44.9 mg, 0.043 mmol) in THF (10 mL) was added to solid $FeBr_2$ (10.1 mg, 0.047 mmol) and stirred at 25 °C for 1 h to yield an orange solution. The volatiles were subsequently removed under reduced pressure, and the remaining orange solid was suspended in Et_2O (5 mL) and allowed to stir for 10 min at 23 °C. The volatiles were removed *in vacuo*, and the resulting dark orange solid was dissolved in 10 mL of benzene and added to Na(Hg) amalgam (2.1 mg of Na, 0.091 mmol). The reaction was allowed to vigorously stir at 25 °C for 2 h, which yielded a dark orange-brown solution. The solution was filtered through Celite and lyophilized. The resulting material was washed with pentane (3 x 5 mL) and extracted with diethyl ether (10 mL) to afford the title complex as a dark orange-brown solid (26.7 mg, 55% yield). Dark orange-brown crystals were grown from slow concentration of a solution of **5.8** (3 mL Et_2O with *ca.* 100 μL pyridine) at -35 °C. ^1H and ^{31}P NMR in C_6D_6 at 25 °C were silent. μ_{eff} (C_6D_6, Evans method, 298 K): 3.1μ_B. μ_{eff} (toluene-d_8, Evans method, 223K): 3.3μ_B. Anal. Calcd. for $C_{59}H_{61}FeN_3P_3S_3SiV$: C, 62.37; H, 5.41; N, 3.70. Found: C, 62.58; H, 5.45; N, 1.73 (Note: low nitrogen content may be due to lability of the coordinated N_2). UV-Vis (THF, 298 K, nm {cm^{-1} M^{-1}}): 446 {5100}, 613 {2700}, 726 {2600}. IR (solid, cm^{-1}): 2054 (N_2), 1898 (Fe–H).

5.4.2.6 Synthesis of $^{Ph}PS_3V$(THF)

A solution of $VMes_3$(THF) (30.1 mg, 0.063 mmol) in THF (5 mL) was added dropwise to a stirring solution of $^{Ph}PS_3H_3$ (36.8 mg, 0.063 mmol) in THF (5 mL) at 25 °C. The reaction was stirred for 2 h, and the volatiles were subsequently removed *in vacuo*. The resulting yellow-brown solid was washed with pentane (3 x 5 mL) and Et_2O (5 mL). The solids were dissolved in THF and filtered through Celite. The solution was concentrated to yield the product as a yellow-orange solid (35.0 mg, 79% yield). The product was recrystallized in a

THF/pentane vapor diffusion cell at 25 °C, which yielded yellow-orange crystals suitable for XRD. ^{1}H and ^{31}P NMR in C_6D_6 at 25 °C were silent. μ_{eff} (C_6D_6, Evans method, 298 K): 2.6μ_B. Anal. Calcd. for $C_{40}H_{32}OPS_3V$: C, 67.97; H, 4.56; N, 0.00. Found: C, 68.04; H, 4.88; N, −0.08. UV-Vis (THF, 298 K, nm {cm^{-1} M^{-1}}): 462 {3800}.

5.4.2.7 Synthesis of $^{Ph}PS_3V(py)$ (5.11)

Pyridine (*ca*. 100 μL) was added to a solution of $^{Ph}PS_3V(THF)$ (0.040 g, 0.056 mmol) in benzene (10 mL) and stirred at 25 °C overnight. The reaction mixture was lyophilized to yield the title compound as a yellow-orange solid. The product was recrystallized in a C_6H_6/pentane vapor diffusion cell at 25 °C, which yielded yellow-orange crystals suitable for XRD. ^{1}H and ^{31}P NMR in C_6D_6 at 25 °C were silent. μ_{eff} (C_6D_6, Evans method, 298 K): 2.4μ_B. Anal. Calcd. for $C_{41}H_{29}NPS_3V$: C, 68.99; H, 4.10; N, 1.96. Found: C, 68.89; H, 4.26; N, 1.94. UV-vis (THF, 298 K, nm {cm^{-1} M^{-1}}): 464 {4800}.

5.4.3 Quantification of H_2 from the protonation of compound 5.8

A solution of $[H(OEt_2)][BAr^F_4]$ in Et_2O (2.4 mM, 1.0 mL) was added dropwise to a stirring solution of **5.8** in Et_2O (1.2 mM, 2.0 mL) in a septum-sealed round bottom, yielding a dark red solution. The solution was stirred at 25 °C for 10 min, then an aliquot of the headspace was sampled and analyzed for H_2 by GC. Yield of H_2: 91%

5.4.4 General procedure for catalytic hydrazine disproportionation

Caution: All catalytic runs were performed on small scales to avoid a significant buildup of pressure from gas generated during catalysis

A solution of catalyst (1 mM catalyst, 2.5 mL solvent, unless otherwise noted) is transferred into a Schlenk tube and frozen. Neat N_2H_4 is added in one portion to the vessel, which is then immediately sealed and allowed to stir at 25 °C. After the appropriate amount of time elapsed, the volatiles are vacuum transferred into a Schlenk tube containing HCl (2M in Et_2O, 5 mL), which is analyzed for ammonia content (in the form of $[NH_4][Cl]$) by the indophenol method.[26] (*Note: Upon thawing of the evacuated frozen vessels, care is taken to allow the

vacuum transfer to proceed at 25 °C. Hydrazine is a thermally-sensitive compound, and heating a vessel containing solely N_2H_4 in THF during the work-up results in positive ammonia detection)

D.5.6 Toepler pump quantification of gaseous products

Neat N_2H_4 (0.1 mmol) was added in one portion at 25 °C to a stirring Et2O solution of **5.8** (2.4 mg, 0.002 mmol) in a 100 mL Kontes Schlenk tube equipped with a ground-glass side arm. The tube was degassed via three freeze-pump-thaw cycles and sealed. The reaction mixture stirred at 25 °C under static vacuum. The volatiles in the tube were passed through a cold trap (77 K), and the non-condensed gaseous products were quantified with a Toepler pump. The frozen volatiles condensed in the traps were vacuum transferred into a Schlenk tube containing an ethereal solution of HCl (5 mL, 2 M) and concentrated to dryness. The resulting material was quantified for ammonia (in the form of $[NH_4][Cl]$) via the indophenol method.[26] Omitting the equivalent of N_2 that is introduced from **5.8**, 4.0 molecules of NH_3 per gas molecule was generated.

5.5 References

(1) (a) Sippel, D.; Einsle, O. *Nat. Chem. Bio.* **2017**, *13*, 956-960. (b) Spatzal, T.; Aksoyoglu, M.; Zhang, L.; Andrade, S. L. A.; Schleicher, E.; Weber, S.; Rees, D. C.; Einsle, O. *Science* **2011**, *334*, 940.

(2) (a) Eady, R. R. *Chem. Rev.* **1996**, *96*, 3013-3030. (b) Hu, Y.; Ribbe, M. W. *J. Biol. Inorg. Chem.* **2015**, *20*, 435-445.

(3) (a) Sippel, D; Rohde, M.; Netzer, J.; Trncik, C.; Gies, J.; Grunau, K.; Djurdjevic, I.; Decamps, L.; Andrade, S. L. A.; Einsle, O. *Science* **2018**, *359*, 1484-1489. (b) Benediktsson, B.; Thorhallsson, A. T.; Bjornsson, R. *Chem. Commun.* **2018**, *54*, 7310-7313.

(4) Sekiguchi, Y.; Arashiba, K.; Tanaka, H.; Eizawa, A.; Nakajima, K.; Yoshizawa, K.; Nishibayashi, Y. *Angew. Chemie. Int. Ed.* **2018**, *57,* 9064-9068.

(5) (a) For representative examples see: Anderson, J. S.; Rittle, J.; Peters, J. C. *Nature* **2013**, *501*, 84-87. (b) Ung, G; Peters, J. C. *Angew. Chemie. Int. Ed.* **2015**, *54*, 532-535. (c)

Kuriyama, S.; Arashiba, K.; Nakajima, K.; Matsuo, Y.; Tanaka, H.; Ishii, K.; Yoshizawa, K.; Nishibayashi, Y. *Nat. Commun.* **2016**, *7*, 12181. (d) Hill, P. J.; Doyle, L. R.; Crawford, A. D.; Myers, W. K.; Ashley, A. E. *J. Am. Chem. Soc.* **2016**, *138*, 13521-13524. (e) Buscagan, T. M.; Oyala, P. H.; Peters, J. C. *Angew. Chem. Int. Ed.* **2017**, *56*, 6921-6926. (f) Creutz, S. E.; Peters, J. C. *J. Am. Chem. Soc.* **2014**, *136*, 1105-1115. (g) Chalkley, M. J.; Del Castillo, T. J.; Matson, B. D.; Roddy, J. P.; Peters, J. C. *ACS Cent. Sci.* **2017**, *3*, 217-223. (h) Chalkley, M. J.; Del Castillo, T. J.; Matson, B. D.; Peters, J. C. *J. Am. Chem. Soc.* **2018**, *140*, 6122-6129.

(6) (a) Malinak, S. M.; Demadis, K. D.; Coucouvanis, D. *J. Am. Chem. Soc.* **1995**, *117*, 3126-3133. (b) Coucouvanis, D.; Demadis, K. D.; Malinak, S. M.; Mosier, P. E.; Tyson, M. A.; Laughlin, L. J. *J. Mol. Catal. A: Chem.* **1996**, *107*, 123-135.

(7) Dilworth, M. J.; Eady, R. R. *Biochem. J.* **1991**, *277*, 465-468.

(8) Davis, L. C. *Arch. Biochem. Biophys.* **1980**, *204,* 270-276.

(9) (a) Kuwata, S.; Mizobe, Y.; Hidai, M. *Inorg. Chem.* **1994**, *33*, 3619-3620. (b) Takei, I.; Dohki, K.; Kobayashi, K.; Suzuki, T.; Hidai, M. *Inorg. Chem*. **2005**, *44*, 3768-3770. (c) Umehara, K.; Kuwata, S.; Ikariya, T. *J. Am. Chem. Soc.* **2013**, *135*, 6754-6757. (d) Hitchcock, P. B.; Hughes, D. L.; Maguire, M. J.; Marjani, K.; Richards, R. L. *J. Chem. Soc., Dalton Trans.* **1997**, 4747-4752. (e) Wu, B.; Gramigna, K. M.; Bezpalko, M. W.; Foxman, B. M.; Thomas, C. M. *Inorg. Chem.* **2015**, *54*, 10909-10917. (f) Malinak, S. M.; Coucouvanis, D. *Prog. Inorg. Chem.* **2001**, *49*, 599-662. (g) Block, E.; Ofori-Okai, G.; Kang, H.; Zubieta, J. *J. Am. Chem. Soc.* **1992**, *114*, 758-759. (h) Under photolysis, $[Mo(CN)_8]^{4-}$ was demonstrated to catalyze N_2H_4 disproportionation with yields of $>10^3$ equivalents of NH_3. See: Szkiarzewicz, J.; Matoga, D.; Klyś, A.; Łasocha, W. *Inorg. Chem.* **2008**, *47*, 5464-5472. (i) Saouma, C. T.; Moore, C. E.; Rheingold, A. L.; Peters, J. C. *Inorg. Chem.* **2011**, *50*, 11285-11287.

(10) Creutz, S. E.; Peters, J. C. *J. Am. Chem. Soc.* **2015**, *137*, 7310-7313.

(11) Mankad, N. P.; Whited, M. T.; Peters, J. C. *Angew. Chem. Int. Ed.* 2007, **46**, 5768-5771.

(12) (a) Chang, Y.-H.; Su, C.-L.; Wu, R.-R.; Liao, J.-H.; Liu, Y.-H.; Hsu, H.-F. *J. Am. Chem. Soc.* **2011**, *133*, 5708-5711. (b) Hsu, H.-F.; Chu, W.-C.; Hung, C.-H.; Liao, J.-H. *Inorg.*

Chem. **2003**, *42*, 7369-7371. (c) Ye, S.; Neese, F.; Ozarowski, A.; Smirnov, D.; Krzystek, J.; Telser, J.; Liao, J.-H.; Hung, C.-H.; Chu, W.-C.; Tsai, Y.-F.; Wang, R.-C.; Chen, K.-Y.; Hsu, H.-F. *Inorg. Chem.* **2010**, *49*, 977-988. (d) Chu, W.-C.; Wu, C.-C.; Hsu, H.-F. *Inorg. Chem.* **2006**, *45*, 3164-3166.

(13) Gu, N. X.; Oyala, P. H.; Peters, J. C. *J. Am. Chem. Soc.* **2018**, *140*, 6374-6382.

(14) Takaoka, A; Mankad, N. P.; Peters, J. C. *J. Am. Chem. Soc.* **2011**, *133*, 8440-8443.

(15) For reference, the Fe–H stretches of **5.9** and **5.10** are 1910 cm^{-1} and 1852 cm^{-1}, respectively.

(16) Volatiles from a catalytic run performed in Et_2O were passed through a 77 K cold trap, and the remaining gas was quantified with a Toepler pump. The ammonia content from the same run was also determined. Representative IR data of catalyst mixtures after turnover do not reveal any Fe–N_2 stretches, indicating that the bound N_2 of **5.8** dissociates during catalysis (see Fig. D.2.4). Omitting the equivalent of N_2 that is introduced into the headspace from **5.8**, a ratio of 4.0 NH_3 molecules per gas molecule is generated, consistent with the anticipated ratios for hydrazine disproportion (3 $N_2H_4 \rightarrow$ 4 NH_3 + N_2).

(17) Carrying out entry C in the presence of elemental Hg or PPh_3 (0.3 equiv./ **5.8**) demonstrated no significant attenuation of catalytic activity. (Hg: 46 equiv. NH_3/**5.8**; PPh_3: 42 equiv. NH_3/**5.8**)

(18) Milsmann, C.; Semproni, S. P.; Chirik, P. J. *J. Am. Chem. Soc.* **2014**, *136*, 12099-12107.

(19) The catalytic runs in Table 5.2 were performed in THF rather than Et_2O because of the poor solubility of **5.9** in Et_2O.

(20) Although complex **5.8** is a more active catalyst in Et_2O, the reaction order on N_2H_4 and **5.8** were determined in THF because it is miscible with hydrazine.

(21) (a) Tang, H. R.; Stanbury, D. M. *Inorg. Chem.* **1994**, *33*, 1388-1391. (b) Wiberg, E.; Wiberg, N. *Inorganic Chemistry*, Academic Press: San Diego, CA, 2001. (c) Wiberg, N.; Bachhuber, H.; Fischer, G. *Angew. Chem. Int. Ed.* **1972**, *11*, 829-830.

(22) McGinley, P. L.; Koh, J. T. *J. Am. Chem. Soc.* **2007**, *129*, 3822-3823.

(23) Seidel, V. W.; Kreisel, G. *Z. anorg. allg. Chem.* **1977**, *435*, 146-152.

(24) Hoang, T. K. A.; Hamaed, A.; Moula, G.; Aroca, R.; Trudeau, M.; Antonelli, D. M. *J. Am. Chem. Soc.* **2011**, *133*, 4955-4964.

(25) Tsai, J.-C. Masters thesis, Stony Brook University, **2011**.

(26) Weatherburn, M. W. *Anal. Chem*. **1967**, *39*, 971-974.

A p p e n d i x A

SUPPLEMENTARY INFORMATION FOR CHAPTER 2

A.1 NMR Spectra

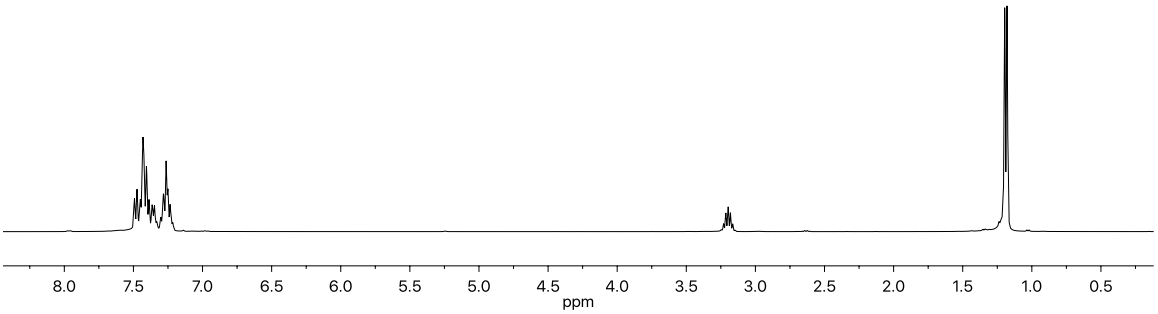

Figure A.1.1. ^{1}H NMR spectrum (400 MHz) of **2.2** in $CDCl_3$

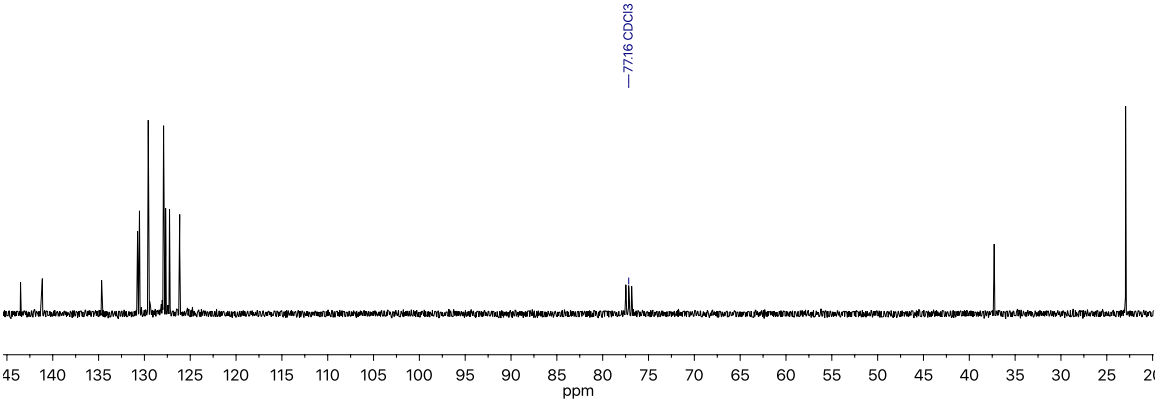

Figure A.1.2. ^{13}C NMR spectrum (101 MHz) of **2.2** in $CDCl_3$

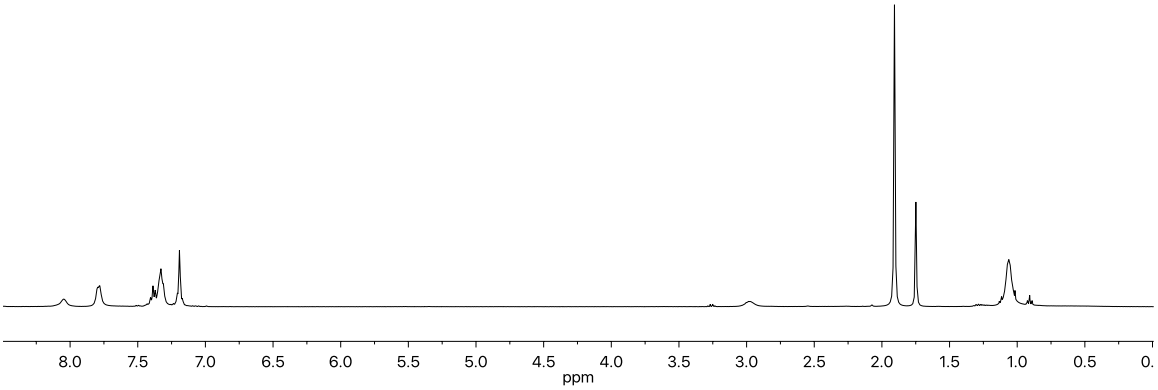

Figure A.1.3. ^{1}H NMR spectrum (400 MHz) of **2.3** in C_6D_6

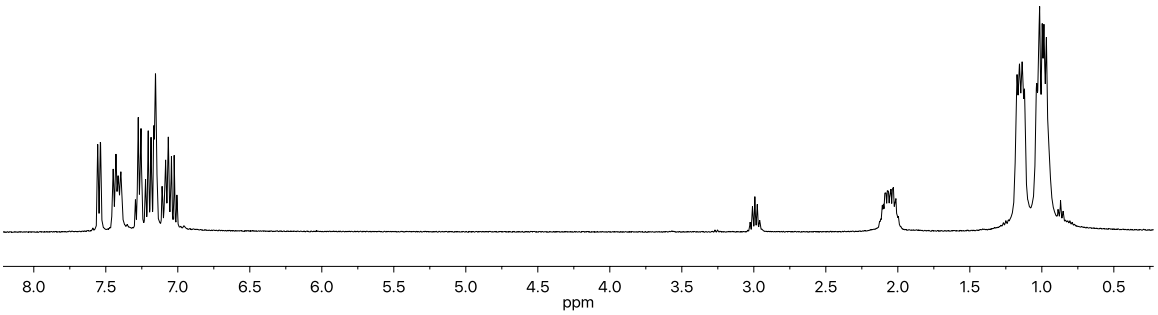

Figure A.1.4. ^{1}H NMR spectrum (400 MHz) of **2.5** in C_6D_6

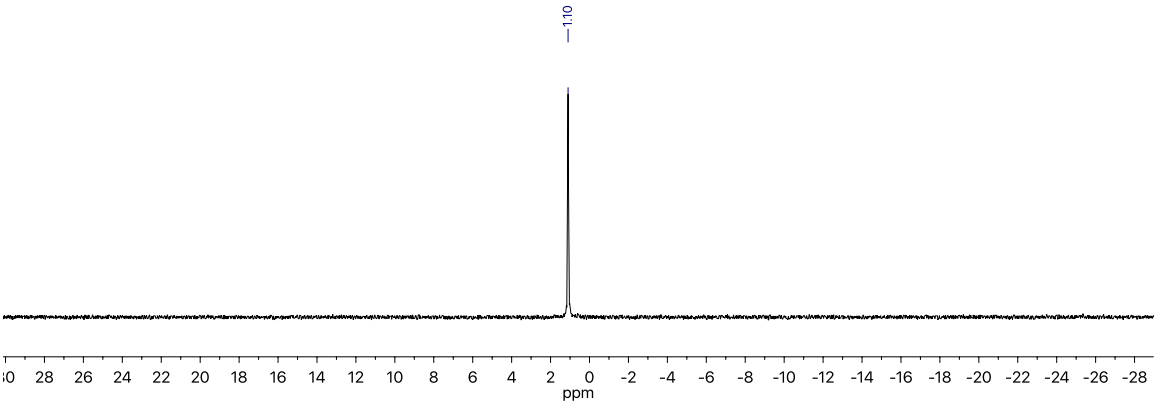

Figure A.1.5. ^{31}P NMR spectrum (162 MHz) of **2.5** in C_6D_6

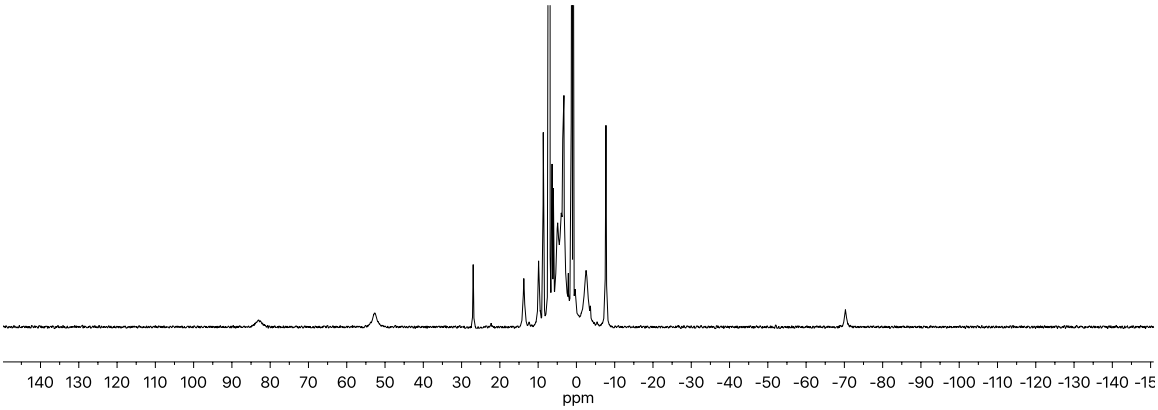

Figure A.1.6. ^{1}H NMR spectrum (300 MHz) of **2.6** in C_6D_6

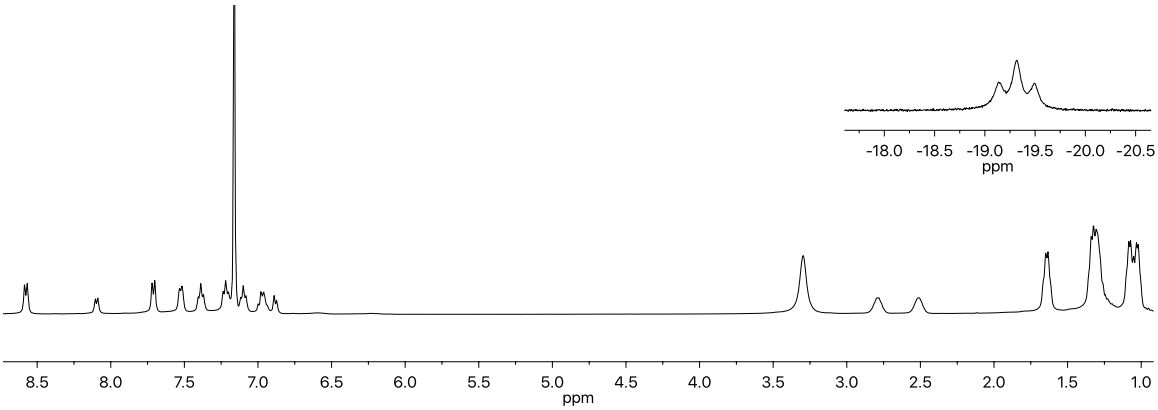

Figure A.1.7. ^{1}H NMR spectrum (300 MHz) of **2.7-H** in C_6D_6

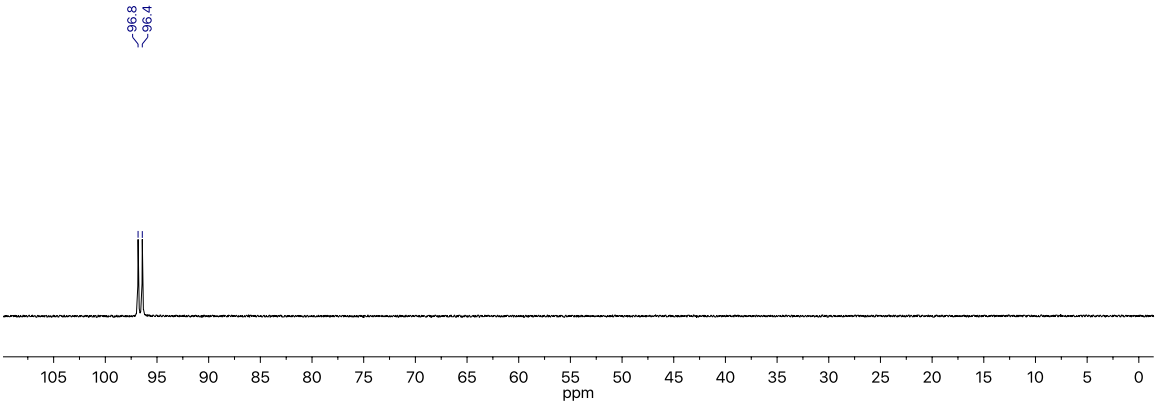

Figure A.1.8. ^{31}P NMR spectrum (162 MHz) of **2.7-H** in C_6D_6

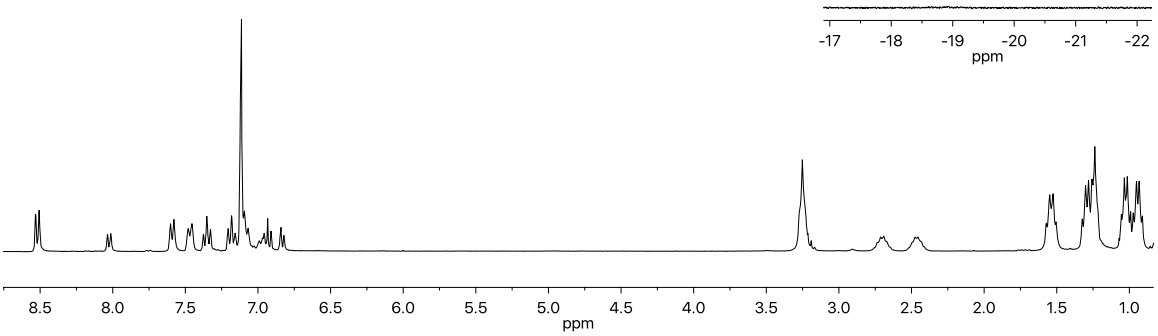

Figure A.1.9. ^{1}H NMR spectrum (300 MHz) of **2.7-D** in C_6D_6

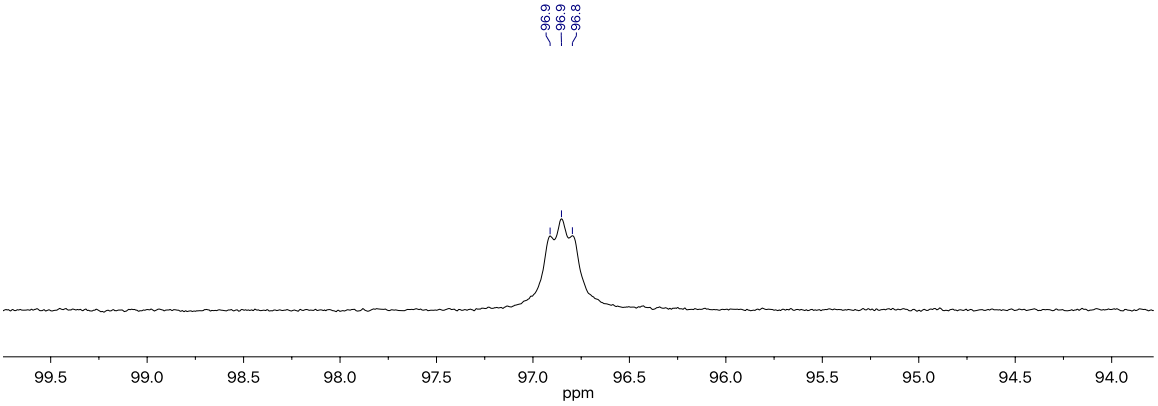

Figure A.1.10. ^{31}P NMR spectrum (162 MHz) of **2.7-D** in C_6D_6

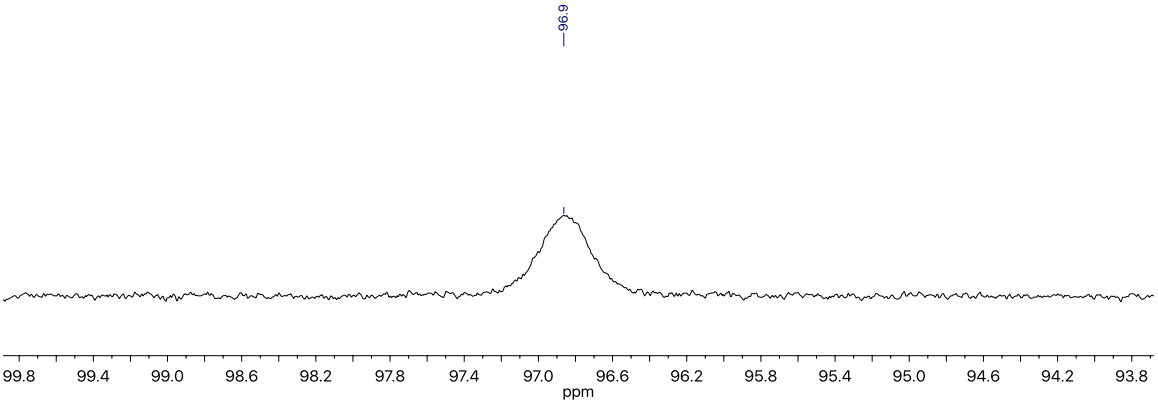

Figure A.1.11. $^{31}P\{^{2}H\}$ NMR spectrum (162 MHz) of **2.7-D** in C_6D_6

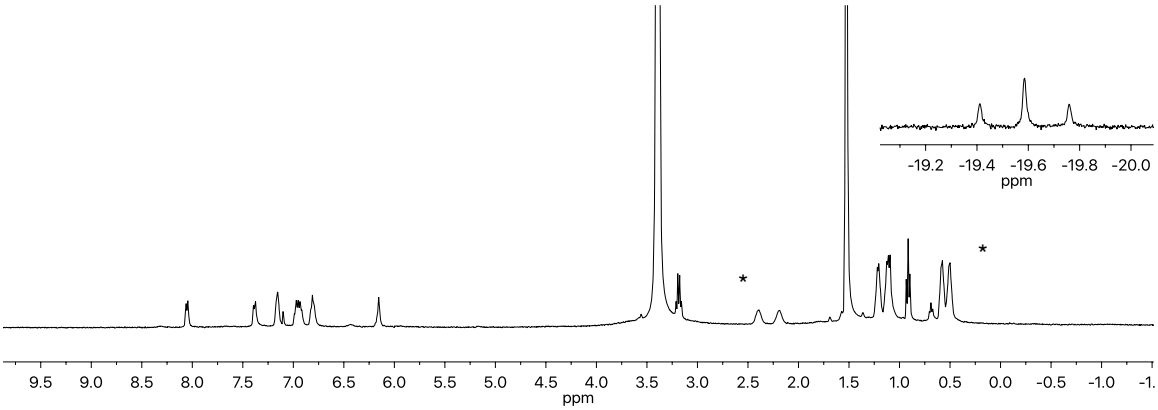

Figure A.1.12. ^{1}H NMR spectrum (400 MHz) of **2.7-H(crown)** in THF-d_8 (*Et_2O)

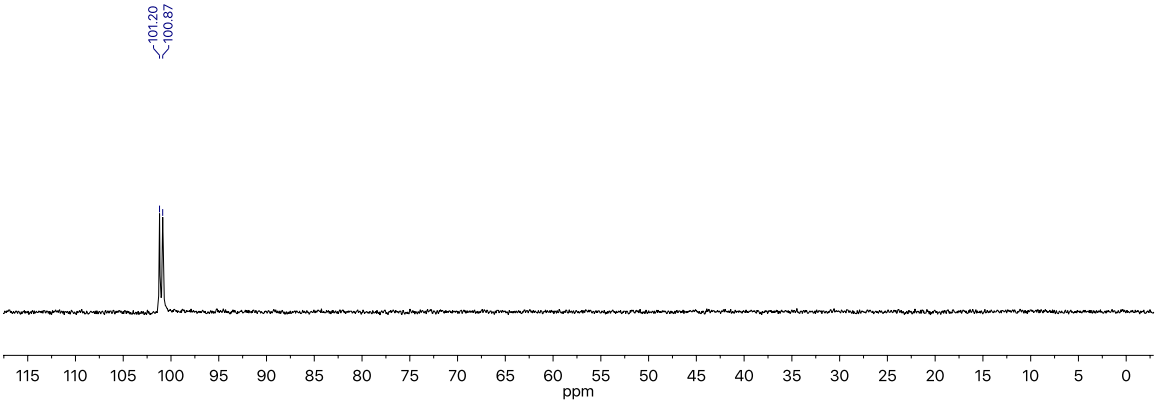

Figure A.1.13. ^{31}P NMR spectrum (162 MHz) of **2.7-H(crown)** in THF-d_8

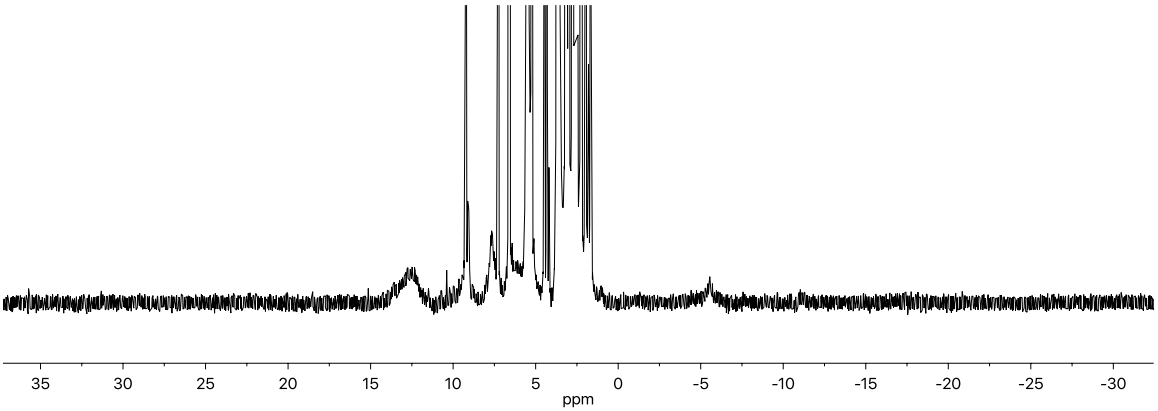

Figure A.1.14. ^{1}H NMR spectrum (500 MHz) of **2.8-H** in THF-d_8 (−78 ºC; generated in the presence of one equivalent of Cp_2Co)

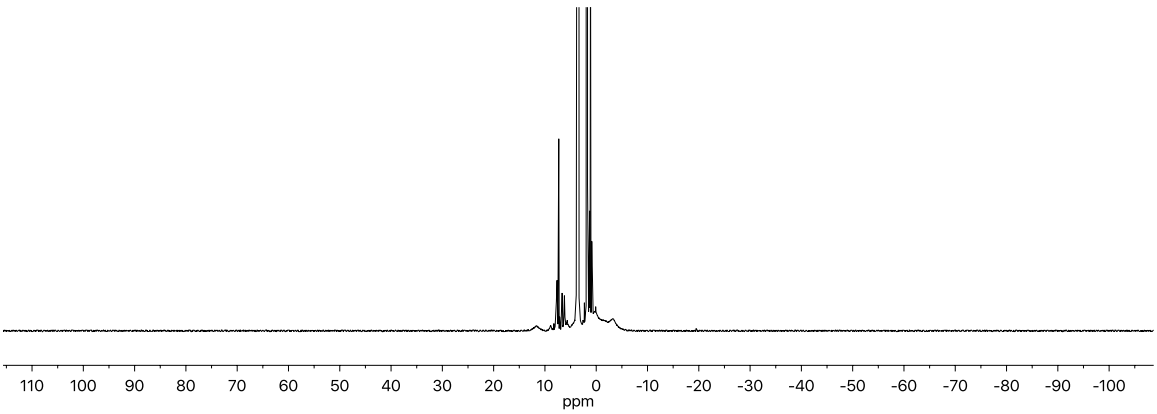

Figure A.1.15. ^{1}H NMR spectrum (400 MHz) of **2.9** in THF-d_8

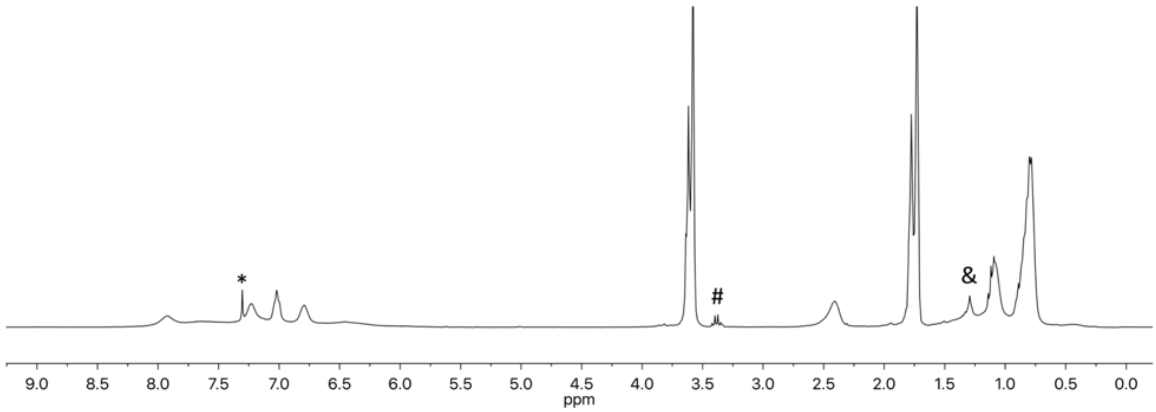

Figure A.1.16. ^{1}H NMR spectrum (300 MHz) of **2.10** in THF-d_8 (*C_6H_6, $^{\#}Et_2O$, $^{\&}$pentane)

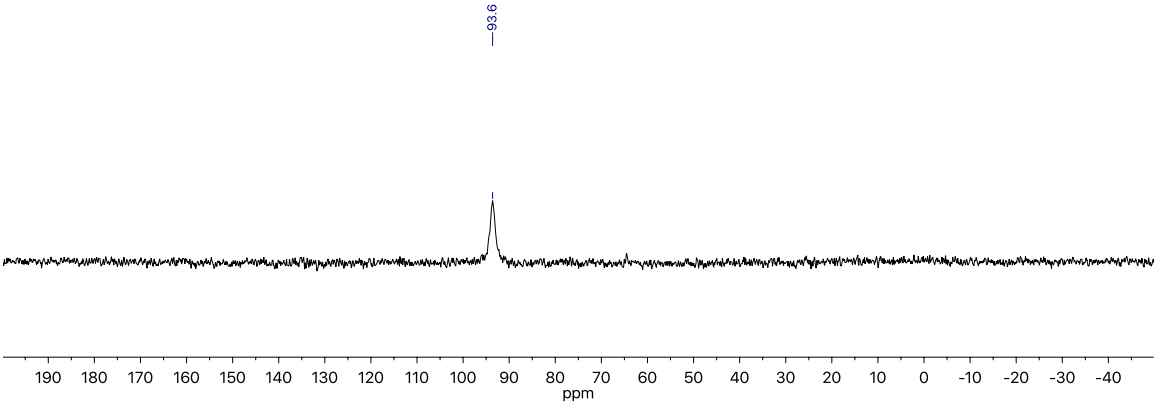

Figure A.1.17. ^{31}H NMR spectrum (121 MHz) of **2.10** in THF-d_8

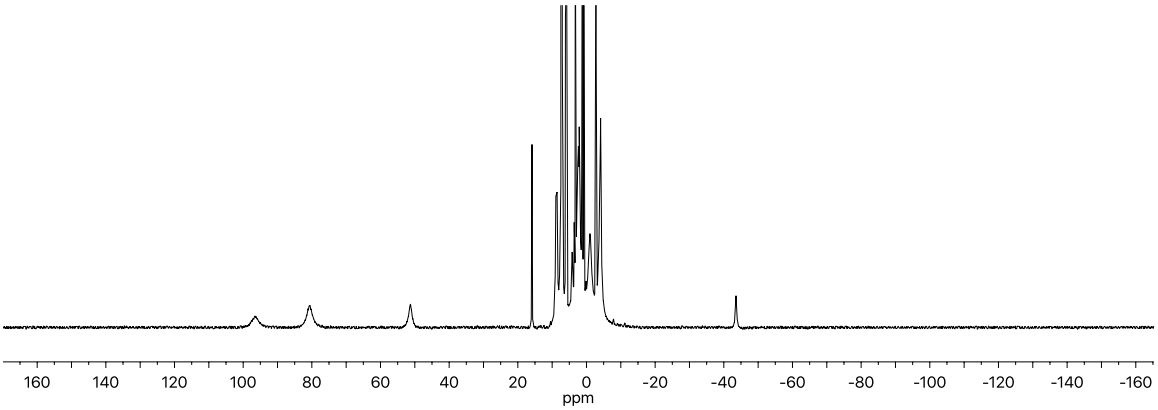

Figure A.1.18. ^{1}H NMR spectrum (400 MHz) of **2.11** in C_6D_6

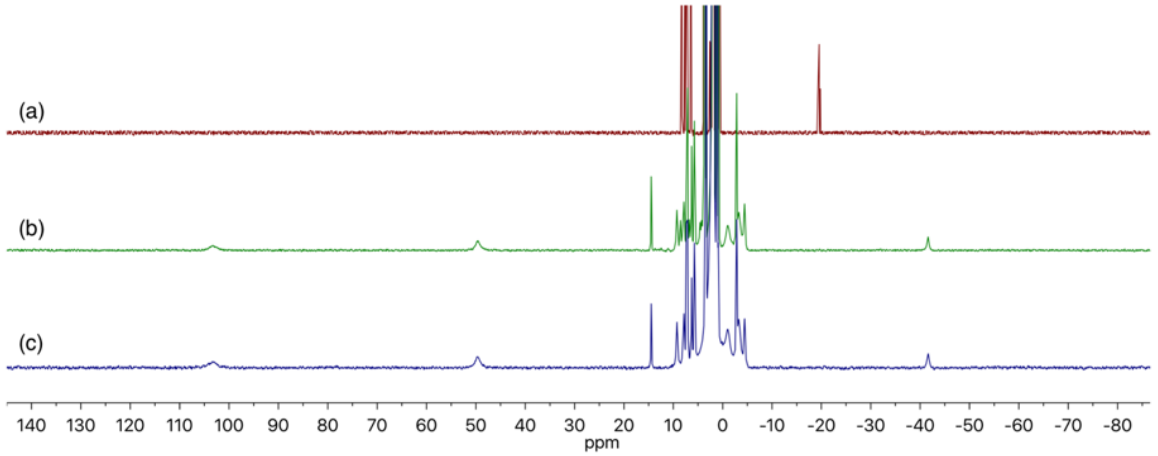

Figure A.1.19. ^{1}H spectra (300 MHz) of (a) complex **2.7-H(crown)** (b) reaction mixture of **2.7-H(crown)** under 1 atm of CO_2, collected 1 h after addition of CO_2 (c) complex **2.11** prepared from diiron **2.6**. All spectra collected in MeCN-d_3

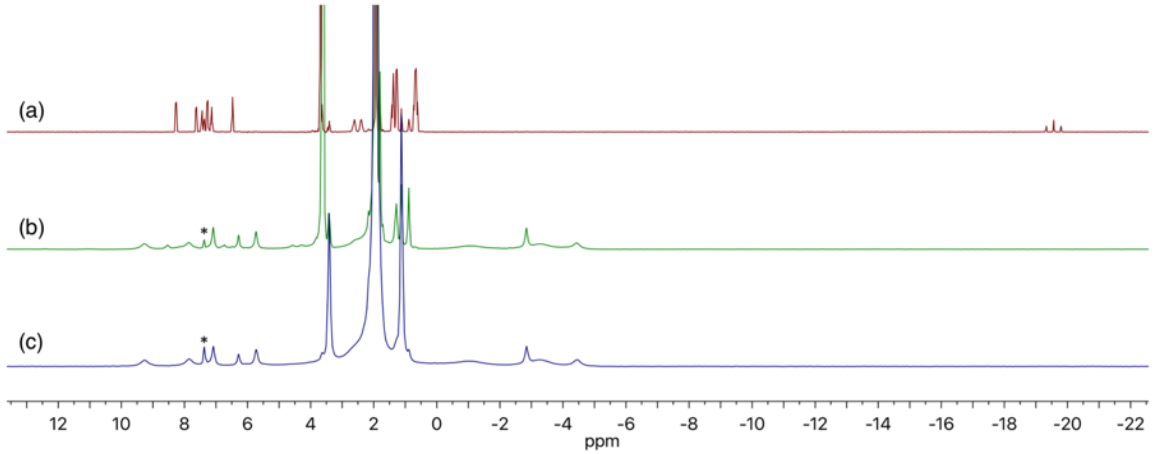

Figure A.1.20. Partial ^{1}H spectra (300 MHz) of (a) complex **2.7-H(crown)** (b) reaction mixture of **2.7-H(crown)** under 1 atm of CO_2, collected 1 h after addition of CO_2 (c) complex **2.11**. All spectra collected in MeCN-d_3 (* = C_6H_6)

A.2 IR Spectra

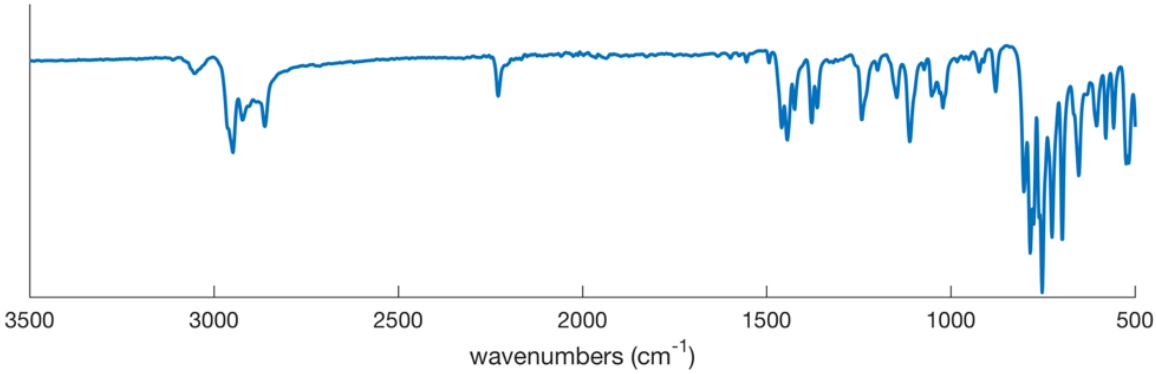

Figure A.2.1. IR spectrum of **2.5** (solid powder sample)

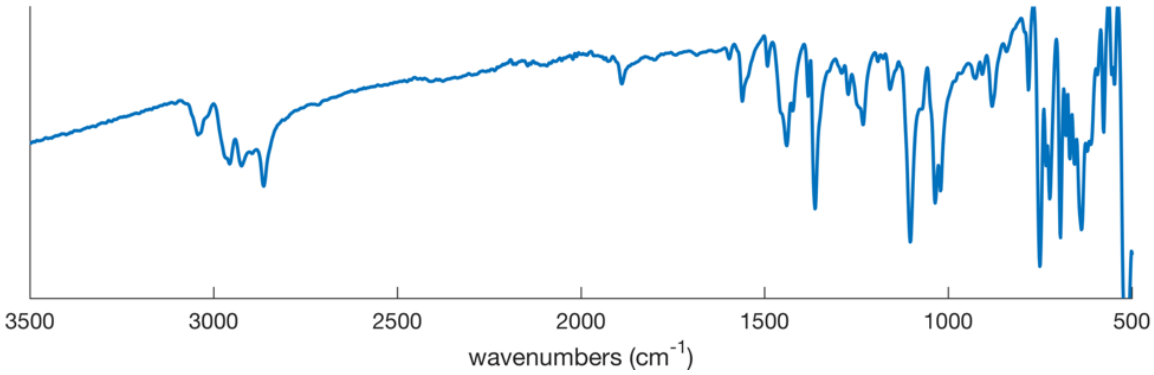

Figure A.2.2. IR spectrum of **2.6** (solid crystalline sample)

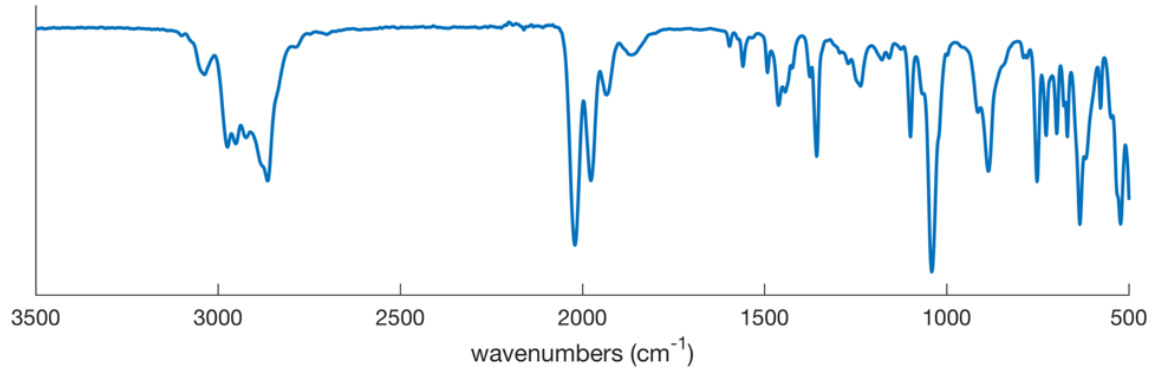

Figure A.2.3. IR spectrum of **2.7-H** (thin-film from THF solution)

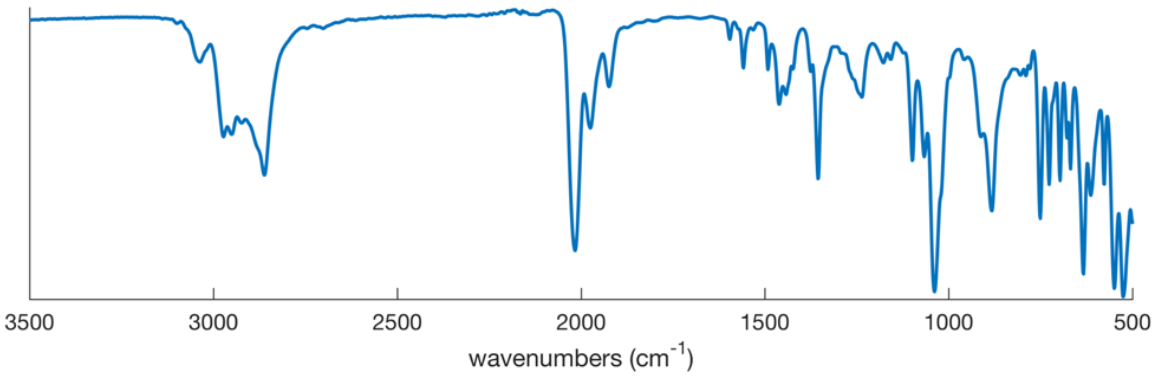

Figure A.2.4. IR spectrum of **2.7-D** (thin-film from THF solution)

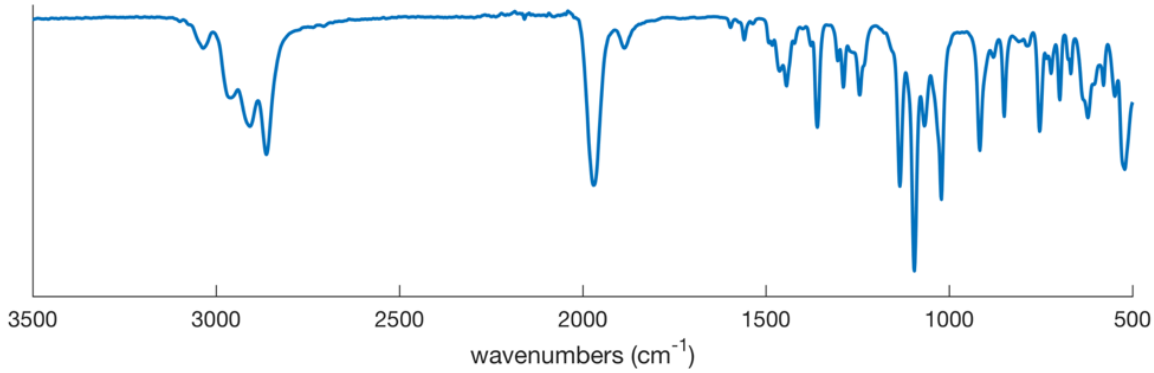

Figure A.2.5. IR spectrum of **2.7-H(crown)** (thin-film from THF solution)

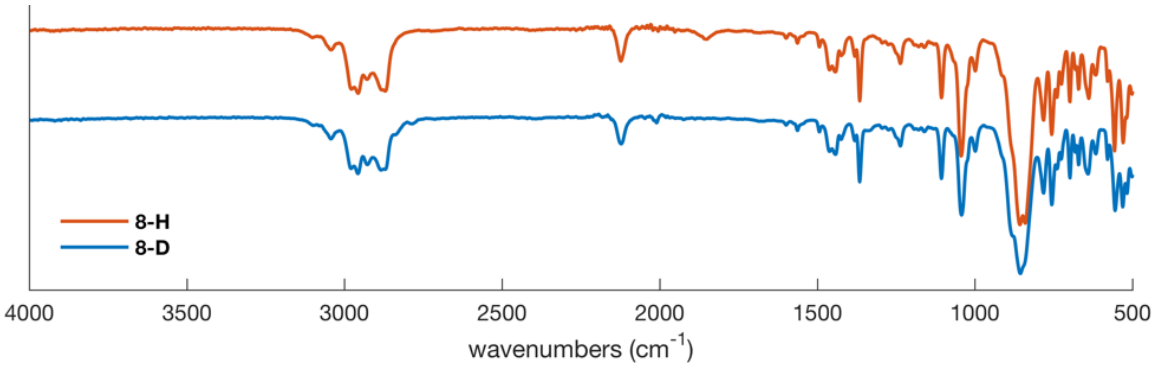

Figure A.2.6. IR spectrum of **2.8-H** and **2.8-D** (thin-film from THF solution; generated in the presence of one equivalent of Cp_2Co)

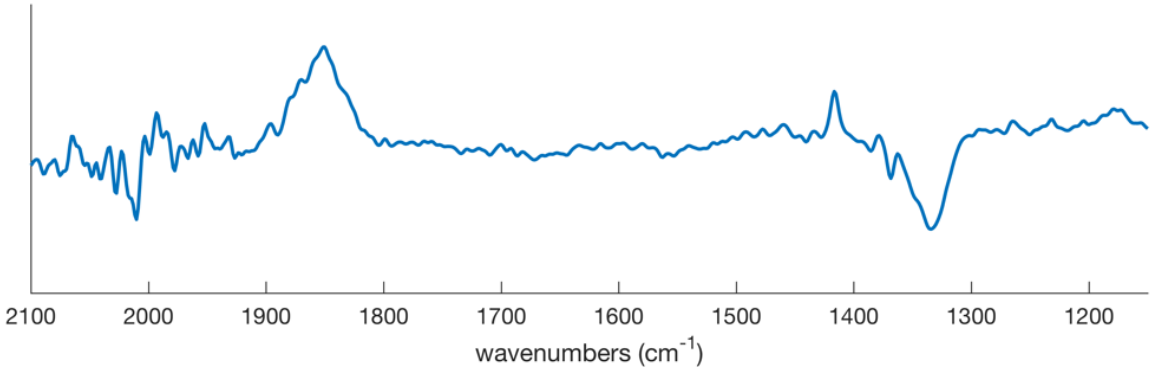

Figure A.2.7. IR difference spectrum of **2.8-H** and **2.8-D** exhibiting an Fe–D stretch at 1333 cm^{-1} and Fe–H stretch at 1852 cm^{-1}

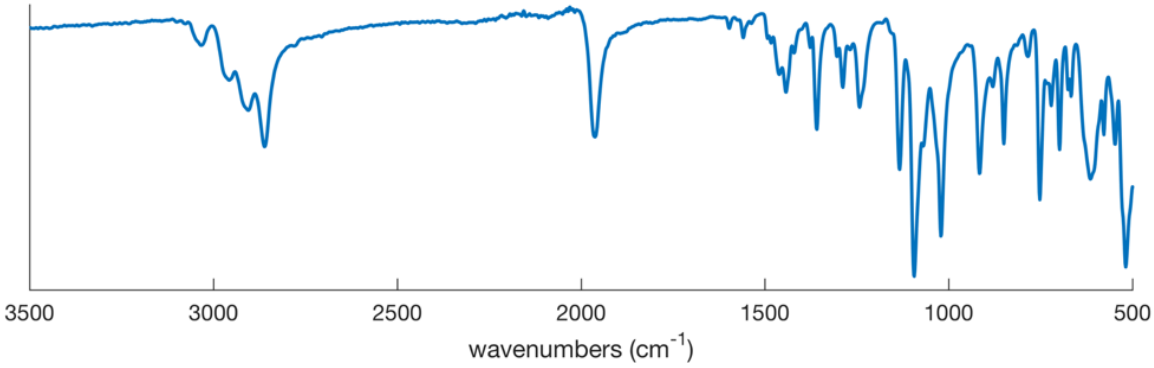

Figure A.2.8. IR spectrum of **2.9** (solid crystalline sample)

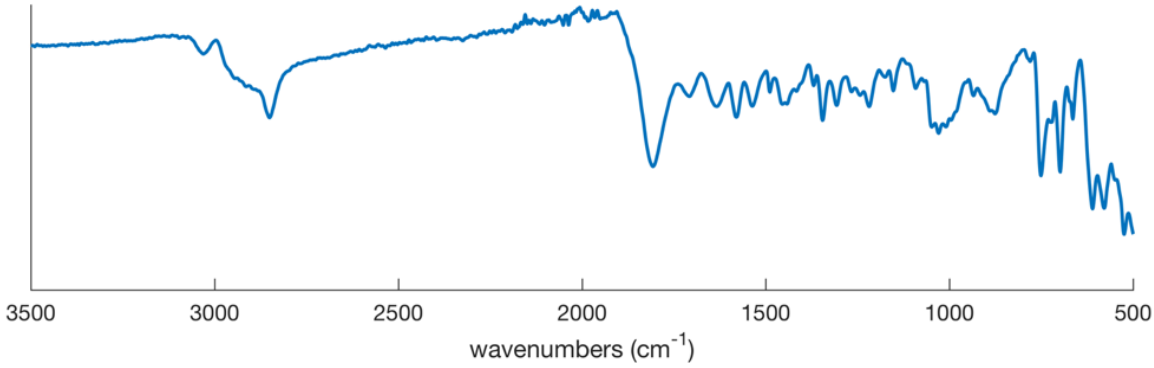

Figure A.2.9. IR spectrum of **2.10** (solid powder sample)

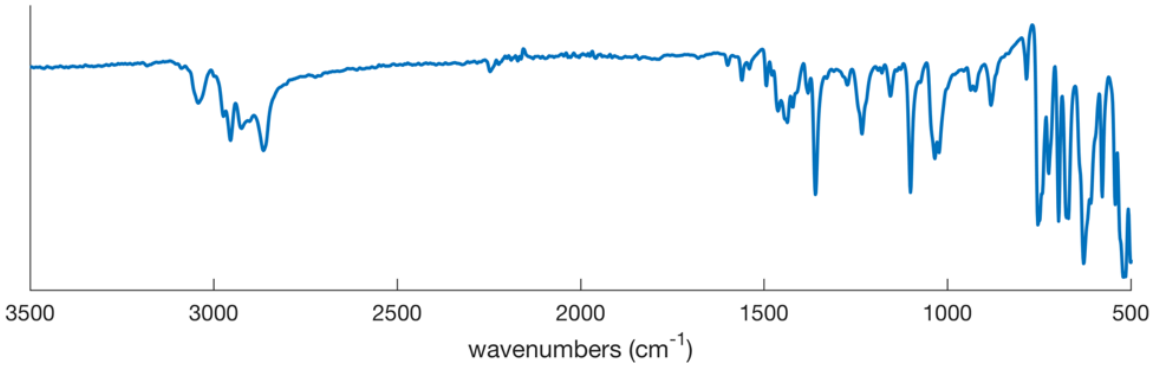

Figure A.2.10. IR spectrum of **2.11** (solid powder sample)

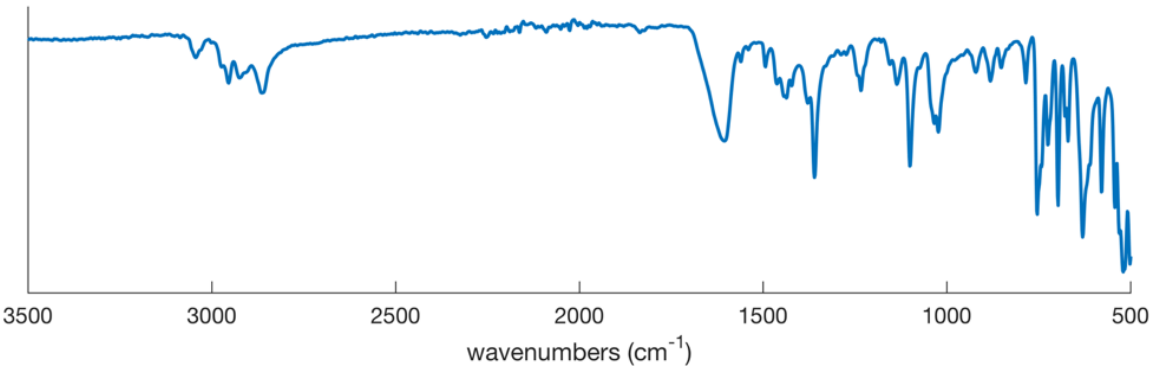

Figure A.2.11. IR spectrum of the reaction of **2.7-H(crown)** with CO_2 (solid powder sample)

A.3 X-Ray Diffraction

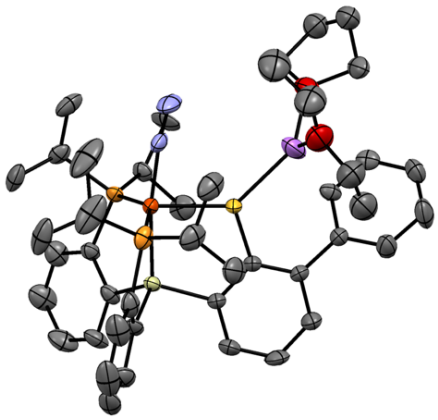

Figure A.3.1. X-ray structure of **2.7-H**. Hydrogen and disordered atoms omitted for clarity. Ellipsoids shown at 50% probability. Partial substitution of diethyl ether in place of THF was observed with regards to the solvent coordination at lithium, due to the crystals being grown from a diethyl ether solution.

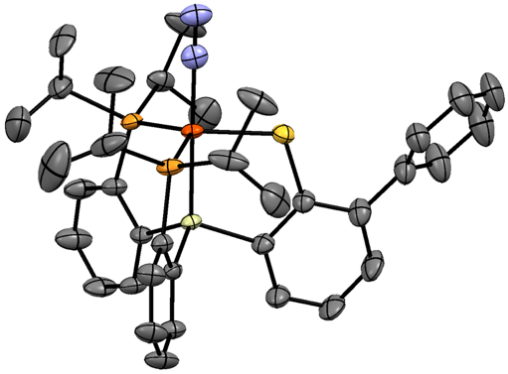

Figure A.3.2. Structure of **2.9** with omission of countercation, disordered components, hydrogen atoms and solvent molecules. Thermal ellipsoids at 50% probability.

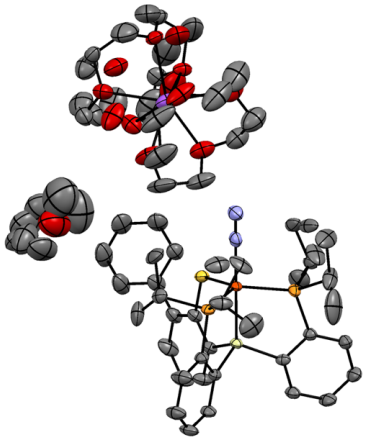

Figure A.3.3. Full asymmetric unit of **2.9** including solvent and disordered components. Hydrogen atoms omitted; thermal ellipsoids at 50% probability.

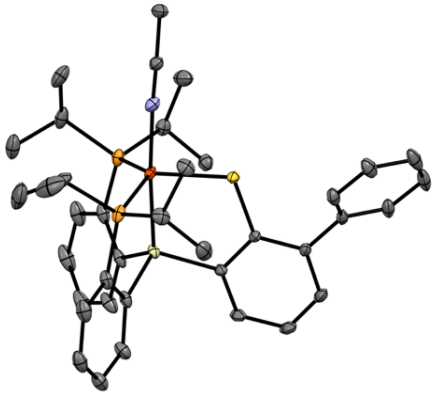

Figure A.3.4. Structure of **2.11** with omission of disordered components and hydrogen atoms. Thermal ellipsoids at 50% probability.

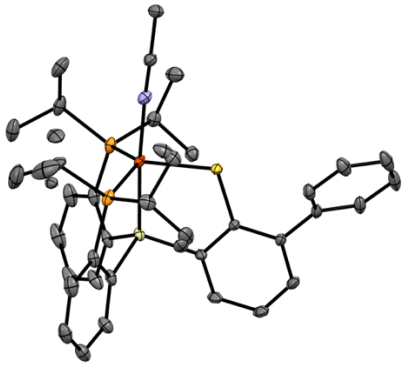

Figure A.3.5. Full asymmetric unit of **2.11** including disordered components. Hydrogen atoms omitted; thermal ellipsoids at 50% probability.

A.4 ^{57}Fe Mössbauer Spectra

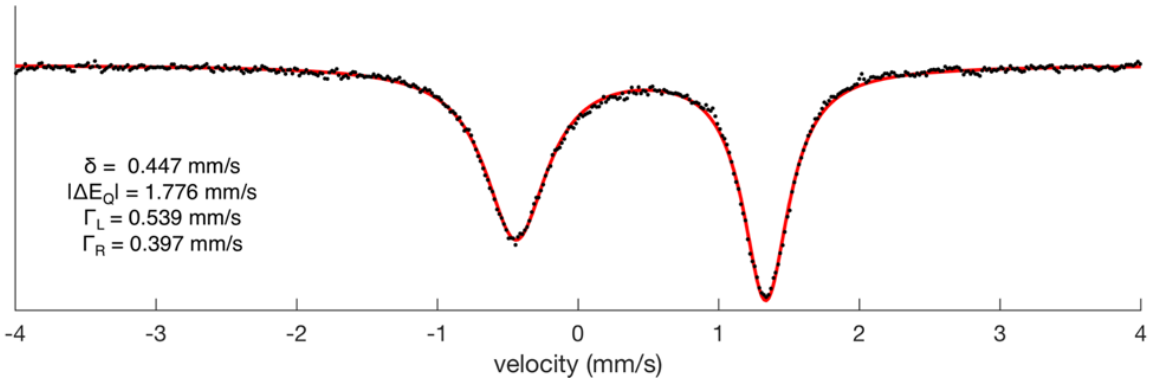

Figure A.4.1. 80K ^{57}Fe Mössbauer spectrum of **2.6** collected in the presence of a 50 mT magnetic field oriented parallel to the propagation of the γ-beam (solid sample suspended in boron nitride)

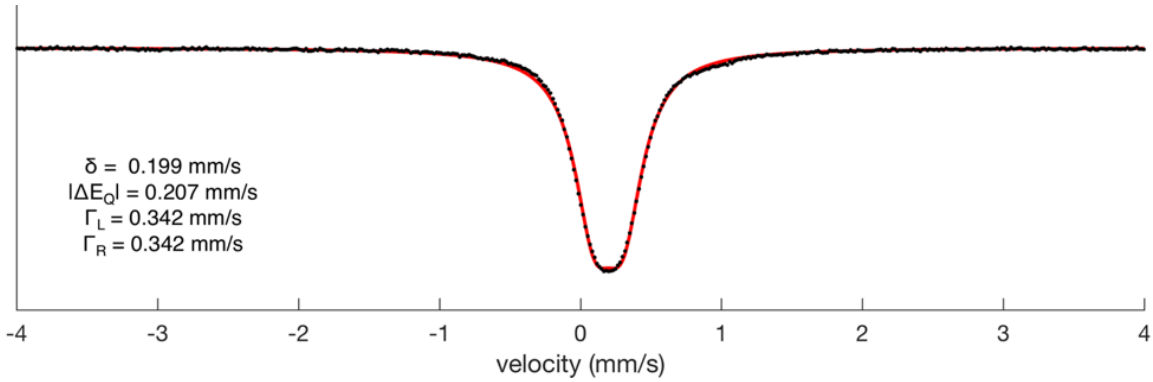

Figure A.4.2. 80 K ^{57}Fe Mössbauer spectrum of **2.7-H** collected in the presence of a 50 mT magnetic field oriented parallel to the propagation of the γ-beam (frozen solution sample in THF)

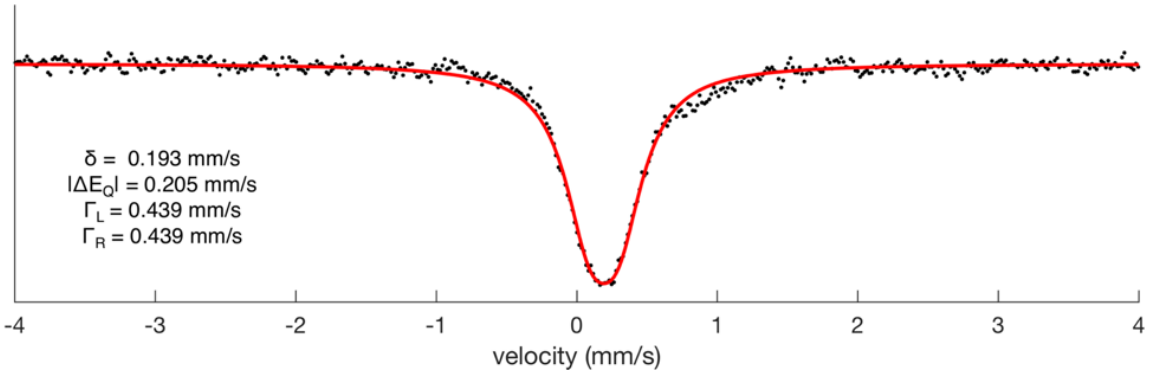

Figure A.4.3. 80K ^{57}Fe Mössbauer spectrum of **2.7-H(crown)** collected in the presence of a 50 mT magnetic field oriented parallel to the propagation of the γ-beam (solid sample suspended in boron nitride)

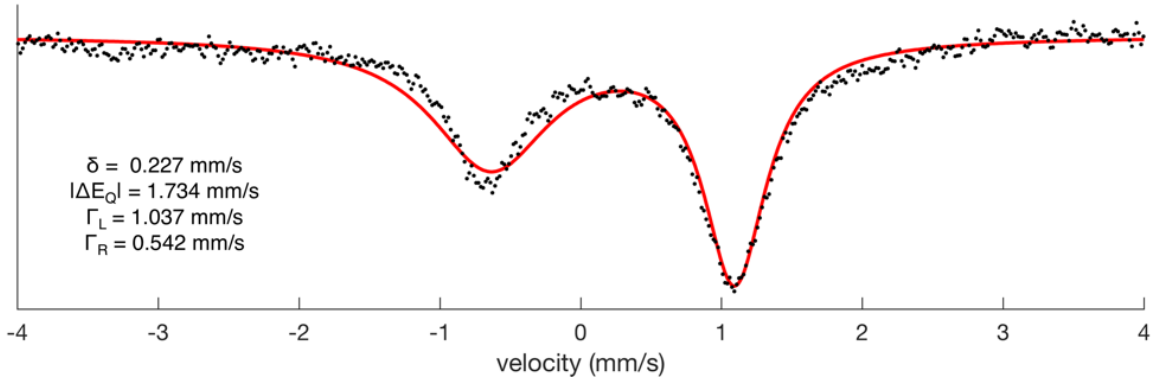

Figure A.4.4. 80K ^{57}Fe Mössbauer spectrum of **2.8-H** collected in the presence of a 50 mT magnetic field oriented parallel to the propagation of the γ-beam (solid sample suspended in boron nitride; generated in the presence of one equivalent of Cp_2Co)

A.5 EPR Spectra

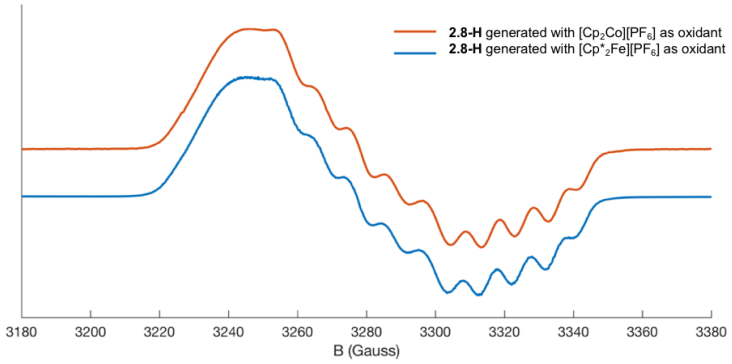

Figure A.5.1. 77 K X-band EPR spectra of **2.8-H** in 2-MeTHF, generated with $[Cp_2Co][PF_6]$ and $[Cp^*_2Fe][PF_6]$ as oxidants

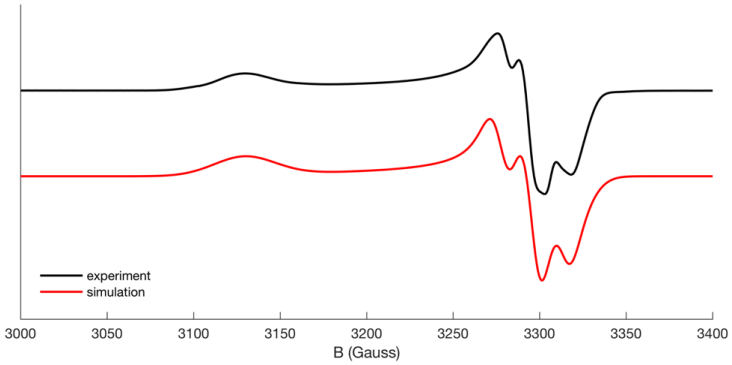

Figure A.5.2. 77K K X-band EPR spectra of **2.9** in 2-MeTHF with simulation (Sys.g = [2.1440 2.0350 2.0300], Sys.lw = 1.2, Sys.Nucs = '31P, 31P', Sys.A = [0 50 45; 0 50 45], Sys.HStrain = [120 0 60], Exp.mwFreq = 9.389)

A.6 ENDOR Spectroscopy

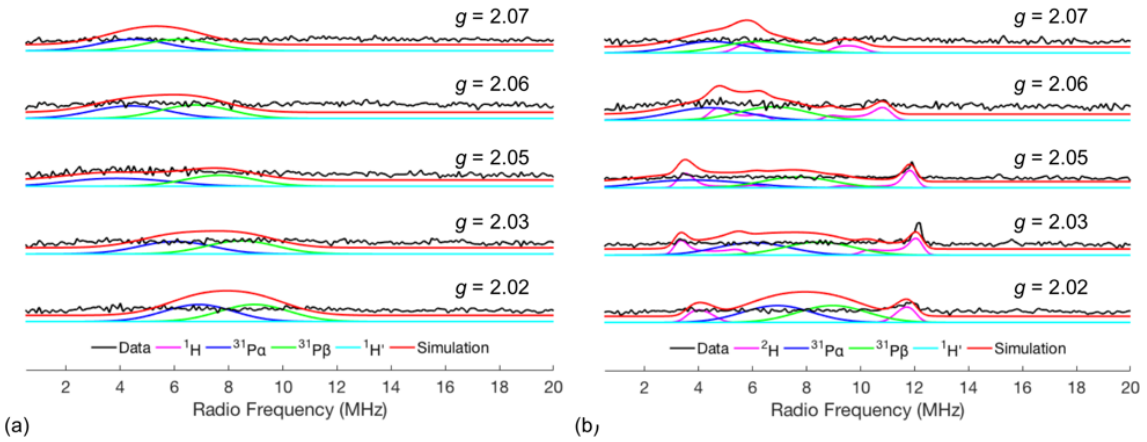

Figure A.6.1. Field-dependent Q-band Davies ENDOR of (a) **2.8-H** and (b) **2.8-D** in 2Me-THF with simulations (partial spectrum of Fig. 5ab). Summation of individual component ENDOR simulations is displayed in red. Experimental conditions: microwave frequency = 33.674 GHz; MW π pulse length = 40 ns; interpulse delay τ = 300 ns; π_{RF} pulse length = 15 µs; TRF delay = 1 µs; shot repetition time (srt) = 5 ms; temperature = 18.5 K; RF frequency randomly sampled. The simulated ^{31}P signals at lower frequencies have very low intensity in the experimental data, possibly as a product of the hyperfine enhancement effect and lower RF magnetic field intensity generated by the ENDOR coils at very low frequencies.

A.7 UV-Visible Spectra

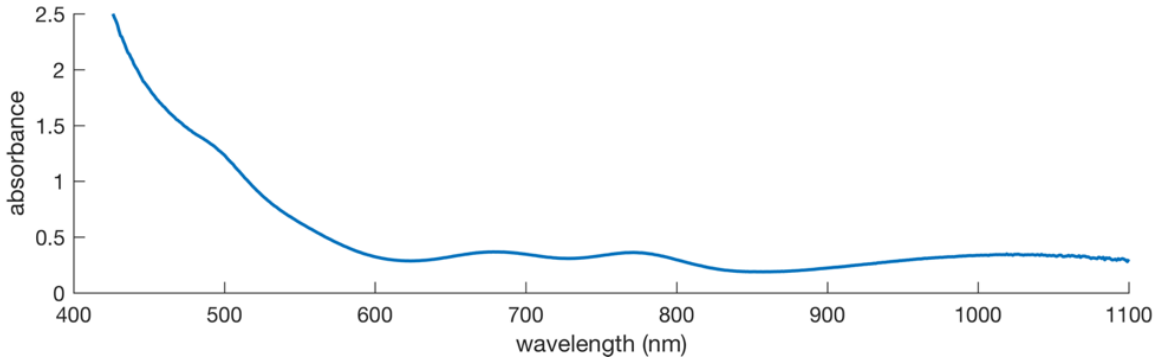

Figure A.7.1. UV-Vis spectrum of **2.6** in THF

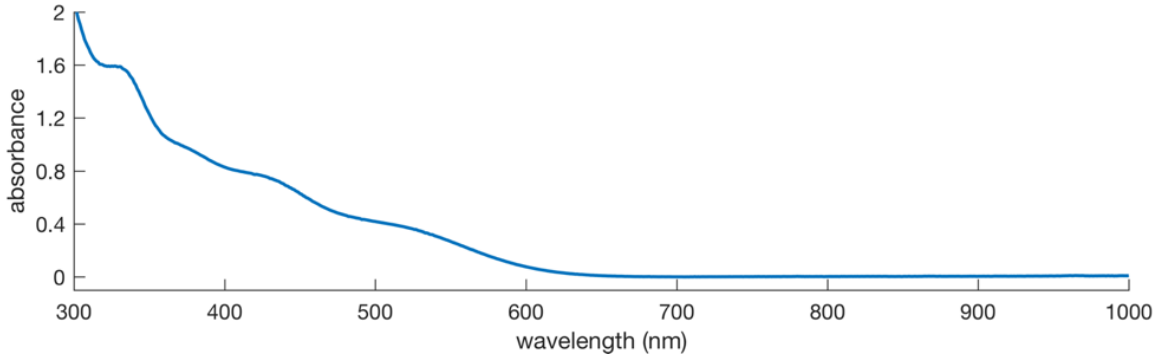

Figure A.7.2. UV-Vis spectrum of **2.7-H** in THF

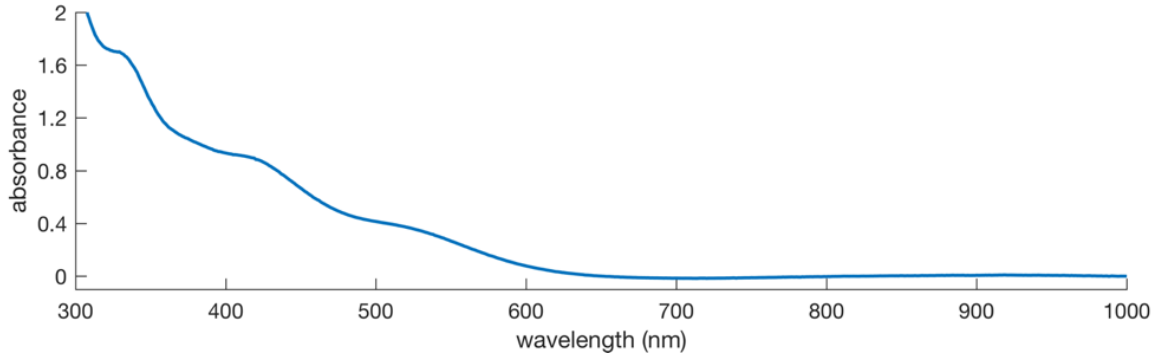

Figure A.7.3. UV-Vis spectrum of **2.7-H(crown)** in THF

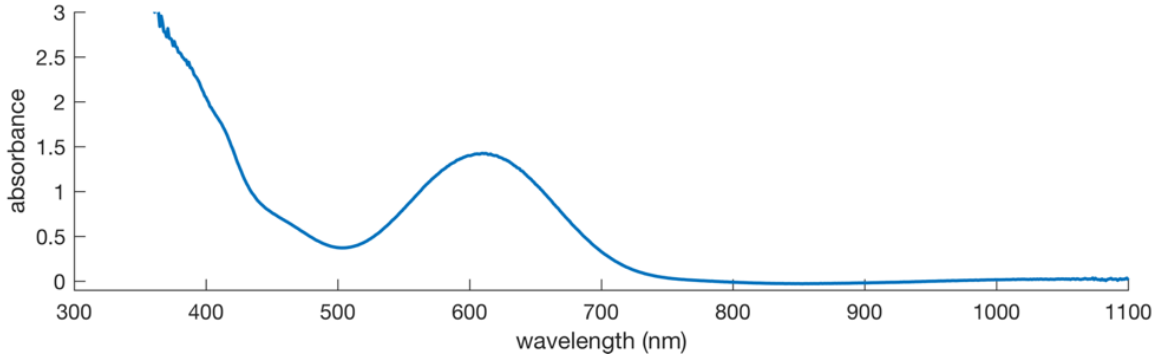

Figure A.7.4. UV-Vis spectrum of **2.8-H** in THF (1 mm cuvette, generated in the presence of one equivalent of Cp_2Co)

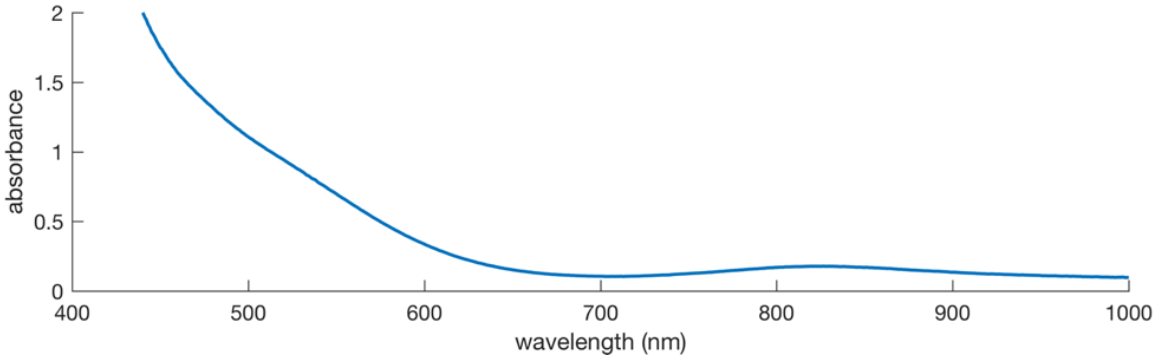

Figure A.7.5 UV-Vis spectrum of **2.9** in THF

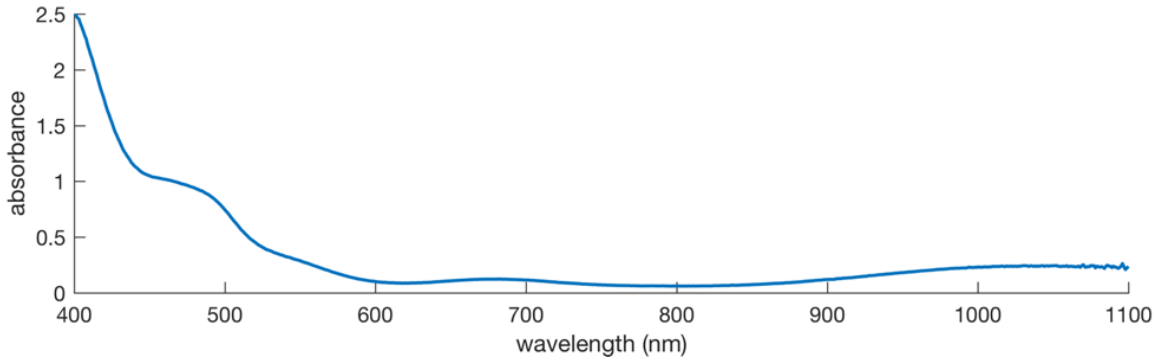

Figure A.7.6. UV-Vis spectrum of **2.11** in THF

A.8 Cyclic Voltammograms

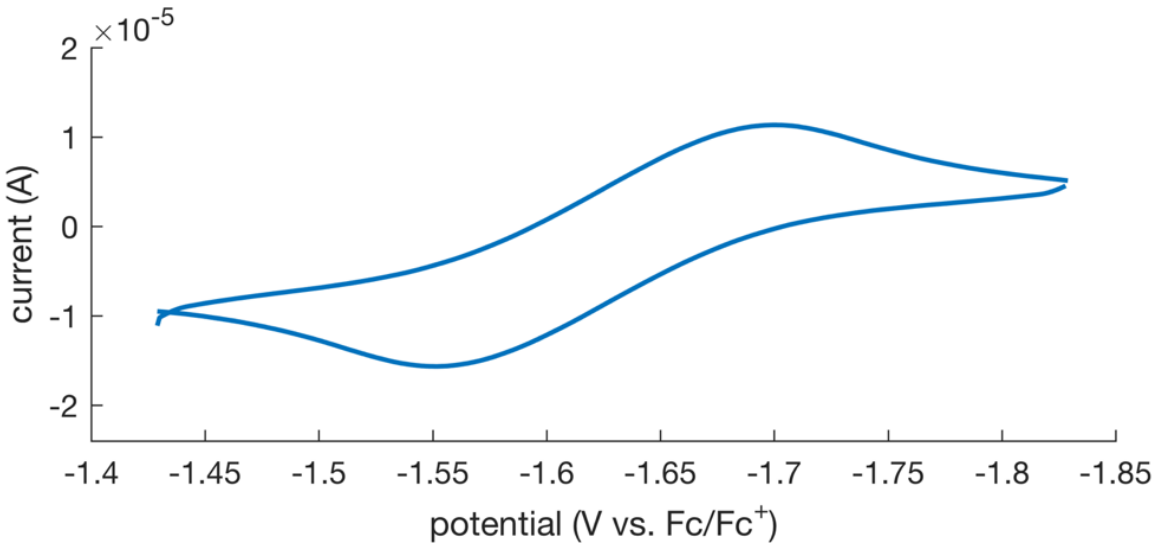

Figure A.8.1. Cyclic voltammogram of **2.7-H(crown)** in THF (0.4 M $[NBu_4][PF_6]$) showing the reversible Fe(II)/Fe(III) couple centered at −1.63 V vs Fc/Fc^+. Data was collected at 400 mV/s with Pt counter, glassy carbon working and Ag/AgOTf reference electrodes

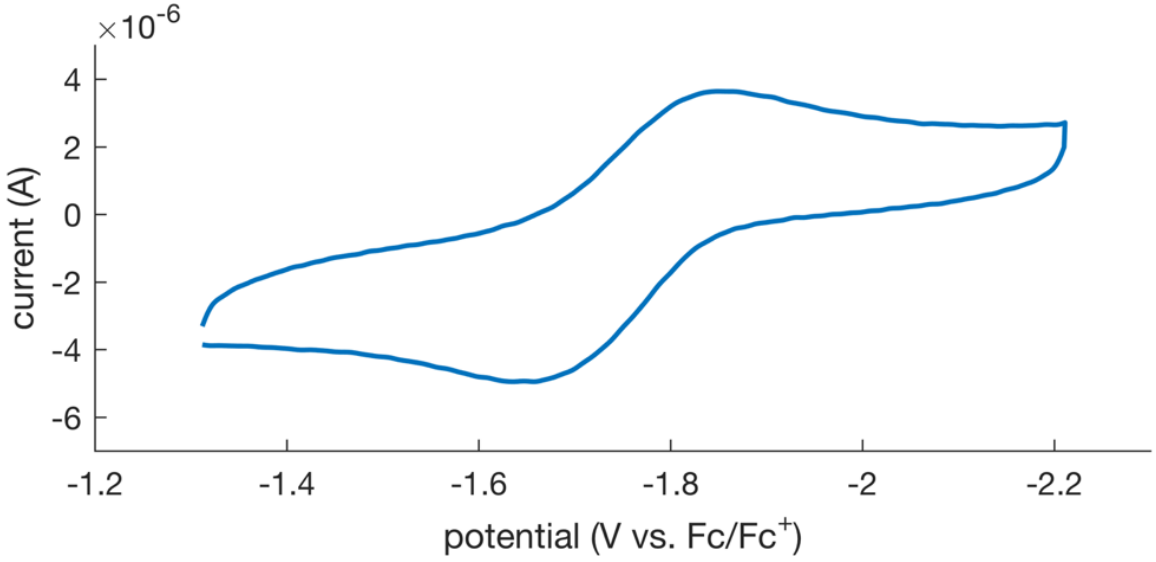

Figure A.8.2. Cyclic voltammogram of **2.9** in THF (0.4 M $[NBu_4][PF_6]$) showing the reversible Fe(I)/Fe(II) couple centered at −1.75 V vs Fc/Fc^+. Data was collected at 400 mV/s with Pt counter, glassy carbon working and Ag/AgOTf reference electrodes

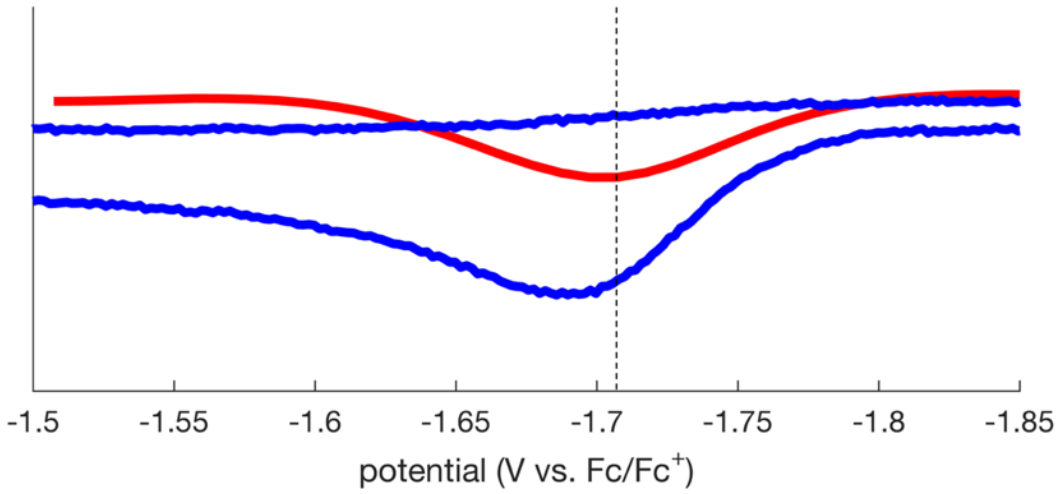

Figure A.8.3. Cyclic voltammogram (blue) and square wave voltammogram (red) of **2.9** in MeCN (0.4 M $[NBu_4][PF_6]$) showing the irreversible Fe(I)/Fe(II) couple centered at −1.71 V vs. Fc/Fc^+. Data was collected at 100 mV/s with Pt counter, glassy carbon working and Ag/AgOTf reference electrodes

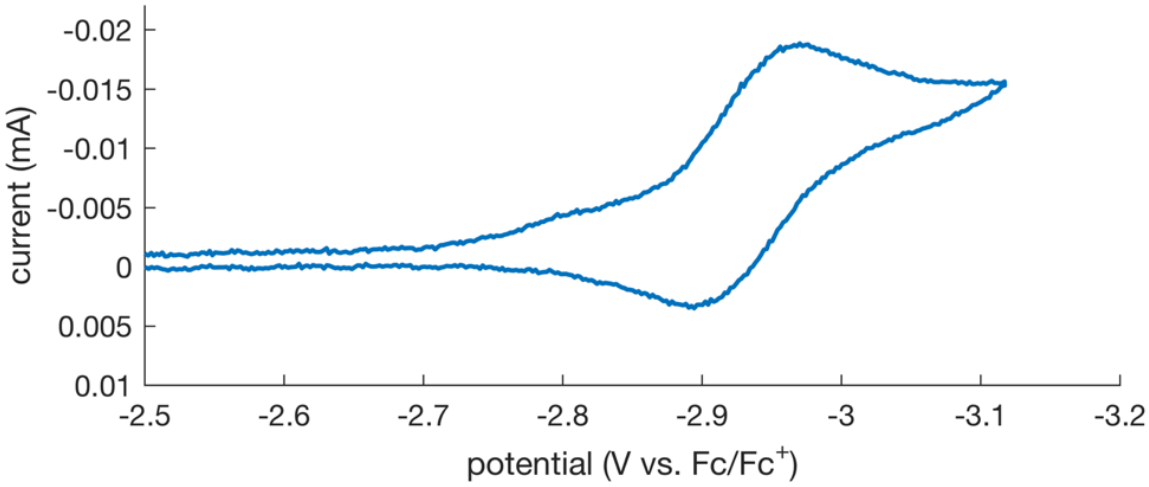

Figure A.8.4. Cyclic voltammogram of **2.9** in MeCN (0.4 M $[NBu_4][PF_6]$) showing the reversible Fe(I)/Fe(0) couple centered at −2.94 V vs. Fc/Fc^+. Data was collected at 100 mV/s with Pt counter, glassy carbon working and Ag/AgOTf reference electrodes

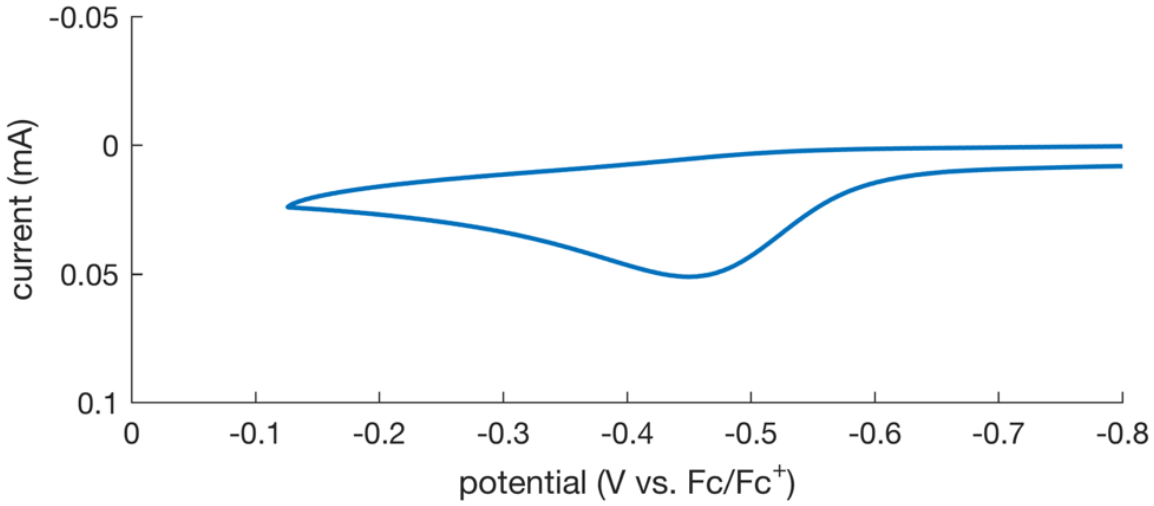

Figure A.8.5. Cyclic voltammogram of **2.7-H(crown)** in MeCN (0.4 M $[NBu_4][PF_6]$) showing the reversible Fe(II)/Fe(III) couple with an onset at −0.58 V vs. Fc/Fc^+. Data was collected with Pt counter, glassy carbon working and Ag/AgOTf reference electrodes

A.9 Variable Temperature Evans Method Measurements

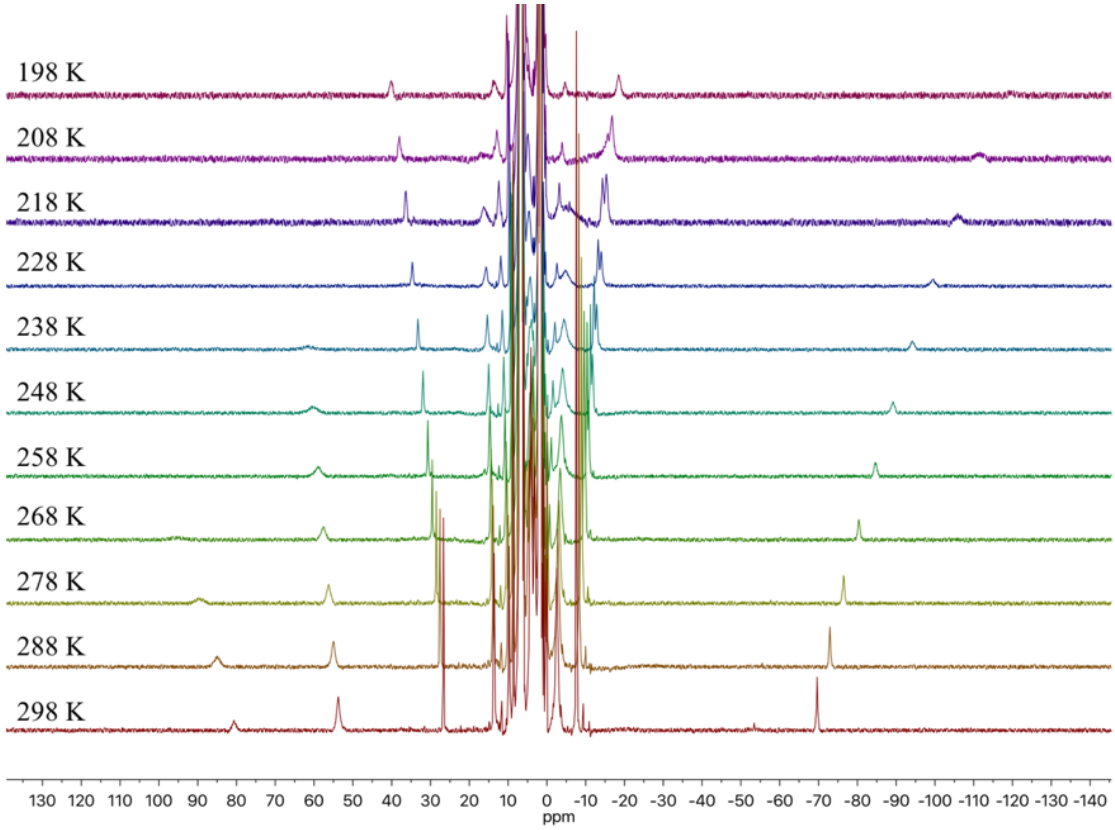

Figure A.9.1. Variable temperature ^1H NMR spectra (500 MHz) of **2.6** in $C_6D_5CD_3$

Temperature (K)	μ_{eff}/μ_B
298	4.79
288	4.82
278	4.83
268	4.86
258	4.88
248	4.90
238	4.93
228	4.95
218	4.98
208	5.00
198	5.02

Table A.9.1. Solution state magnetic susceptibility of **2.6** in $C_6D_5CD_3$ at variable temperatures

A.10 Time-Course UV-Visible Spectra

* Note: For Tables A.10.1-A.10.7, concentrations of **2.8-H** and **2.8-D** over time were obtained by fitting the 640 nm – 900 nm region of the corresponding time-course UV-vis traces following the conversion of **2.8-H** or **2.8-D** to **2.6**. The absorbance data (Abs) were fit to Gaussian lineshapes with the following equation:

$$Abs = a * e^{\left(-\left(\frac{\lambda-606.5}{b^2}\right)^2\right)} + c * e^{\left(-\left(\frac{\lambda-677.3}{d^2}\right)^2\right)} + f * e^{\left(-\left(\frac{\lambda-774.5}{g^2}\right)^2\right)} + \mathrm{h}$$

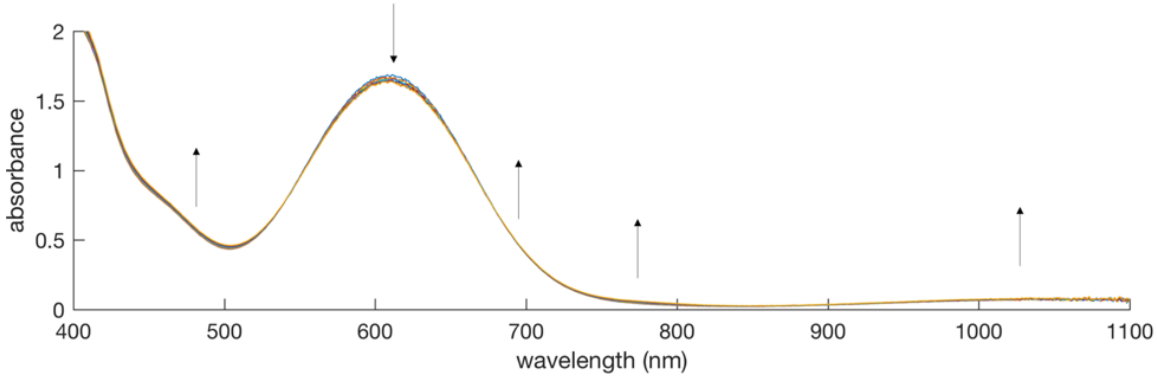

Figure A.10.1. UV-visible spectra showing the conversion of **2.8-H** to **2.6** at 15 °C in a 1 mm cuvette; traces collected every 30 min for 270 min

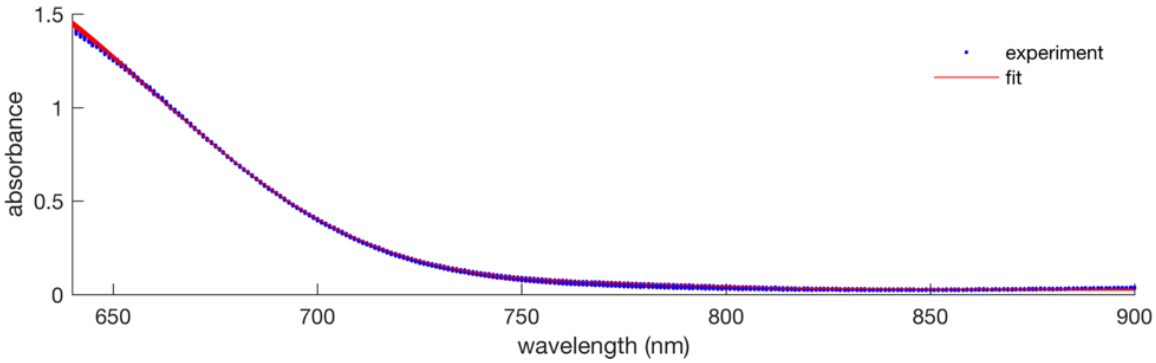

Figure A.10.2. Partial UV-vis spectra and fits (640 nm to 900 nm region of Fig. A.10.1)

Time (min)	[2.8-H] (mol/L)
0	0.006212
30	0.006191
60	0.006163
90	0.006148
120	0.006113
150	0.006081
180	0.006095
210	0.006078
240	0.006039
270	0.006049

Table A.10.1. Fitted concentration of **2.8-H** vs. time (at 15 °C)

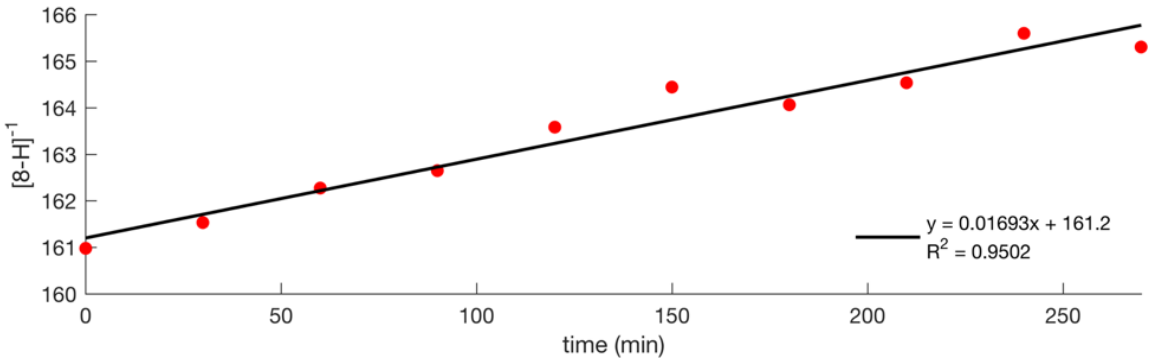

Figure A.10.3. Plot of [**2.8-H**]$^{-1}$ vs. time (at 15 °C)

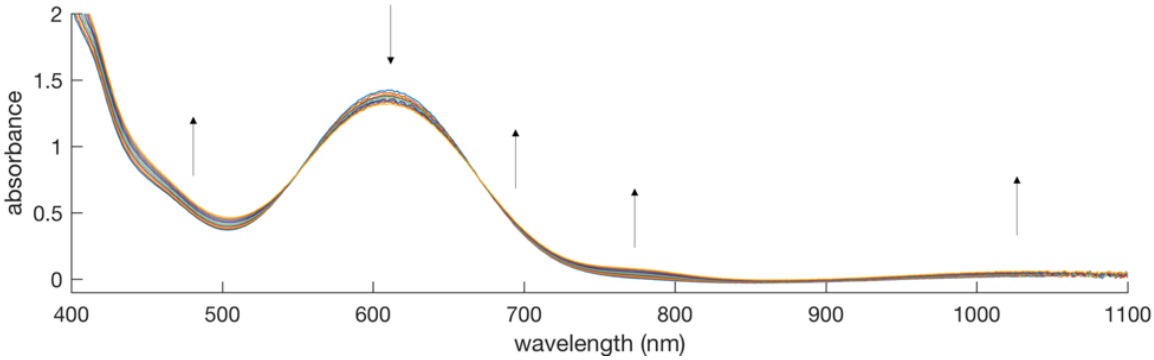

Figure A.10.4. UV-visible spectra showing the conversion of **2.8-H** to **2.6** at 25 °C in a 1 mm cuvette; traces collected every 30 min for 270 min

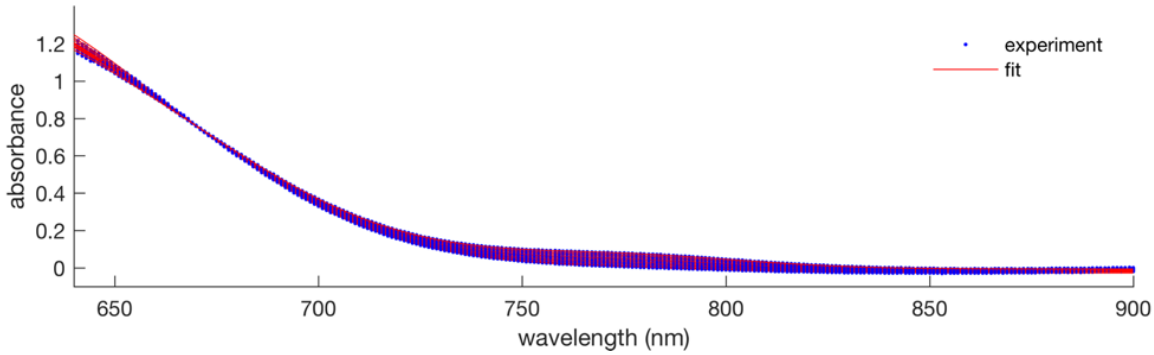

Figure A.10.5. Partial UV-vis spectra and fits (640 nm to 900 nm region of Fig. A.10.4)

Time (min)	[2.8-H] (mol/L)
0	0.005435
30	0.005346
60	0.005276
90	0.005261
120	0.005184
150	0.005144
180	0.005095
210	0.005032
240	0.004993
270	0.004908

Table A.10.2. Fitted concentration of **2.8-H** vs. time (at 25 °C)

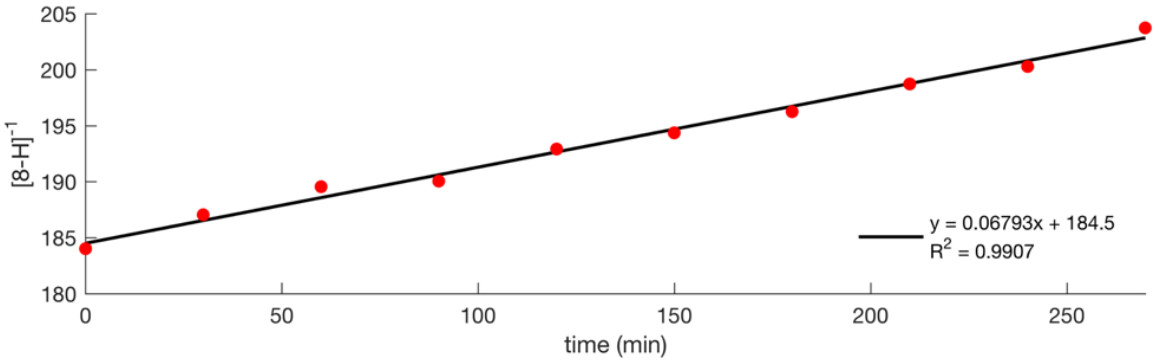

Figure A.10.6. Plot of [**2.8-H**]$^{-1}$ vs time (at 25 °C)

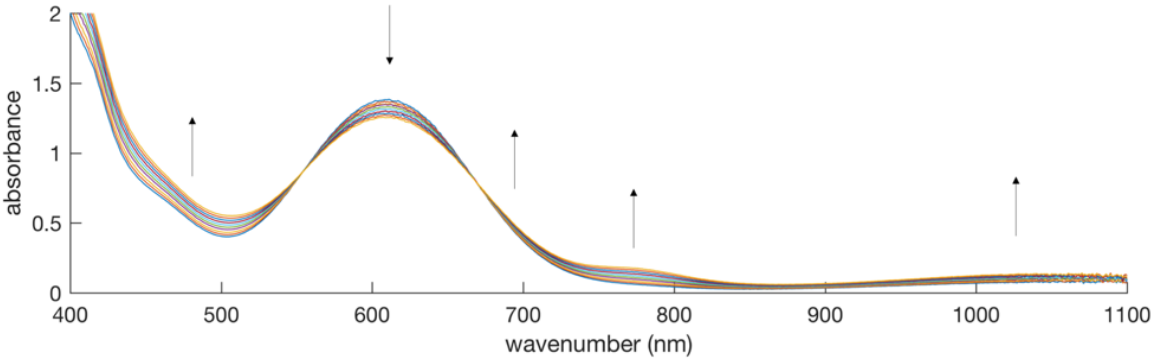

Figure A.10.7. UV-visible spectra showing the conversion of **2.8-H** to **2.6** at 30 °C in a 1 mm cuvette; traces collected every 30 min for 270 min

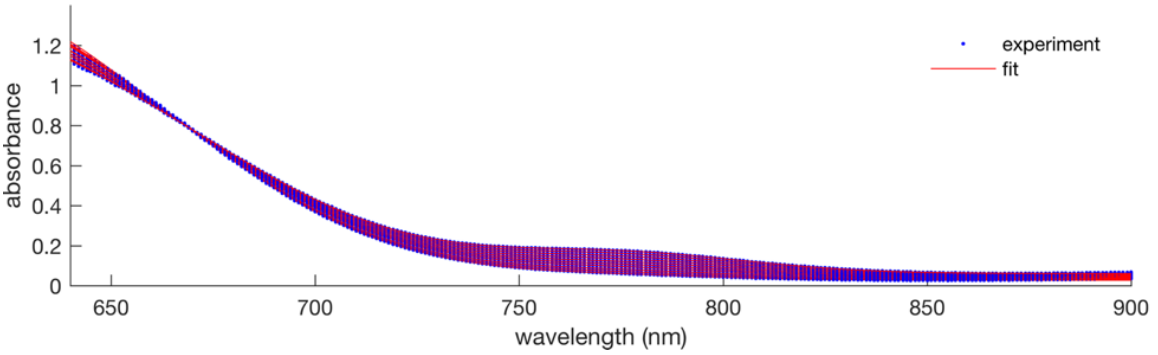

Figure A.10.8. Partial UV-vis spectra and fits (640 nm to 900 nm region of Fig. A.10.7)

Time (min)	[2.8-H] (mol/L)
0	0.005067
30	0.004989

60	0.004936
90	0.004869
120	0.004756
150	0.004721
180	0.004625
210	0.004551
240	0.004449
270	0.004389

Table A.10.3. Fitted concentration of **2.8-H** vs. time (at 30 °C)

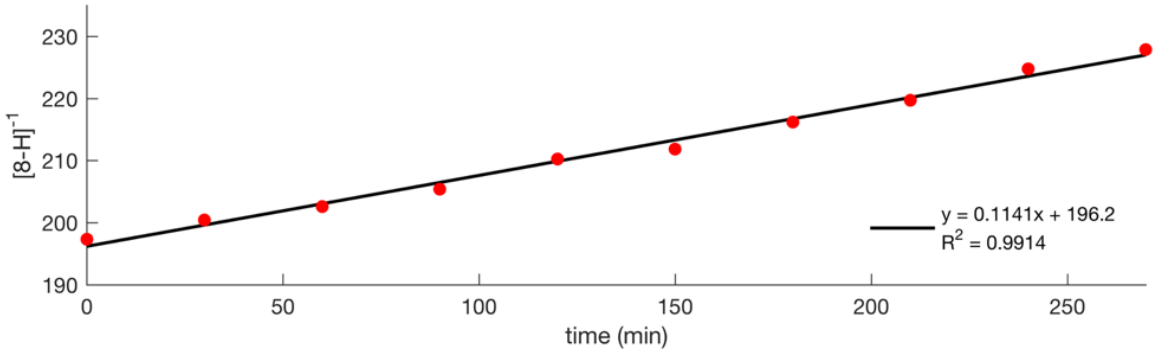

Figure A.10.9. Plot of [**2.8-H**]$^{-1}$ vs. time (at 30 °C)

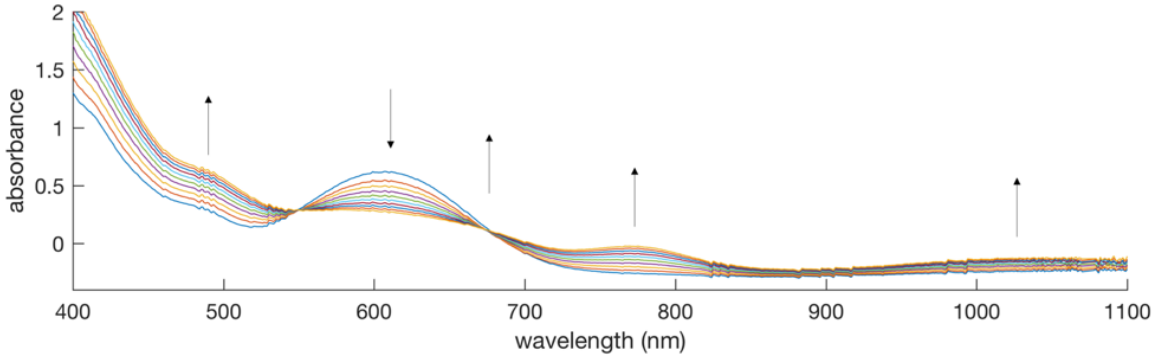

Figure A.10.10. UV-visible spectra showing the conversion of **2.8-H** to **2.6** at 40 °C in a 1 mm cuvette; traces collected every 30 min for 270 min

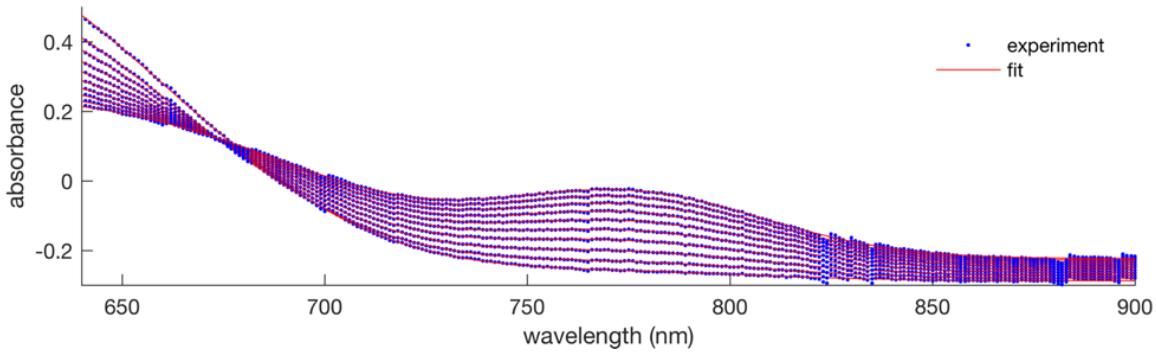

Figure A.10.11. Partial UV-vis spectra and fits (640 nm to 900 nm region of Fig. A.10.10)

Time (min)	[2.8-H] (mol/L)
0	0.003282
30	0.002946
60	0.002723
90	0.002510
120	0.002307
150	0.002124
180	0.001949
210	0.001806
240	0.001668
270	0.001547

Table A.10.4. Fitted concentration of **2.8-H** vs. time (at 40 °C)

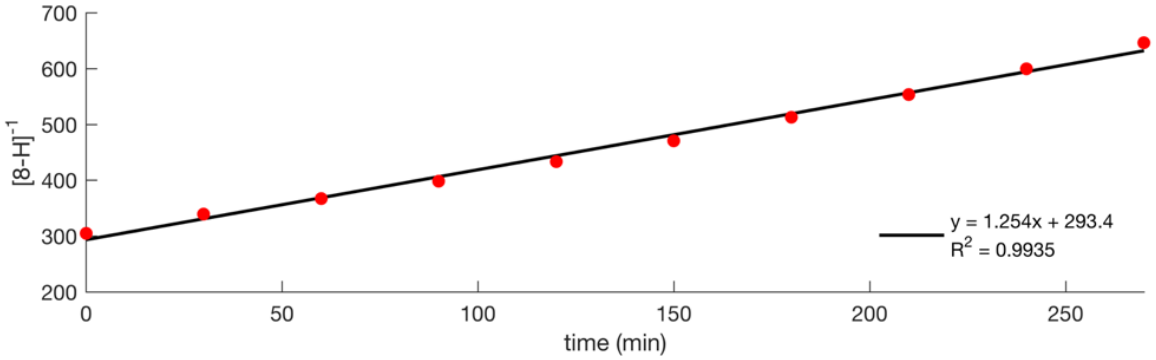

Figure A.10.12. Plot of [**2.8-H**]$^{-1}$ vs. time (at 40 °C)

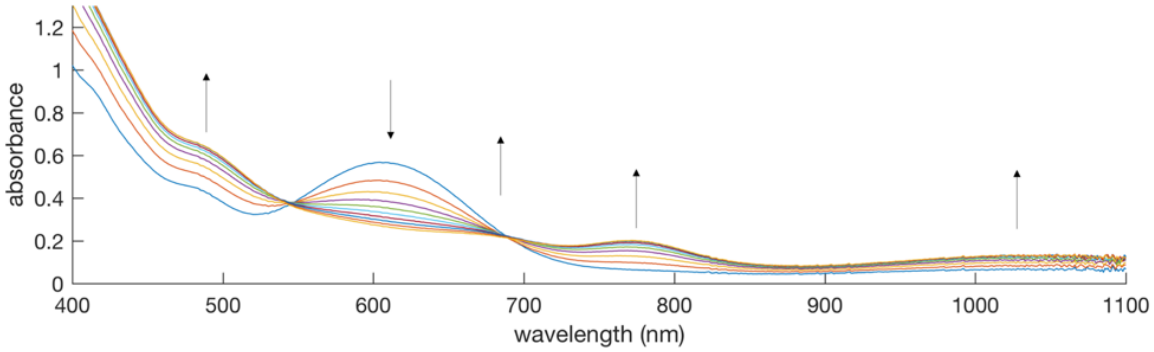

Figure A.10.13. UV-visible spectra showing the conversion of **2.8-H** to **2.6** at 50 °C in a 1 mm cuvette; traces collected every 30 min for 270 min

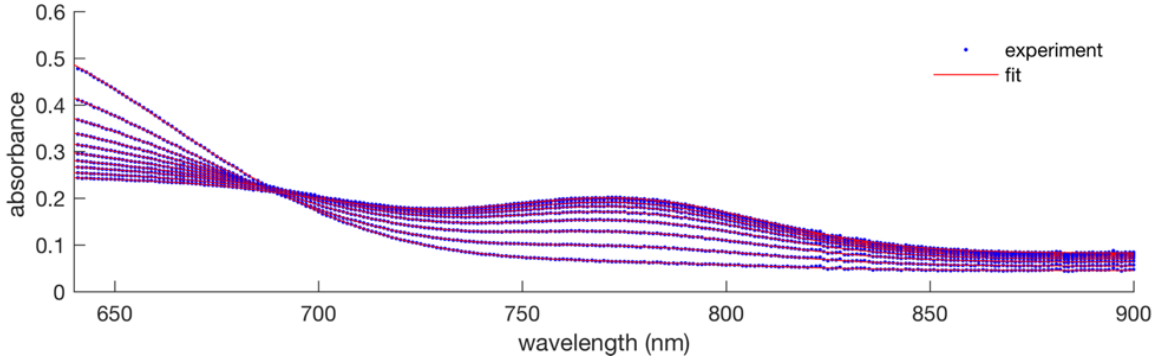

Figure A.10.14. Partial UV-vis spectra and fits (640 nm to 900 nm region of Fig. A.10.13)

Time (min)	[2.8-H] (mol/L)
0	0.001873
30	0.001438
60	0.001155
90	0.0009611
120	0.0008223
150	0.0007216
180	0.0006399
210	0.0005678
240	0.0005187
270	0.0004784

Table A.10.5. Fitted concentration of **2.8-H** vs. time (at 50 °C)

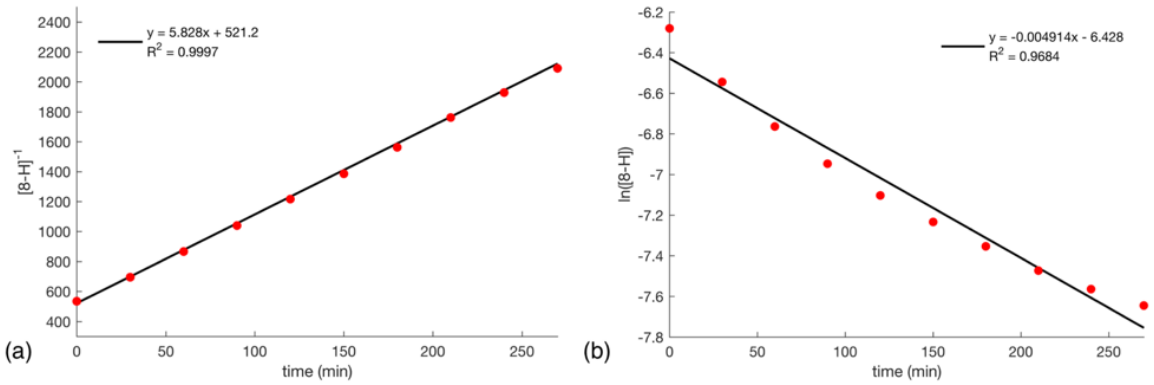

Figure A.10.15. (a) Plot of [**2.8-H**]$^{-1}$ vs. time (at 50 °C) (b) Plot of ln([**2.8-H**]) vs. time (at 50 °C)

T (K)	k ($M^{-1}min^{-1}$)
288	0.01693
298	0.06793
303	0.1141
313	1.254
323	5.828

Table A.10.6. Temperature dependence of the second order rate constant (k) for the conversion of **2.8-H** to **2.6**

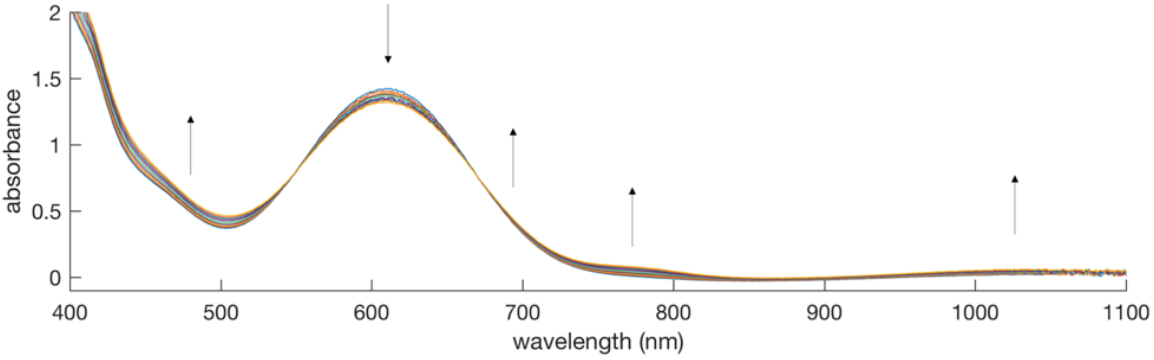

Figure A.10.16. UV-visible spectra showing the conversion of **2.8-D** to **2.6** at 25 °C in a 1 mm cuvette; traces collected every 30 min for 270 min

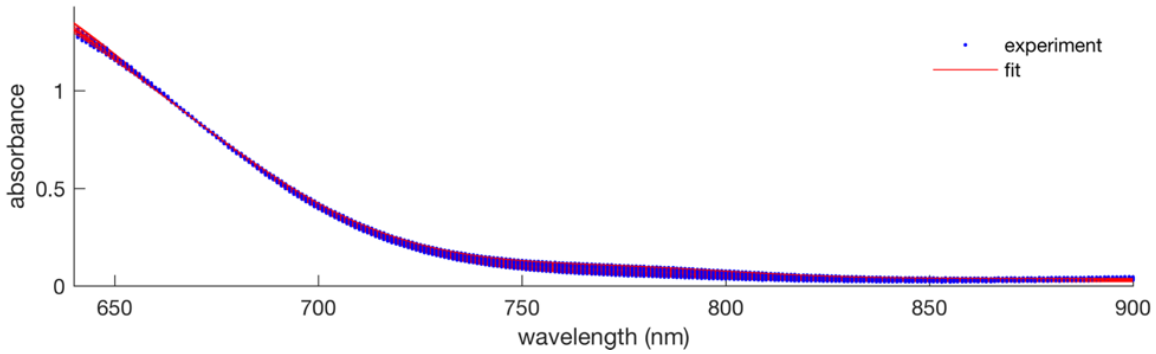

Figure A.10.17. Partial UV-vis spectra and fits (640 nm to 900 nm region of Fig. A.10.16)

Time (min)	[2.8-D] (mol/L)
0	0.005650
30	0.005604
60	0.005534
90	0.005523
120	0.005466
150	0.005452
180	0.005420
210	0.005371
240	0.005378
270	0.005304

Table A.10.7. Fitted concentration of **2.8-D** vs. time (at 25 °C)

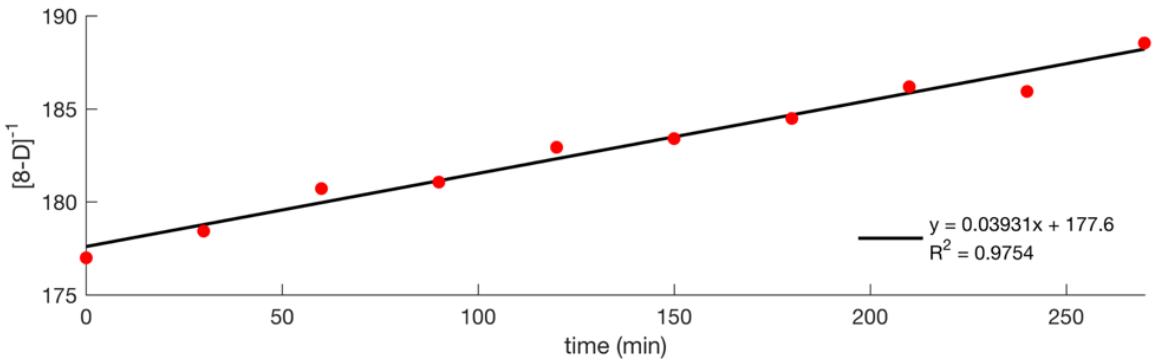

Figure A.10.18. Plot of [**2.8-D**]$^{-1}$ vs. time (at 25 °C)

A.11 DFT-Optimized Structures

Fe	0.51351100	0.05922200	-1.03017400
P	1.38765300	-1.99402600	-0.80215900
S	-1.71508100	-0.14263000	-0.79525400
P	1.05446900	2.21884800	-0.77401200
Si	0.60659500	0.05068200	1.24023200
N	0.23385300	0.04219400	-2.87573300
C	2.05136100	-2.32109200	0.87337700
C	2.78554100	-2.48360700	-1.93306000
H	2.97617200	-3.54564700	-1.69634900
C	1.55693400	2.65748400	0.93360400
C	-3.53858000	-0.17437400	1.30077700
C	1.36786000	1.66557100	1.90902300
C	-3.84306400	-0.21410100	2.66995700
H	-4.89541600	-0.26191500	2.96501000
C	0.11806900	-3.36551600	-1.02362700
H	-0.51582500	-2.98556600	-1.84531000
C	2.77406700	-2.81946800	3.51871600
H	3.05124800	-3.01623200	4.55755400
C	-0.30566400	3.47812400	-1.07459500
H	0.22290800	4.45108700	-1.08557200
C	2.84490100	-3.43330100	1.18651200
H	3.19218400	-4.11215100	0.40128600
C	-2.85275700	-0.16608500	3.64651400
H	-3.12464200	-0.18637200	4.70452400
C	2.48741800	2.85356900	-1.80672600
H	2.36561000	3.95292700	-1.82998500
C	1.62901900	-1.42952600	1.87731700
C	1.99659600	-1.70670700	3.20315600
H	1.67318400	-1.04463400	4.01268300
C	4.05687000	-1.70046500	-1.65359400
H	3.93062700	-0.63702500	-1.90748400
H	4.88497600	-2.08449300	-2.26822500
H	4.37011600	-1.75606000	-0.60123600
C	-1.16237000	-0.05528300	1.90623700
C	3.20822400	-3.67884100	2.50817600
H	3.82949400	-4.54395500	2.75247100
C	-0.73885000	-3.47953500	0.22907700
H	-0.18654400	-3.97226800	1.04407300
H	-1.63524300	-4.08295800	0.02412500
H	-1.08282200	-2.50551900	0.60168200
C	-4.65929900	-0.23083700	0.33392800
C	-2.17354400	-0.10392800	0.92144800

C	2.45502100	2.32318900	-3.23196300
H	2.65142000	1.23972900	-3.24509100
H	3.24098200	2.80395300	-3.83320700
H	1.50057700	2.48751600	-3.74801800
C	2.15245900	3.24455600	3.58925200
H	2.38630000	3.47308900	4.63223100
C	-1.51664900	-0.08320000	3.25849300
H	-0.73717300	-0.04194900	4.02778900
C	-1.00032000	3.27047600	-2.41066500
H	-0.31240400	3.27797500	-3.26697400
H	-1.73923200	4.06768700	-2.58186300
H	-1.54409600	2.31322400	-2.42192500
C	2.02809900	3.93142100	1.27978800
H	2.16433100	4.70249600	0.51341700
C	2.32828200	4.22286400	2.60674500
H	2.69796200	5.21439500	2.87960500
C	3.82638600	2.51682000	-1.16533800
H	3.98919000	3.02134800	-0.20500400
H	4.65018200	2.80212500	-1.83666100
H	3.91600300	1.43393900	-0.98370400
N	-0.02147200	0.03228300	-3.97141000
C	1.67558800	1.98339200	3.24210000
H	1.53661500	1.23760000	4.03101000
C	-1.31272000	3.47638800	0.06507100
H	-1.79419400	2.49251900	0.16744000
H	-2.10912700	4.20922700	-0.13456200
H	-0.86441800	3.73111400	1.03483900
C	-5.64232600	-1.22308900	0.46891100
H	-5.53639300	-1.96953000	1.26156600
C	-6.72900300	-1.28274300	-0.40071800
H	-7.47562300	-2.07215600	-0.28312600
C	-4.80826900	0.71348600	-0.69423700
H	-4.06361800	1.50530400	-0.80583700
C	-6.86083300	-0.34068300	-1.41911400
H	-7.71225400	-0.38357300	-2.10267500
C	2.38522300	-2.37470400	-3.39645400
H	1.40738300	-2.82686100	-3.61844500
H	3.12964400	-2.86749000	-4.03945200
H	2.33389700	-1.32286600	-3.71089300
C	-5.89834300	0.65998000	-1.55803600
H	-5.99937200	1.40955400	-2.34681400
C	0.68229100	-4.72295200	-1.41064000
H	1.21633300	-4.72330000	-2.37056600

H	-0.13729300	-5.45202600	-1.50030600
H	1.36501100	-5.11500800	-0.64046200
H	2.05682000	0.17816000	-1.08009400

Table A.11.1. Gas-phase optimized coordinates for **2.8-H** (m06l, $S = 1/2$)

Fe	-0.40651200	-0.02742200	-1.05973600
P	-1.43431500	-1.97339400	-0.67790500
P	-1.47887300	1.90612200	-0.82623600
S	1.88980900	0.04304100	-0.87360400
Si	-0.38392000	0.06386500	1.20164500
C	-0.20460800	-3.40847500	-0.91118300
H	-0.82326500	-4.32563600	-0.98560600
N	-0.37449700	-0.10237400	-2.88106500
C	-0.46129900	3.39985700	-1.40816200
H	-1.15610800	4.26289800	-1.40683700
N	-0.34305500	-0.15563500	-4.01698500
C	-1.77546700	2.46941900	0.90585200
C	-1.20236000	1.65625700	1.89688700
C	1.40432300	0.02232900	1.84428300
C	2.39150100	0.05601300	0.82501400
C	-1.92292100	-2.27864500	1.08060000
C	3.76805300	0.03633800	1.18984800
C	-2.41834300	3.66788700	1.24311000
H	-2.85458700	4.30070700	0.46096600
C	4.88003000	0.02388600	0.21155200
C	0.68241700	3.68080300	-0.44340800
H	0.33745000	3.98733100	0.55378800
H	1.32541600	4.48606000	-0.83464100
H	1.31482700	2.78660600	-0.31997200
C	-1.63166400	-1.57200000	3.36991500
H	-1.22545300	-0.87423400	4.11080000
C	-1.28145900	2.08441000	3.23205100
H	-0.82541600	1.48435300	4.02775900
C	-1.92284300	3.27472800	3.57152700
H	-1.97466300	3.59124400	4.61779100
C	4.97186900	0.93932000	-0.85099900
H	4.17406400	1.67164500	-0.98880900
C	-1.38294800	-1.36453300	2.00478000
C	0.61512300	-3.23876400	-2.18322000
H	0.01057600	-3.05712400	-3.08128200
H	1.22831200	-4.13588800	-2.36818700
H	1.30000400	-2.38292900	-2.08216900
C	-2.93231700	-3.54707000	2.88429900

H	-3.53643500	-4.39388600	3.22351500
C	3.13831800	-0.05071400	3.55221800
H	3.43334400	-0.08706100	4.60456300
C	0.72764900	-3.53665100	0.28488800
H	1.27143300	-2.59352600	0.46132100
H	1.48800000	-4.31183900	0.09728100
H	0.20237800	-3.80037900	1.21349600
C	-2.68935900	-3.36522500	1.52363200
H	-3.09876900	-4.08675400	0.80871000
C	1.79201600	-0.03185500	3.18508200
H	1.02628800	-0.06885400	3.96959100
C	6.06222700	0.92220400	-1.71662100
H	6.11239700	1.64892400	-2.53235600
C	-2.39968400	-2.64898900	3.81117000
H	-2.58801600	-2.78979100	4.87994400
C	7.08467900	-0.01488500	-1.55471700
H	7.93295100	-0.03152000	-2.24468100
C	-2.92928000	-2.71066000	-1.57385100
H	-3.03334800	-3.74105200	-1.18475600
C	-3.15962400	2.26070500	-1.62529700
H	-3.25088500	3.35734400	-1.74795600
C	0.08380600	3.19219700	-2.81132100
H	0.79248600	2.34982400	-2.82368600
H	0.62894100	4.08749900	-3.15232600
H	-0.69455800	2.97953000	-3.55771400
C	-2.49820000	4.06776000	2.57505600
H	-3.00208800	5.00238600	2.83929300
C	4.10482600	-0.02007600	2.55165500
H	5.16589100	-0.02370000	2.82258100
C	7.00905700	-0.93065300	-0.50730100
H	7.79729600	-1.67679100	-0.37138200
C	-4.19967100	-1.94277800	-1.25194400
H	-4.35214000	-1.80022500	-0.17176300
H	-5.08474400	-2.46755200	-1.64753200
H	-4.18235400	-0.94588400	-1.71620800
C	5.92196100	-0.90558100	0.36415000
H	5.85817200	-1.63705400	1.17522900
C	-4.28078800	1.76207300	-0.72221400
H	-4.05218400	0.75977200	-0.32437700
H	-5.23272600	1.68697100	-1.27330600
H	-4.44543700	2.41369700	0.14567300
C	-3.23584400	1.60036100	-2.99251800
H	-2.46586400	1.95801000	-3.68904100

H	-4.21850600	1.77078400	-3.46235600
H	-3.08691400	0.51254000	-2.90119400
C	-2.72991600	-2.79457000	-3.07860200
H	-2.47058600	-1.81481600	-3.50887900
H	-3.65538100	-3.13391500	-3.57273400
H	-1.93743900	-3.49890300	-3.36360100

Table A.11.2. Gas-phase optimized coordinates for **2.9** (m06l, $S = 1/2$)

Fe	0.51937400	0.06404600	-1.02451700
P	1.40648300	-1.99850900	-0.80591400
S	-1.72736800	-0.12756600	-0.82249300
P	1.08641900	2.23212000	-0.75962900
Si	0.58462200	0.04165800	1.24653400
N	0.29356300	0.06672600	-2.86412100
C	2.03901100	-2.32546600	0.88245900
C	2.82252300	-2.46267100	-1.91736700
H	3.01923300	-3.52234200	-1.67811100
C	1.52205600	2.65825300	0.96963700
C	-3.57213700	-0.18872400	1.26456400
C	1.31530100	1.66053700	1.93700800
C	-3.88555500	-0.25027300	2.63248700
H	-4.93888300	-0.30721500	2.92313200
C	0.14401300	-3.36863200	-1.05790500
H	-0.47076300	-2.98954900	-1.89417600
C	2.73318700	-2.83190900	3.53558600
H	3.00009600	-3.03224400	4.57668900
C	-0.24681600	3.49911300	-1.11844400
H	0.29569400	4.46262000	-1.10649700
C	2.83365400	-3.43662700	1.19908800
H	3.19028000	-4.11042500	0.41413600
C	-2.90099600	-0.21684300	3.61627900
H	-3.17904500	-0.25538800	4.67249800
C	2.57523000	2.82990800	-1.72661700
H	2.47838900	3.93079900	-1.74358400
C	1.60093100	-1.44006000	1.88677400
C	1.95465900	-1.71916300	3.21748700
H	1.62092200	-1.06005700	4.02519000
C	4.07968000	-1.66666400	-1.61764300
H	3.95737200	-0.60699400	-1.88982100
H	4.92328700	-2.05551400	-2.20797800
H	4.37437400	-1.70802000	-0.55865200
C	-1.19936900	-0.07745100	1.88507800
C	3.18135400	-3.68579000	2.52527300

H	3.80243300	-4.55041600	2.77281500
C	-0.73588000	-3.49058900	0.17665000
H	-0.20223300	-3.99560700	0.99710300
H	-1.63053500	-4.09102400	-0.04786300
H	-1.08167200	-2.51733100	0.55303500
C	-4.69242100	-0.23425200	0.29448400
C	-2.20417500	-0.11158200	0.89060800
C	2.59326300	2.31065100	-3.15567900
H	2.76570900	1.22278000	-3.17784000
H	3.41942500	2.77862700	-3.71195300
H	1.67049100	2.51326300	-3.71498400
C	2.05300700	3.23545100	3.64266000
H	2.26200400	3.46068000	4.69192200
C	-1.56173800	-0.12764000	3.23581800
H	-0.78558200	-0.10146000	4.00924900
C	-0.88357100	3.30405000	-2.48387200
H	-0.15554900	3.30972200	-3.30618500
H	-1.60285300	4.11297100	-2.68327400
H	-1.44064300	2.35496700	-2.53042600
C	1.98000600	3.93341700	1.33176400
H	2.12955400	4.70631300	0.57032800
C	2.24688100	4.21911800	2.66774000
H	2.60539100	5.21131000	2.95386800
C	3.87436300	2.45749300	-1.02778000
H	4.01796300	2.97444000	-0.07024500
H	4.73106400	2.71241000	-1.66974400
H	3.93091500	1.37414100	-0.83189000
N	0.06687200	0.07061500	-3.96813400
C	1.58959100	1.97219100	3.28048900
H	1.43580400	1.22214200	4.06266300
C	-1.30227100	3.51381600	-0.02473900
H	-1.79760900	2.53495900	0.06795500
H	-2.08393000	4.25010100	-0.26763600
H	-0.89661800	3.78160600	0.96097000
C	-5.67738000	-1.22778400	0.41965400
H	-5.57603600	-1.98302700	1.20472000
C	-6.76654900	-1.27592200	-0.44934300
H	-7.51416800	-2.06563900	-0.33842300
C	-4.84408400	0.72410900	-0.72217700
H	-4.10233400	1.52046500	-0.82396300
C	-6.90059200	-0.32083500	-1.45656700
H	-7.75396600	-0.35434700	-2.13861300
C	2.44256900	-2.35217600	-3.38579700

H	1.46284900	-2.79400500	-3.62077500
H	3.19053800	-2.85981500	-4.01316200
H	2.41634900	-1.30052600	-3.70627700
C	-5.93717700	0.68209700	-1.58495700
H	-6.04095700	1.44369000	-2.36224400
C	0.72193800	-4.72021600	-1.44186400
H	1.26952600	-4.71017700	-2.39385200
H	-0.09510900	-5.45022600	-1.55000600
H	1.39668600	-5.11421100	-0.66602300
H	2.05996600	0.17104800	-1.02231200

Table A.11.3. Optimized coordinates for **2.8-H** with MeCN solvation (m06l, $S = 1/2$)

Fe	0.48346400	0.07403100	-1.09971000
P	1.50080400	-2.00381700	-0.79711900
S	-1.81017900	-0.07945800	-0.87777700
P	1.16000500	2.27375100	-0.74716800
Si	0.52214500	0.04646900	1.20664600
N	0.27529700	0.06980100	-2.94778000
C	2.06720800	-2.29739500	0.91979100
C	2.95866200	-2.45705200	-1.85947200
H	3.18043600	-3.51200200	-1.61962000
C	1.45179800	2.69435600	1.01100000
C	-3.64523100	-0.22657600	1.21944000
C	1.18688400	1.67952500	1.94703300
C	-3.94651600	-0.33448500	2.58734100
H	-4.99691800	-0.40996600	2.88474300
C	0.25167300	-3.37583200	-1.07887400
H	-0.33053100	-3.01741500	-1.94718600
C	2.67802600	-2.73017400	3.60592800
H	2.91382800	-2.89942900	4.66005100
C	-0.04946100	3.59810000	-1.26887100
H	0.53401300	4.53670200	-1.23251000
C	2.87663000	-3.38144100	1.28915000
H	3.27516700	-4.06241400	0.53088800
C	-2.95478600	-0.32682000	3.56428600
H	-3.22352600	-0.40213200	4.62101200
C	2.78016000	2.70850000	-1.57882500
H	2.78941000	3.81008400	-1.66826300
C	1.56697000	-1.40345500	1.88830500
C	1.88085700	-1.64706300	3.23616300
H	1.50300900	-0.98076000	4.01812300
C	4.17462100	-1.61439900	-1.51940800
H	3.98913600	-0.54959500	-1.72879700

H	5.03617300	-1.91910100	-2.13272400
H	4.47578700	-1.70043300	-0.46521500
C	-1.26903100	-0.11779300	1.82338700
C	3.18387700	-3.59370500	2.63155400
H	3.81777500	-4.43617200	2.91971200
C	-0.67855000	-3.47213500	0.12065700
H	-0.17597700	-3.94628100	0.97838800
H	-1.55705500	-4.08840000	-0.12344200
H	-1.04756800	-2.48970100	0.44962600
C	-4.77451500	-0.26309700	0.25892200
C	-2.28072700	-0.12316700	0.83355600
C	2.87587300	2.09178700	-2.96573500
H	2.90845300	0.99182100	-2.90767700
H	3.80095800	2.41956500	-3.46361200
H	2.03811500	2.35809300	-3.62369200
C	1.82175800	3.22868200	3.71868600
H	1.96571100	3.43685200	4.78239700
C	-1.61961700	-0.21650200	3.17482000
H	-0.83707000	-0.21167900	3.94262600
C	-0.56482900	3.38388100	-2.68204800
H	0.23546900	3.31512700	-3.43153200
H	-1.21386900	4.22206600	-2.97749700
H	-1.16955200	2.46556400	-2.74624500
C	1.89111600	3.96188000	1.41975900
H	2.08951800	4.74421300	0.67932000
C	2.07859500	4.22651400	2.77317600
H	2.42403800	5.21205100	3.09608300
C	3.95284400	2.26561400	-0.71449100
H	4.05041700	2.85575200	0.20603500
H	4.89655300	2.36561100	-1.27198600
H	3.86369000	1.20759300	-0.41674300
N	0.08540600	0.06395900	-4.06118800
C	1.37758700	1.97265700	3.30955300
H	1.17325500	1.21293400	4.07094000
C	-1.20540700	3.69250900	-0.28412000
H	-1.75678200	2.74031400	-0.22444200
H	-1.91830200	4.46311900	-0.61477100
H	-0.88369900	3.95977300	0.73210400
C	-5.75228600	-1.26508900	0.37795200
H	-5.63957400	-2.03081100	1.15127200
C	-6.84820800	-1.31042800	-0.48288700
H	-7.58871200	-2.10747100	-0.37619400
C	-4.94277600	0.70638000	-0.74476400

H	-4.20855000	1.50909200	-0.84422700
C	-6.99733200	-0.34429300	-1.47736500
H	-7.85517700	-0.37615400	-2.15391300
C	2.60635300	-2.34482400	-3.33475100
H	1.64297600	-2.80990600	-3.59200700
H	3.37957300	-2.82602400	-3.95226800
H	2.55625400	-1.29085600	-3.64653200
C	-6.04218600	0.66719000	-1.59965900
H	-6.15682000	1.43761400	-2.36674000
C	0.85507800	-4.72947000	-1.41049200
H	1.44047400	-4.73154000	-2.33989700
H	0.05113000	-5.47093500	-1.53640400
H	1.50340900	-5.09841000	-0.60043600

Table A.11.4. Optimized coordinates for $(SiP_2S)FeN_2$ with MeCN solvation (m06l, $S = 1$)

Atom	Mulliken atomic spin density (e^-)	Percentage of total spin density (%)
1 Fe	0.918617	57.54
2 P	0.017703	1.11
3 S	0.176109	11.03
4 P	0.00877	0.55
5 Si	-0.086852	5.44
6 N	-0.007824	0.49
7 C	-0.004151	0.26
8 C	-0.004923	0.31
9 H	-0.000571	0.04
10 C	-0.003273	0.21
11 C	0.039217	2.46
12 C	0.002189	0.14
13 C	-0.021828	1.37
14 H	0.000714	0.04
15 C	0.008125	0.51
16 H	0.00059	0.04
17 C	-0.000679	0.04
18 H	-0.000058	0
19 C	0.00837	0.52
20 H	0.002665	0.17
21 C	-0.000748	0.05
22 H	0.000084	0.01
23 C	0.042411	2.66
24 H	-0.002586	0.16
25 C	-0.004668	0.29

26 H	-0.000517	0.03
27 C	0.003183	0.2
28 C	0.000803	0.05
29 H	-0.000086	0.01
30 C	0.000523	0.03
31 H	-0.000615	0.04
32 H	-0.000202	0.01
33 H	0.000013	0
34 C	0.047127	2.95
35 C	0.00096	0.06
36 H	-0.000086	0.01
37 C	-0.000735	0.05
38 H	0.000194	0.01
39 H	0.000108	0.01
40 H	0.001205	0.08
41 C	-0.00438	0.27
42 C	-0.03821	2.39
43 C	0.000202	0.01
44 H	0.000416	0.03
45 H	-0.000009	0
46 H	0.000274	0.02
47 C	-0.000714	0.04
48 H	-0.000067	0
49 C	-0.020507	1.28
50 H	0.00072	0.05
51 C	0.000177	0.01
52 H	0.000025	0
53 H	0.000139	0.01
54 H	0.001091	0.07
55 C	-0.000763	0.05
56 H	0.000027	0
57 C	0.000792	0.05
58 H	-0.000076	0
59 C	-0.000393	0.02
60 H	-0.000019	0
61 H	-0.000194	0.01
62 H	0.000553	0.03
63 N	-0.061058	3.82
64 C	0.000775	0.05
65 H	-0.00012	0.01
66 C	0.000773	0.05
67 H	0.000602	0.04

68 H	0.000277	0.02
69 H	-0.000104	0.01
70 C	0.003106	0.19
71 H	-0.000147	0.01
72 C	-0.000981	0.06
73 H	0.000074	0
74 C	0.002351	0.15
75 H	0.000382	0.02
76 C	0.002736	0.17
77 H	-0.000133	0.01
78 C	0.000223	0.01
79 H	0.000135	0.01
80 H	0.000069	0
81 H	0.000715	0.04
82 C	-0.00105	0.07
83 H	0.000133	0.01
84 C	0.00053	0.03
85 H	-0.000059	0
86 H	0.001241	0.08
87 H	0.000052	0
88 H	-0.028886	1.81

Table A.11.5. Mulliken atomic spin densities calculated for **2.8-H** (gas-phase, m06l, $S = 1/2$)

Appendix B

SUPPLEMENTARY INFORMATION FOR CHAPTER 3

B.1 NMR Spectra

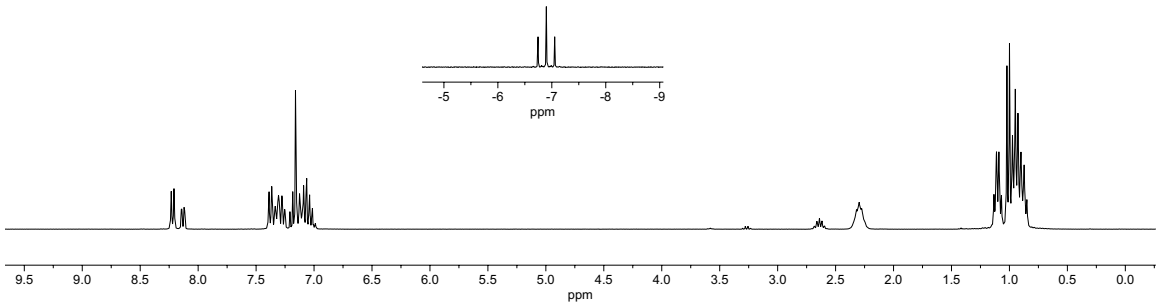

Figure B.1.1. ^{1}H NMR spectrum of **3.2** in C_6D_6 (300 MHz)

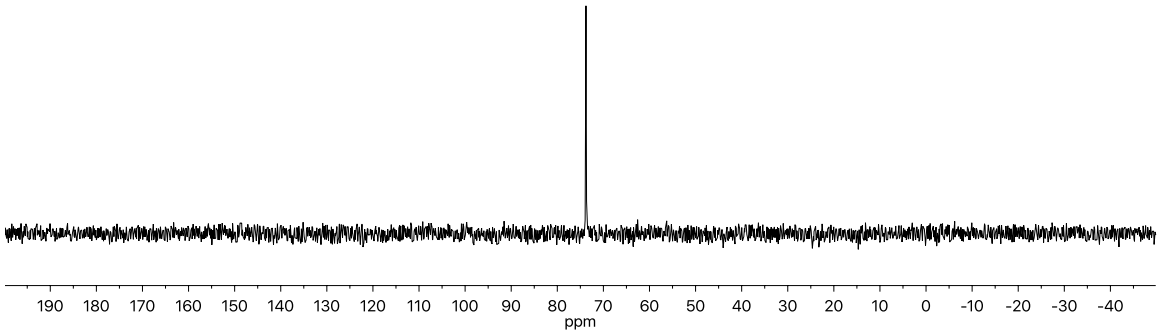

Figure B.1.2. ^{31}P NMR of **3.2** in C_6D_6 (121 MHz)

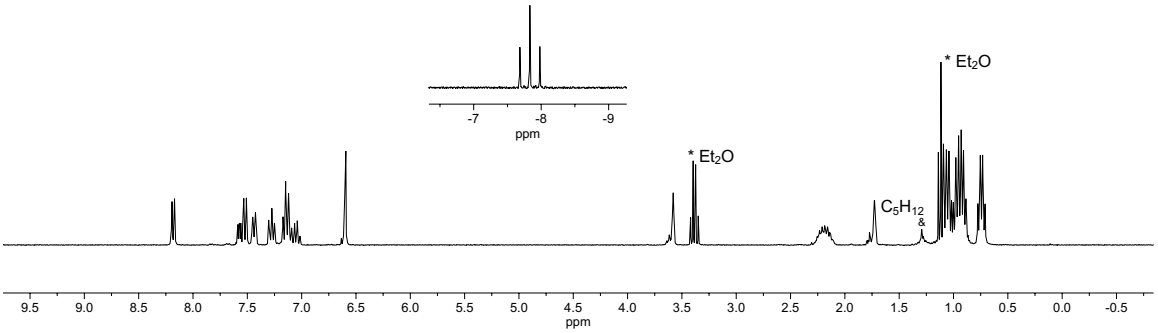

Figure B.1.3. ^{1}H NMR spectrum of **3.3-H** in THF-d_8 (300 MHz)

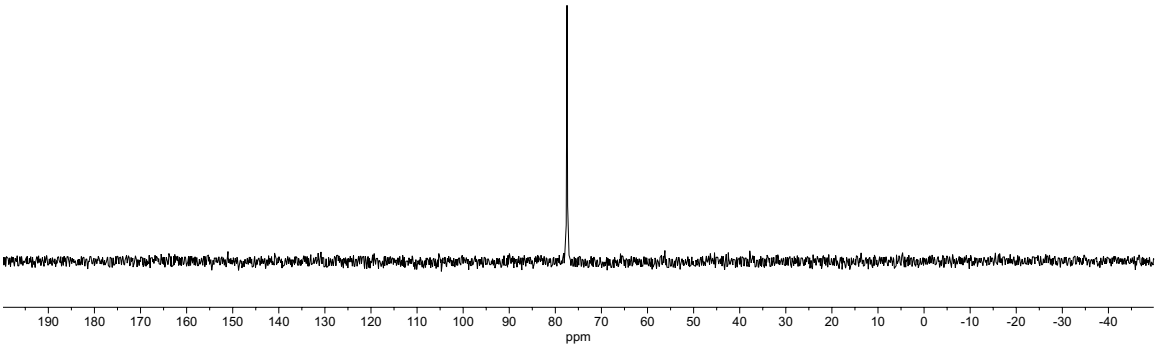

Figure B.1.4. ^{31}P NMR spectrum of **3.3-H** in THF-d_8 (121 MHz)

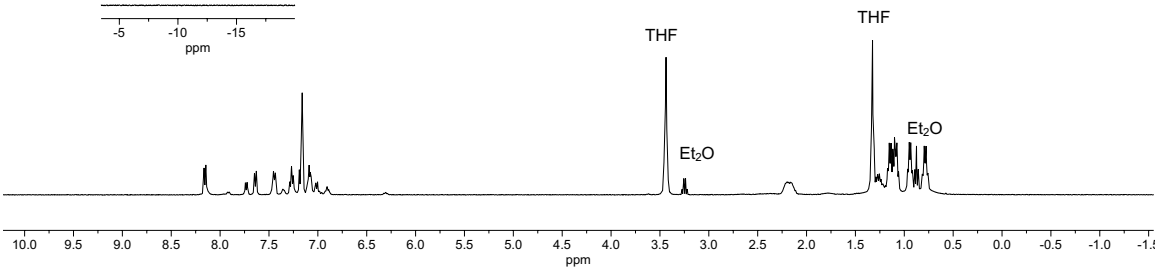

Figure B.1.5. ^{1}H NMR spectrum of **3.3-D** in C_6H_6 (400 MHz)

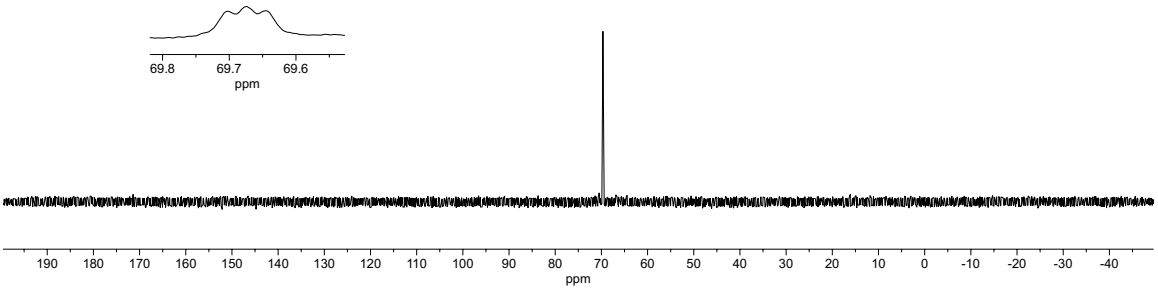

Figure B.1.6. ^{31}P NMR spectrum of **3.3-D** in C_6H_6 (162 MHz)

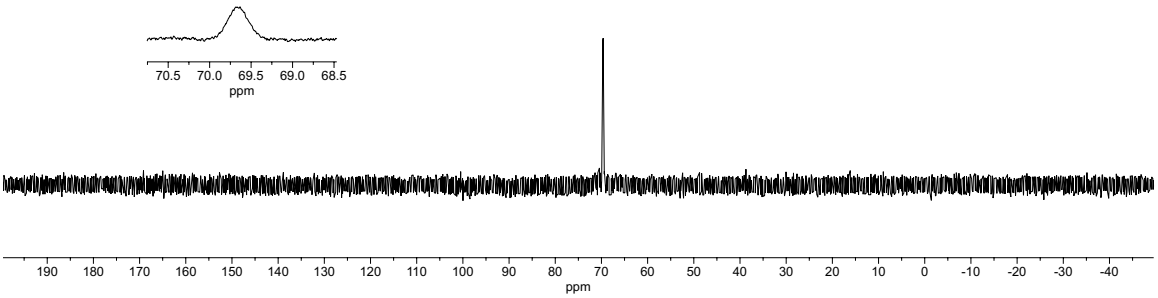

Figure B.1.7. $^{31}P\{^{2}H\}$ NMR spectrum of **3.3-D** in C_6H_6 (162 MHz)

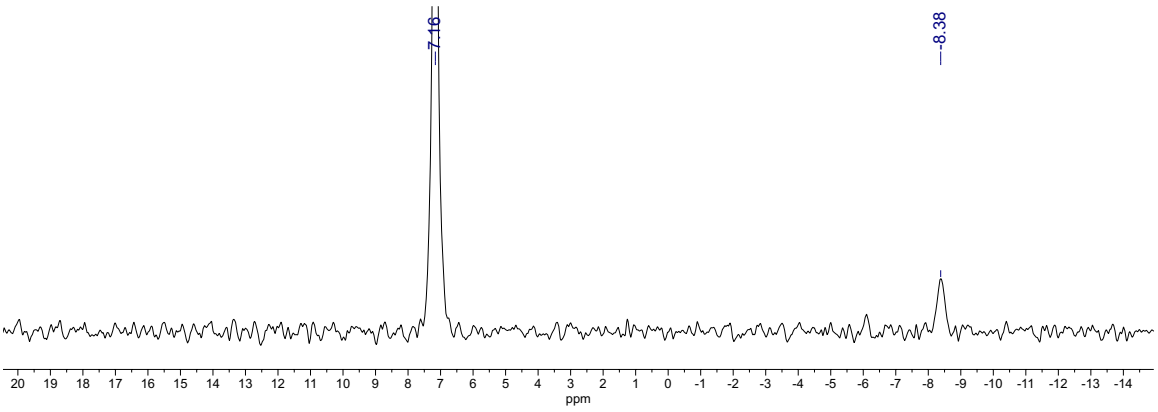

Figure B.1.8. ^{2}H NMR spectrum of **3.3-D** in C_6H_6 (61 MHz)

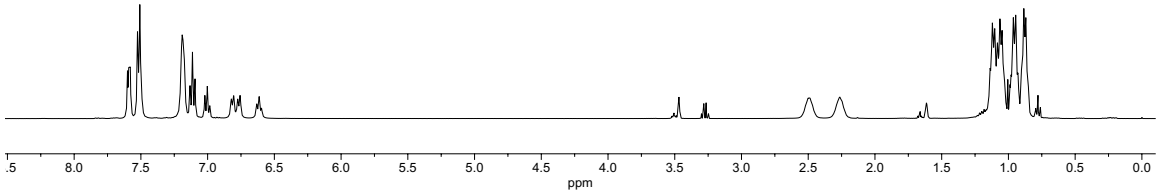

Figure B.1.9. ^{1}H NMR spectrum of **3.4** in THF-d_8 (400 MHz)

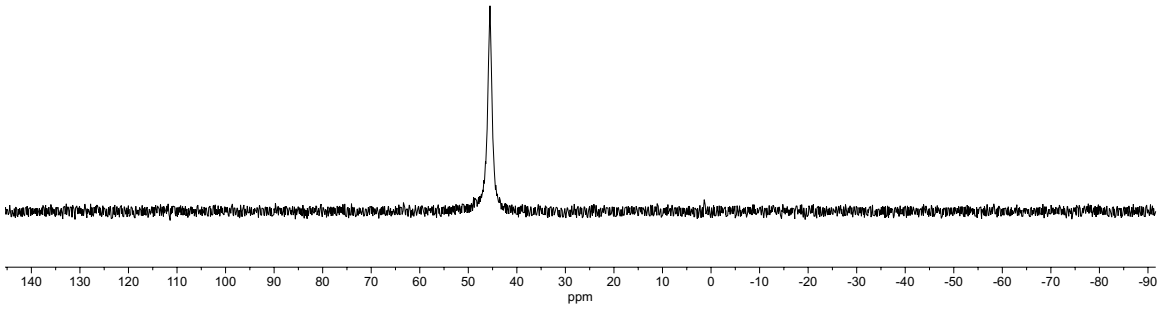

Figure B.1.10. ^{31}P NMR spectrum of **3.4** in THF-d_8 (162 MHz)

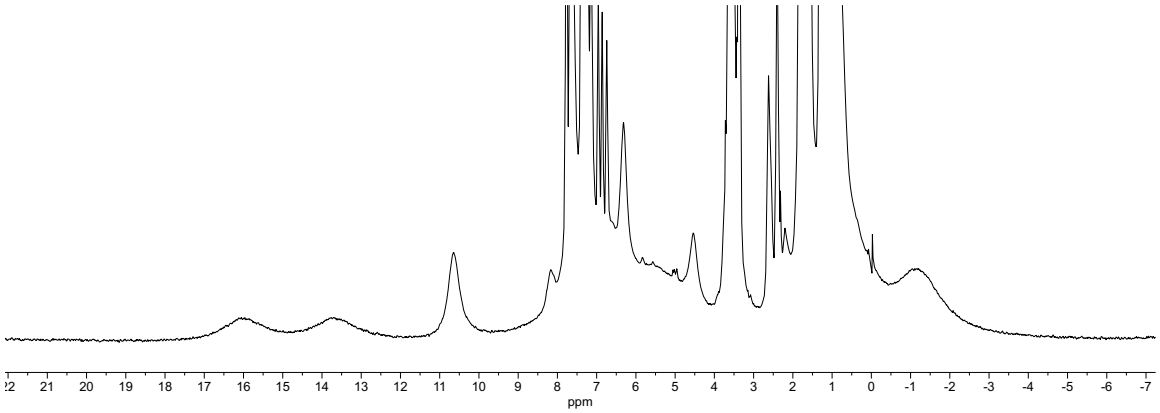

Figure B.1.11. ^{1}H NMR spectrum of **3.5-H** in THF-d_8 (500 MHz, −40 °C) *****Note: Due to facile decay of **3.5-H** to **3.4**, observable amounts of **3.4** are also present in the sample

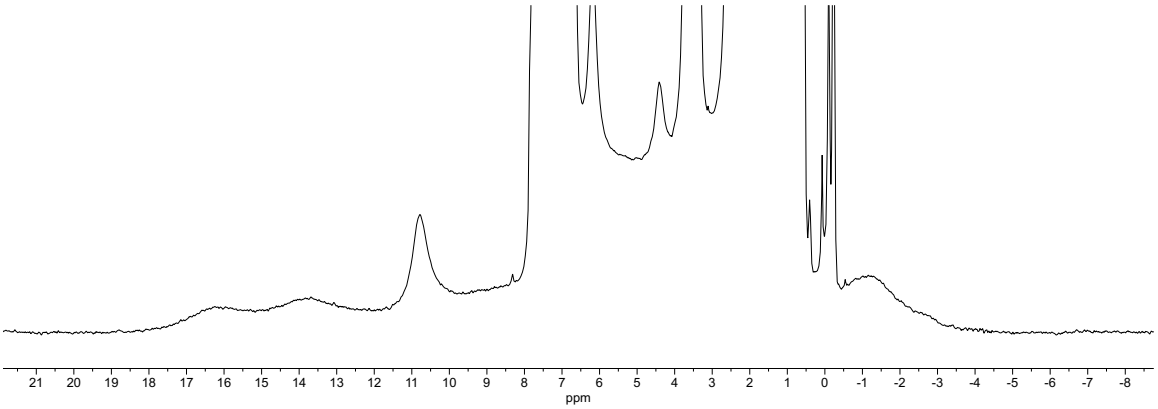

Figure B.1.12. ^{1}H NMR spectrum of **3.5-D** in THF-d_8 (500 MHz, −40 °C) *Note: Due to facile decay of **3.5-D** to **3.4**, observable amounts of **3.4** are also present in the sample

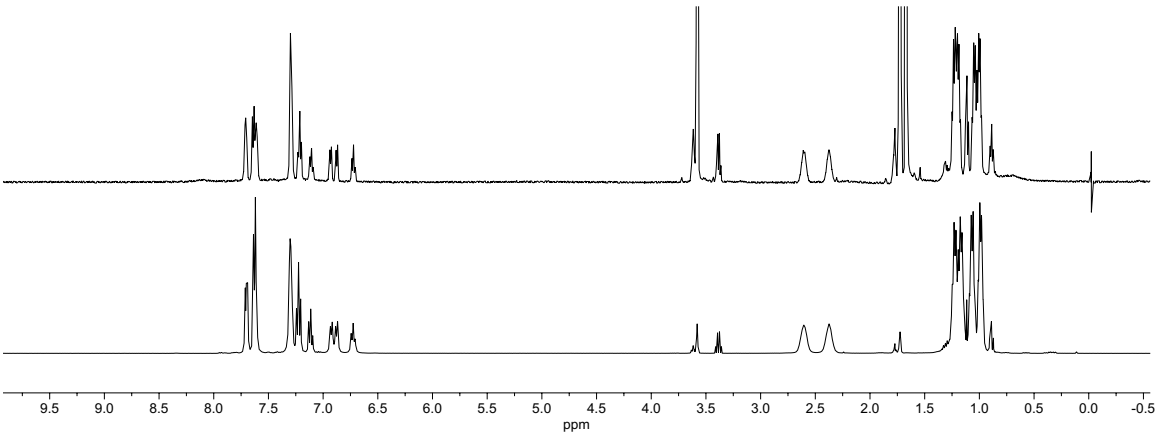

Figure B.1.13. (top) ^{1}H NMR spectrum of **3.4** generated upon warming a solution of **3.5-H** in THF-d_8 (500 MHz, 298 K) (bottom) ^{1}H NMR spectrum of an authentic sample of **3.4** in THF-d_8 (400 MHz)

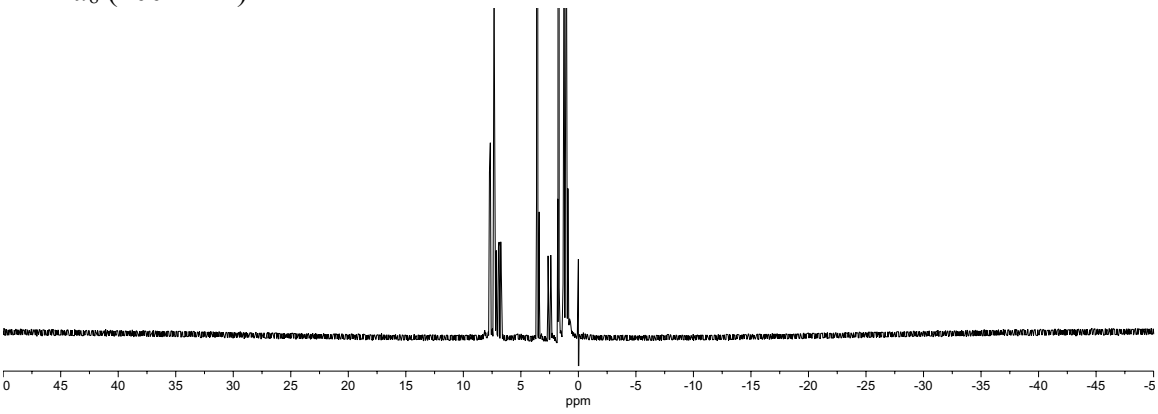

Figure B.1.14. ^{1}H NMR spectrum of **3.4** generated upon warming a solution of **3.5-H** in THF-d_8 (500 MHz, 298 K)

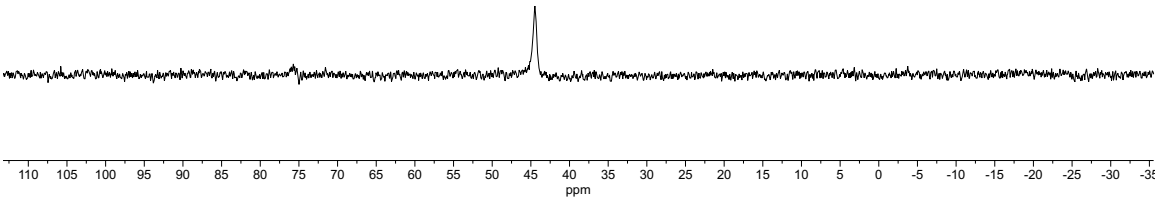

Figure B.1.15. ^{31}P NMR spectrum of **3.4** generated upon warming a solution of **3.5-H** in THF-d_8 (202 MHz, 298 K)

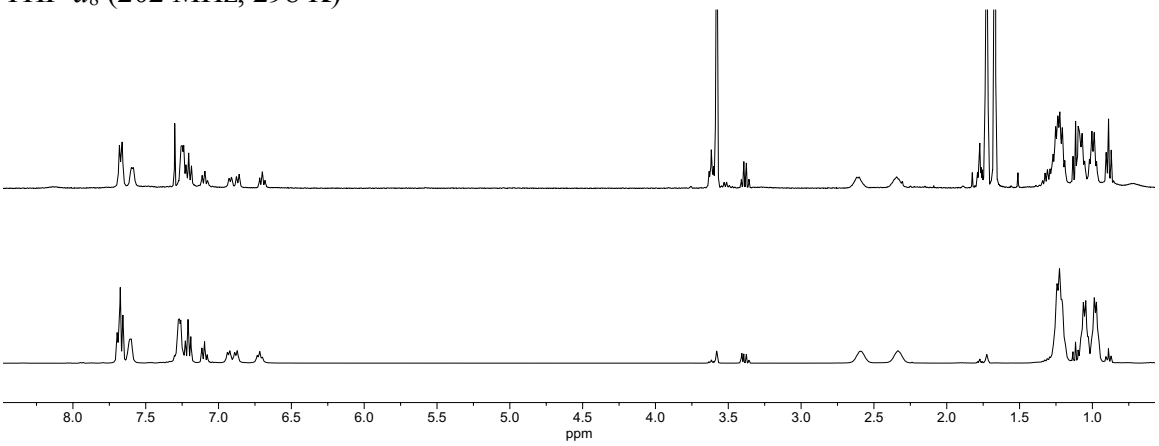

Figure B.1.16. (top) ^{1}H NMR spectrum of **3.6** generated upon warming a solution of **3.5-H** in THF-d_8 under vacuum (400 MHz, 298 K) (bottom) ^{1}H NMR spectrum of an authentic sample of **3.6** in THF-d_8 (400 MHz)

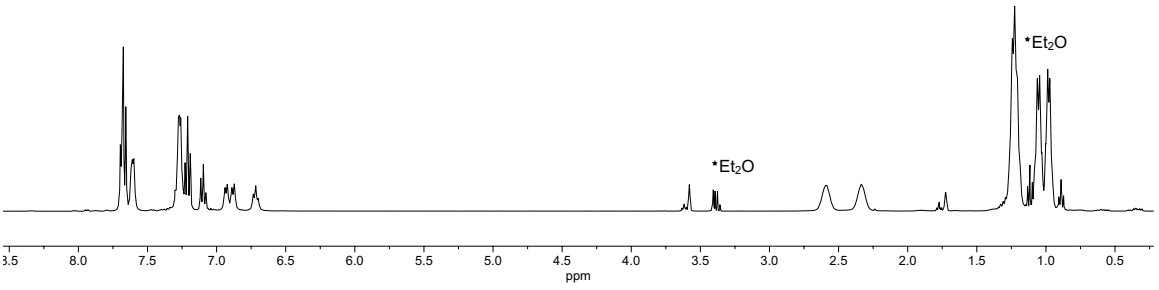

Figure B.1.17. ^{1}H NMR spectrum of **3.6** in THF-d_8 (400 MHz)

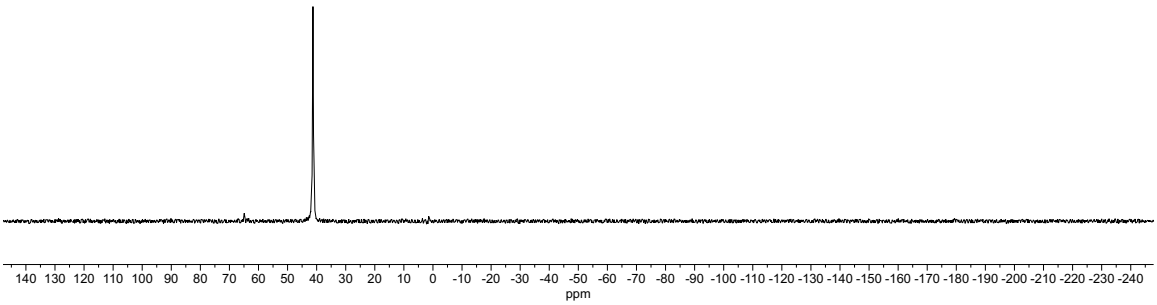

Figure B.1.18. ^{31}P NMR spectrum of **3.6** in THF-d_8 (162 MHz)

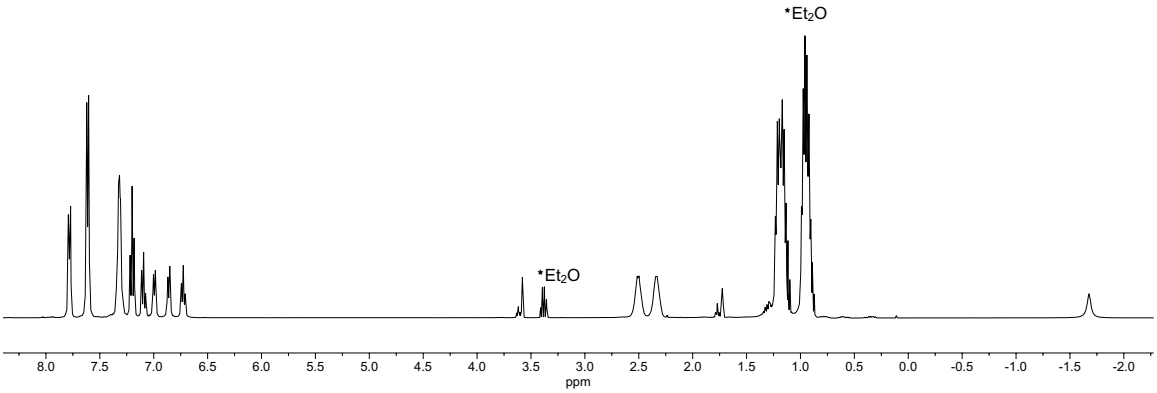

Figure B.1.19. ^{1}H NMR spectrum of **3.7** in THF-d_8 (400 MHz, 23 °C)

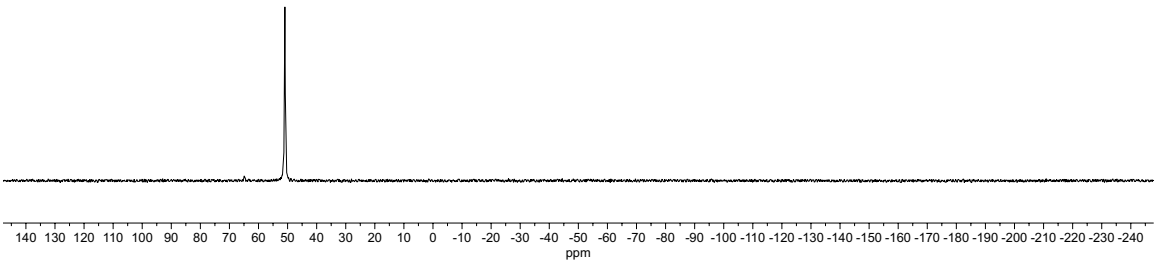

Figure B.1.20. ^{31}P NMR spectrum of **3.7** in THF-d_8 (162 MHz, 23 °C)

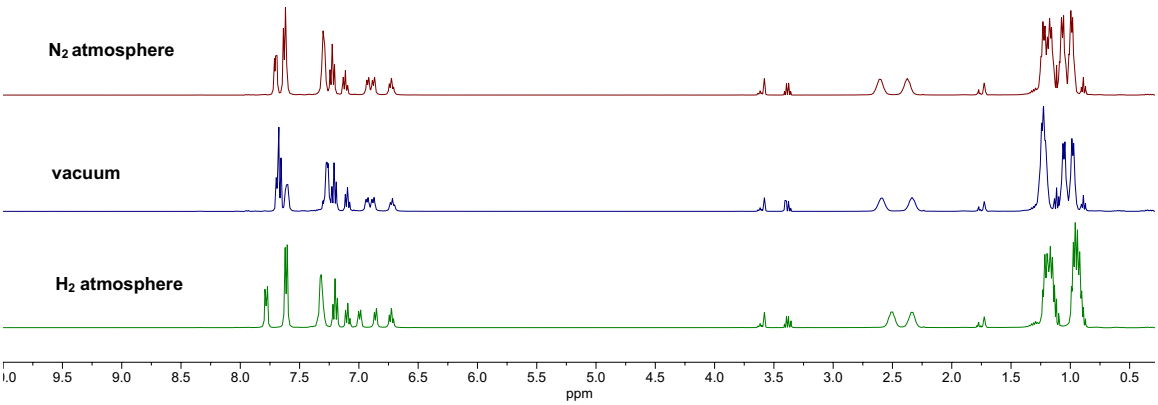

Figure B.1.21. ^{1}H NMR spectra of **3.4** (top), **3.6** (middle), and **3.7** (bottom) in THF-d_8 (400 MHz)

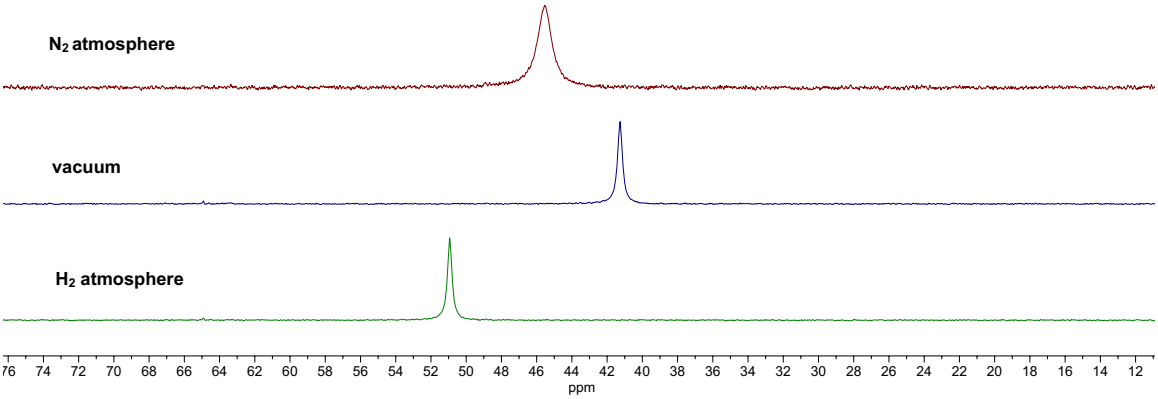

Figure B.1.22. ^{31}P NMR spectra of **3.4** (top), **3.6** (middle), and **3.7** (bottom) in THF-d_8 (162 MHz, 23 °C)

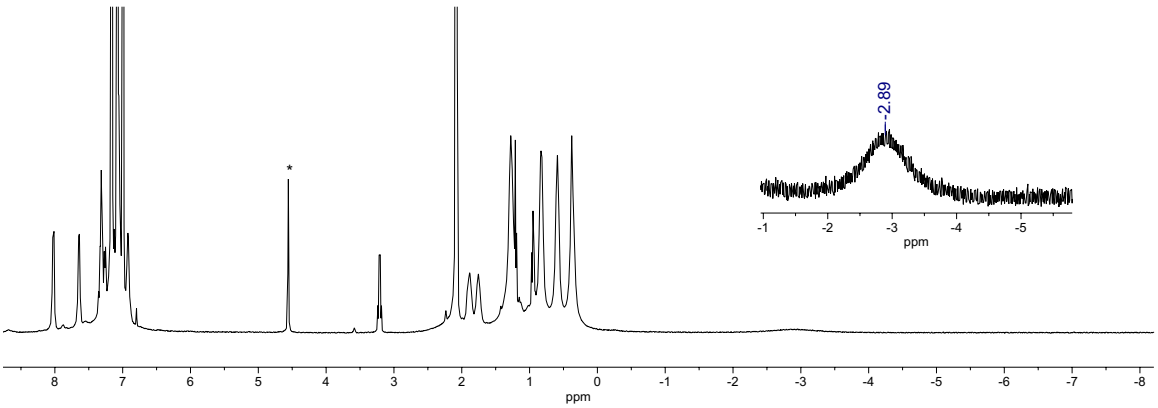

Figure B.1.23. ^{1}H NMR spectrum of **3.7** in toluene-d_8. Inset shows the peak corresponding to the bound H_2. (400 MHz, −80°C, *free H_2)

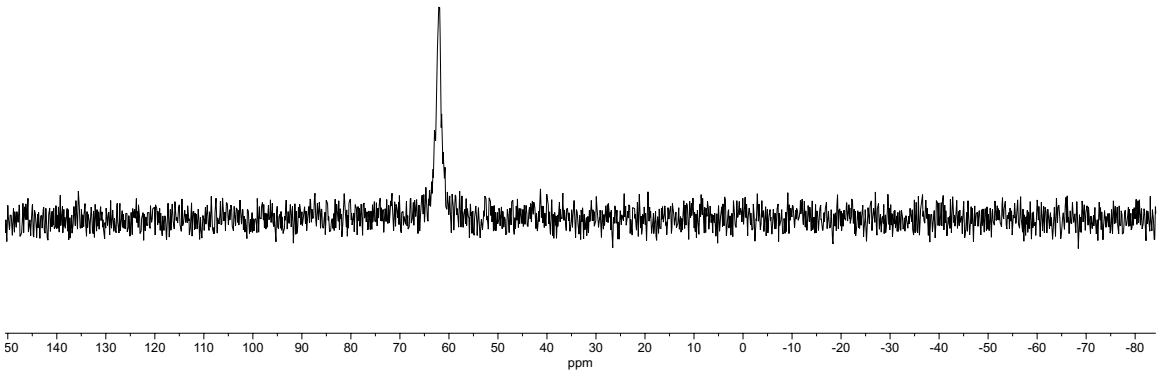

Figure B.1.24. ^{31}P NMR spectrum of **3.7** in toluene-d_8 (162 MHz, −80°C)

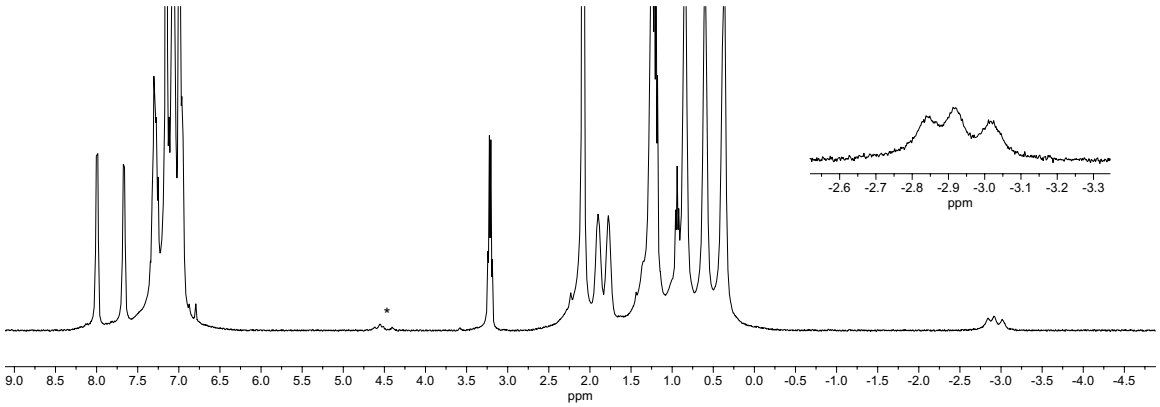

Figure B.1.25. ^{1}H NMR spectrum of **(SiP$_2$S)Ni(HD)** in toluene-d_8. Inset shows the peak corresponding to the bound HD. (400 MHz, −70°C, *free H_2 and HD, generated from CaH_2 and D_2O)

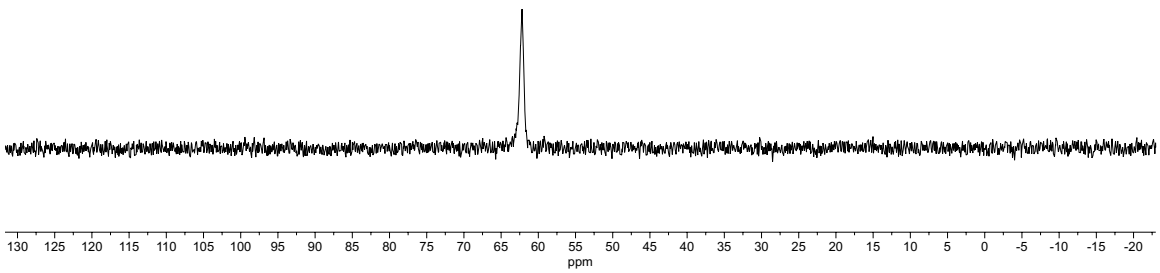

Figure B.1.26. ^{31}P NMR spectrum of **(SiP$_2$S)Ni(HD)** in toluene-d_8 (162 MHz, −70°C)

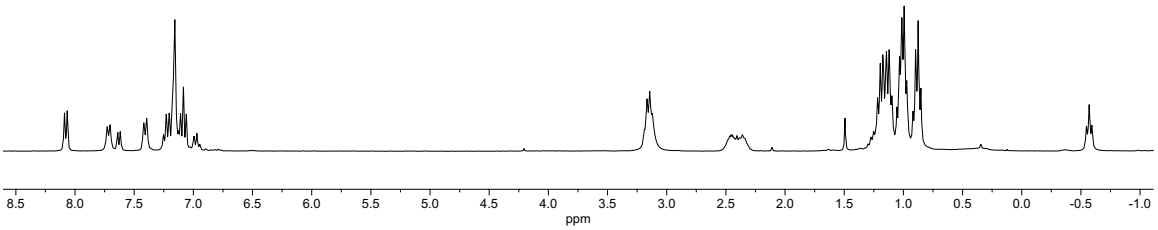

Figure B.1.27. ^{1}H NMR spectrum of **3.8** (C_6D_6, 300 MHz)

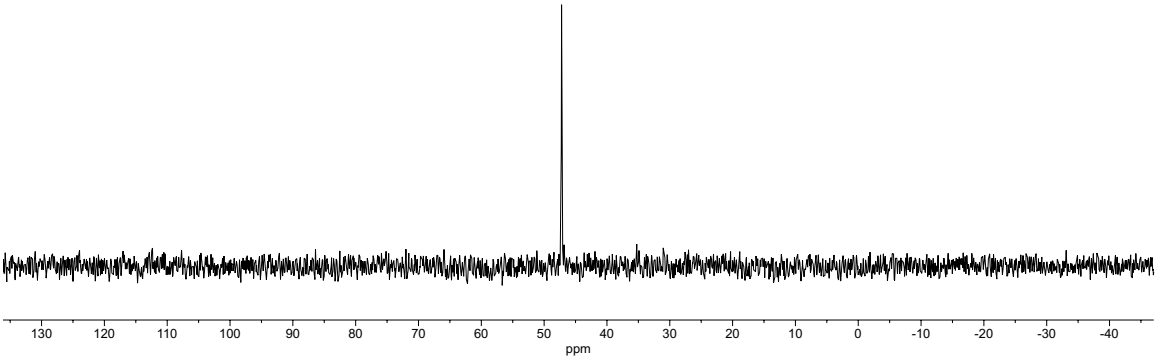

Figure B.1.28. ^{31}P NMR spectrum of **3.8** (C_6D_6, 121 MHz)

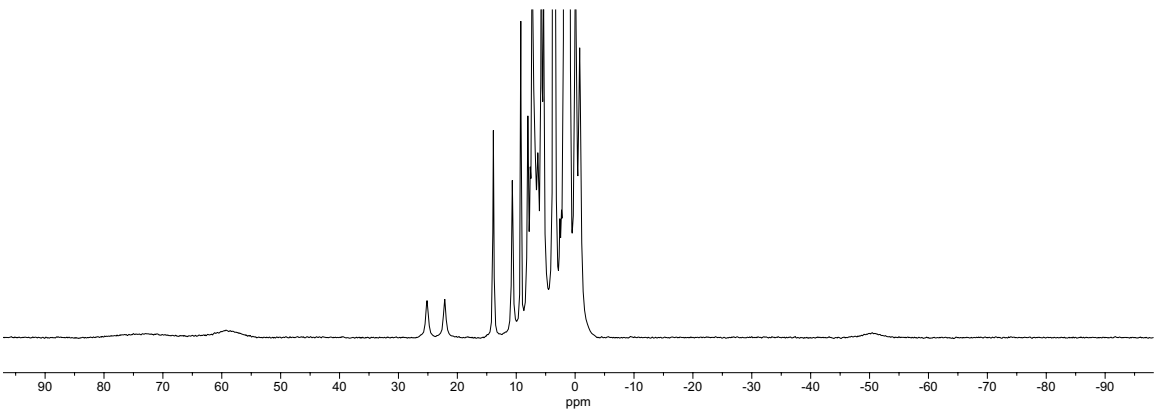

Figure B.1.29. ^{1}H NMR spectrum of **3.9** (THF-d_8, 400 MHz)

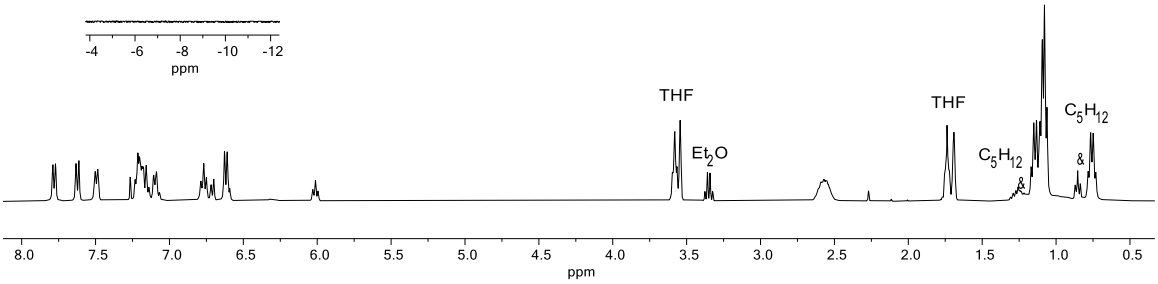

Figure B.1.30. ^{1}H NMR spectrum of the crude protonation reaction of **3.3-H** with PhOH in THF-d_8 (400 MHz)

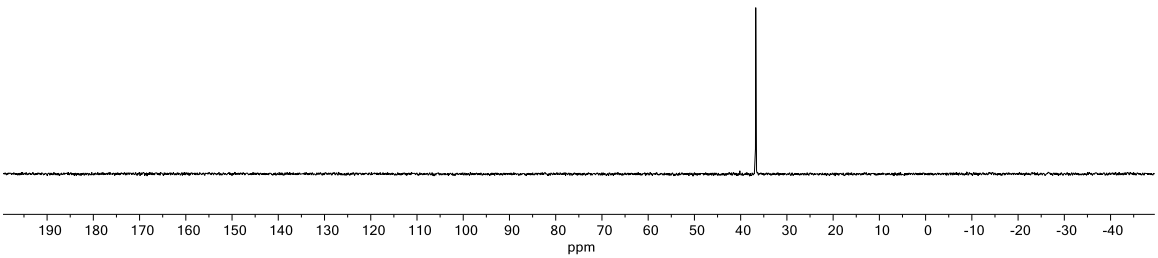

Figure B.1.31. ^{31}P NMR spectrum of the crude protonation reaction of **3.3-H** with PhOH in THF-d_8 (162 MHz)

B.2 IR Spectra

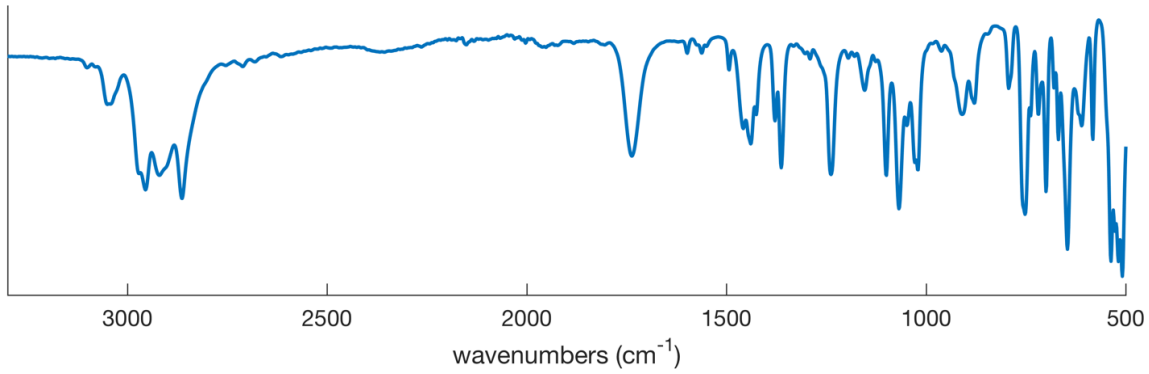

Figure B.2.1. IR spectrum of **3.2** (thin film from THF solution)

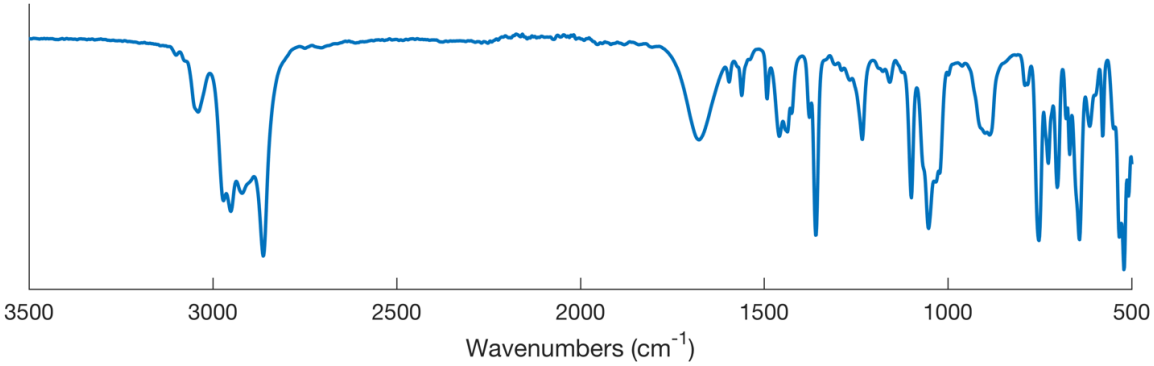

Figure B.2.2. IR spectrum of **3.3-H** (thin film from THF solution)

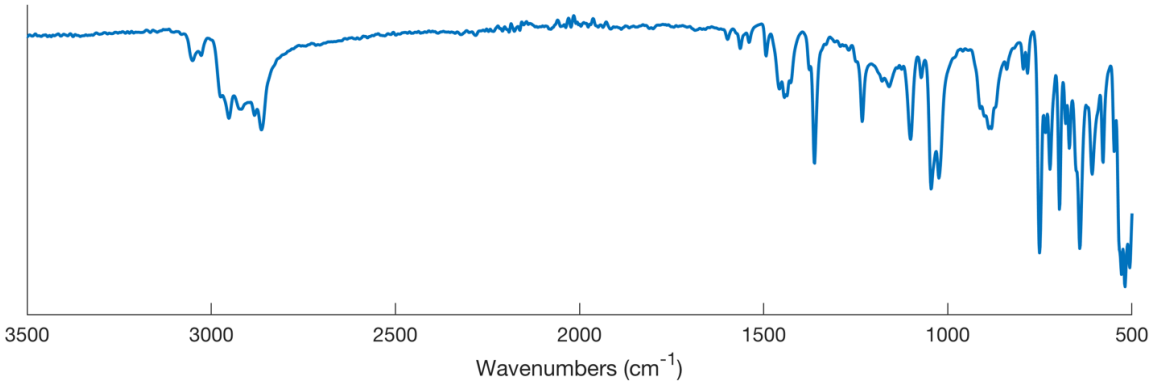

Figure B.2.3. IR spectrum of **3.3-D** (solid powder sample)

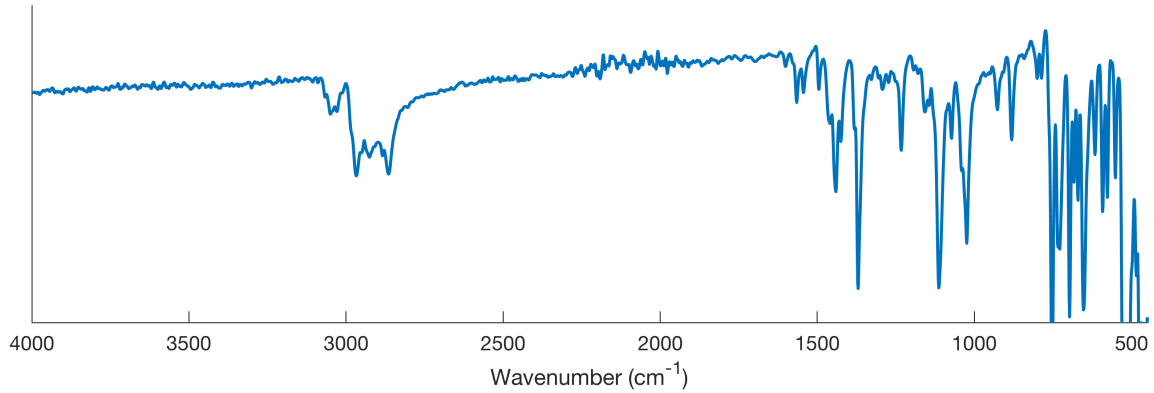

Figure B.2.4. IR spectrum of **3.4'** (solid crystalline sample)

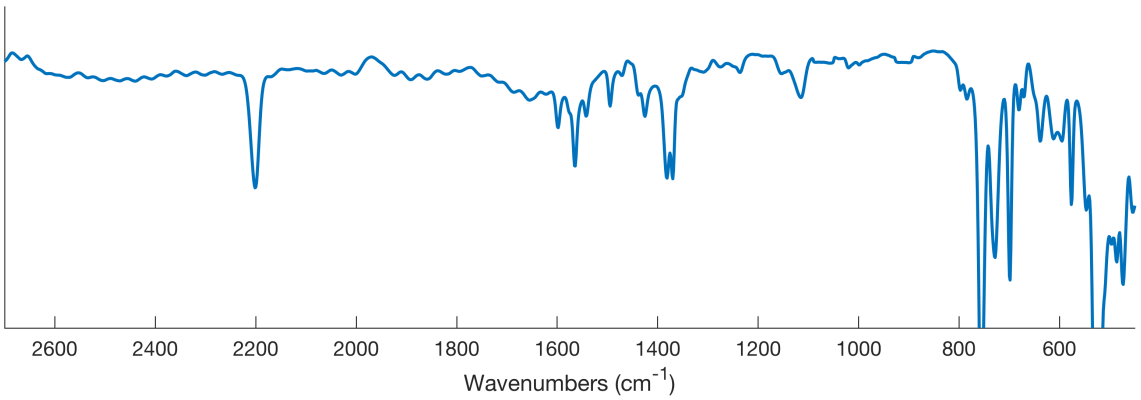

Figure B.2.5. IR spectrum of **3.4** (THF solution sample)

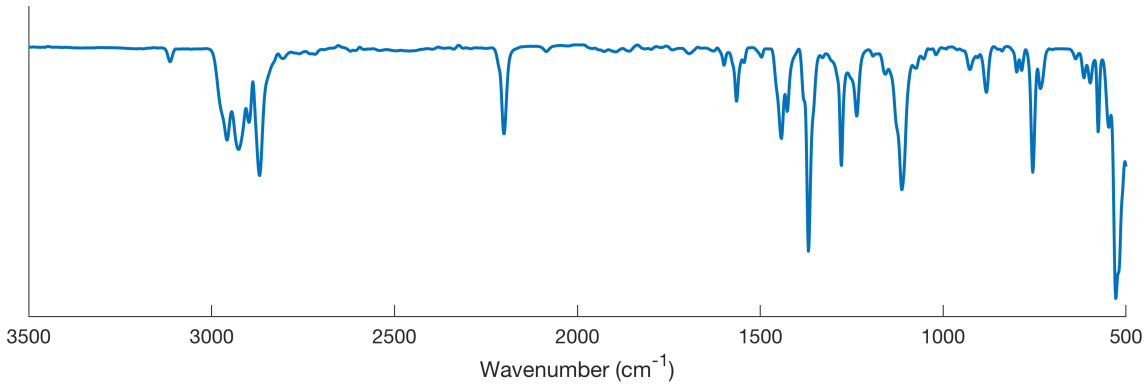

Figure B.2.6. IR spectrum of **3.4** (C_6H_6 solution sample)

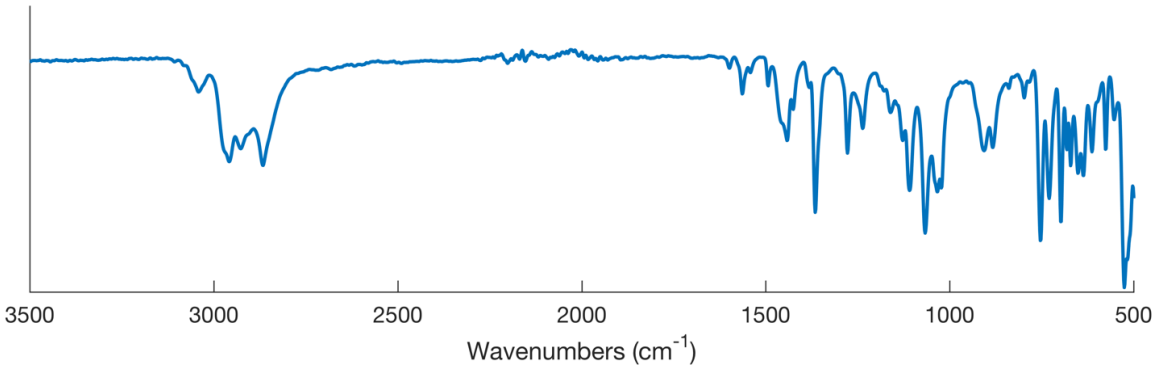

Figure B.2.7. IR spectrum of **3.4'** (thin film from THF solution dried under N_2 stream, collected in N_2 glovebox)

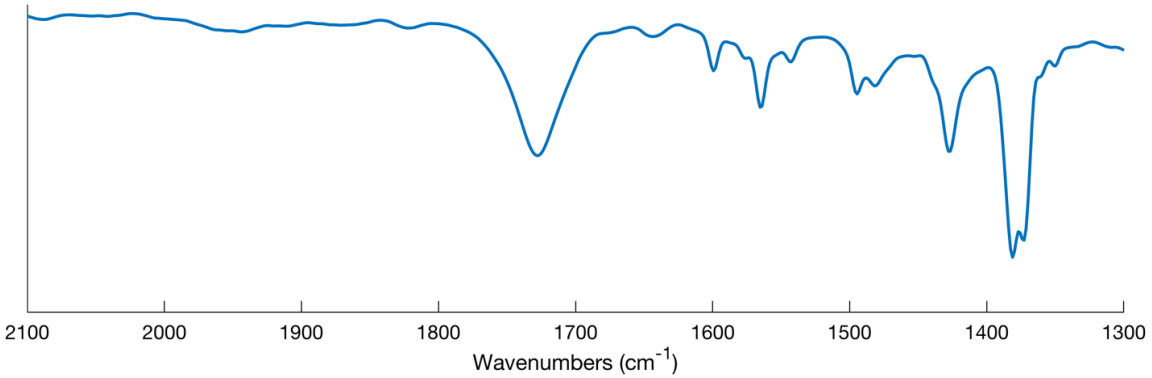

Figure B.2.8. IR spectrum of **3.5-H** (THF solution sample, −78 °C)

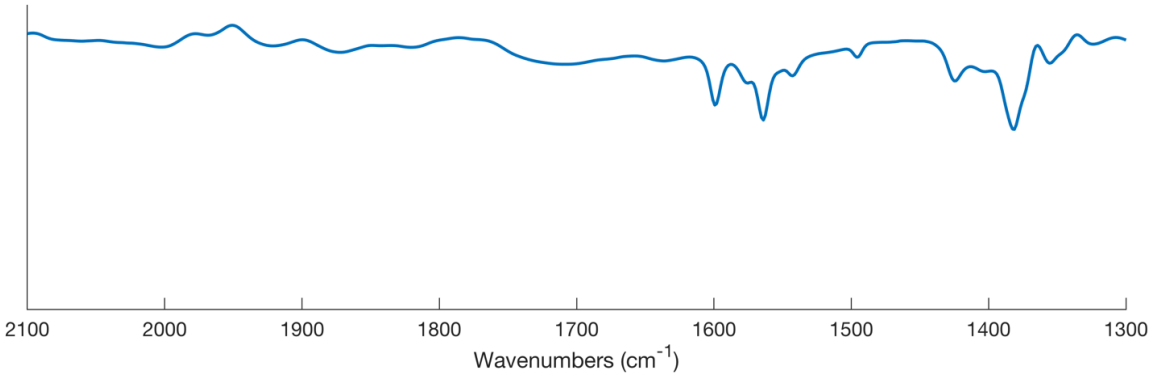

Figure B.2.9. IR spectrum of **3.5-D** (THF solution sample, −78 °C)

B.3 X-Ray Diffraction Data

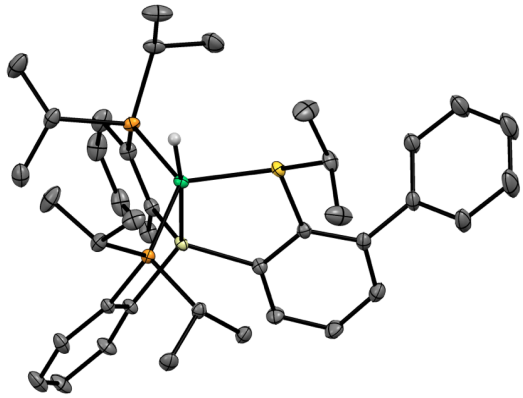

Figure B.3.1. Full asymmetric unit of **3.2**. C–*H* hydrogen atoms omitted; thermal ellipsoids at 50% probability.

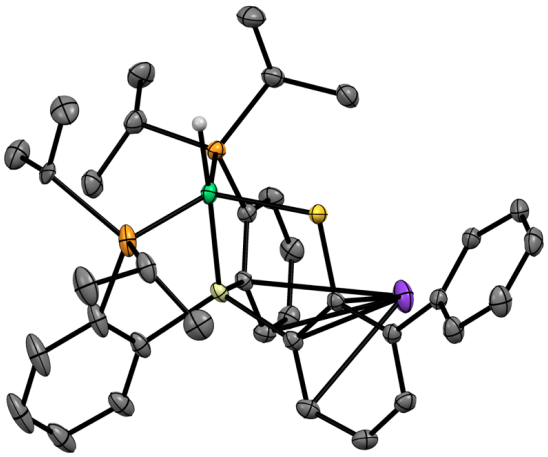

Figure B.3.2. Structure of **3.3** with omission of disordered components, C–*H* hydrogen atoms, and solvent molecules. Thermal ellipsoids at 50% probability.

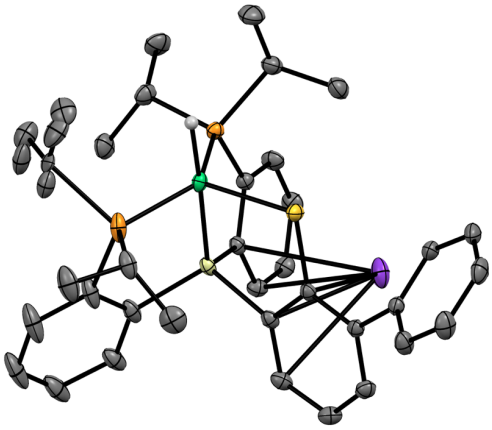

Figure B.3.3. Full asymmetric unit of **3.3** including disordered components. C–*H* hydrogen atoms omitted; thermal ellipsoids at 50% probability.

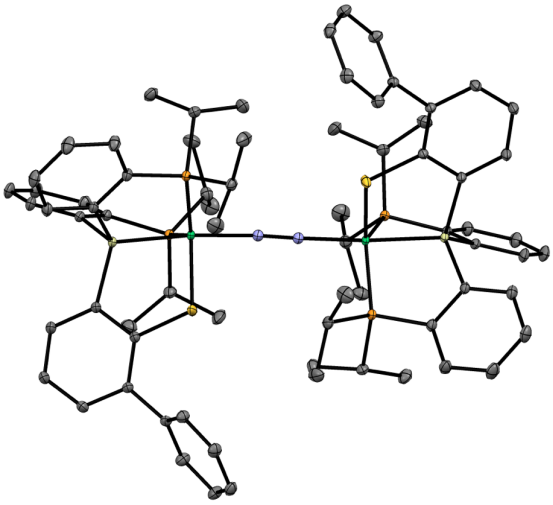

Figure B.3.4. Structure of **3.4'** with omission of C–*H* hydrogen atoms and solvent molecules. Thermal ellipsoids at 50% probability.

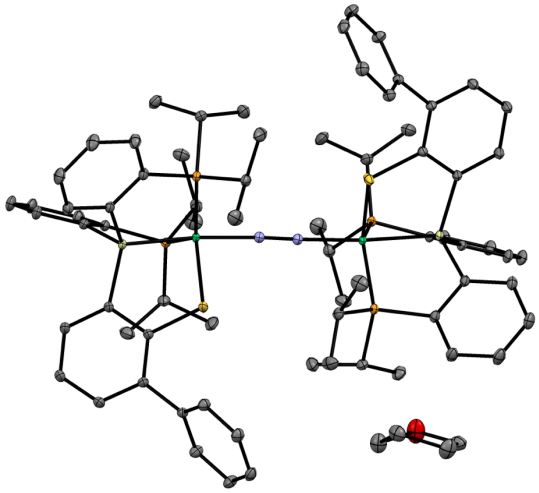

Figure B.3.5. Full asymmetric unit of **3.4'** including solvent. C–*H* hydrogen atoms omitted; thermal ellipsoids at 50% probability.

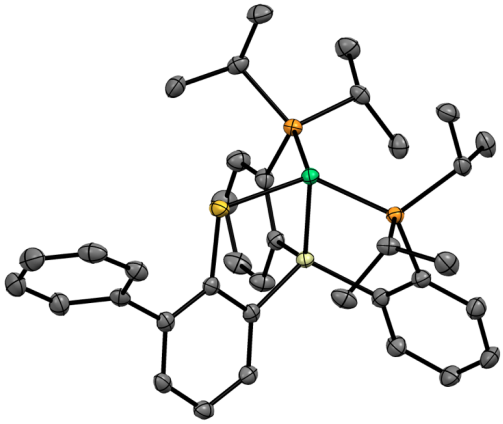

Figure B.3.6. Full asymmetric unit of **3.7**. C–*H* hydrogen atoms omitted; thermal ellipsoids at 50% probability.

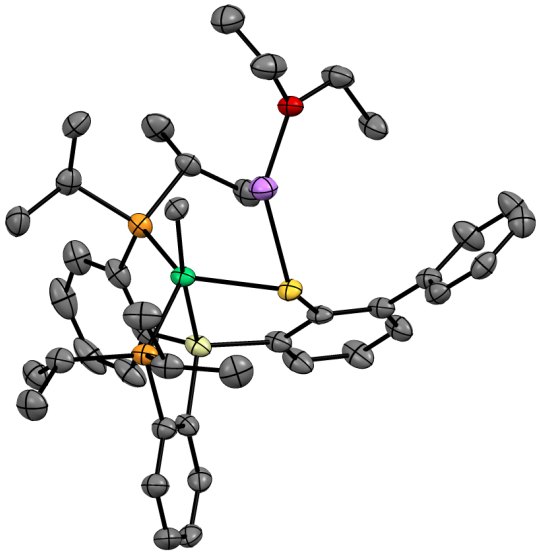

Figure B.3.7. Structure of **3.8** with omission of disordered components and hydrogen atoms. Thermal ellipsoids at 50% probability.

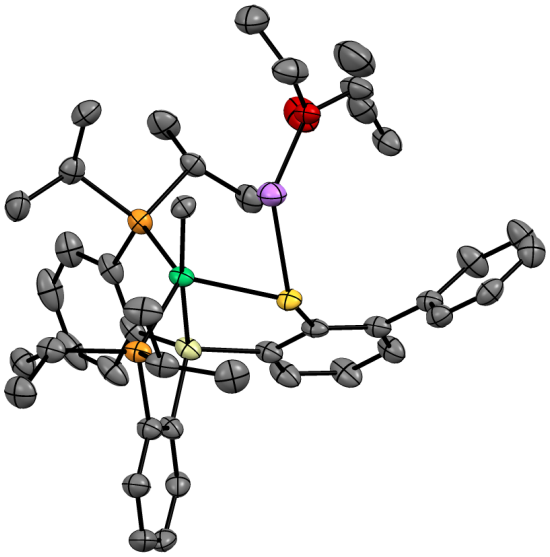

Figure B.3.8. Full asymmetric unit of **3.8** including disordered components. Hydrogen atoms omitted; thermal ellipsoids at 50% probability.

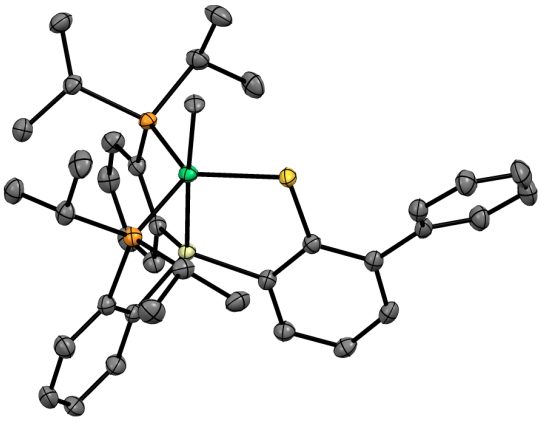

Figure B.3.9. Structure of **3.9** with omission of disordered components, hydrogen atoms, and solvent molecules. Thermal ellipsoids at 50% probability.

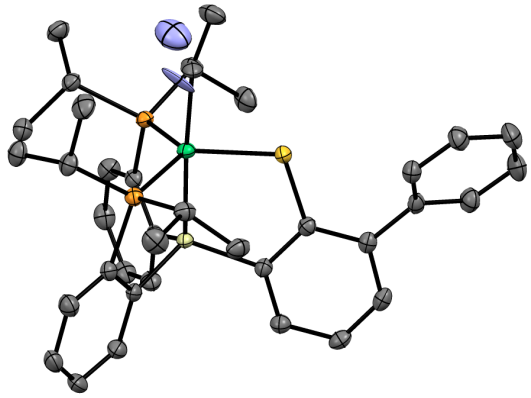

Figure B.3.10. Full asymmetric unit of **3.9** including disordered components. The apical ligand is modeled with 87% occupancy as Ni–CH_3 and 13% occupancy as Ni–N_2. Hydrogen atoms omitted; thermal ellipsoids at 50% probability.

B.4 UV-Visible Data

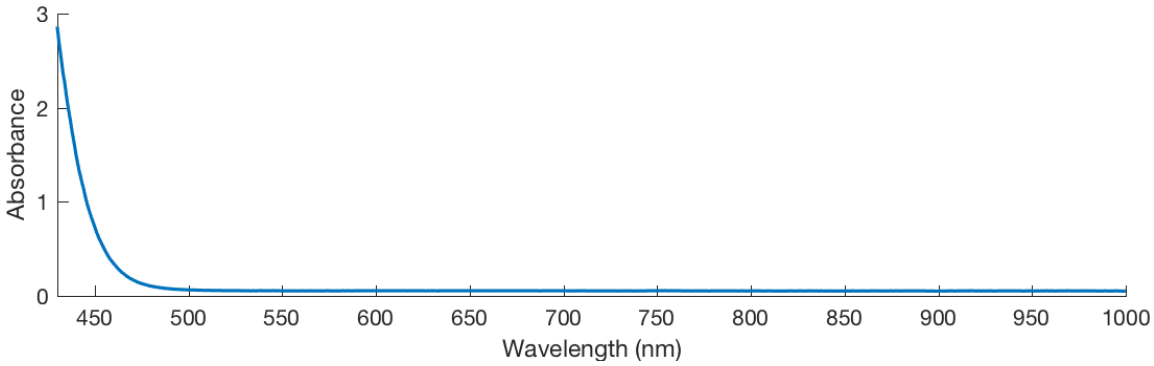

Figure B.4.1. UV-vis spectrum of **3.2** in THF

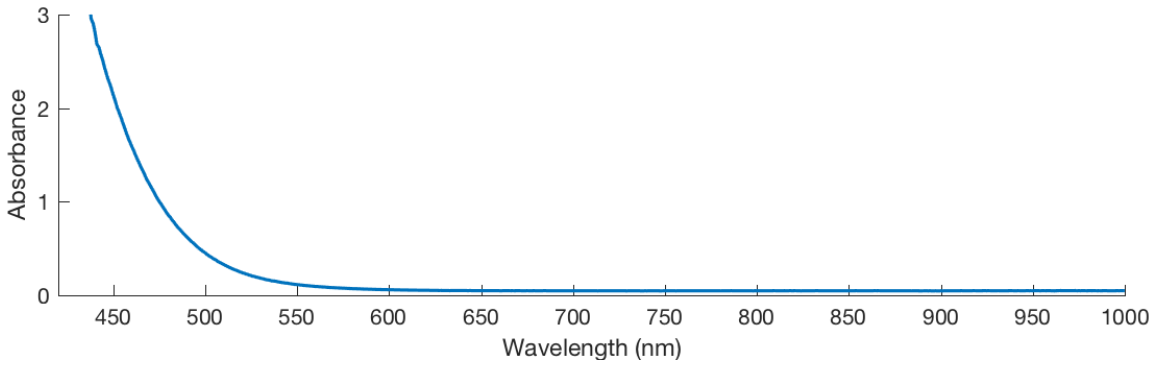

Figure B.4.2. UV-vis spectrum of **3.3-H** in THF

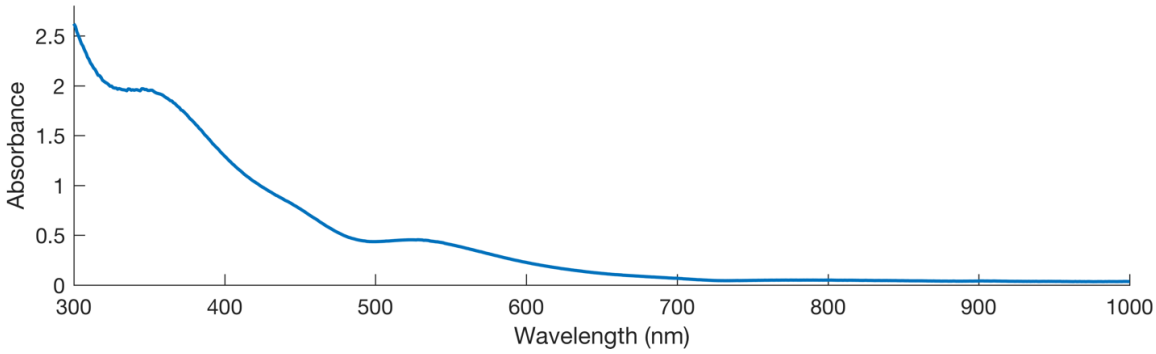

Figure B.4.3. UV-vis spectrum of **3.4** in THF (1 mm cuvette)

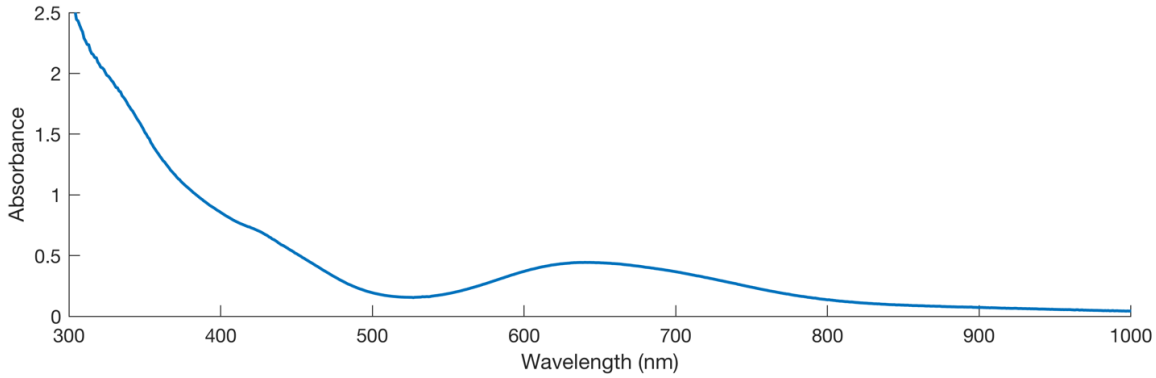

Figure B.4.4. UV-vis spectrum of **3.5-H** in THF

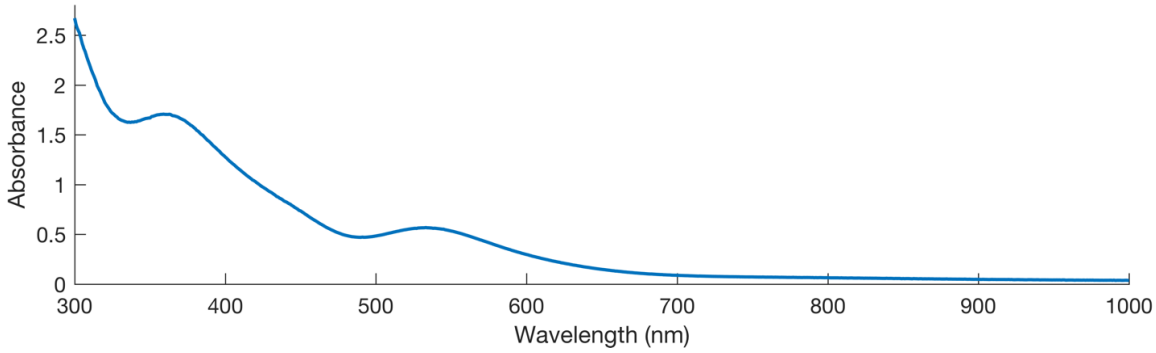

Figure B.4.5. UV-vis spectrum of **3.6** in THF (1 mm cuvette)

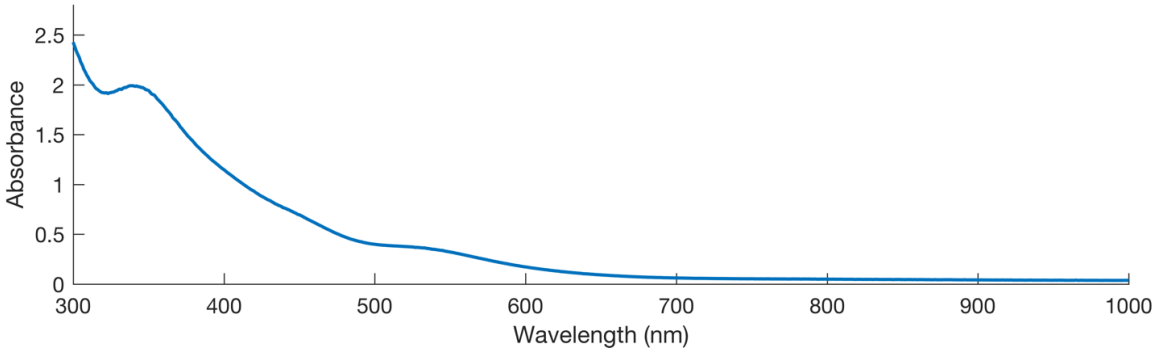

Figure B.4.6. UV-vis spectrum of **3.7** in THF (1 mm cuvette)

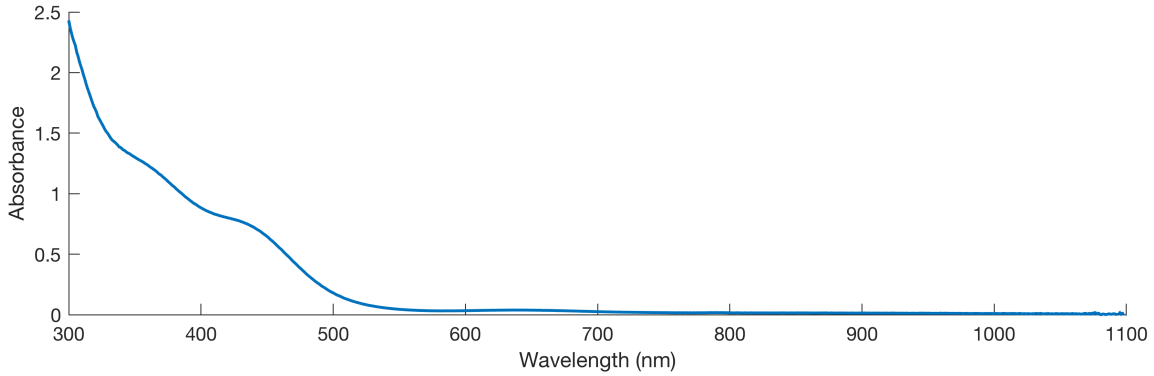

Figure B.4.7. UV-vis spectrum of **3.8** in C_6H_6

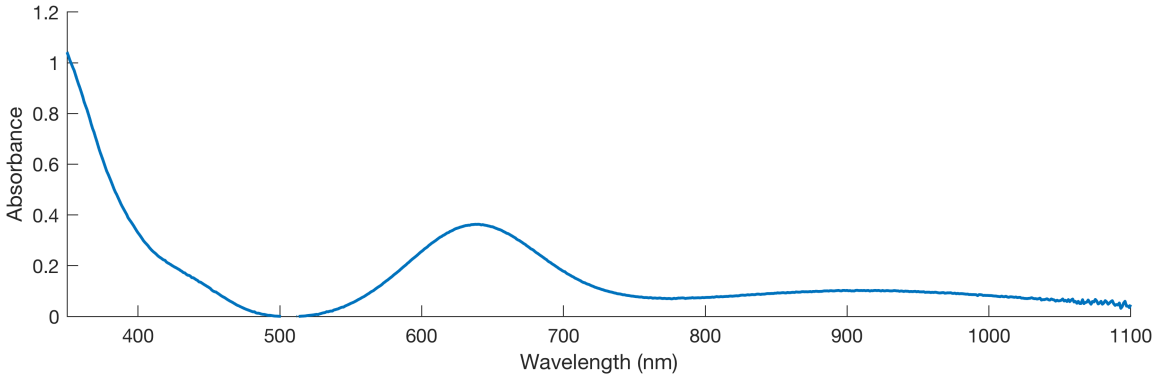

Figure B.4.8. UV-vis spectrum of **3.9** in THF

B.5 Cyclic Voltammetry Data

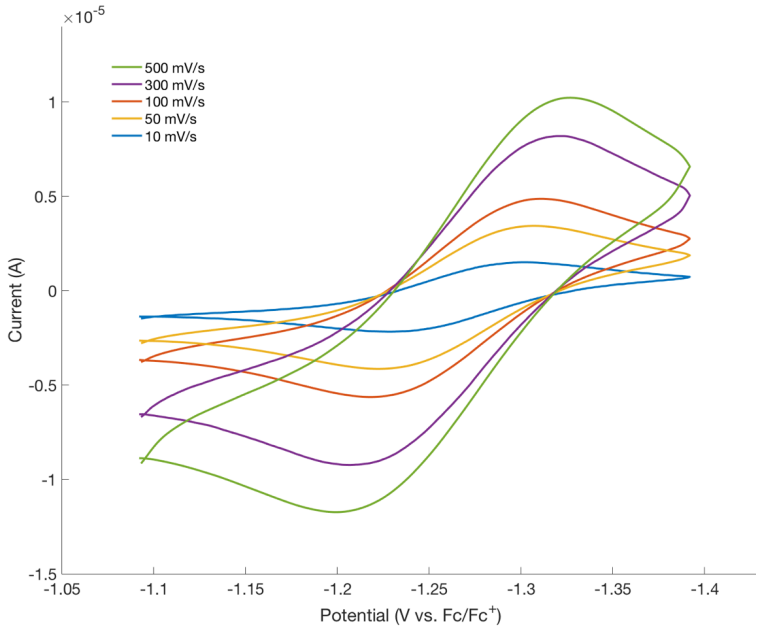

Figure B.5.1. Cyclic voltammograms of **3.3-H** at various scan rates, depicting the $Ni^{III/II}$ couple at −1.26 V vs Fc/Fc^+ (0.4 M $[NBu_4][PF_6]$ in THF). A glassy carbon working, Pt counter, and Ag/Ag^+ reference electrodes were utilized.

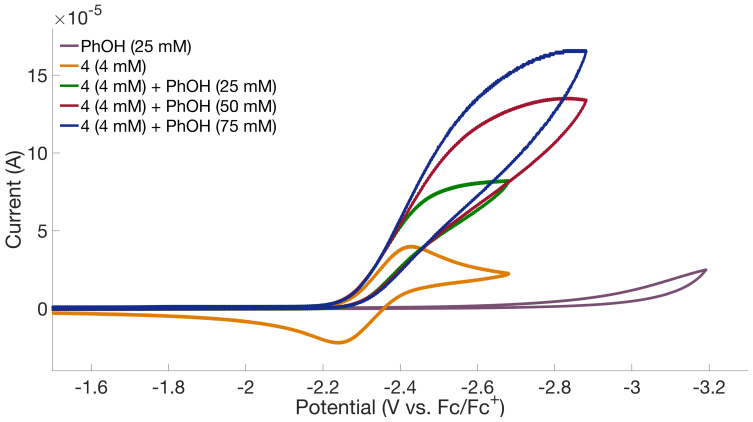

Figure B.5.2. Cyclic voltammograms of **3.4** in the presence of PhOH in 0.4 M $[NBu_4][PF_6]$ in THF (scan rate = 100 mV/s). A glassy carbon working electrode, Ag/AgOTf reference electrode and Pt counter electrodes were utilized.

B.6 Bulk Electrolysis Data

Table B.6.1. H_2 generation from catalyzed reduction of PhOH

Entry	Complex 3.4 (mM)	PhOH (mM)	Equiv. H_2/Ni[a]	Faradaic eff. (%)
a	0.5	50	6.4±0.6	106±5
b	0	50	0.6±0.2	96±6
c	0.5	0	0.0±0.0	-
d[b]	0	50	0.9	103

Yields are an average of 2 runs; the spread between the two runs is shown as a standard deviation for N = 2. [a]Equivalents of H_2 are listed per Ni center. [b]A working electrode from Entry A was rinsed with THF after electrolysis and then used directly as the working electrode in Entry D. Yield of H_2 from a single run.

B.7 CW EPR Data

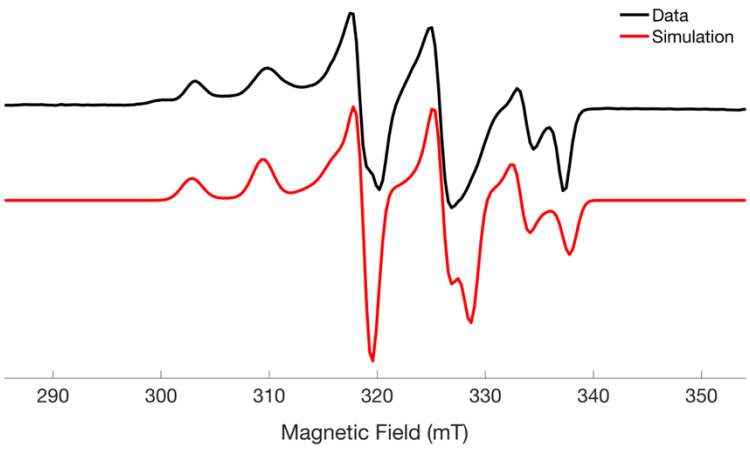

Figure B.7.1. X-band CW EPR spectrum of **3.5-D** in 2-MeTHF with simulations. Simulation parameters: **g** = [2.166, 2.056, 2.039]; **A**(^{31}Pα) = **A**(^{31}Pβ) = [200, 210, 260] MHz); **A**(^{2}H) = [0.25, 0.25, 4.9] MHz.; Acquisition parameters: MW frequency = 9.371 GHz; temperature = 77 K; MW power = 2 mW; modulation amplitude = 2 G; conversion time = 82 ms.

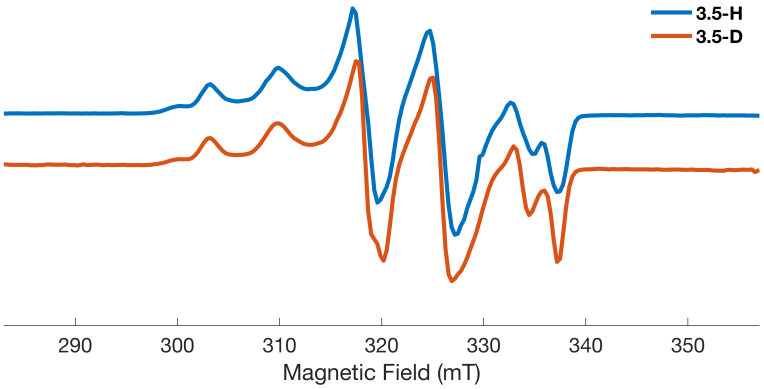

Figure B.7.2. X-band CW EPR spectra of **3.5-H** (blue) and **3.5-D** (orange) in 2-MeTHF. Acquisition parameters: MW frequency = 9.371 GHz; temperature = 77 K; MW power = 2 mW; modulation amplitude = 2 G; conversion time = 82 ms.

B.8 ESE-EPR Data

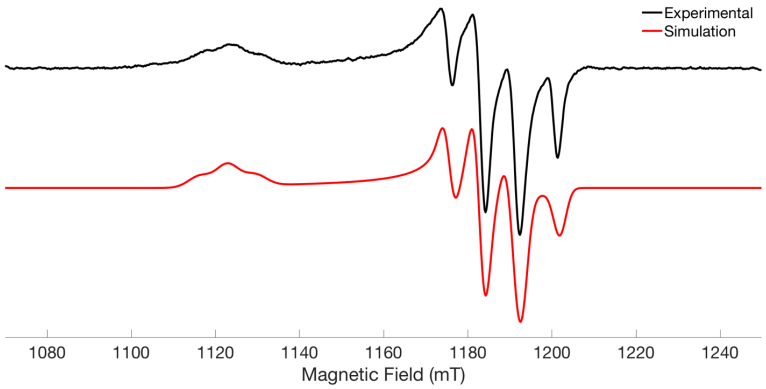

Figure B.8.1. Q-band ESE-EPR spectrum of **3.5-D** in 2Me-THF with simulations. Simulation parameters: $\mathbf{g} = [2.166, 2.056, 2.039]$; $\mathbf{A}(^{31}\text{P}\alpha) = \mathbf{A}(^{31}\text{P}\beta) = [200, 210, 260]$ MHz; $\mathbf{A}(^{2}\text{H}) = [0.25, 0.25, 4.9]$ MHz. Acquisition parameters: MW frequency = 34.032 GHz, temperature = 12 K; π pulse length = 160 ns, τ = 400 ns, shot rep time (srt) = 1 ms.

B.9 HYSCORE Data

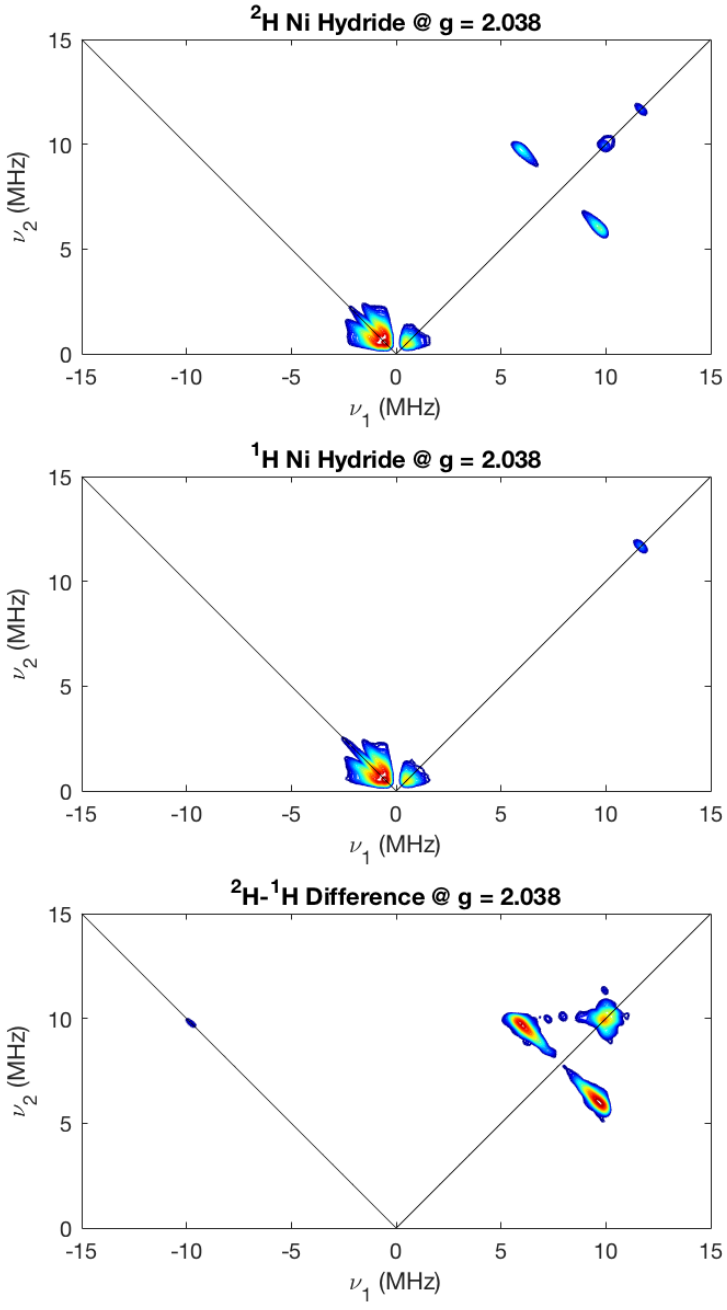

Figure B.9.1. Q-band HYSCORE spectra of **3.5-D** (top) and **3.5-H** (middle) in 2Me-THF measured at magnetic fields corresponding to g = 2.038. The corresponding ^{2}H – ^{1}H difference spectrum is depicted on the bottom. Experimental conditions: microwave frequency = 34.055 GHz; temperature = 14 K; B_0 = 1194 mT; τ = 100 µs $t_1 = t_2$ = 100 ns; $\Delta t_1 = \Delta t_2$ = 16 ns; shot repetition time (srt) = 1 ms.

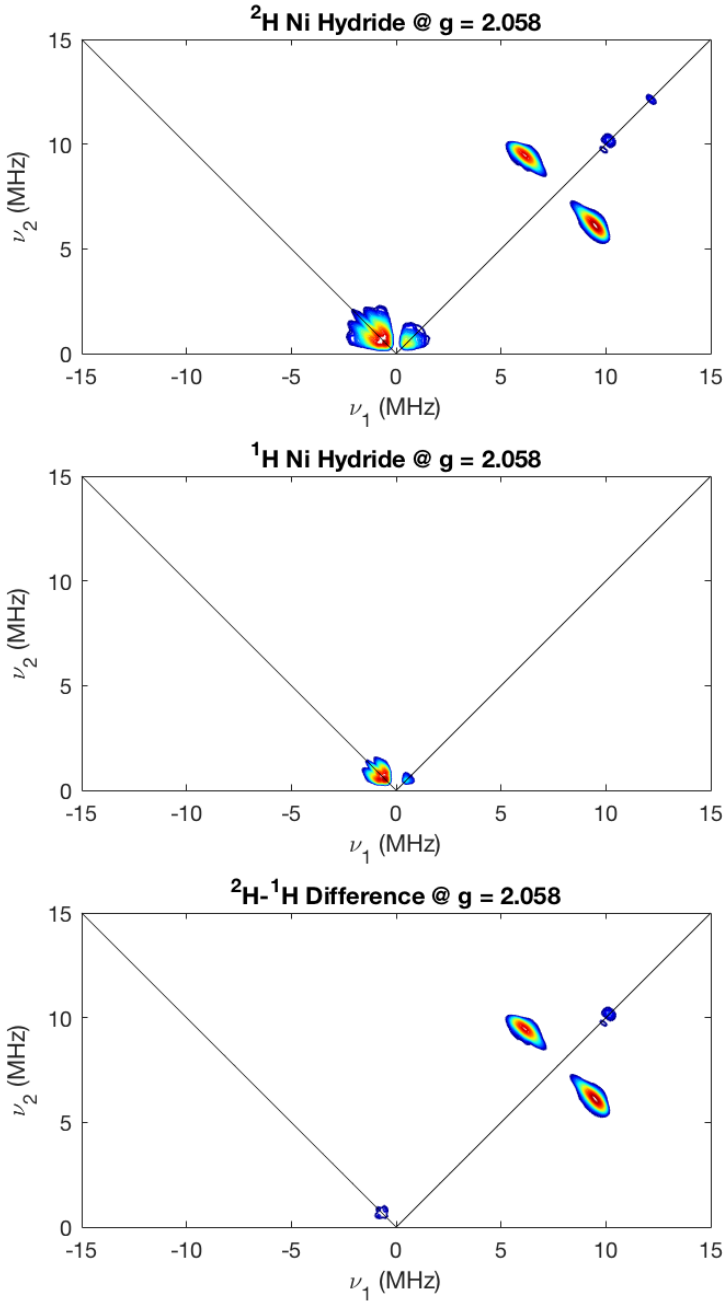

Figure B.9.2. Q-band HYSCORE spectra of **3.5-D** (top) and **3.5-H** (middle) in 2Me-THF measured at magnetic fields corresponding to g = 2.058. The corresponding ^{2}H – ^{1}H difference spectrum is depicted on the bottom. Experimental conditions: microwave frequency = 34.05514 GHz; temperature = 14 K; B_0 = 1182.4 mT G; τ = 100 µs; $t_1 = t_2$ = 100 ns; $\Delta t_1 = \Delta t_2$ = 16 ns; shot repetition time (srt) = 1 ms.

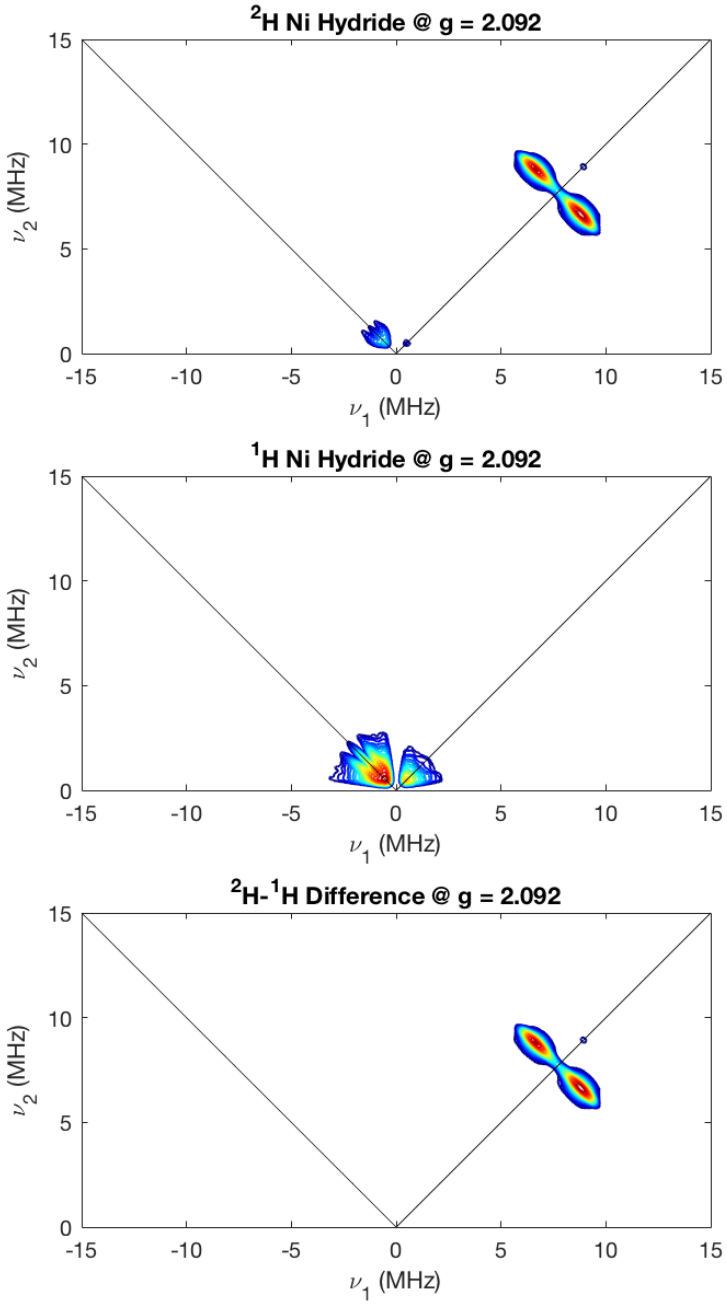

Figure B.9.3. Q-band HYSCORE spectra of **3.5-D** (top) and **3.5-H** (middle) in 2Me-THF measured at magnetic fields corresponding to g = 2.092. The corresponding ^{2}H – ^{1}H difference spectrum is depicted on the bottom. Experimental conditions: microwave frequency = 34.05514 GHz; temperature = 14 K; B_0 = 1163 mT; τ = 100 µs; $t_1 = t_2$ = 100 ns; $\Delta t_1 = \Delta t_2$ = 16 ns; shot repetition time (srt) = 1 ms.

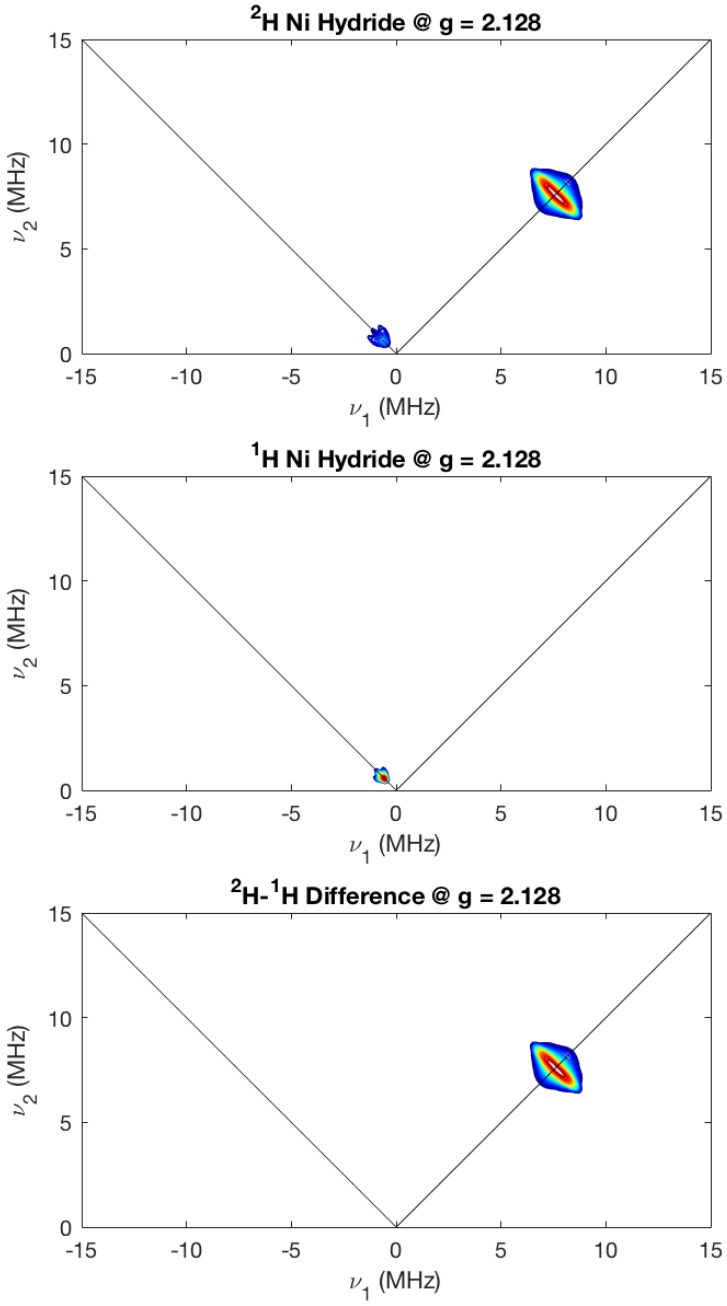

Figure B.9.4. Q-band HYSCORE spectra of **3.5-D** (top) and **3.5-H** (middle) in 2Me-THF measured at magnetic fields corresponding to g = 2.128. The corresponding ^{2}H – ^{1}H difference spectrum is depicted on the bottom. Experimental conditions: microwave frequency = 34.05514 GHz; temperature = 14 K; B_0 = 1143.6 mT; τ = 100 µs $t_1 = t_2$ = 100 ns; $\Delta t_1 = \Delta t_2$ = 16 ns; shot repetition time (srt) = 1 ms.

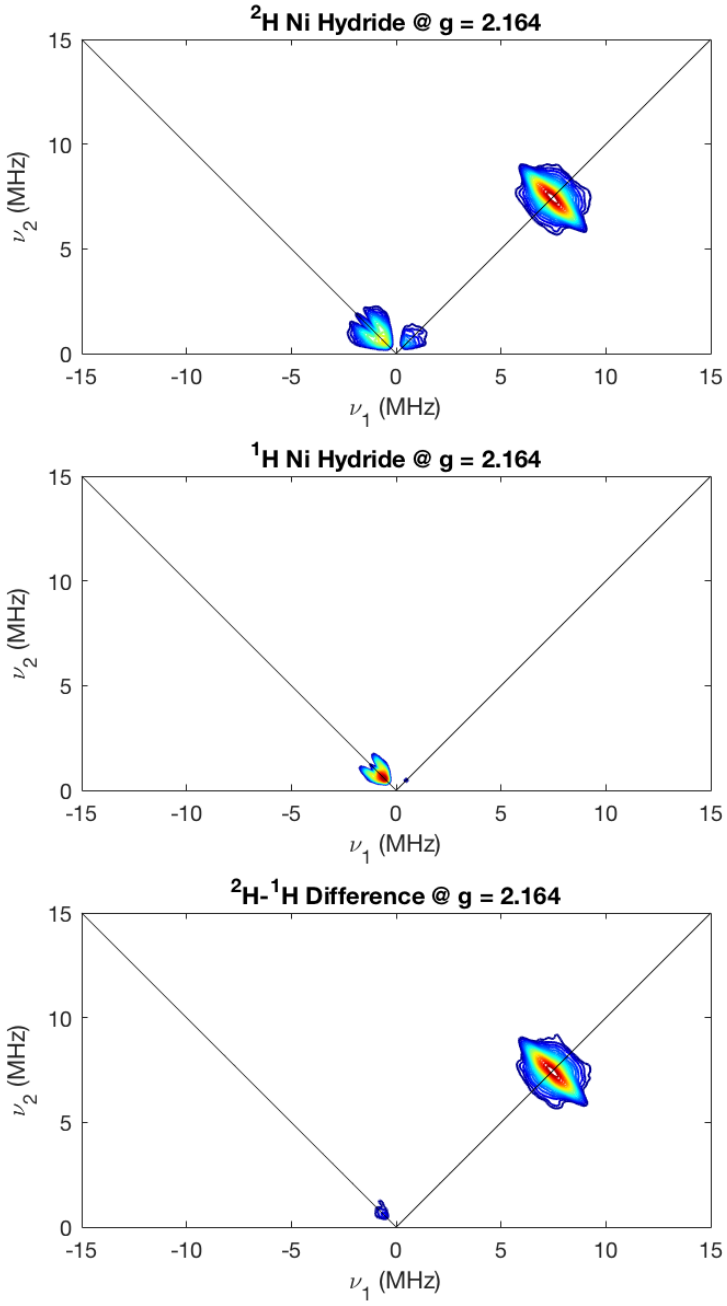

Figure B.9.5. Q-band HYSCORE spectra of **3.5-D** (top) and **3.5-H** (middle) in 2Me-THF measured at magnetic fields corresponding to g = 2.164. The corresponding ^{2}H – ^{1}H difference spectrum is depicted on the bottom. Experimental conditions: microwave frequency = 34.05514 GHz; temperature = 14 K; B_0 = 1124.2 mT; τ = 100 µs; $t_1 = t_2$ = 100 ns; $\Delta t_1 = \Delta t_2$ = 16 ns; shot repetition time (srt) = 1 ms.

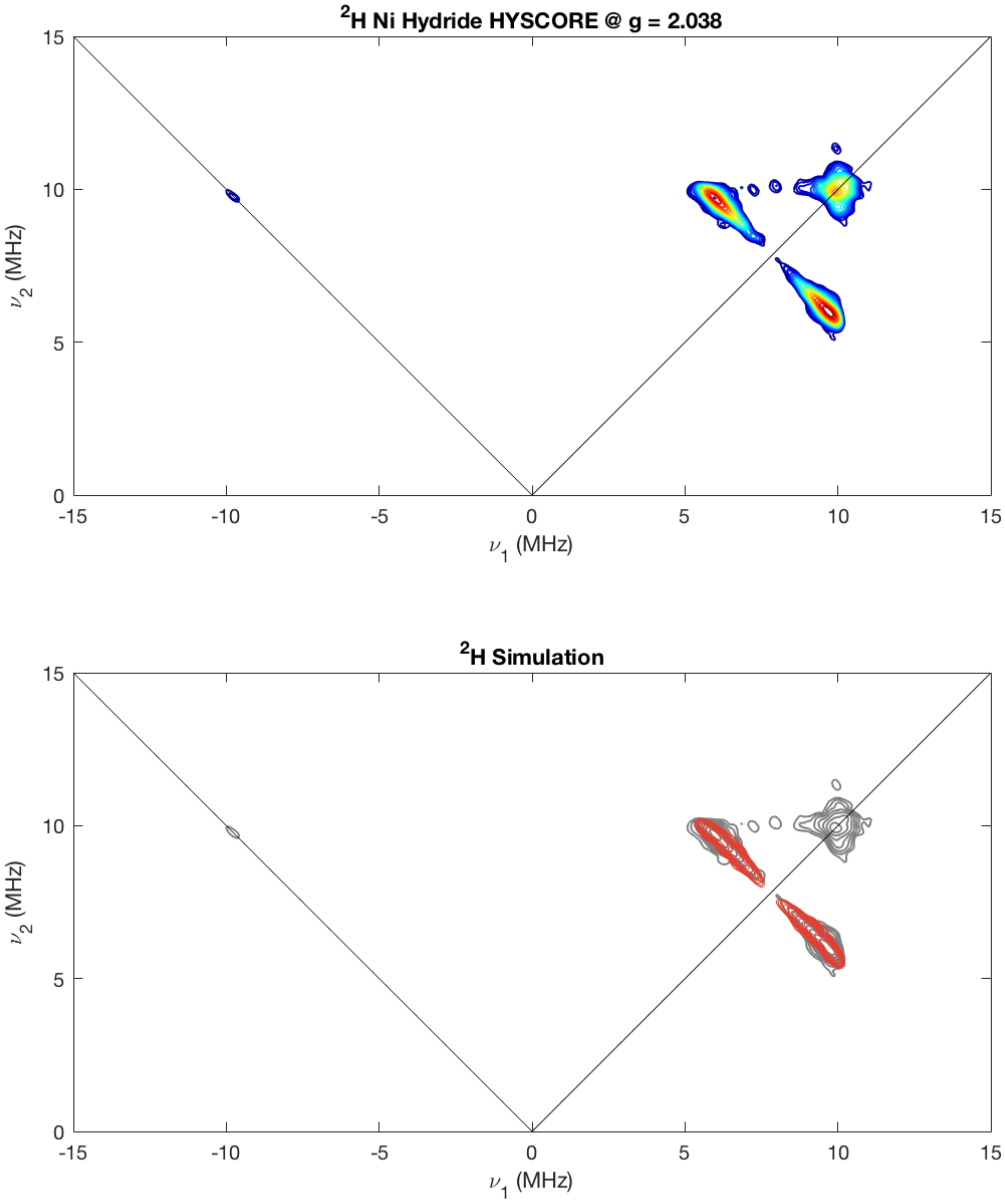

Figure B.9.6. Q-band HYSCORE ^{2}H – ^{1}H difference spectrum of **3.5-D** and **3.5-H** (top) in 2Me-THF measured at magnetic fields corresponding to $g = 2.038$. Overlay of 2H simulation contours (red) with experimental difference contours (gray). Experimental conditions: microwave frequency = 34.055 GHz; temperature = 14 K; B_0 = 1194 mT; τ = 100 µs $t_1 = t_2$ = 100 ns; $\Delta t_1 = \Delta t_2$ = 16 ns; shot repetition time (srt) = 1 ms). Simulation parameters: **g** = [2.166, 2.056, 2.039]; **A**(^{2}H) = [0.25, 0.25, 4.9] MHz.

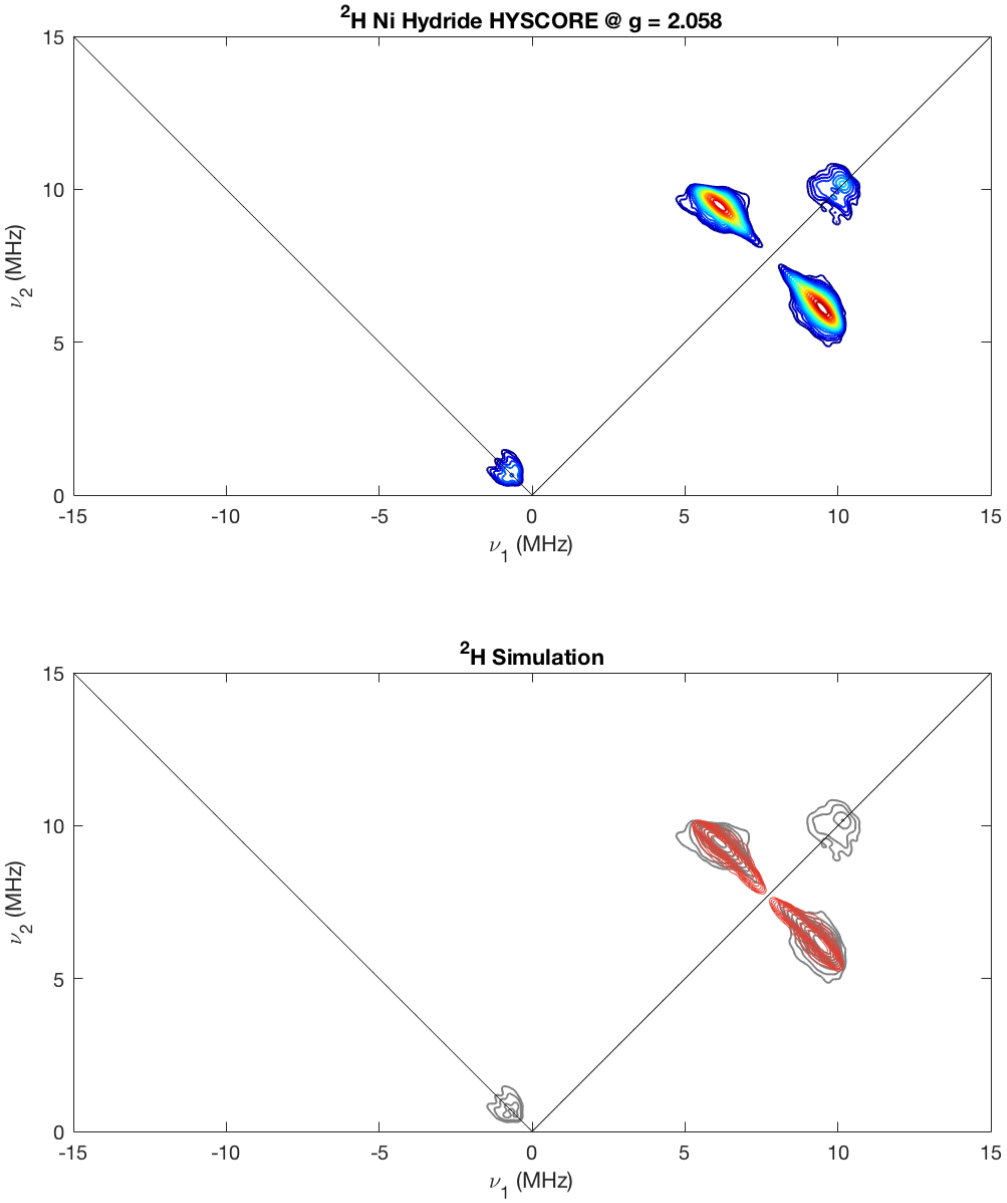

Figure B.9.7. Q-band HYSCORE ^{2}H – ^{1}H difference spectrum of **3.5-D** and **3.5-H** (top) in 2Me-THF measured at magnetic fields corresponding to $g = 2.058$. Overlay of ^{2}H simulation contours (red) with experimental difference contours (gray). Experimental conditions: microwave frequency = 34.05514 GHz; temperature = 14 K; B_0 = 1182.4 mT G; τ = 100 µs; $t_1 = t_2$ = 100 ns; $\Delta t_1 = \Delta t_2$ = 16 ns; shot repetition time (srt) = 1 ms). Simulation parameters: **g** = [2.166, 2.056, 2.039]; **A**(^{2}H) = [0.25, 0.25, 4.9] MHz.

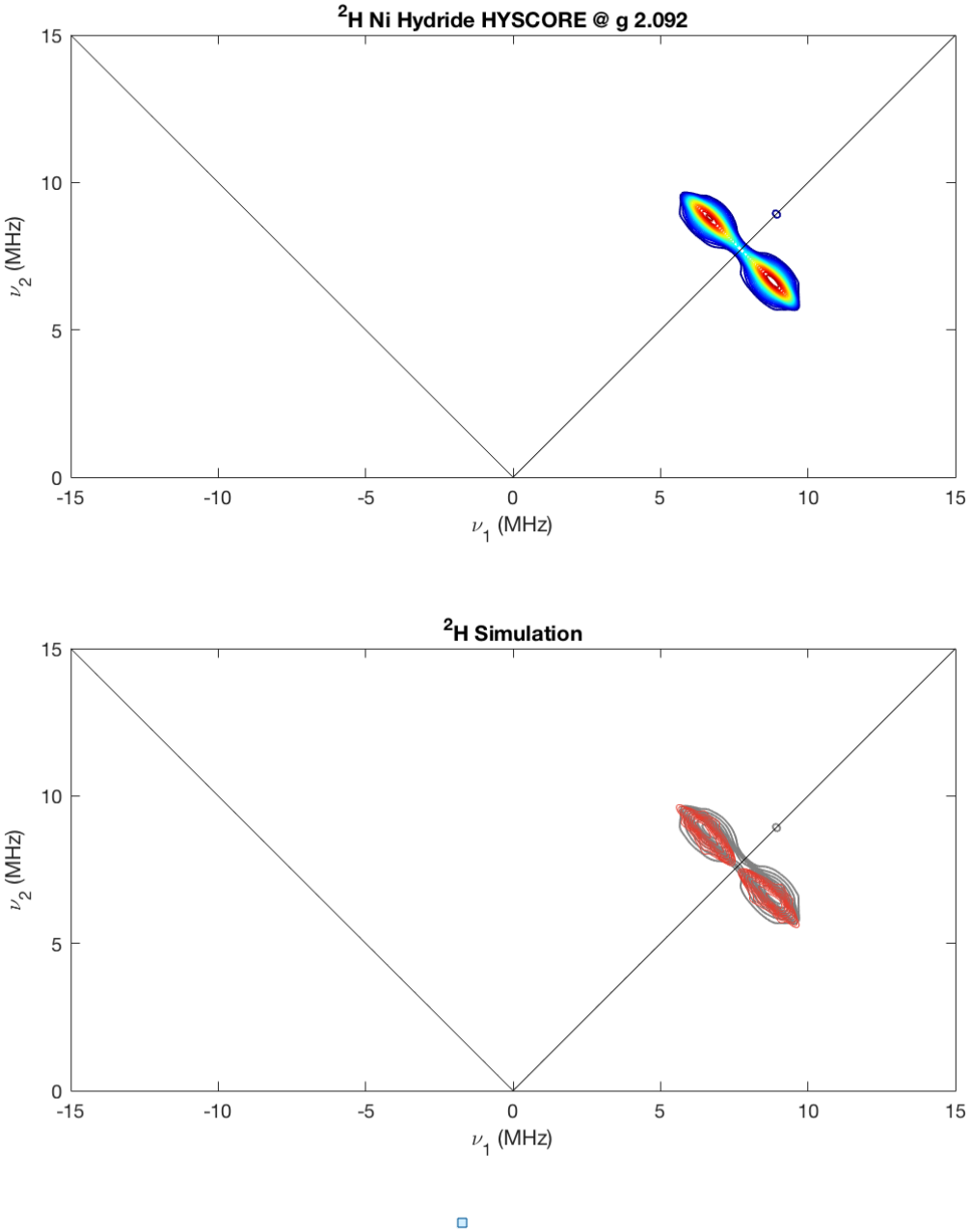

Figure B.9.8. Q-band HYSCORE ^{2}H – ^{1}H difference spectrum of **3.5-D** and **3.5-H** (top) in 2Me-THF measured at magnetic fields corresponding to $g = 2.092$. Overlay of ^{2}H simulation contours (red) with experimental difference contours (gray). Experimental conditions: microwave frequency = 34.05514 GHz; temperature = 14 K; B_0 = 1163 mT; τ = 100 µs; t_1 = t_2 = 100 ns; $\Delta t_1 = \Delta t_2$ = 16 ns; shot repetition time (srt) = 1 ms). Simulation parameters: **g** = [2.166, 2.056, 2.039]; **A**(^{2}H) = [0.25, 0.25, 4.9] MHz.

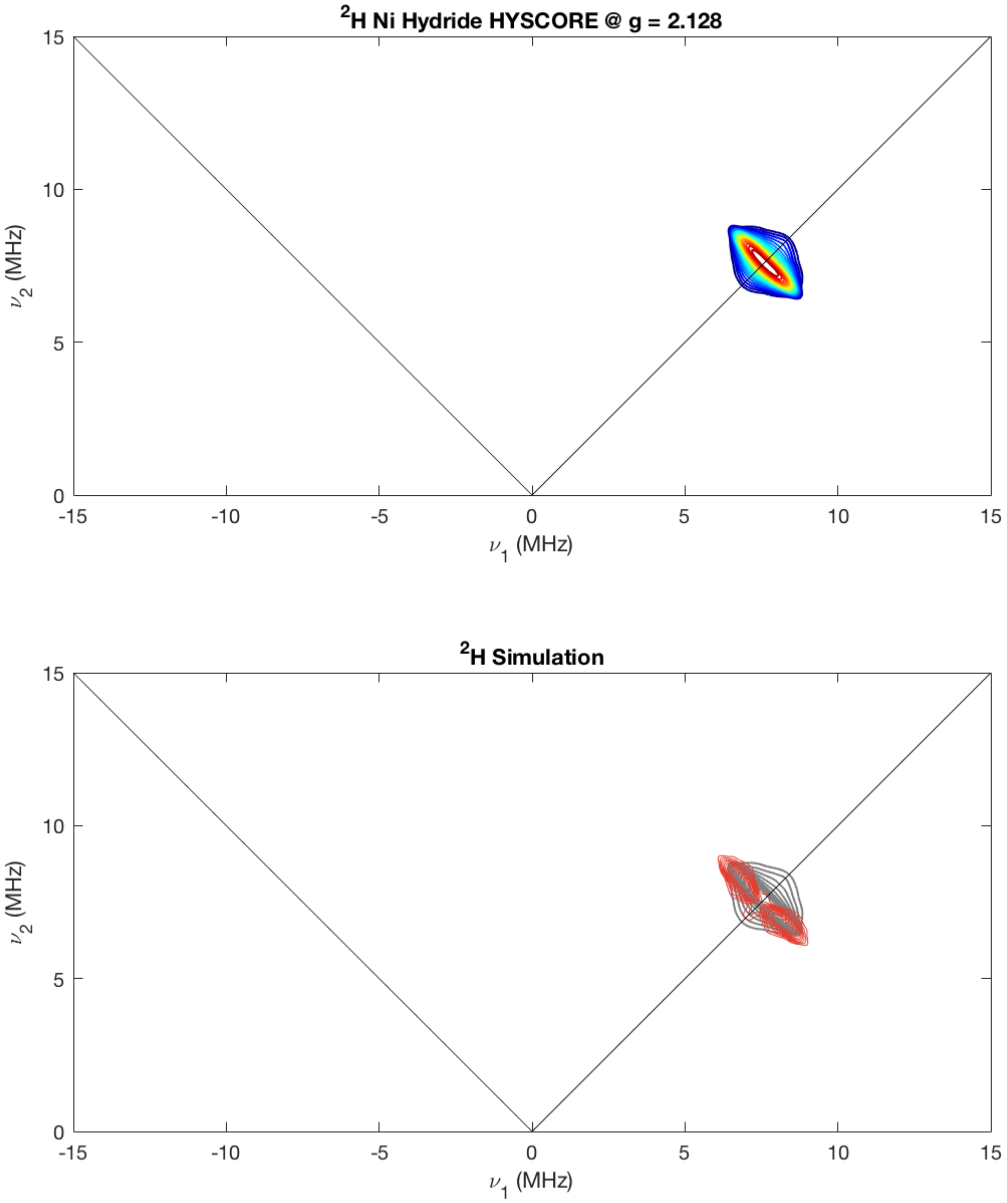

Figure B.9.9. Q-band HYSCORE ^{2}H – ^{1}H difference spectrum of **3.5-D** and **3.5-H** (top) in 2Me-THF measured at magnetic fields corresponding to $g = 2.128$. Overlay of ^{2}H simulation contours (red) with experimental difference contours (gray). Experimental conditions: microwave frequency = 34.05514 GHz; temperature = 14 K; B_0 = 1143.6 mT; τ = 100 µs t_1 = t_2 = 100 ns; $\Delta t_1 = \Delta t_2$ = 16 ns; shot repetition time (srt) = 1 ms). Simulation parameters: **g** = [2.166, 2.056, 2.039]; **A**(^{2}H) = [0.25, 0.25, 4.9] MHz.

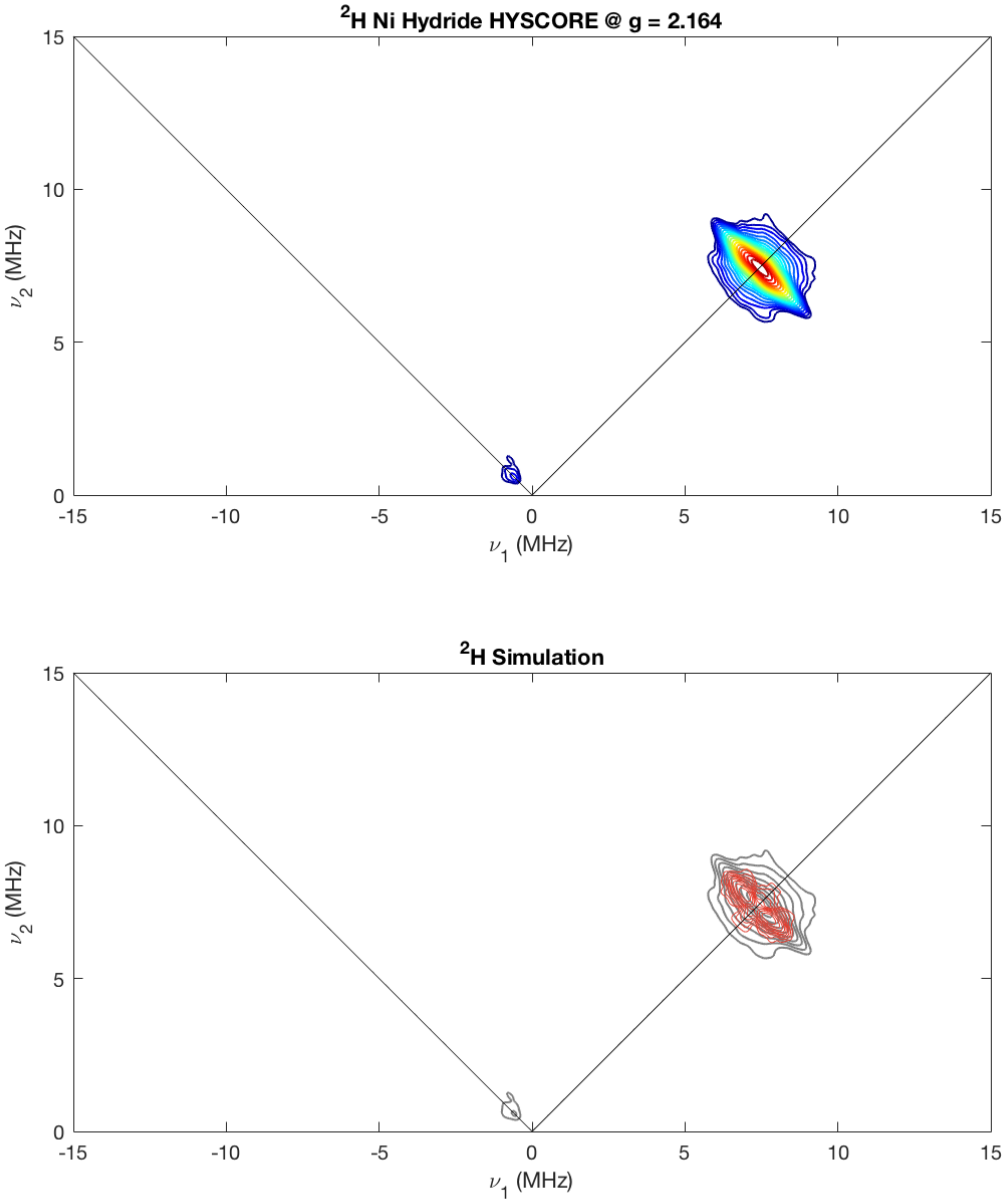

Figure B.9.10. Q-band HYSCORE ^{2}H – ^{1}H difference spectrum of **3.5-D** and **3.5-H** (top) in 2Me-THF measured at magnetic fields corresponding to $g = 2.164$. Overlay of ^{2}H simulation contours (red) with experimental difference contours (gray). Experimental conditions: microwave frequency = 34.05514 GHz; temperature = 14 K; B_0 = 1124.2 mT; τ = 100 µs; $t_1 = t_2$ = 100 ns; $\Delta t_1 = \Delta t_2$ = 16 ns; shot repetition time (srt) = 1 ms). Simulation parameters: **g** = [2.166, 2.056, 2.039]; **A**(^{2}H) = [0.25, 0.25, 4.9] MHz.

B.10 UV-Visible Data for the Conversion of 3.5-H to 3.4

Table B.10.1. Rate of the conversion of **3.5-H** to **3.4**

T (K)	*K (M^{-1} S^{-1})*
228	0.0015
243	0.0103
258	0.0145
273	0.0411
298	0.3293

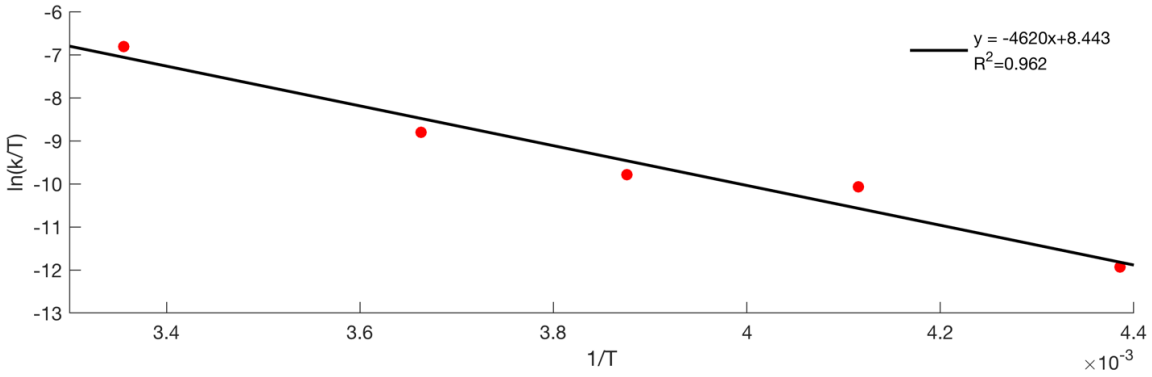

Figure B.10.1. Eyring plot for the conversion of **3.5-H** to **3.4**. T in K, k in $M^{-1}s^{-1}$

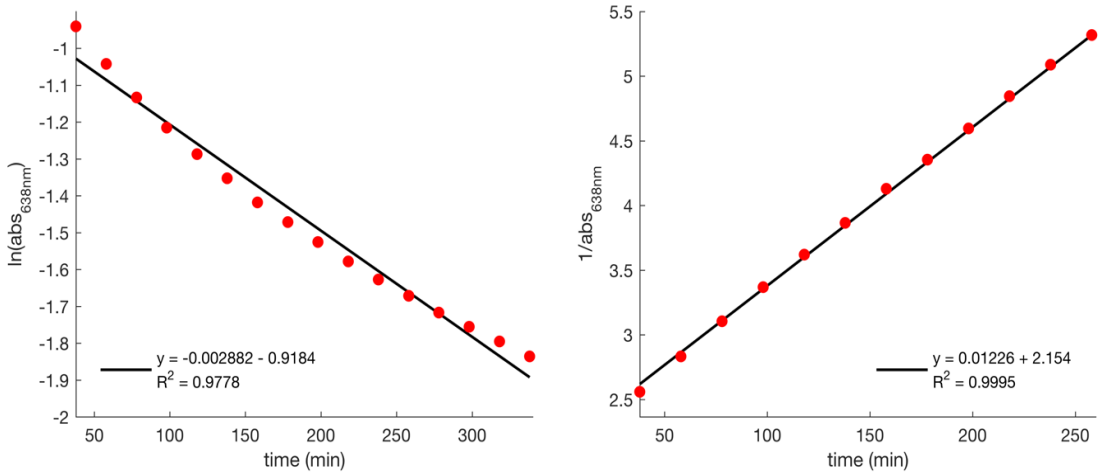

Figure B.10.2. Plot of time vs. $\ln(Abs_{638nm})$ (left) and time vs. $1/Abs_{638nm}$ (right) for the conversion of **3.5-H** to **3.4** at 25 °C

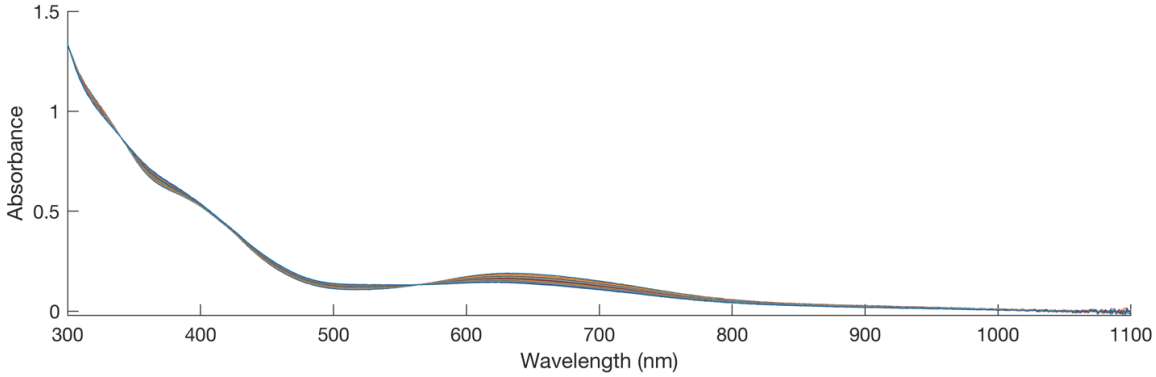

Figure B.10.3. UV-visible spectra showing the conversion of **3.5-H** to **3.4** at 25 °C in a 1 cm cuvette; traces collected every 10 min

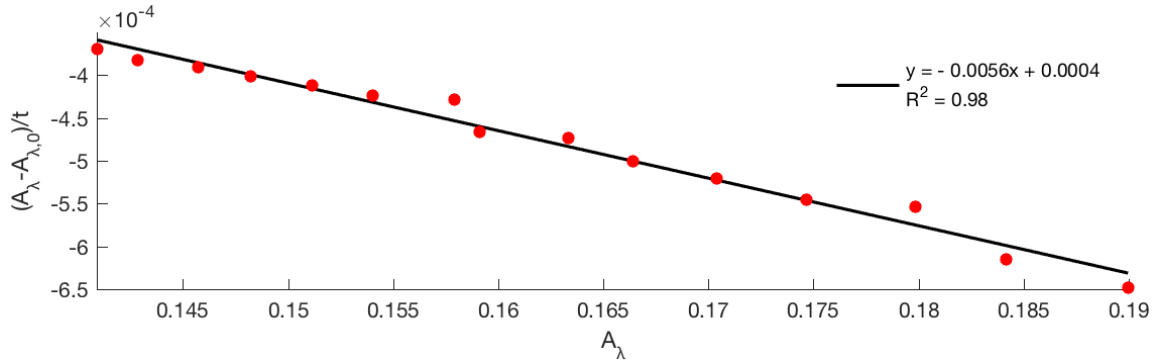

Figure B.10.4. Plot of A_λ vs. $(A_\lambda - A_{\lambda,0})/t$ at 25 °C ($[\mathbf{3.5\text{-}H}]_0 = 0.00014$ M, $\Delta t = 10$ min, $k = 0.3293\ M^{-1}s^{-1}$

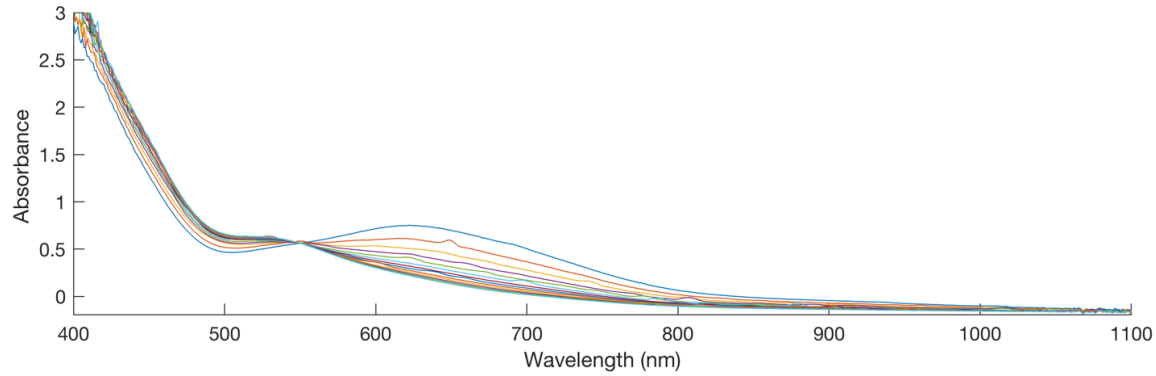

Figure B.10.5. UV-visible spectra showing the conversion of **3.5-H** to **3.4** at 0 °C in a 1 mm cuvette; traces collected every 10 min

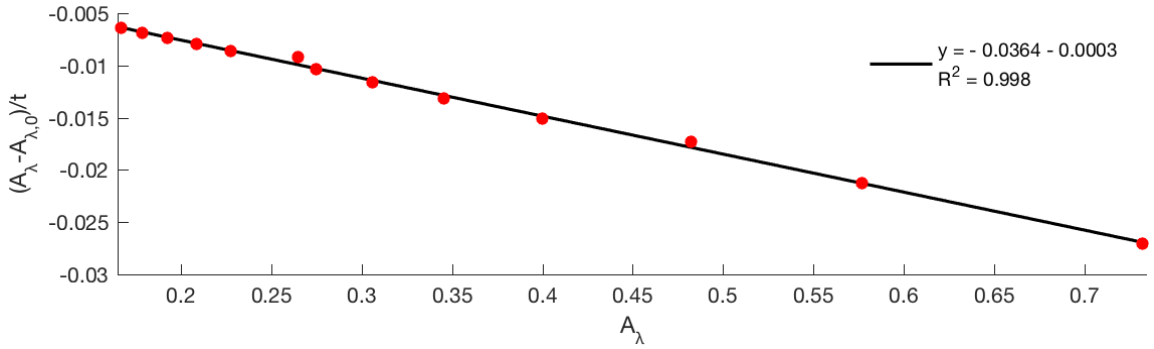

Figure B.10.6. Plot of A_λ vs. $(A_\lambda - A_{\lambda,0})/t$ at 0 °C ([**3.5-H**]$_0$ = 0.0074 M, Δt = 10 min, k = 0.0411 $M^{-1}s^{-1}$)

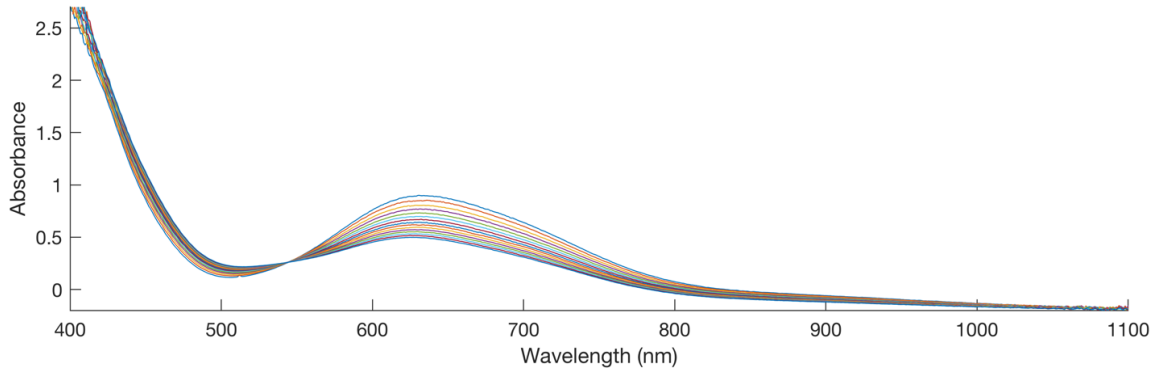

Figure B.10.7. UV-visible spectra showing the conversion of **3.5-H** to **3.4** at -15 °C in a 1 mm cuvette; traces collected every 5 min

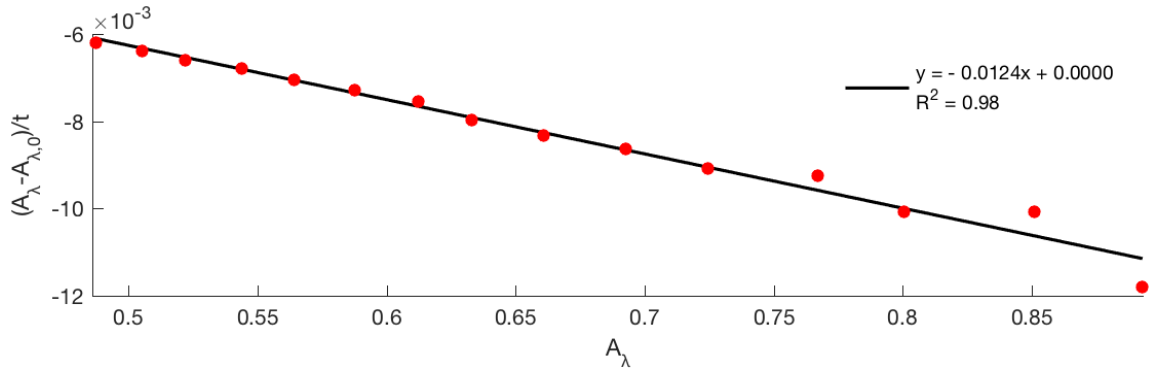

Figure B.10.8. Plot of A_λ vs. $(A_\lambda - A_{\lambda,0})/t$ at -15 °C ([**3.5-H**]$_0$ = 0.0072 M, Δt = 5 min, k = 0.0145 $M^{-1}s^{-1}$

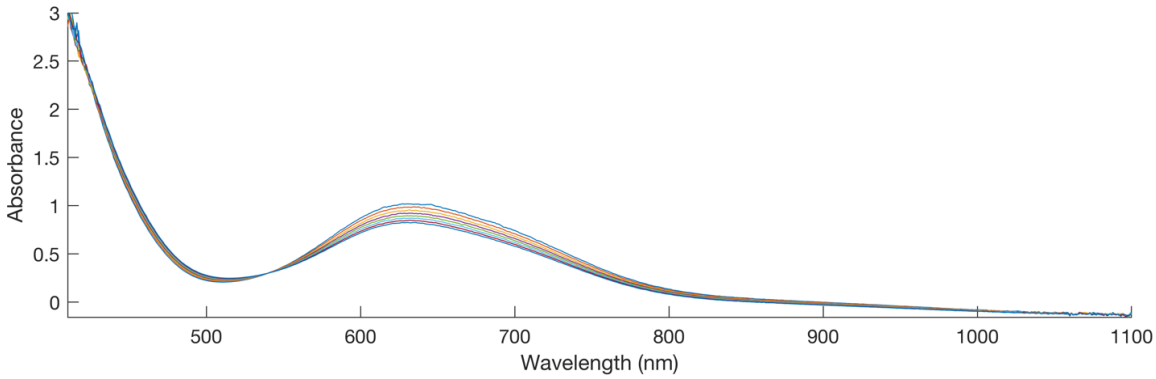

Figure B.10.9. UV-visible spectra showing the conversion of **3.5-H** to **3.4** at -30 °C in a 1 mm cuvette; traces collected every 10 min

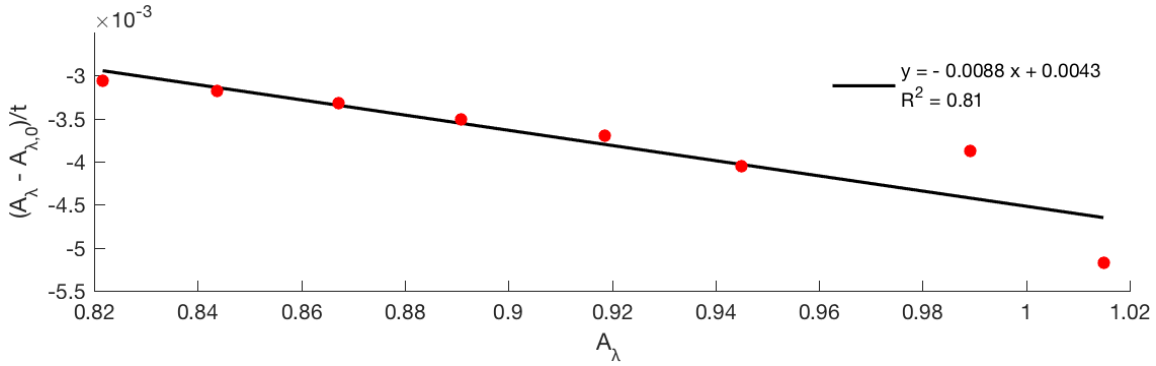

Figure B.10.10. Plot of A_λ vs. $(A_\lambda - A_{\lambda,0})/t$ at -30 °C ($[\mathbf{3.5\text{-}H}]_0 = 0.0072$ M, $\Delta t = 10$ min, $k = 0.0103$ $M^{-1}s^{-1}$)

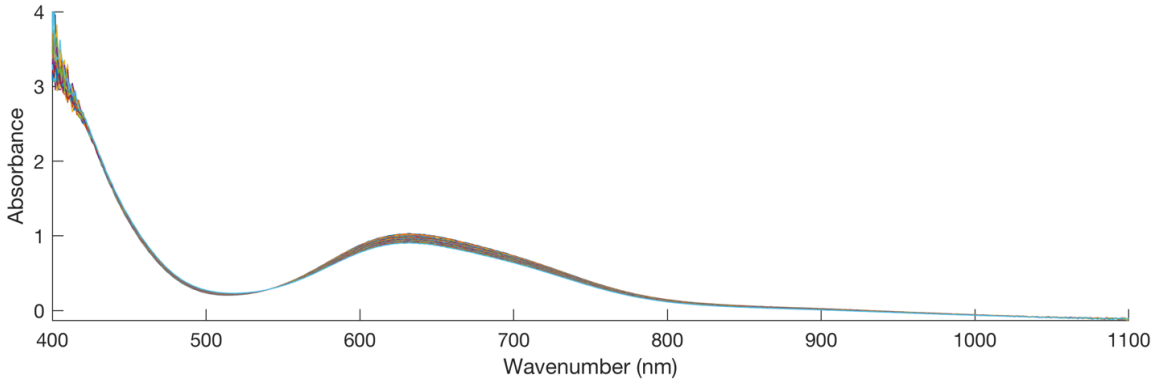

Figure B.10.11. UV-visible spectra showing the conversion of **3.5-H** to **3.4** at -45 °C in a 1 mm cuvette; traces collected every 10 min.

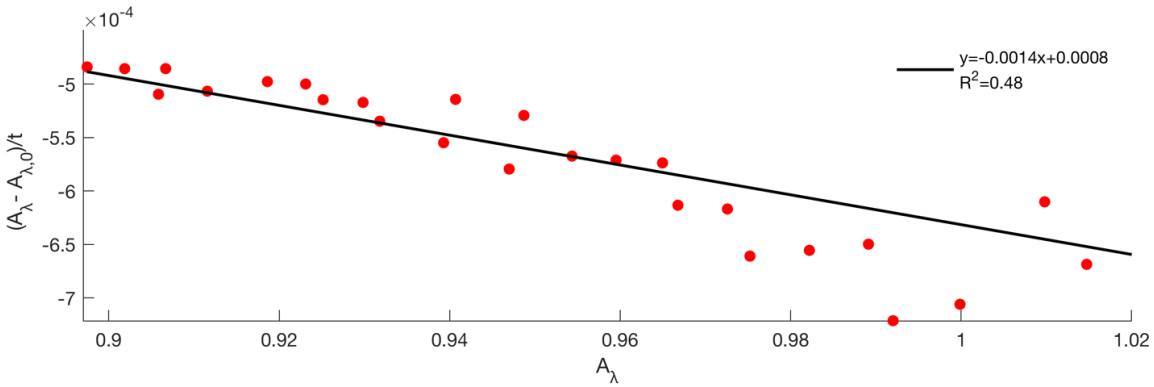

Figure B.10.12. Plot of A_λ vs. $(A_\lambda - A_{\lambda,0})/t$ at -45 °C ([**3.5-H**]$_0$ = 0.0078 M, Δt = 10 min, k = 0.0015 $M^{-1}s^{-1}$

B.11 DFT Calculations

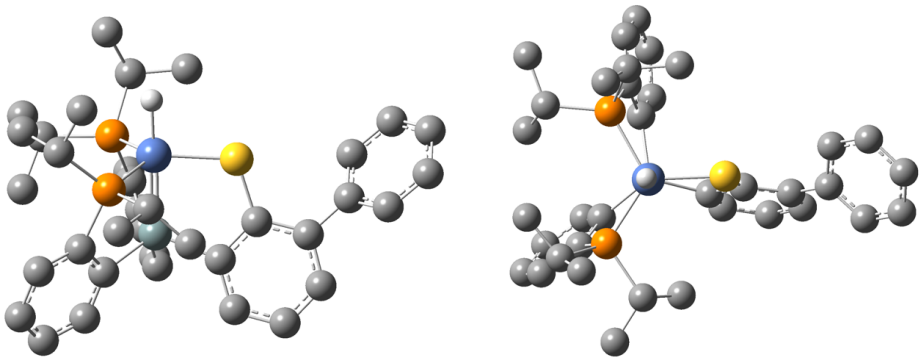

Figure B.11.1. Gas-phase optimized DFT structure of **3.5-H**. C-*H* hydrogens not depicted for clarity. (M06L: def2tzvp (Ni), def2svp (all other atoms))

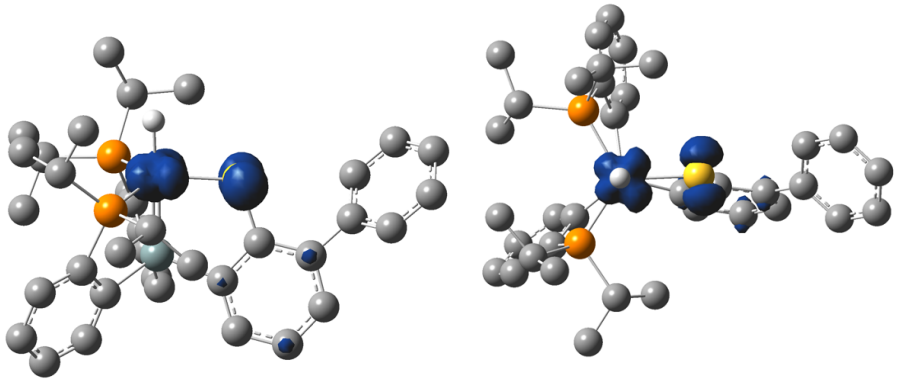

Figure B.11.2. Gas-phase optimized DFT spin density plot of **3.5-H**. C-*H* hydrogens not depicted for clarity. (isovalue: 0.005; M06L: def2tzvp (Ni), def2svp (all other atoms))

Table B.11.1. Gas-phase optimized coordinates for **3.5-H** (M06l, $S = 1/2$)

Ni	0.33404900	0.03766300	-1.11190900
S	-1.88209400	0.11591200	-0.97158800
P	1.43418100	1.97516600	-0.71237300
Si	0.27831300	-0.16112300	1.13234400
P	1.53628800	-1.83406700	-1.00297300
C	-1.46400000	-0.64669100	1.64807200
C	-2.43065300	-0.36194300	0.65530400
C	-3.80863500	-0.55941700	0.93389800
C	-1.85691600	-1.16698200	2.88162000
H	-1.10388800	-1.40070500	3.64307100
C	-4.15713200	-1.09389700	2.18568300
H	-5.21757400	-1.25060900	2.40345900
C	0.51588000	1.59053600	1.84817300
C	-3.20518400	-1.40492000	3.15083500
H	-3.51650700	-1.81850600	4.11313100
C	1.65401100	-1.35386300	1.70034500
C	-4.89521200	-0.25794900	-0.02445400
C	3.29972400	2.13079000	-0.59838000
H	3.66140500	1.69211400	-1.54314400
C	0.91947600	2.58888100	0.93867700
C	2.14753000	-1.49511300	3.00420900
H	1.68062100	-0.94476900	3.82816300
C	0.19042400	1.97186700	3.15836500
H	-0.15364200	1.21942400	3.87634600
C	0.26044700	3.30521200	3.55739600
H	-0.00231300	3.58490900	4.58085500
C	-4.96329100	0.96545600	-0.71050500
H	-4.17661000	1.70719100	-0.55743100
C	0.48819300	-3.37299700	-1.20069700
H	0.03678900	-3.24093800	-2.20029300
C	-5.92954600	-1.18579800	-0.22400400
H	-5.88765900	-2.14907000	0.29246600
C	-6.02547400	1.24551700	-1.56497800
H	-6.06157700	2.20708400	-2.08312500
C	0.96475800	3.93237800	1.33451700
H	1.24245600	4.71392100	0.62103100
C	0.95474800	3.31758000	-1.90506700
H	1.35692200	4.25704700	-1.48418900
C	-0.55727100	3.43435800	-2.00236400
H	-0.99336700	2.52696600	-2.44549400
H	-0.83441100	4.28847700	-2.63805500
H	-1.03090700	3.57785700	-1.02002300

C	0.63713800	4.28818200	2.64136700
H	0.66656700	5.33784300	2.94366300
C	-6.98895100	-0.90908000	-1.08493300
H	-7.77581100	-1.65297800	-1.23282100
C	2.29074900	-2.06755600	0.65852000
C	3.81881900	1.28739200	0.55508800
H	3.52450100	1.71188300	1.52815500
H	4.91824300	1.23862700	0.53864300
H	3.43857600	0.25701700	0.52463600
C	-0.63455100	-3.40589400	-0.17946000
H	-0.25051100	-3.44010600	0.85311500
H	-1.25350900	-4.30369600	-0.32380700
H	-1.29130600	-2.53279300	-0.27079900
C	-7.04115100	0.30902600	-1.75973100
H	-7.87104200	0.52951100	-2.43559400
C	3.25435000	-2.30111200	3.27151800
H	3.63803800	-2.38395900	4.29162900
C	3.81762600	3.55693800	-0.50299300
H	3.53245000	4.18412500	-1.35854400
H	4.91776700	3.55203300	-0.46443100
H	3.47369400	4.05553400	0.41580300
C	1.58857500	3.07333600	-3.26538400
H	2.68815000	3.07613900	-3.23470700
H	1.28086000	3.85156900	-3.97946000
H	1.26518600	2.10171400	-3.67068700
C	1.29295400	-4.66289800	-1.17440800
H	2.07013800	-4.71584500	-1.94931900
H	0.62562000	-5.52360000	-1.33285400
H	1.77772500	-4.81437700	-0.19754400
C	2.88971000	-2.11773800	-2.25450700
H	3.43772600	-3.02094200	-1.93162800
C	3.88385000	-2.98779500	2.23356200
H	4.75872700	-3.60943800	2.43919000
C	3.39832200	-2.87963200	0.93055900
H	3.90201500	-3.42435400	0.12596500
C	3.85143000	-0.94497000	-2.29032200
H	3.32738300	-0.04024600	-2.63706400
H	4.67455200	-1.13863800	-2.99440300
H	4.30027900	-0.73098600	-1.30937500
C	2.29023800	-2.36466400	-3.63153400
H	1.71353300	-3.29772700	-3.69060300
H	3.08664500	-2.42735800	-4.38783200
H	1.62149200	-1.53814700	-3.92009800

H	0.40336600	0.21962900	-2.65366100

Table B.11.2. Gas-phase optimized coordinates for **3.6** (M06l, $S = 0$)

Ni	0.40716700	0.13111300	-0.96350100
S	-1.69248300	0.73762800	-0.52163600
P	1.32445200	-1.82612600	-1.16952800
P	1.58059800	2.01010900	-0.58325500
Si	0.25899200	-0.33035500	1.17029600
C	-2.38934100	-0.32867600	0.71566900
C	-1.46773100	-0.87697500	1.63659800
C	-4.80522700	-0.03009900	-0.04590000
C	-3.77518800	-0.57371100	0.86553900
C	0.70169400	1.33105500	1.98026100
C	-1.90702200	-1.70074000	2.67326700
H	-1.18273600	-2.14719700	3.36435800
C	-4.67053700	-0.09852200	-1.44218100
H	-3.77120200	-0.54660300	-1.87081600
C	-4.17702400	-1.39295500	1.93336100
H	-5.24302400	-1.61676700	2.03847400
C	-3.26881500	-1.95986400	2.82603200
H	-3.62612900	-2.60640500	3.63097600
C	0.46491200	1.57192900	3.34112200
H	0.05636200	0.77353000	3.97067000
C	3.91578700	0.95720900	0.51285500
H	3.75914400	1.35809800	1.52647400
H	4.98901700	0.73431100	0.41151600
H	3.37139500	0.00244400	0.45377100
C	0.70575300	2.82286900	3.90767700
H	0.50699200	2.99167700	4.96907500
C	1.20043700	2.38565500	1.18067400
C	0.19893700	-3.24491400	-1.66774600
H	0.84118900	-4.14636200	-1.63780100
C	3.46315700	1.95029400	-0.54702700
H	3.72330200	1.54278700	-1.54273200
C	1.51240900	-1.71106900	1.55666400
C	-5.67666200	0.37463300	-2.28010300
H	-5.55477300	0.30233300	-3.36380200
C	1.96353200	-2.43739100	0.43571600
C	1.92820600	-2.11946500	2.83162800
H	1.60036100	-1.56800700	3.71952800
C	1.41987700	3.64527000	1.75420300
H	1.77293700	4.47828700	1.13878000
C	1.17576700	3.86385800	3.10947200

H	1.34596500	4.85360300	3.54051900
C	1.22515100	3.59936000	-1.49119300
H	1.80668500	4.40569900	-1.00912900
C	-0.92787100	-3.39858600	-0.66137900
H	-0.56656100	-3.51101500	0.37134900
H	-1.53541300	-4.28535300	-0.89660500
H	-1.59670100	-2.52405000	-0.68239000
C	-0.25250700	3.94366700	-1.40574500
H	-0.87283500	3.17935100	-1.89772100
H	-0.45605700	4.90469400	-1.90222100
H	-0.60522700	4.02029600	-0.36751800
C	2.70817900	-2.00211900	-2.43563500
H	2.67860000	-3.05365600	-2.77986800
C	-5.98317900	0.52685900	0.47713000
H	-6.09996500	0.59874000	1.56222500
C	2.78019500	-3.56237000	0.59740100
H	3.10434000	-4.14135300	-0.27392300
C	4.16904700	3.28459400	-0.37372600
H	3.95285500	4.00000300	-1.17917100
H	5.26051400	3.13953900	-0.36064200
H	3.90372800	3.76072300	0.58257600
C	1.68735600	3.46165600	-2.93479700
H	2.76187300	3.24057600	-3.02137900
H	1.49896800	4.38774400	-3.49875900
H	1.14322700	2.65288500	-3.44883600
C	-6.83746000	0.93292100	-1.74496000
H	-7.62319800	1.30849600	-2.40502000
C	-0.35060800	-3.07439000	-3.07454000
H	-0.88075800	-2.11331700	-3.18008500
H	-1.07957500	-3.86787000	-3.29815800
H	0.42488000	-3.12669400	-3.85093700
C	3.18415200	-3.95103100	1.87369900
H	3.82886800	-4.82423400	1.99996700
C	-6.98666600	1.00685400	-0.36086400
H	-7.88937700	1.44648000	0.07099300
C	2.76564900	-3.22356800	2.98921500
H	3.09080300	-3.52485600	3.98835900
C	4.09341000	-1.69880500	-1.89005500
H	4.16774400	-0.64847100	-1.57517000
H	4.85049200	-1.85069600	-2.67445500
H	4.37822700	-2.31858200	-1.03007000
C	2.41325100	-1.07540400	-3.61068800
H	1.41421800	-1.21746900	-4.04433800

H	3.14785200	-1.21719000	-4.41777800
H	2.47427300	-0.02232800	-3.28835100

Table B.11.3. Optimized coordinates for **3.5-H** (M06l, $S = ½$, MeCN solvation)

Ni	0.33898600	0.04737800	-1.13646800
S	-1.90037100	0.15979100	-0.99695000
P	1.49897500	1.98333800	-0.68193600
Si	0.25389000	-0.16391400	1.11422700
P	1.56424800	-1.84312500	-1.00635700
C	-1.49842900	-0.65401400	1.60241400
C	-2.46450000	-0.35211300	0.61570400
C	-3.84238600	-0.55456900	0.89055100
C	-1.89061000	-1.19264000	2.82964000
H	-1.13614700	-1.43237400	3.58724200
C	-4.19219100	-1.11142500	2.13380400
H	-5.25186900	-1.27836200	2.34870400
C	0.46844600	1.58555700	1.83382900
C	-3.23970900	-1.43601900	3.09490900
H	-3.55124600	-1.86500600	4.05055400
C	1.59681500	-1.37134300	1.70257600
C	-4.93107800	-0.23690700	-0.06207700
C	3.35563900	2.10499900	-0.47894400
H	3.75306100	1.66723200	-1.40903800
C	0.90814300	2.58772800	0.94521200
C	2.03523700	-1.53170100	3.02470800
H	1.54871100	-0.97938000	3.83576200
C	0.10577600	1.95504200	3.13866800
H	-0.25334900	1.19701700	3.84334300
C	0.17058500	3.28603900	3.54950200
H	-0.11824500	3.55886100	4.56794000
C	-5.01156100	1.00651900	-0.71237200
H	-4.23604700	1.75518000	-0.53484000
C	0.51106800	-3.36550900	-1.26697200
H	0.10170200	-3.21878900	-2.28277400
C	-5.95833100	-1.16848100	-0.28717500
H	-5.91337400	-2.14406800	0.20552100
C	-6.07788700	1.30276500	-1.55844200
H	-6.12520500	2.28038800	-2.04530900
C	0.95232800	3.92822400	1.35381100
H	1.26876400	4.71278300	0.66077400
C	1.09578900	3.33056800	-1.89459500
H	1.48060300	4.25890600	-1.43787200
C	-0.40437200	3.47091200	-2.08260600

H	-0.82969500	2.58212300	-2.57341400
H	-0.62770300	4.34006200	-2.71940400
H	-0.93980500	3.60969100	-1.13119800
C	0.58257500	4.27386800	2.65286300
H	0.61255600	5.32065800	2.96533200
C	-7.02165300	-0.87524600	-1.13972300
H	-7.80374000	-1.62063000	-1.30539600
C	2.25173000	-2.09080200	0.67794800
C	3.82013300	1.25611400	0.69257900
H	3.48380400	1.67375800	1.65568700
H	4.91968500	1.21869900	0.72301400
H	3.45820700	0.22046000	0.63622700
C	-0.64814700	-3.40631800	-0.28838400
H	-0.29956500	-3.47825900	0.75509200
H	-1.27442300	-4.29033300	-0.48062500
H	-1.29017900	-2.52032100	-0.37595900
C	-7.08575800	0.36214100	-1.77974900
H	-7.91979100	0.59560700	-2.44638000
C	3.11127500	-2.36861000	3.32309500
H	3.45490800	-2.46992600	4.35585500
C	3.87921600	3.52648900	-0.35684800
H	3.63591400	4.16020000	-1.22019900
H	4.97699300	3.50442000	-0.27781200
H	3.50781700	4.02789000	0.54982900
C	1.81046400	3.10660600	-3.21741000
H	2.90529300	3.07715700	-3.11907600
H	1.57002300	3.91933200	-3.91912000
H	1.49083200	2.16406300	-3.68979400
C	1.30210900	-4.66272200	-1.22537700
H	2.13697300	-4.69846500	-1.93849300
H	0.63840100	-5.50742900	-1.46529200
H	1.70904800	-4.85425600	-0.22039400
C	2.96002800	-2.09873800	-2.21020300
H	3.49646100	-2.99689400	-1.85798000
C	3.75907900	-3.06501600	2.30160600
H	4.60834400	-3.71248700	2.53382200
C	3.32680200	-2.93557100	0.98136300
H	3.84157900	-3.49060500	0.19180200
C	3.92095100	-0.92535700	-2.20448200
H	3.43199100	-0.01815900	-2.59431600
H	4.78091400	-1.13516300	-2.85805200
H	4.31742800	-0.70337800	-1.20324600
C	2.43086900	-2.36059400	-3.61141900

H	1.84663700	-3.28727500	-3.69147300
H	3.27093000	-2.44565500	-4.31670800
H	1.79559400	-1.53178000	-3.96318100
H	0.40807300	0.22362300	-2.69964000

Table B.11.4. Optimized coordinates for **3.6** (M06l, $S = 0$, MeCN solvation)

Ni	0.42104400	0.11667700	-0.99020100
S	-1.72916800	0.75619400	-0.60660800
P	1.26989600	-1.89115800	-1.12923200
P	1.65056400	1.98061800	-0.61483100
Si	0.29284000	-0.28873400	1.14907200
C	-2.39531800	-0.25230000	0.68901300
C	-1.46012300	-0.78029400	1.61270800
C	-4.83504700	0.03017500	-0.02216400
C	-3.78208500	-0.48215200	0.88444000
C	0.73553800	1.38030400	1.94742500
C	-1.88812900	-1.55869900	2.69005600
H	-1.15363500	-1.98271900	3.38468100
C	-4.75271200	-0.11837000	-1.41788400
H	-3.87537300	-0.60197600	-1.85446500
C	-4.17173500	-1.25285500	1.99383000
H	-5.23809000	-1.45552700	2.13527100
C	-3.24957800	-1.79663400	2.88726500
H	-3.59424900	-2.40544100	3.72687000
C	0.49451800	1.64837900	3.30405600
H	0.08128500	0.86587300	3.95050500
C	3.94953800	0.88064100	0.51526600
H	3.80057800	1.29617500	1.52528400
H	5.01870600	0.63482300	0.42338200
H	3.38867200	-0.06537100	0.46175300
C	0.75175800	2.90774900	3.84685200
H	0.55253000	3.09961500	4.90452800
C	1.25829700	2.41098400	1.13209800
C	0.12971500	-3.30375100	-1.59924900
H	0.77257000	-4.20343500	-1.57098700
C	3.52738200	1.86840600	-0.56071400
H	3.77954000	1.43666500	-1.54702000
C	1.49497800	-1.69308700	1.58939100
C	-5.78439200	0.32009200	-2.24531000
H	-5.70468500	0.18235000	-3.32690800
C	1.91142600	-2.46806800	0.48712500
C	1.91189400	-2.06883500	2.87471400
H	1.60729800	-1.48114100	3.74740500

C	1.49685200	3.67874400	1.68146800
H	1.87674000	4.49079100	1.05419700
C	1.24455000	3.92627400	3.03115200
H	1.43075200	4.92035600	3.44593600
C	1.34557500	3.55070600	-1.56932000
H	1.94402100	4.34893700	-1.09658500
C	-0.98702600	-3.45624300	-0.58282900
H	-0.61503700	-3.57530600	0.44632800
H	-1.59752600	-4.34272000	-0.81413000
H	-1.65890600	-2.58301400	-0.59600800
C	-0.11927200	3.94684200	-1.51257900
H	-0.75986400	3.20001700	-2.00657200
H	-0.27855500	4.90618100	-2.02895600
H	-0.48563800	4.06379400	-0.48185300
C	2.62961800	-2.08177400	-2.41417000
H	2.55751100	-3.12681200	-2.76819700
C	-5.98823800	0.63120700	0.51020100
H	-6.07071400	0.75978900	1.59341700
C	2.69931100	-3.60983800	0.67575800
H	2.99729900	-4.22366600	-0.18018700
C	4.26475400	3.18682500	-0.40825900
H	4.07513500	3.88854700	-1.23213300
H	5.35173800	3.01047900	-0.38507200
H	4.00628600	3.69470900	0.53402400
C	1.81711900	3.36845800	-3.00428100
H	2.88298400	3.10522200	-3.07595700
H	1.67204300	4.29466100	-3.58127700
H	1.24607100	2.57571200	-3.51457500
C	-6.91863600	0.92565900	-1.70097400
H	-7.72366000	1.27403800	-2.35307400
C	-0.42735700	-3.13987600	-3.00261100
H	-0.97756700	-2.18995100	-3.10963200
H	-1.13828500	-3.95004500	-3.22657300
H	0.34868900	-3.17319200	-3.77931200
C	3.10650300	-3.96587200	1.96156700
H	3.72890500	-4.85193700	2.11020000
C	-7.01636700	1.07896400	-0.31807400
H	-7.89832100	1.55253000	0.12130700
C	2.72025300	-3.19162900	3.05835500
H	3.04711200	-3.47064900	4.06363500
C	4.03197000	-1.83598800	-1.88855300
H	4.15492000	-0.79848400	-1.54565000
H	4.76427300	-1.99151700	-2.69580400

H	4.31541000	-2.49808200	-1.05961200
C	2.33973100	-1.13142300	-3.57040300
H	1.31648300	-1.21305300	-3.96370900
H	3.02953100	-1.31475300	-4.40833900
H	2.48224700	-0.08446000	-3.253052003

Table B.11.5. DFT-calculated spin density of **3.5-H** (gas phase)

ATOM LABEL	ATOM	SPIN DENSITY (E^-)	SPIN DENSITY (%)
1	Ni	0.598	44.0
2	S	0.224	16.5
3	P	0.083	6.1
4	Si	-0.043	3.1
5	P	0.069	5.1
6	C	0.056	4.1
7	C	-0.042	3.1
8	C	0.052	3.8
9	C	-0.028	2.0
10	H	0.001	0.1
11	C	-0.029	2.1
12	H	0.001	0.1
13	C	0.009	0.7
14	C	0.056	4.1
15	H	-0.003	0.2
16	C	0.000	0.0
17	C	-0.006	0.4
18	C	-0.005	0.3
19	H	0.000	0.0
20	C	-0.001	0.1
21	C	0.000	0.0
22	H	0.000	0.0
23	C	-0.001	0.1
24	H	0.000	0.0
25	C	0.000	0.0
26	H	0.000	0.0
27	C	0.004	0.3
28	H	0.000	0.0
29	C	0.002	0.2
30	H	0.000	0.0
31	C	0.004	0.3
32	H	0.000	0.0
33	C	-0.002	0.2
34	H	0.000	0.0

35	C	0.000	0.0
36	H	0.000	0.0
37	C	0.000	0.0
38	H	0.003	0.2
39	C	0.000	0.0
40	H	0.001	0.1
41	H	0.000	0.0
42	H	0.000	0.0
43	C	0.000	0.0
44	H	0.000	0.0
45	C	-0.002	0.1
46	H	0.000	0.0
47	C	-0.004	0.3
48	C	0.000	0.0
49	H	0.000	0.0
50	H	0.000	0.0
51	H	-0.001	0.0
52	C	0.000	0.0
53	H	0.000	0.0
54	H	0.000	0.0
55	H	-0.001	0.0
56	C	0.004	0.3
57	H	0.000	0.0
58	C	0.000	0.0
59	H	0.000	0.0
60	C	0.001	0.1
61	H	0.000	0.0
62	H	0.000	0.0
63	H	0.000	0.0
64	C	0.000	0.0
65	H	0.000	0.0
66	H	0.000	0.0
67	H	0.000	0.0
68	C	0.002	0.2
69	H	0.000	0.0
70	H	0.002	0.1
71	H	0.000	0.0
72	C	0.004	0.3
73	H	0.001	0.1
74	C	0.000	0.0
75	H	0.000	0.0
76	C	0.000	0.0
77	H	0.000	0.0

78	C	0.001	0.1
79	H	0.000	0.0
80	H	0.000	0.0
81	H	0.000	0.0
82	C	0.000	0.0
83	H	0.000	0.0
84	H	0.000	0.0
85	H	0.001	0.1
86	H	0.005	0.4

B.12 Discussion on the Characterization of [(PS$_3$)NiH][PPN]

Prepared according to the published synthesis,[17] treatment of **[(PS$_3$)NiOPh][PPN]** in THF with 1.3 equivalents of HBPin at −78 °C resulted generation of a dark red solution containing the terminal Ni^{III} hydride [**(PS$_3$)NiH][PPN]**. The UV-Visible data that we obtained of this dark red sample are in good agreement with the reported spectrum with respect to spectral features, although we determined larger extinction coefficients for the transitions. In our hands, EPR samples of this dark red sample contained the approximate axial signal assigned as **[(PS$_3$)NiH][PPN]**, with additional $S = ½$ signals present. However, although impurities were present in the sample, we were able to obtain X-band HYSCORE data on the signal corresponding to [**(PS$_3$)NiH][PPN]** at $g = 2.42$ and $g = 1.99$, with minimal overlap with the additional $S = ½$ signals. The Ni^{III} deuteride, **[(PS$_3$)NiD][PPN]**, was analogously generated by treatment of **[(PS$_3$)NiOPh][PPN]** with 1.3 equivalents of DBPin at −78 °C in THF. X-band HYSCORE data of the Ni^{III} deuteride revealed ^{2}H hyperfine coupling of $\mathbf{A}(^2\text{H}) = [1.6, 9.3, 9.3]$ MHz. Scaling $\mathbf{A}(^2\text{H})$ by the ratio of $^1\text{H}/^2\text{H}$ gyromagnetic ratios approximates a ^{1}H hyperfine coupling of $\mathbf{A}(^1\text{H}) = [10.4, 60.6, 60.6]$ MHz in [**(PS$_3$)NiH][PPN]** ($a_{iso} = 43.9$ MHz; $\mathbf{T} = [-33.5, 16.7, 16.7]$ MHz). Additional hyperfine coupling to ^{31}P and ^{13}C (natural abundance) was resolved in the HYSCORE data: $\mathbf{A}(^{31}\text{P}) = [16, 22, 16]$ MHz; $\mathbf{A}(^{13}\text{C}) = [-0.5, 4, -0.5]$ MHz. The $|a_{iso}(^1\text{H})|$ of 43.9 MHz corresponds to approximately ±0.03 e$^-$ of spin density localized on the hydride of **[(PS$_3$)NiH][PPN]**, in agreement with the DFT-estimated value of −0.05 e$^-$ (gas phase, M06l).

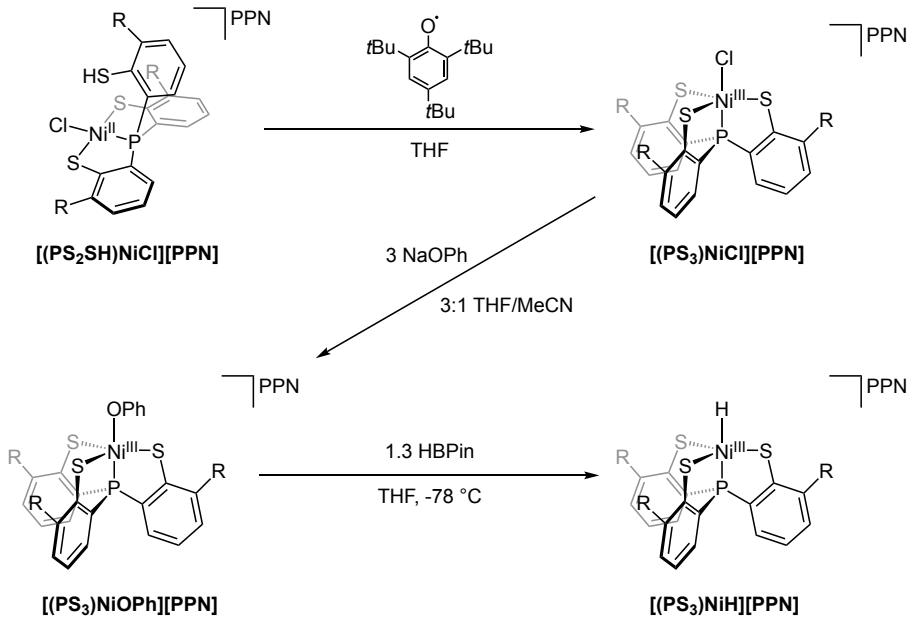

Scheme B.12.1. Synthesis of **[(PS$_3$)NiH][PPN]** (R = SiMe$_3$).

B.12.1 Modified Preparation of [(PS$_3$)NiCl][PPN]

A THF solution of 2,4,6-tri-*tert*-butylphenoxy radical (12.5 mg, 0.048 mmol, 2 mL) was added to a THF solution of **[(PS$_2$SH)NiCl][PPN]** (58 mg, 0.048 mmol, 2 mL) at 23 °C, resulting in the formation of a dark green solution. The reaction was stirred at 23 °C for 15 min and then concentrated to dryness. The resulting dark green material was washed with pentane (5 mL), then extracted with THF (10 mL) and filtered through Celite. Pentane (3 mL) was layered over the THF solution and stored at −35 °C overnight, which yielded dark green crystals of the title compound (0.040 g, 69%). ^{1}H NMR data on the material obtained through this route is in agreement with the published characterization of **[(PS$_3$)NiCl][PPN]**.

B.12.2 NMR Data

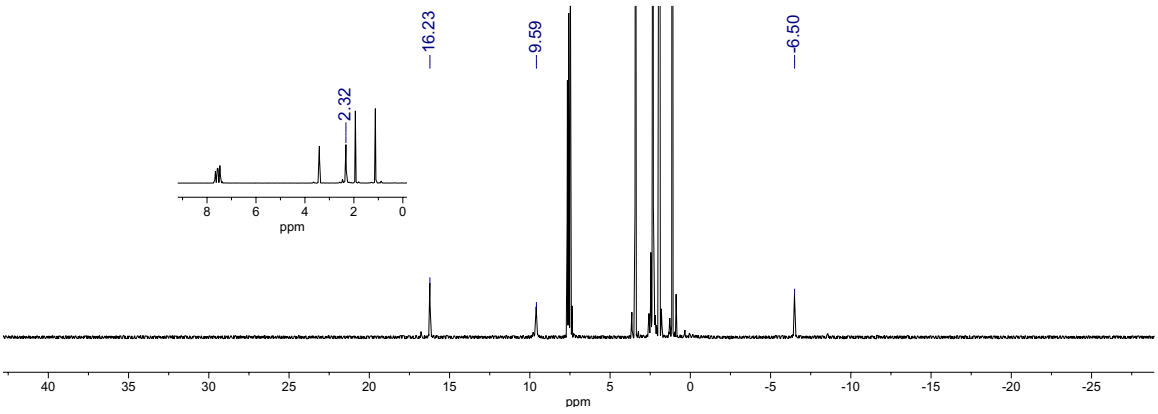

Figure B.12.2.1. ^{1}H NMR spectra of **[(PS$_3$)NiCl][PPN]** in CD_3CN (300 MHz)

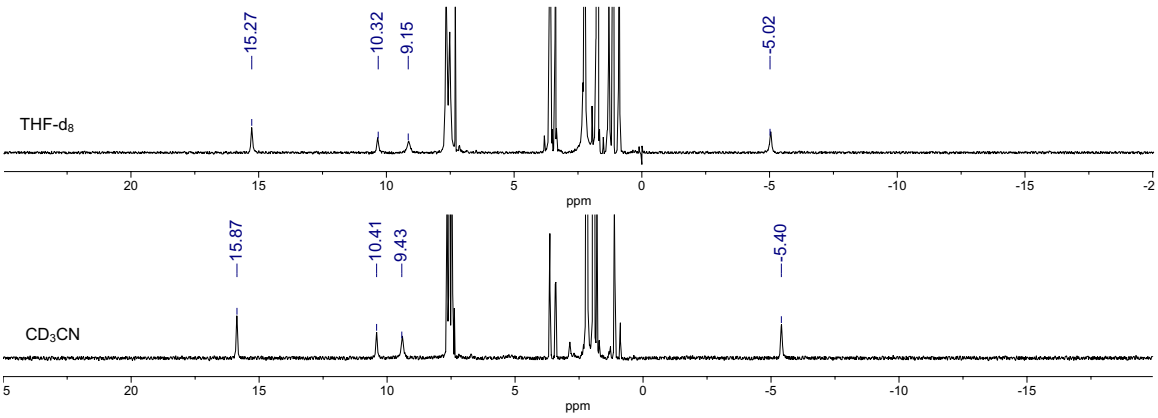

Figure B.12.2.2. ^{1}H NMR spectra of **[(PS$_3$)NiOPh][PPN]** (300 MHz)

B.12.3 UV-Visible data

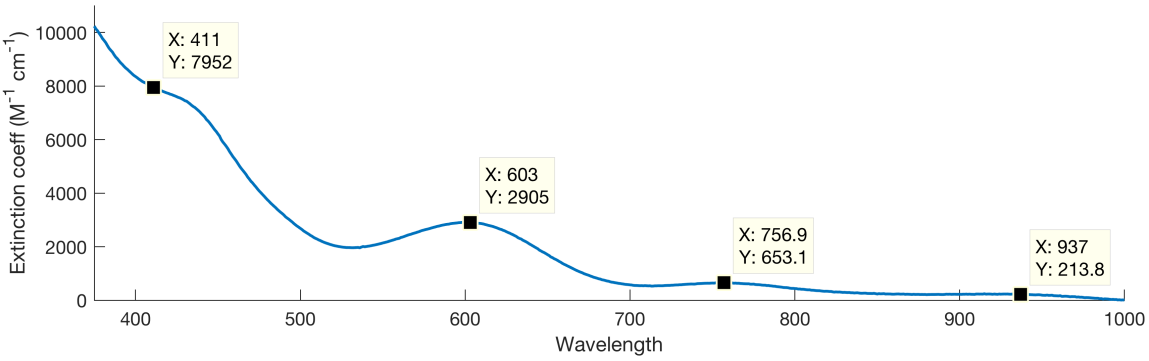

Figure B.12.3.1 UV-vis spectrum of **[(PS$_3$)NiOPh][PPN]** in THF (1 cm cuvette)

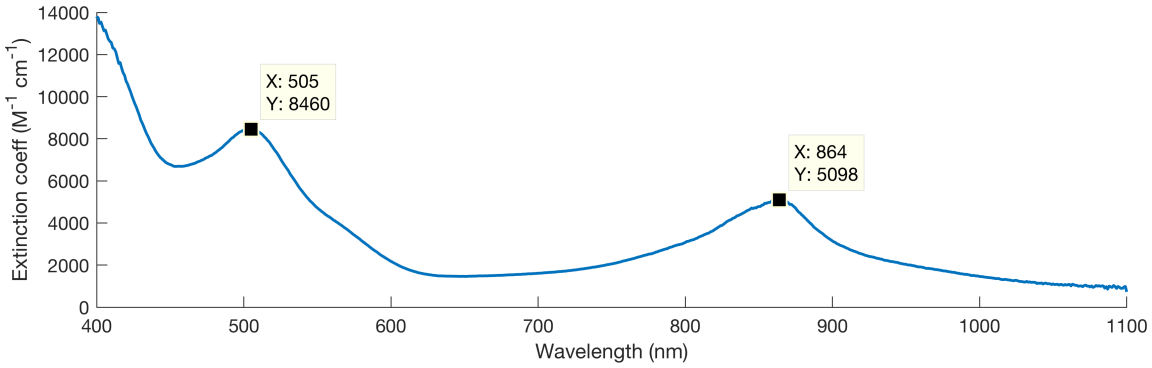

Figure B.12.3.2 UV-vis spectrum of **[(PS$_3$)NiH][PPN]** in THF (1 mm cuvette, −80 °C)

B.12.4 CW EPR Data

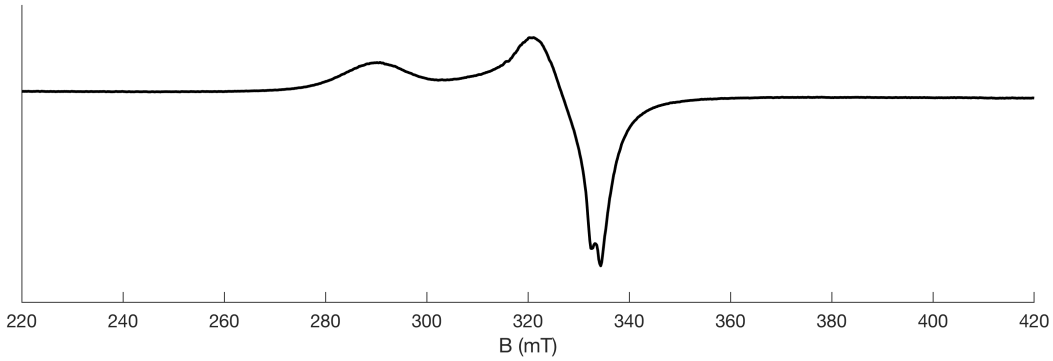

Figure B.12.4.1. X-band CW EPR spectrum of **[(PS$_3$)NiOPh][PPN]** in 3:1 THF/MeCN. Acquisition parameters: MW frequency = 9.371 GHz; temperature = 77 K; MW power = 2 mW; modulation amplitude = 2 G; conversion time = 82 ms.

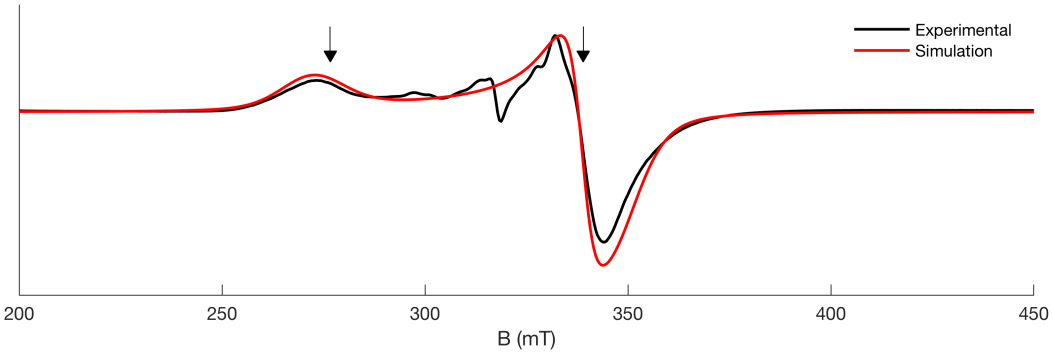

Figure B.12.4.2. X-band CW EPR spectrum of **[(PS$_3$)NiH][PPN]** generated *in situ* in THF (black trace) and simulation in red. Arrows indicate field positions at which X-band HYSCORE spectra were acquired. Simulation parameters: **g** = [2.46, 1.974, 1.93]; gStrain = [0.13 0.002 0.07]. Acquisition parameters: MW frequency = 9.370 GHz; temperature = 5 K; MW power = 8 mW; modulation amplitude = 8 G; conversion time = 41 ms.

B.12.5 HYSCORE Data

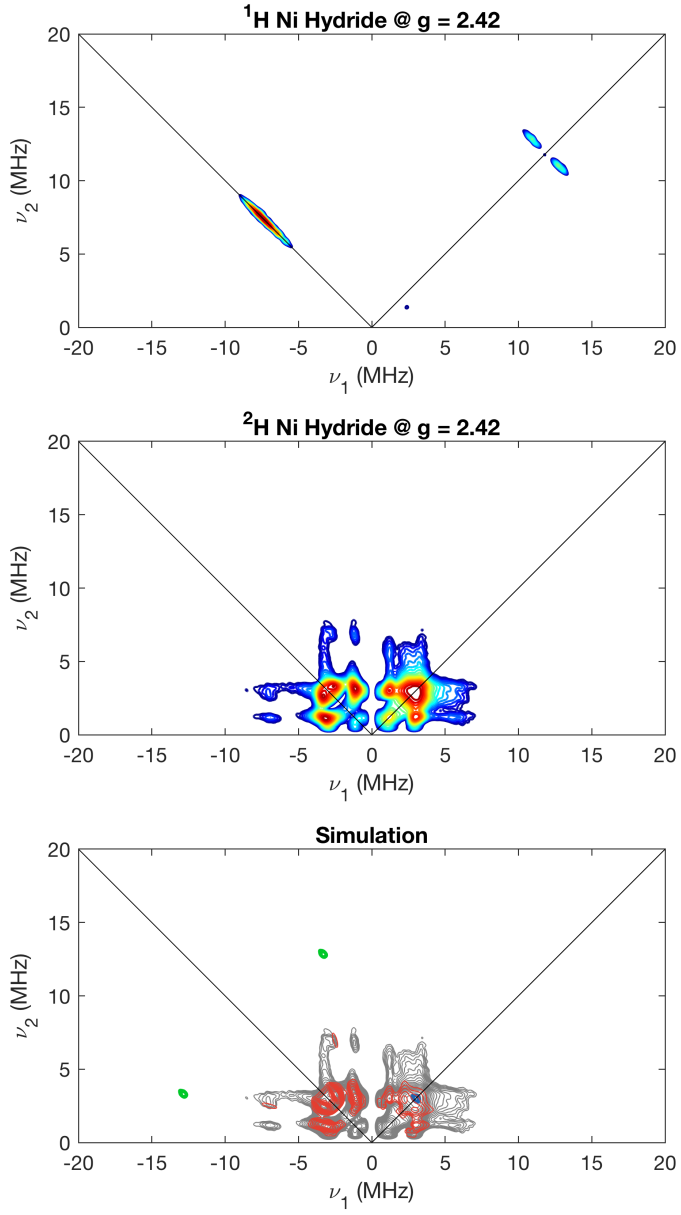

Figure B.12.5.1. X-band HYSCORE spectra of **[(PS$_3$)NiH][PPN]** (top) and **[(PS$_3$)NiD][PPN]** (middle) in THF measured at magnetic fields corresponding to g = 2.42. The ^{2}H spectrum is depicted on the bottom in grey, with simulations of ^{2}H (red) ^{31}P (green), natural abundance ^{13}C (blue) features overlaid. Simulation Parameters: **g** = [2.43, 1.99, 1.99]; **A**(^{2}H) = [1.6, 9.3, 9.3] MHz; **A**(^{31}P) = [16, 22, 16] MHz; **A**(^{13}C) = [−0.5, 4, −0.5] MHz. Acquisition Parameters: microwave frequency = 9.399 GHz; temperature = 5.6 K; B_0 = 277.5 mT; τ = 170 ns; $t_1 = t_2$ = 100 ns; $\Delta t_1 = \Delta t_2$ = 16 ns; shot repetition time (srt) = 1 ms.

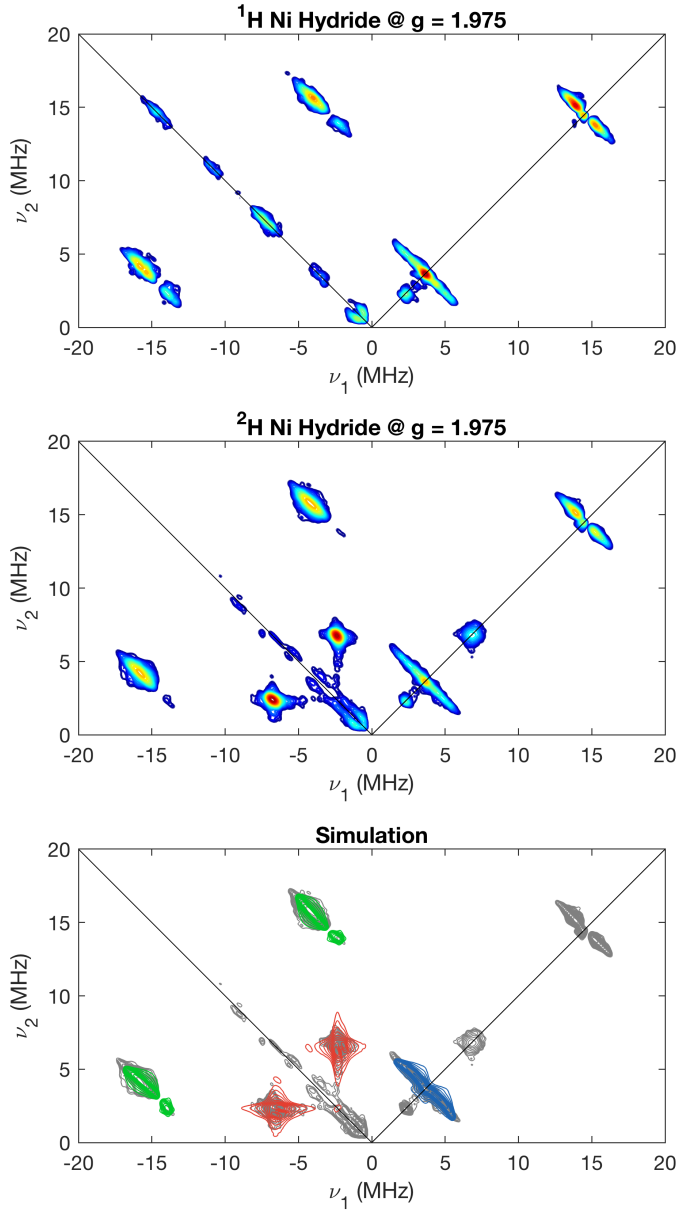

Figure B.12.5.2. X-band HYSCORE spectra of **[(PS$_3$)NiH][PPN]** (top) and **[(PS$_3$)NiD][PPN]** (middle) in THF measured at magnetic fields corresponding to $g = 1.975$. The ^{2}H spectrum is depicted on the bottom in grey, with simulations of ^{2}H (red) ^{31}P (green), natural abundance ^{13}C (blue) features overlaid. Simulation Parameters: **g** = [2.43, 1.99, 1.99]; **A**(^{2}H) = [1.6, 9.3, 9.3] MHz; **A**(^{31}P) = [16, 22, 16] MHz; **A**(^{13}C) = [−0.5, 4, −0.5] MHz. Acquisition Parameters: microwave frequency = 9.399 GHz; temperature = 5.6 K; B_0 = 277.5 mT; τ = 138 ns; $t_1 = t_2$ = 100 ns; $\Delta t_1 = \Delta t_2$ = 16 ns; shot repetition time (srt) = 1 ms.

B.12.6 DFT Data

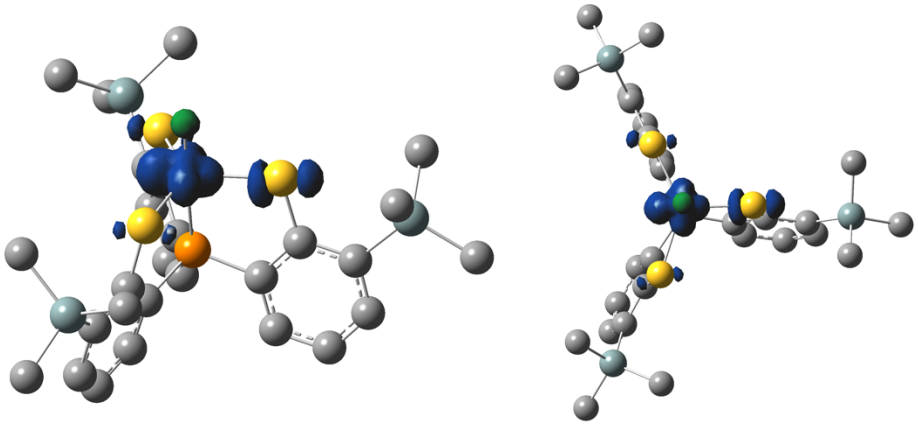

Figure B.12.6.1. Gas-phase optimized DFT spin density plot of **[(PS$_3$)NiH][PPN]**. C-*H* hydrogens not depicted for clarity. (isovalue: 0.005; M06L: def2tzvp (Ni), def2svp (all other atoms))

Table B.12.6.1. Gas-phase optimized coordinates for **[(PS$_3$)NiH]**$^-$ (M06l, $S = 1/2$)

Ni	0.07752900	-0.14827000	-1.51955100
S	-1.97980500	-1.16344700	-1.41979400
S	2.26573300	-0.78157300	-1.44866800
S	-0.17820000	2.15969400	-1.38328400
P	0.06789100	-0.18113800	0.65366900
Si	-4.55175400	-3.11755500	-0.61602200
Si	5.33256100	-1.74904000	-0.60684500
Si	-0.91998600	5.27291800	-0.44991900
C	-1.17900500	-1.36872000	1.23127100
C	-1.26259800	-1.87031600	2.53078400
H	-0.49478600	-1.60834400	3.26576000
C	-2.30714700	-2.71764500	2.89098400
H	-2.37015600	-3.12017600	3.90491100
C	-3.26896000	-3.04584600	1.93398100
H	-4.09021100	-3.70708500	2.23105500
C	-3.21749300	-2.57726800	0.61368700
C	-2.13414000	-1.72757000	0.24452300
C	-5.78456600	-4.21241000	0.30995000
H	-5.31598100	-5.11868400	0.72381600
H	-6.57938700	-4.54471100	-0.37608000
H	-6.27563700	-3.68281200	1.14099600
C	-3.82653300	-4.15171600	-2.00915300

H	-3.06626400	-3.58744600	-2.56705300
H	-4.60888100	-4.47125000	-2.71546400
H	-3.34400600	-5.05850700	-1.61382300
C	-5.51552100	-1.65331400	-1.29438000
H	-6.00290600	-1.09318000	-0.48212300
H	-6.30322100	-1.98879000	-1.98720900
H	-4.85843900	-0.95529500	-1.83069300
C	1.72179100	-0.60531900	1.27252200
C	2.08188100	-0.61499900	2.62222100
H	1.34987900	-0.32642700	3.38340300
C	3.37114100	-0.97104300	3.00513800
H	3.65352200	-0.97942300	4.06058000
C	4.29768200	-1.31318200	2.01776700
H	5.30698000	-1.60010200	2.33198600
C	3.99254700	-1.28669400	0.65049400
C	2.67385100	-0.90673900	0.26356700
C	5.79977500	-0.30804400	-1.71978700
H	6.10837600	0.56615100	-1.12723300
H	4.95581200	0.00140200	-2.35030700
H	6.64132300	-0.58002800	-2.37637500
C	6.88604200	-2.22643200	0.36046800
H	7.68642100	-2.52140200	-0.33621100
H	6.71516900	-3.07844700	1.03659000
H	7.27649000	-1.39440300	0.96679700
C	4.83596600	-3.24591400	-1.63093400
H	3.92555300	-3.04542500	-2.21239900
H	4.63541100	-4.11639100	-0.98825000
H	5.63851400	-3.52590800	-2.33128400
C	-0.40803900	1.45421900	1.27945400
C	-0.70039900	1.70102700	2.62297100
H	-0.68464900	0.87416600	3.34165200
C	-1.03173300	2.98283700	3.04741600
H	-1.26539300	3.17861700	4.09664700
C	-1.06895000	4.01403000	2.10371400
H	-1.33019900	5.02080400	2.44803700
C	-0.80501000	3.81073700	0.74419500
C	-0.47399400	2.48956300	0.30969300
C	0.71614500	5.60877000	-1.31450000
H	0.63714600	6.48574400	-1.97616500
H	1.03565500	4.74859700	-1.91833700
H	1.51225500	5.81384300	-0.58296000
C	-1.33438000	6.81813400	0.55988100
H	-0.57190500	7.03805000	1.32320700

H	-2.30524600	6.73847800	1.07313100
H	-1.39086300	7.69583400	-0.10306100
C	-2.30260500	5.04932300	-1.70429100
H	-2.36473500	5.91742100	-2.37932800
H	-3.27627500	4.94552200	-1.20225800
H	-2.14710100	4.14910700	-2.31386600
H	0.06892100	-0.07698900	-3.01855200

Table B.12.6.2. DFT-calculated spin density of **[(PS$_3$)NiH]$^-$** (gas phase)

ATOM LABEL	ATOM	SPIN DENSITY (E^-)	SPIN DENSITY (%)
1	Ni	0.734	60.6
2	S	0.067	5.5
3	S	0.067	5.5
4	S	0.156	12.9
5	P	-0.009	0.8
6	Si	0.001	0.1
7	Si	0.000	0.0
8	Si	0.007	0.6
9	C	0.009	0.7
10	C	-0.004	0.3
11	H	0.000	0.0
12	C	0.008	0.7
13	H	-0.001	0.0
14	C	-0.003	0.3
15	H	0.000	0.0
16	C	0.007	0.6
17	C	-0.005	0.4
18	C	0.000	0.0
19	H	0.000	0.0
20	H	0.000	0.0
21	H	0.000	0.0
22	C	0.000	0.0
23	H	0.001	0.1
24	H	0.000	0.0
25	H	0.000	0.0
26	C	0.000	0.0
27	H	0.000	0.0
28	H	0.000	0.0
29	H	0.001	0.0
30	C	0.015	1.2
31	C	-0.007	0.5
32	H	0.000	0.0

33	C	0.014	1.1
34	H	-0.001	0.1
35	C	-0.006	0.5
36	H	0.000	0.0
37	C	0.011	0.9
38	C	-0.008	0.7
39	C	0.000	0.0
40	H	0.000	0.0
41	H	-0.001	0.0
42	H	0.000	0.0
43	C	0.000	0.0
44	H	0.000	0.0
45	H	0.000	0.0
46	H	0.000	0.0
47	C	0.000	0.0
48	H	0.001	0.1
49	H	0.000	0.0
50	H	0.000	0.0
51	C	0.002	0.2
52	C	0.001	0.1
53	H	0.000	0.0
54	C	-0.003	0.2
55	H	0.000	0.0
56	C	0.000	0.0
57	H	0.000	0.0
58	C	0.000	0.0
59	C	-0.007	0.6
60	C	-0.001	0.0
61	H	0.000	0.0
62	H	0.001	0.1
63	H	0.000	0.0
64	C	0.000	0.0
65	H	0.000	0.0
66	H	0.000	0.0
67	H	0.000	0.0
68	C	-0.001	0.1
69	H	0.000	0.0
70	H	0.000	0.0
71	H	0.000	0.0
72	H	-0.049	4.0

A p p e n d i x C

SUPPLEMENTARY INFORMATION FOR CHAPTER 4

C.1 NMR Spectra

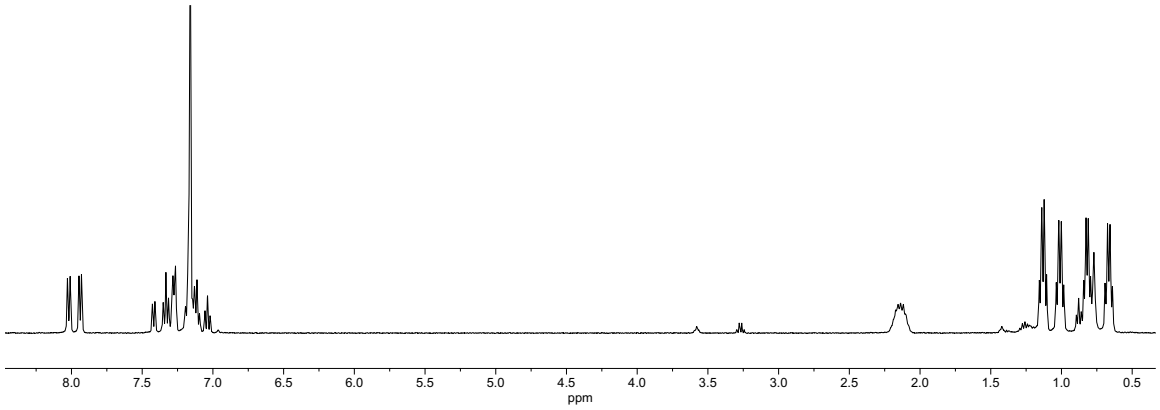

Figure C.1.1. ^{1}H NMR spectrum of **4.2** in C_6D_6 (400 MHz)

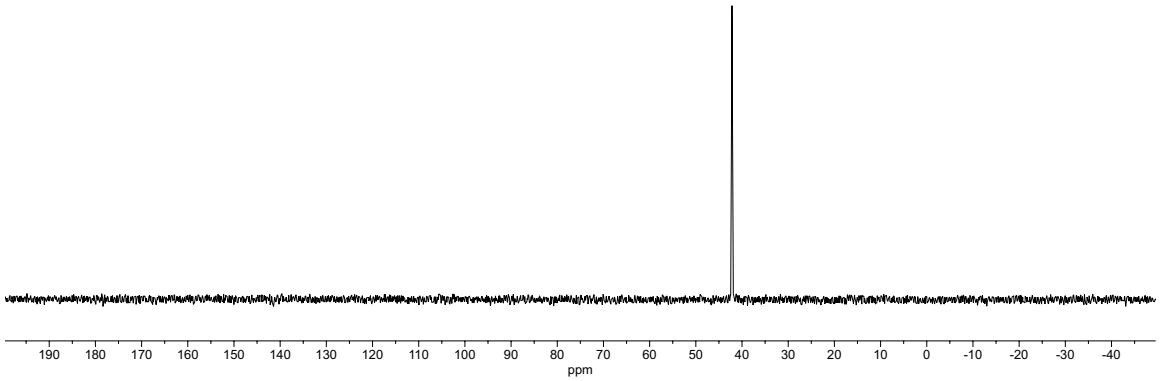

Figure C.1.2. ^{31}P NMR spectrum of **4.2** in C_6D_6 (162 MHz)

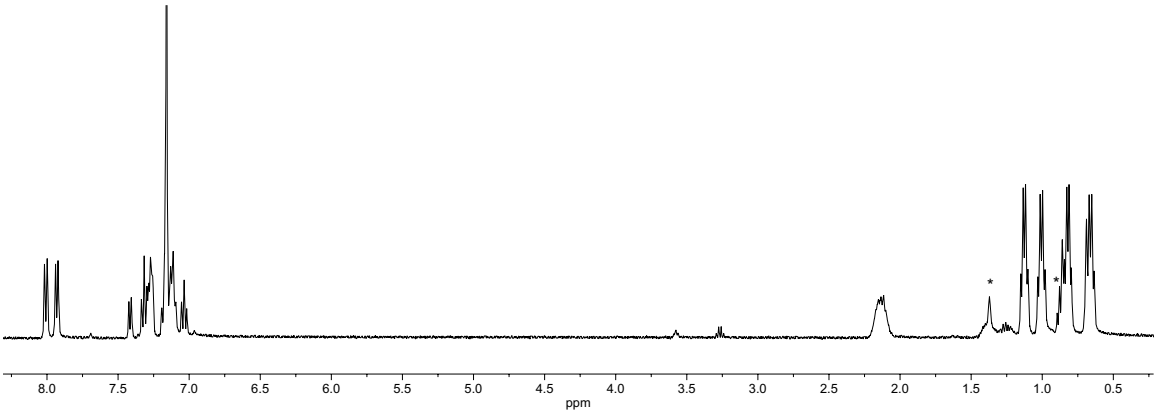

Figure C.1.3. ^{1}H NMR spectrum of **4.2-^{15}N** in C_6D_6 (400 MHz, *H grease)

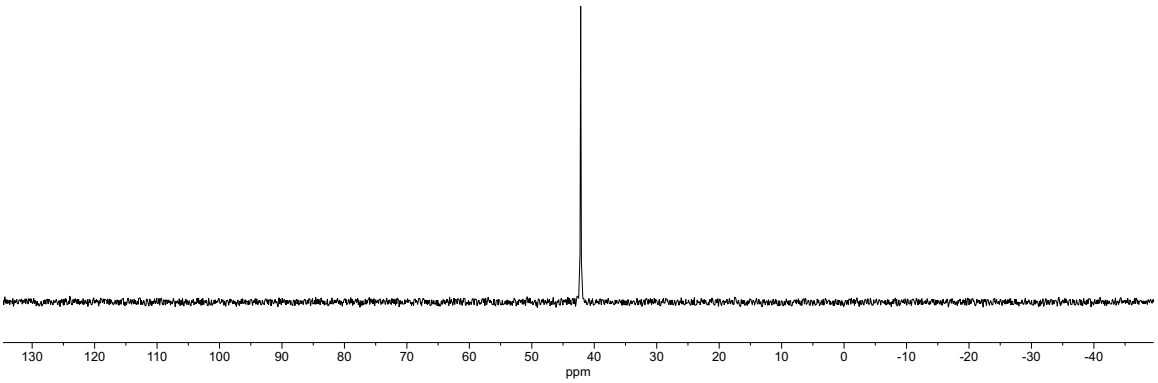

Figure C.1.4. ^{31}P NMR spectrum of **4.2-^{15}N** in C_6D_6 (162 MHz)

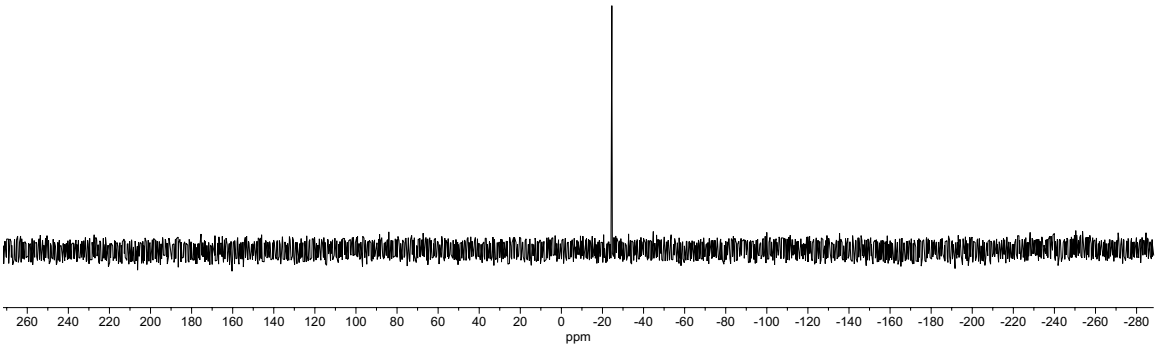

Figure C.1.5. ^{15}N NMR spectrum of **4.2-^{15}N** in C_6D_6 (41 MHz)

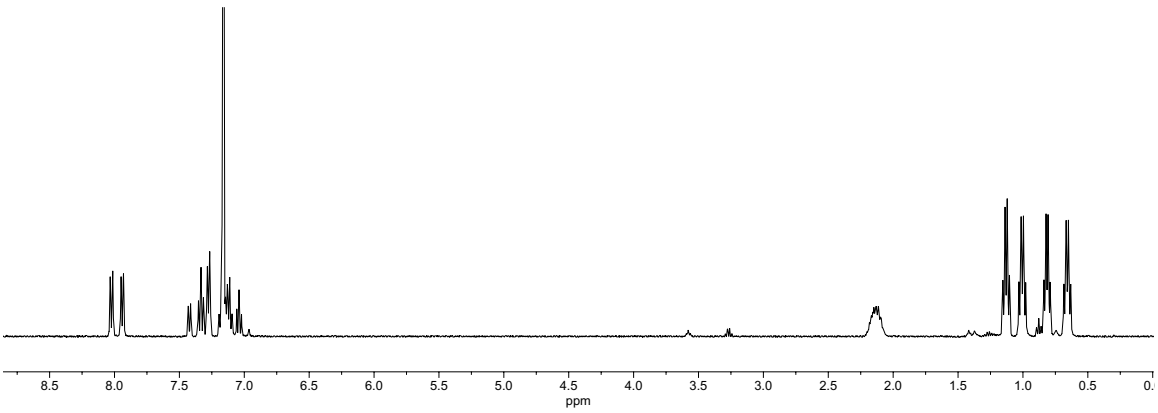

Figure C.1.6. ^{1}H NMR spectrum of **4.2-^{2}H** in C_6D_6 (400 MHz)

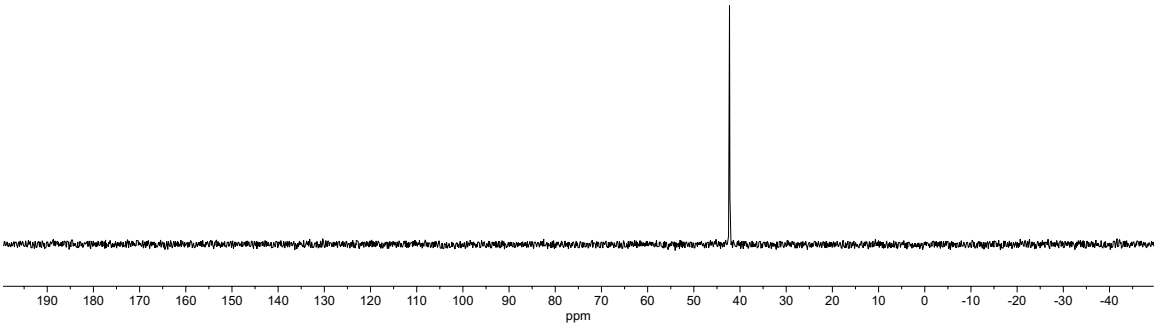

Figure C.1.7. ^{31}P NMR spectrum of **4.2-^{2}H** in C_6D_6 (162 MHz)

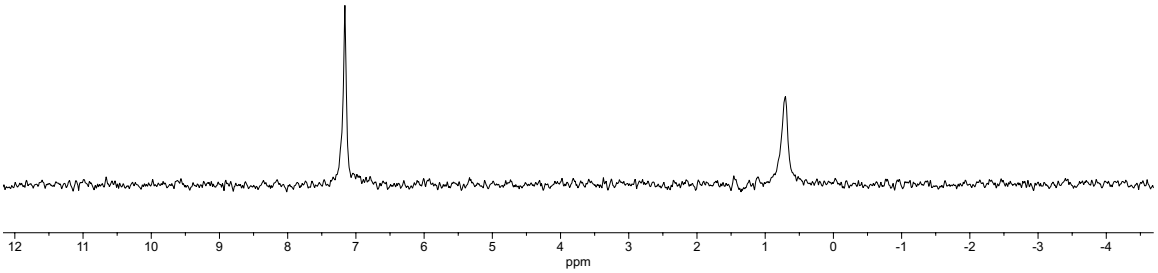

Figure C.1.8. ^{2}H NMR spectrum of **4.2-^{2}H** in C_6H_6 (61 MHz)

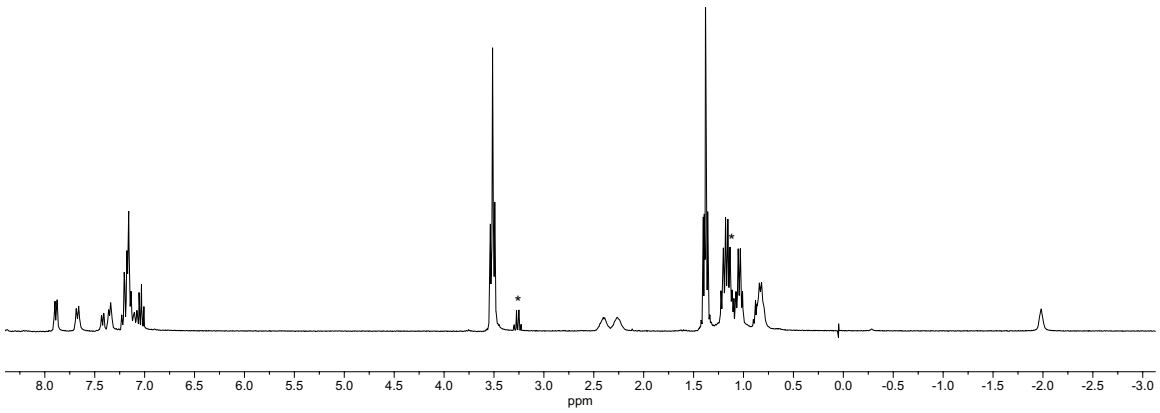

Figure C.1.9. ^{1}H NMR spectrum of **4.3** in C_6D_6 (300 MHz , *Et_2O)

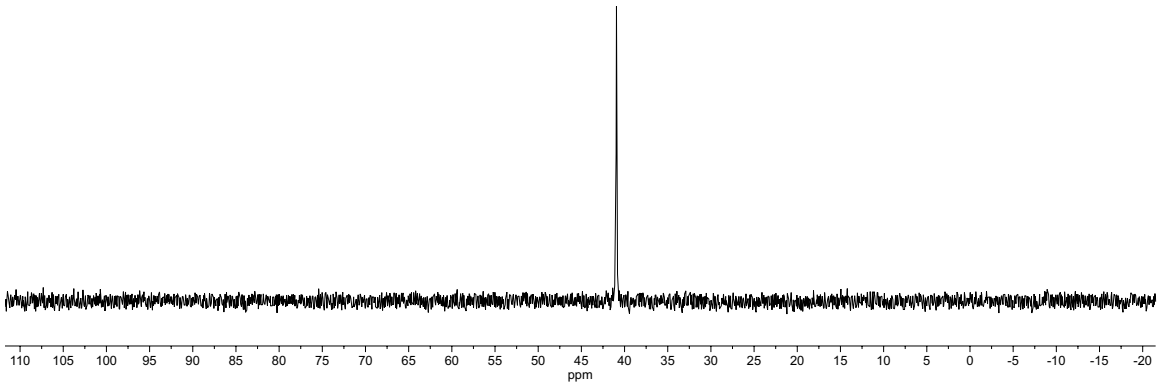

Figure C.1.10. ^{31}P NMR spectrum of **4.3** in C_6D_6 (121 MHz)

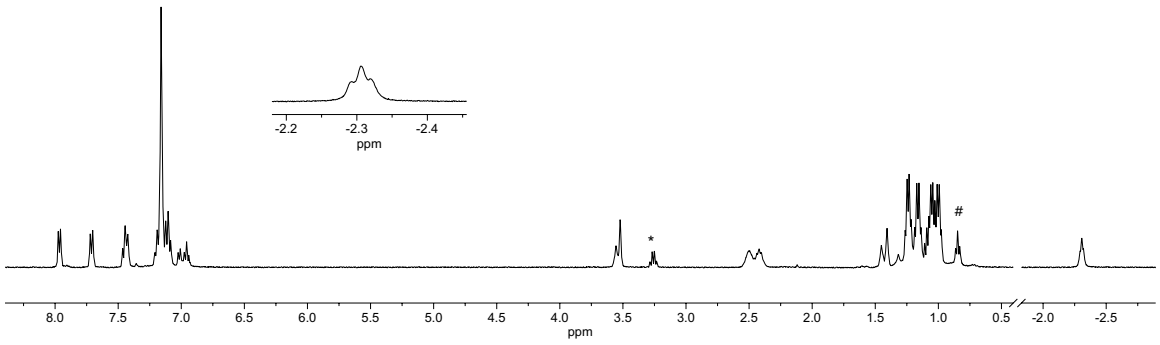

Figure C.1.11. ^{1}H NMR spectrum of **4.3** in 1:5 THF-d_8/C_6D_6 (400 MHz, *Et_2O, $^{\#}$pentane)

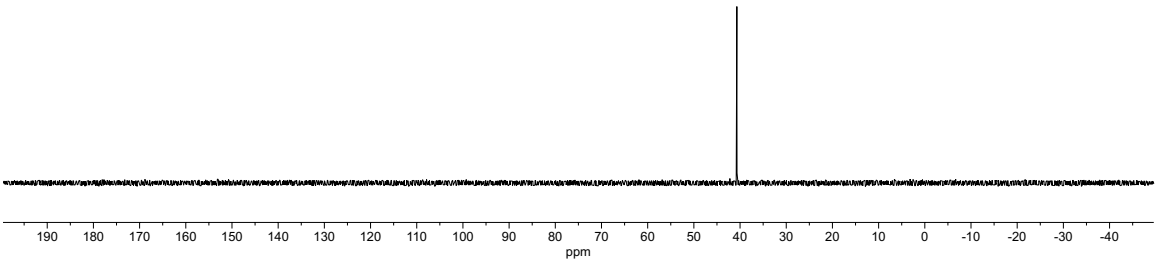

Figure C.1.12. ^{31}P NMR spectrum of **4.3** in 1:5 THF-d_8/C_6D_6 (162 MHz)

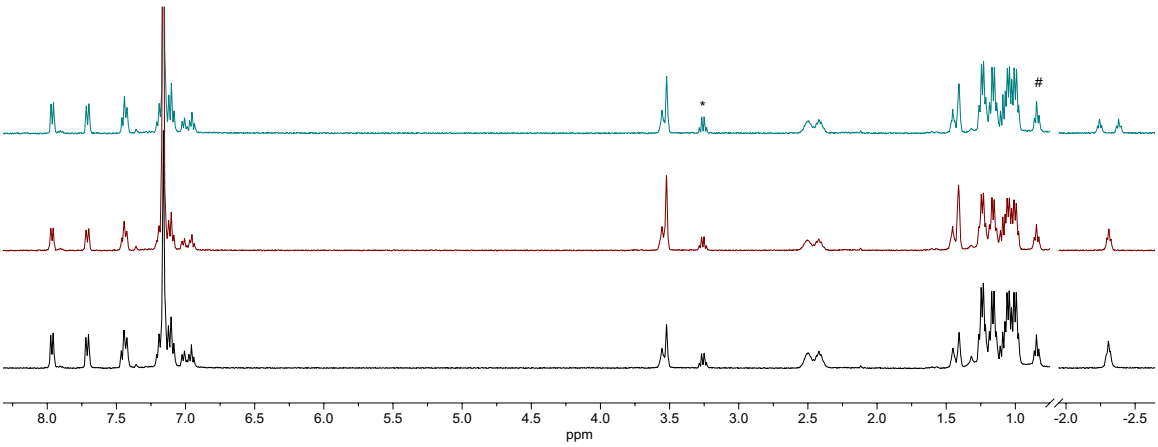

Figure C.1.13. {top} ^{1}H NMR spectrum of **4.3-^{15}N** in 1:5 THF-d_8/C_6D_6 (400 MHz, *Et_2O, $^{\#}$pentane), {middle} ^{1}H{^{15}N} NMR spectrum of **4.3-^{15}N** in 1:5 THF-d_8/C_6D_6 (400 MHz), {bottom} ^{1}H NMR spectrum of **4.3** in 1:5 THF-d_8/C_6D_6 (400 MHz)

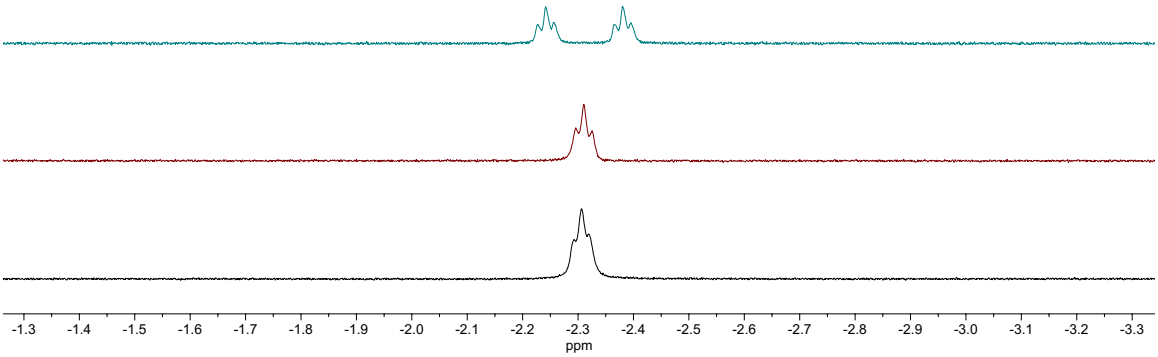

Figure C.1.14. {top} Partial ^{1}H NMR spectrum of **4.3-^{15}N** in 1:5 THF-d_8/C_6D_6 (400 MHz), {middle} Partial ^{1}H{^{15}N} NMR spectrum of **4.3-^{15}N** in 1:5 THF-d_8/C_6D_6 (400 MHz), {bottom} Partial ^{1}H NMR spectrum of **4.3** in 1:5 THF-d_8/C_6D_6 (400 MHz)

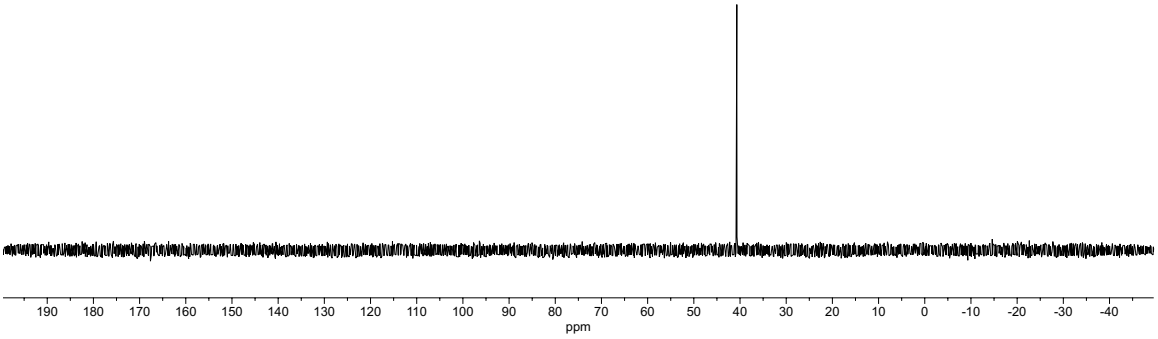

Figure C.1.15. ^{31}P NMR spectrum of **4.3-^{15}N** in 1:5 THF-d_8/C_6D_6 (162 MHz)

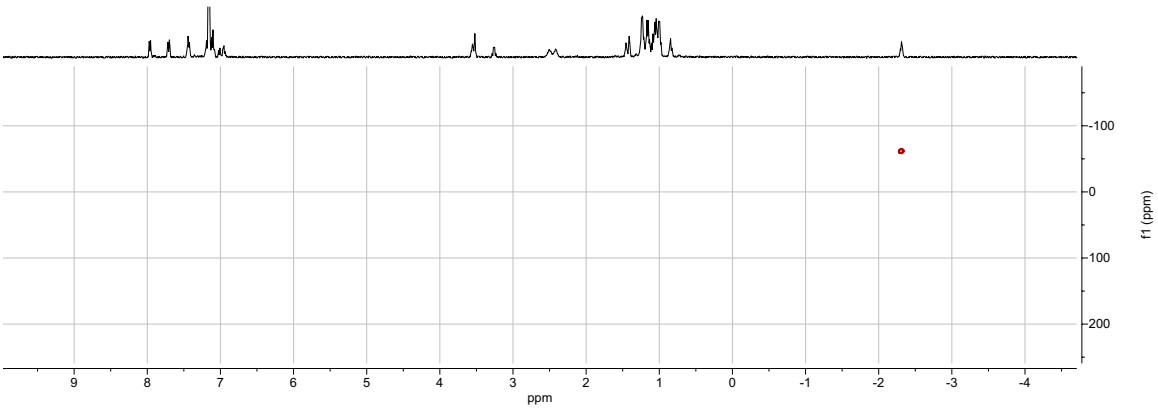

Figure C.1.16. ^{1}H-^{15}N HSQC of **4.3-^{15}N** in 1:5 THF-d_8/C_6D_6 (^{1}H{^{15}N} spectrum on top; 400 MHz, 41 MHz)

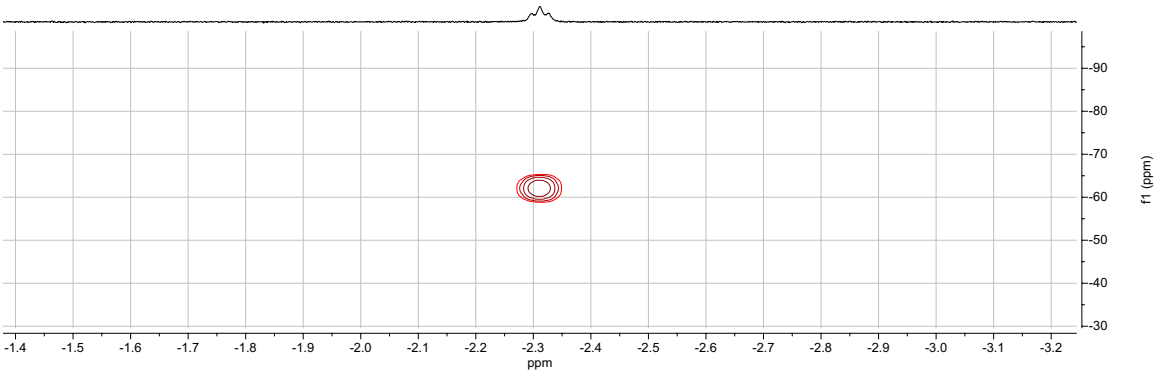

Figure C.1.17. Partial ^{1}H-^{15}N HSQC of **4.3-^{15}N** in 1:5 THF-d_8/C_6D_6 (^{1}H{^{15}N} spectrum on top; 400 MHz, 41 MHz)

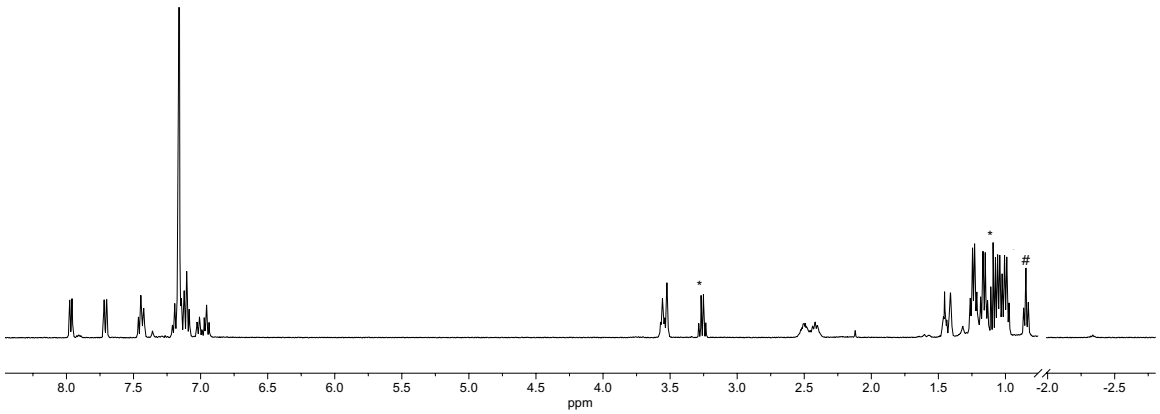

Figure C.1.18. ^{1}H NMR spectrum of **4.3-^{2}H** in 1:5 THF-d_8/C_6D_6 (400 MHz, *Et_2O, $^{\#}$pentane)

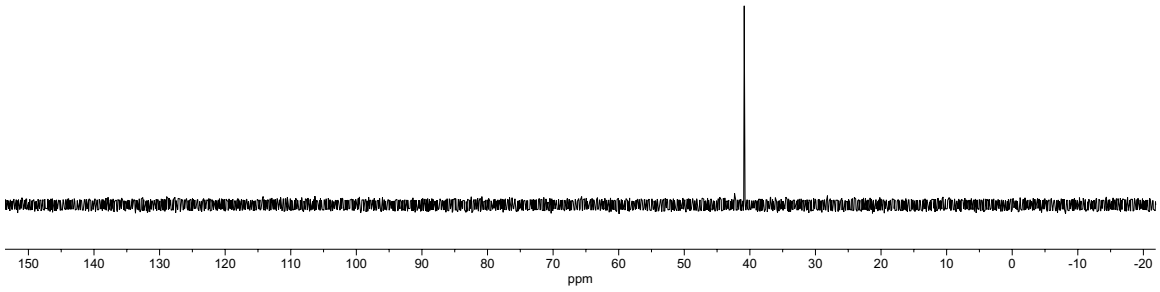

Figure C.1.19. ^{31}P NMR spectrum of **4.3-^{2}H** in 1:5 THF-d_8/C_6D_6 (162 MHz)

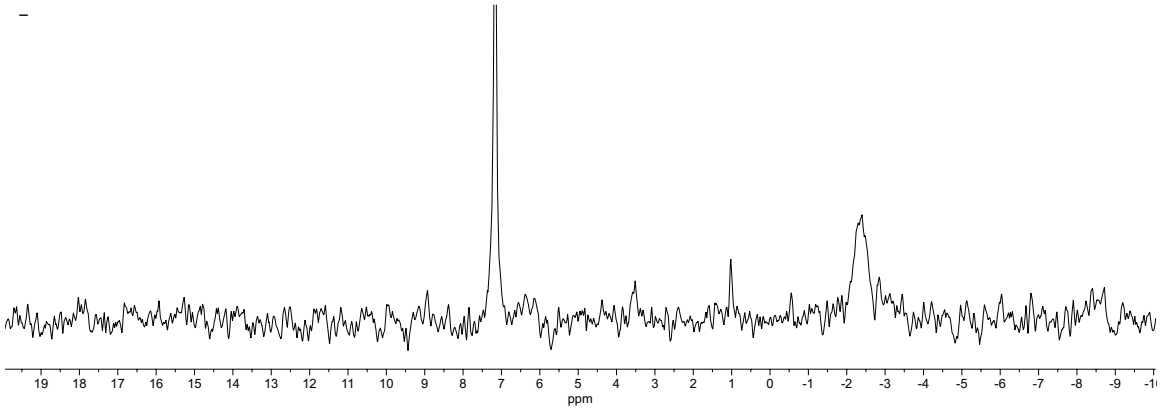

Figure C.1.20. ^{2}H NMR spectrum of **4.3-^{2}H** in 1:5 THF-h_8/C_6H_6 (61 MHz)

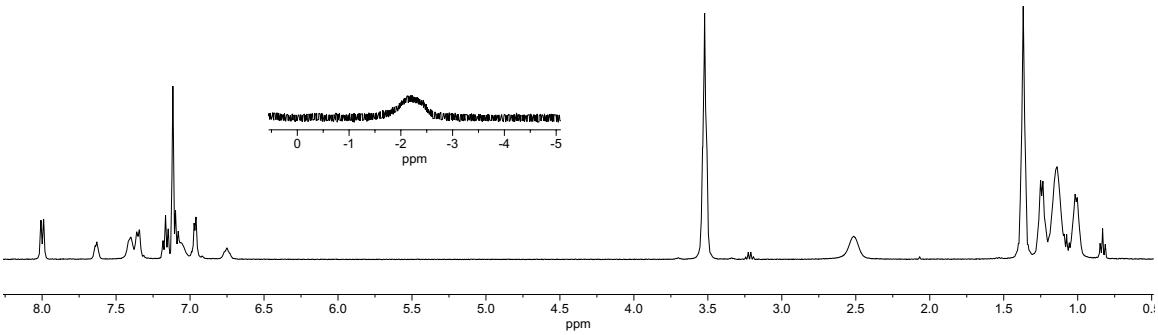

Figure C.1.21. ^{1}H NMR spectrum of $(SiP_2S)NiNH_2Na(THF)_3$ in C_6D_6 (400 MHz)

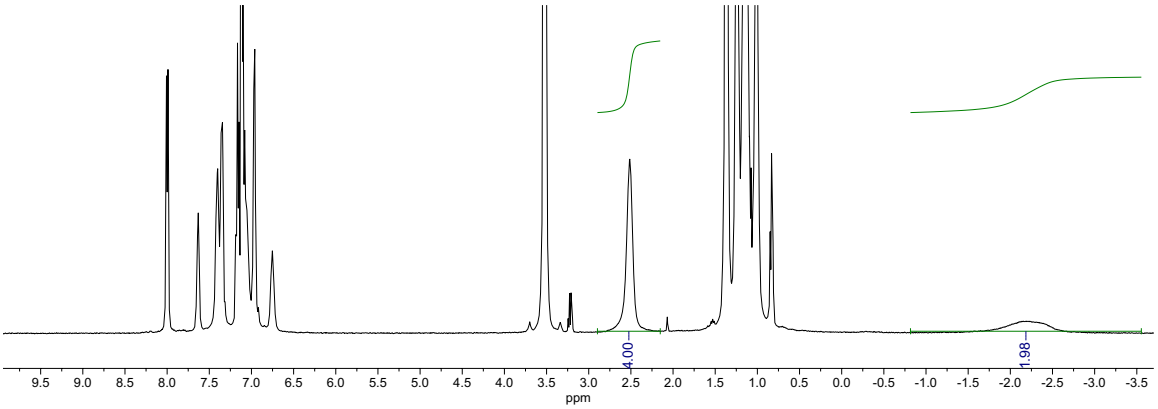

Figure C.1.22. ^{1}H NMR spectrum of $(SiP_2S)NiNH_2Na(THF)_3$ in C_6D_6 (400 MHz)

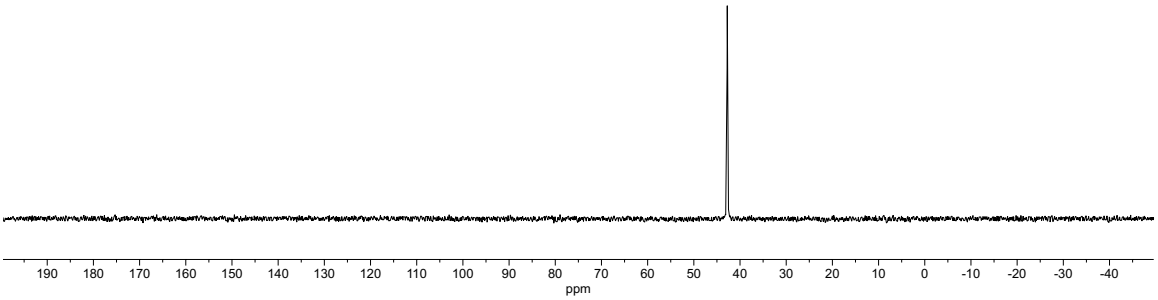

Figure C.1.23. ^{31}P NMR spectrum $(SiP_2S)NiNH_2Na(THF)_3$ in C_6D_6 (162 MHz)

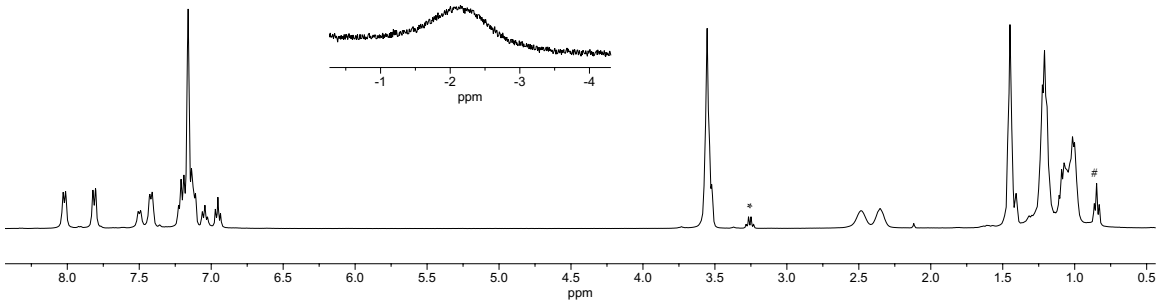

Figure C.1.24. ^{1}H NMR spectrum of $(SiP_2S)NiNH_2Na(THF)_3$ in 1:5 THF-d_8/C_6D_6 (400 MHz)

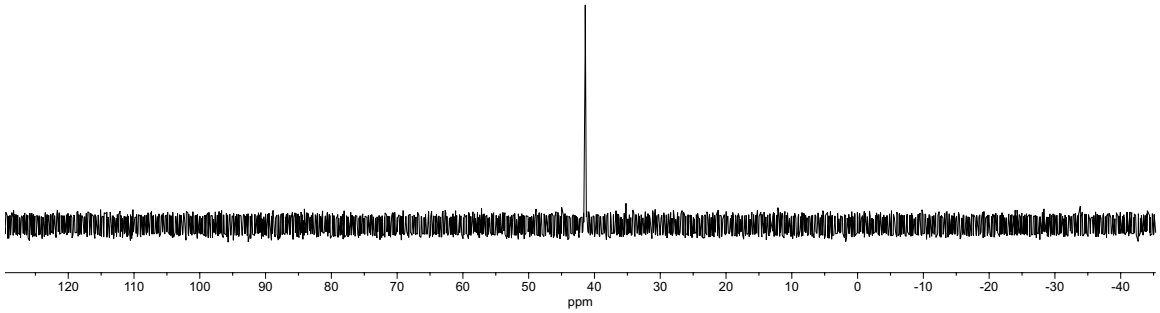

Figure C.1.25. ^{31}P NMR spectrum of $(SiP_2S)NiNH_2Na(THF)_3$ in 1:5 THF-d_8/C_6D_6 (162 MHz)

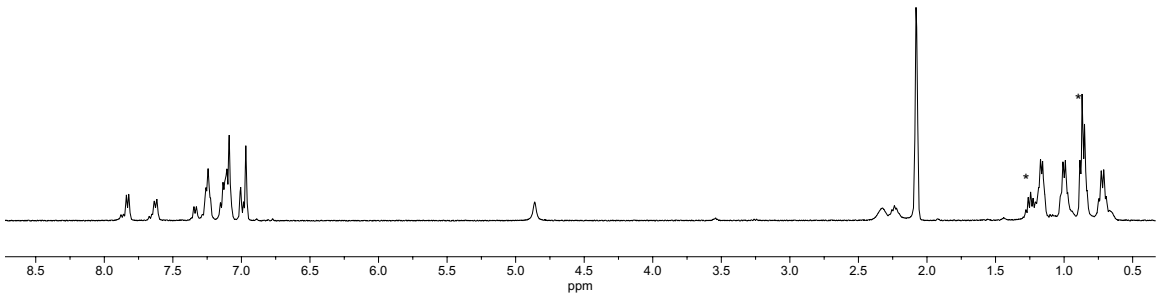

Figure C.1.26. ^{1}H NMR spectrum of **4.4** in toluene-d_8 (400 MHz, *pentane)

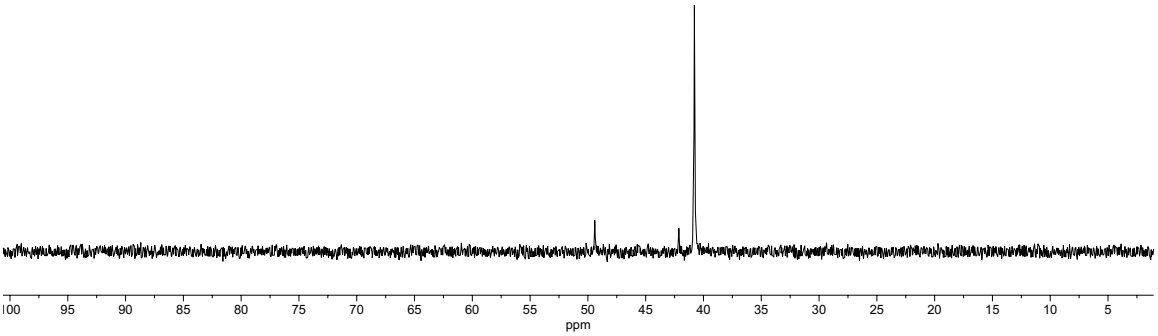

Figure C.1.27. ^{31}P NMR spectrum of **4.4** in toluene-d_8 (162 MHz). Minor ^{31}P shifts at 42.1 ppm and 49.4 ppm correspond to **4.2** and **4.5**, respectively, due to the disproportionation of **4.4** in solution.

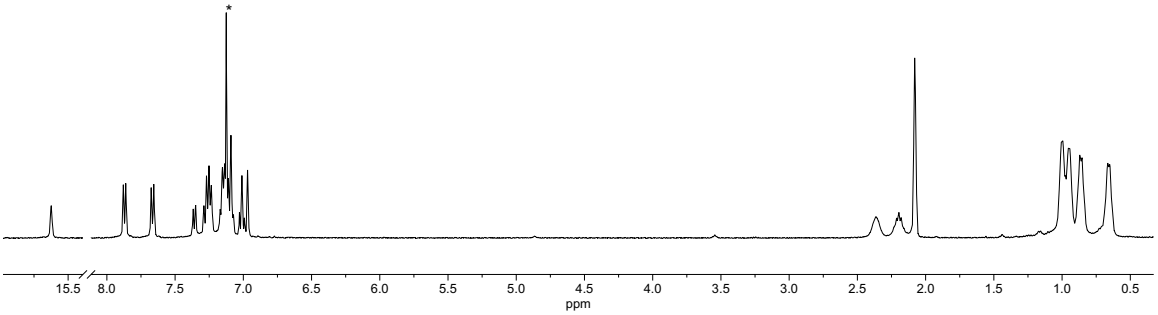

Figure C.1.28. ^{1}H NMR spectrum of **4.5** in toluene-d_8 (400 MHz, *C_6H_6)

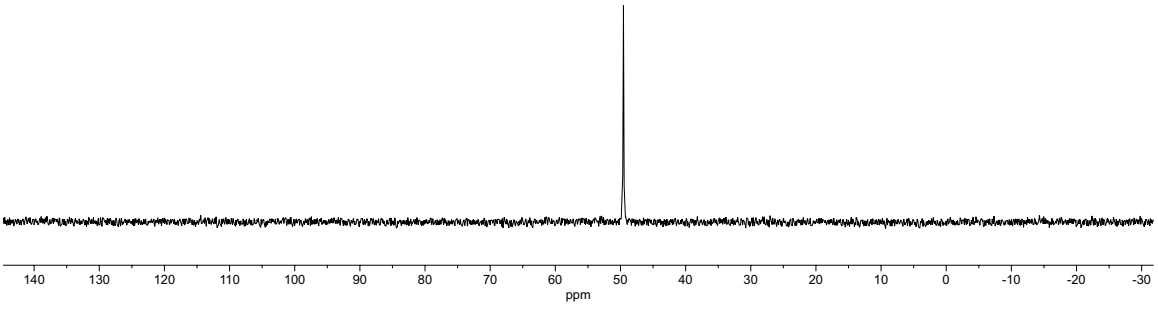

Figure C.1.29. ^{31}P NMR spectrum of **4.5** in C_6D_6 (162 MHz)

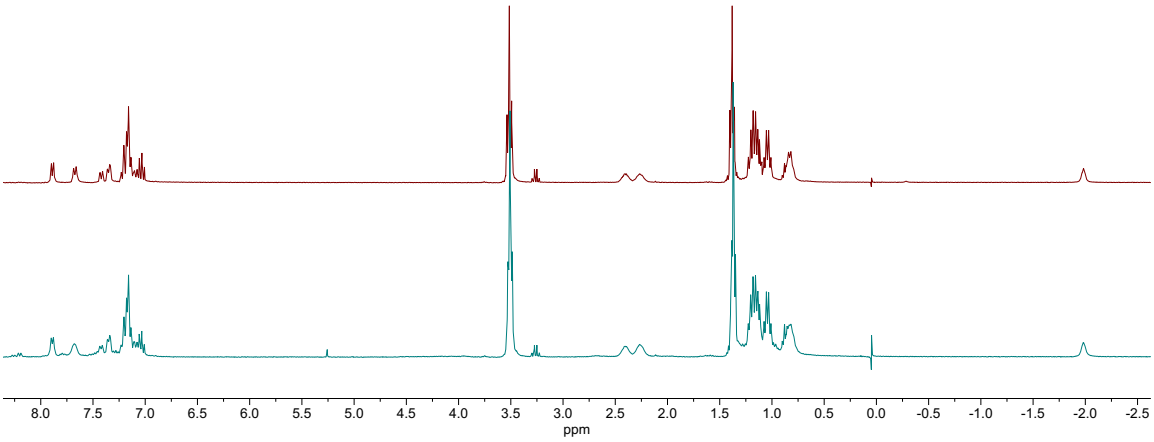

Figure C.1.30. {top} ^{1}H NMR spectrum of **4.3** in C_6D_6, generated from $LiNH_2$ and **4.1** (300 MHz) {bottom} ^{1}H NMR spectrum in C_6D_6 of the crude reaction mixture upon treatment of **4.2** with *n*BuLi (300MHz)

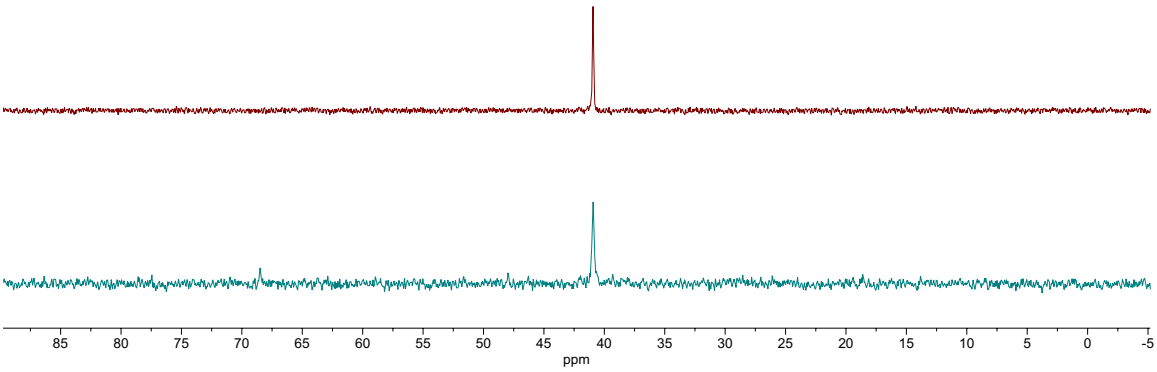

Figure C.1.31. {top} ^{31}P NMR spectrum of **4.3** in C_6D_6, generated from $LiNH_2$ and **4.1** (121MHz) {bottom} ^{31}P NMR spectrum in C_6D_6 of the crude reaction mixture upon treatment of **4.2** with *n*BuLi (121 MHz)

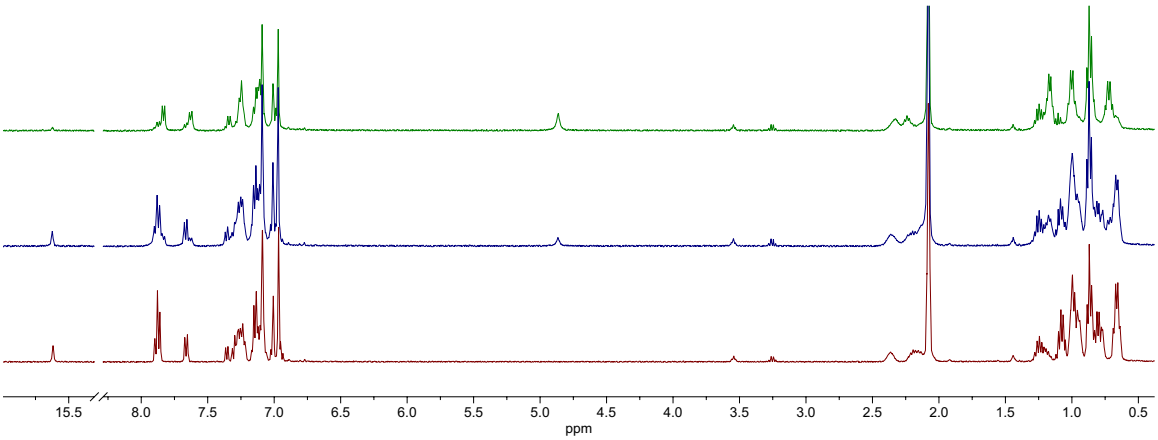

Figure C.1.32. {top} ^{1}H NMR spectrum of **4.4** in toluene-d_8 (400 MHz) {middle} ^{1}H NMR spectrum of sample after 1 h at 25 ºC in toluene-d_8 (400 MHz) {bottom} ^{1}H NMR spectrum of sample after 1 d at 25 ºC in toluene-d_8 (400 MHz)

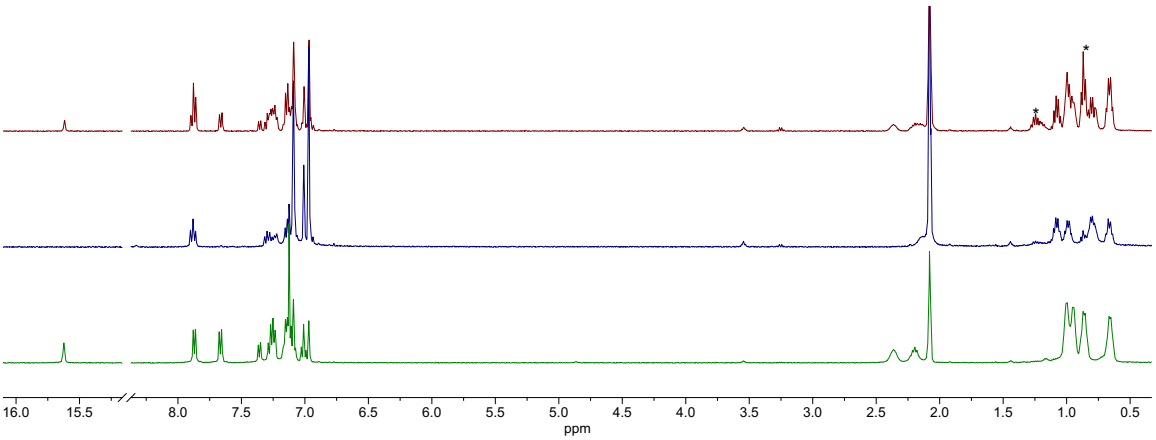

Figure C.1.33. {top} ^{1}H NMR spectrum of **4.2** and **4.5** (generated via disproportionation of **4.4** after 1 d at 25 ºC) in toluene-d_8 (400 MHz,*pentane) {middle} ^{1}H NMR spectrum of **4.2** in toluene-d_8 (400 MHz) {bottom} ^{1}H NMR spectrum of **4.5** in toluene-d_8 (400 MHz)

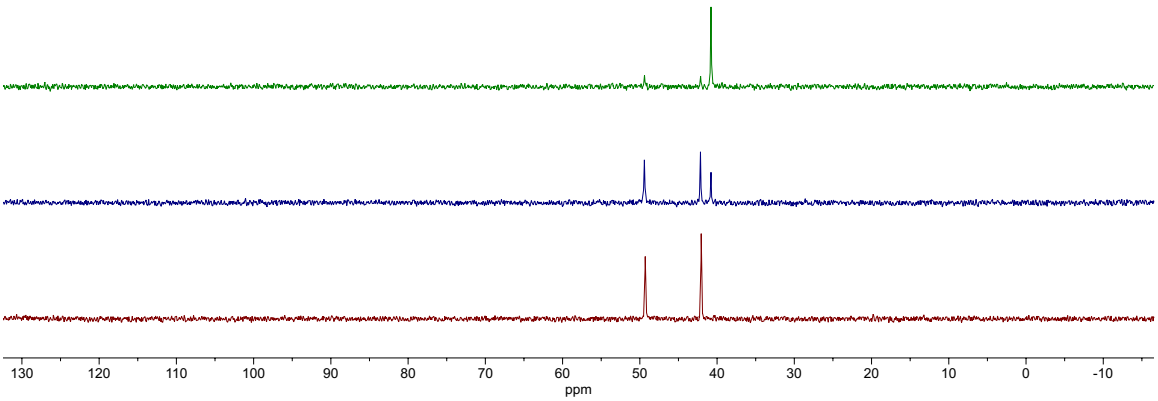

Figure C.1.34. {top} ^{31}P NMR spectrum of **4.4** in toluene-d_8 (162 MHz) {middle} ^{31}P NMR spectrum of sample after 1 h at 25 ºC in toluene-d_8 (162 MHz) {bottom} ^{31}P NMR spectrum of sample after 1 d at 25 ºC in toluene-d_8 (162 MHz)

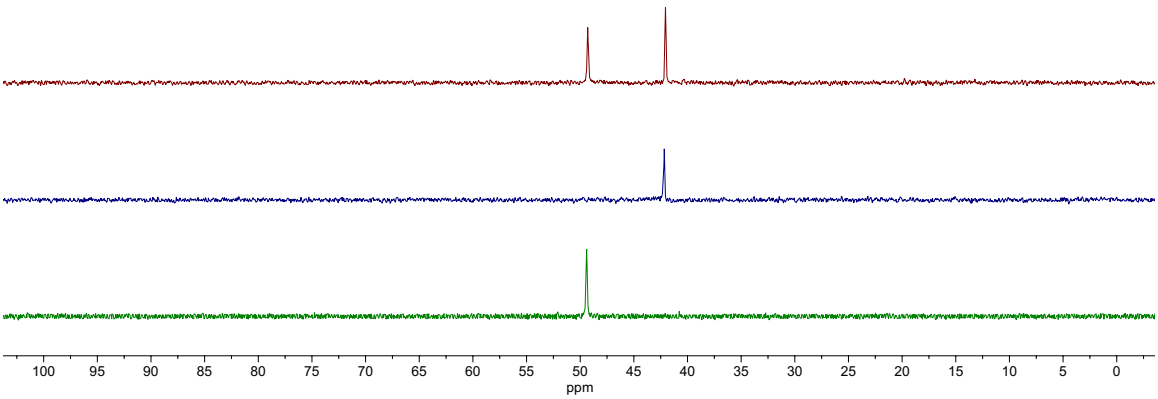

Figure C.1.35. {top} ^{31}P NMR spectrum of **4.2** and **4.5** (generated via disproportionation of **4.4** after 1 d at 25 ºC) in toluene-d_8 (162 MHz) {middle} ^{31}P NMR spectrum of **4.2** in toluene-d_8 (162 MHz) {bottom} ^{31}P NMR spectrum of **4.5** in toluene-d_8 (162 MHz)

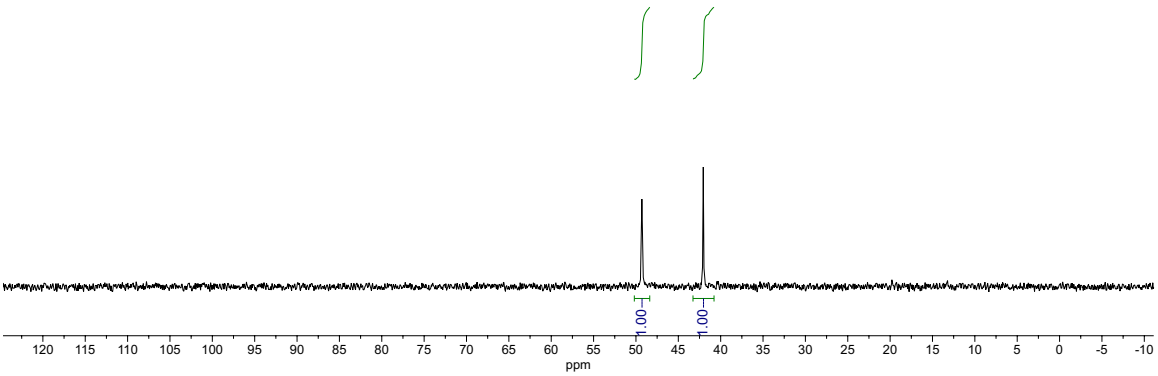

Figure C.1.36. ^{31}P NMR spectrum of **4.2** and **4.5** (generated via disproportionation of **4.4** after 1 d at 25 ºC) in toluene-d_8 with integrations (162 MHz)

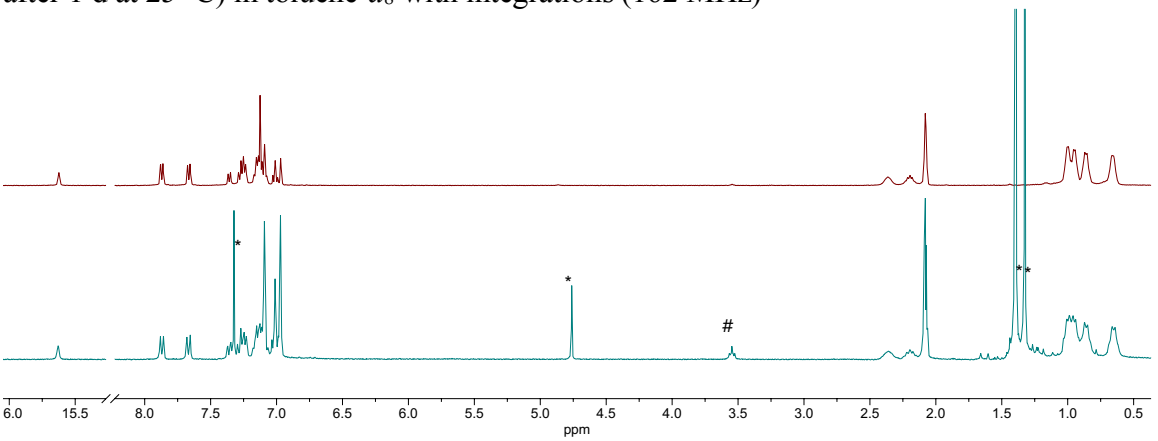

Figure C.1.37. {top} ^{1}H NMR spectrum of **4.5** in toluene-d_8 (400 MHz) {bottom} ^{1}H NMR spectrum in toluene-d_8 of the crude reaction mixture upon treatment of **4.4** with 2,4,6-tri-*ter*t-butylphenoxyl radical (300 MHz, *2,4,6-tri-*ter*t-butylphenol, $^{\#}$THF)

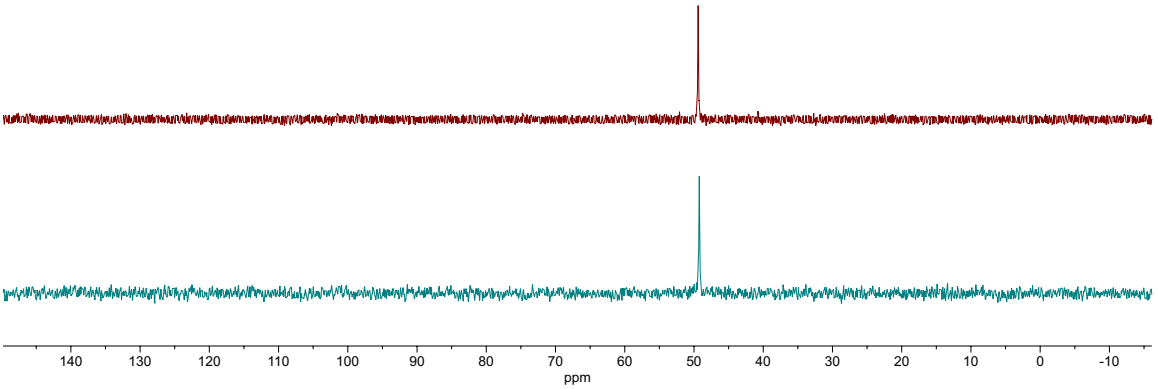

Figure C.1.38. {top} ^{31}P NMR spectrum of **4.5** in toluene-d_8 (162 MHz) {bottom} ^{31}P NMR spectrum in toluene-d_8 of the crude reaction mixture upon treatment of **4.4** with 2,4,6-tri-*ter*t-butylphenoxyl radical (121 MHz)

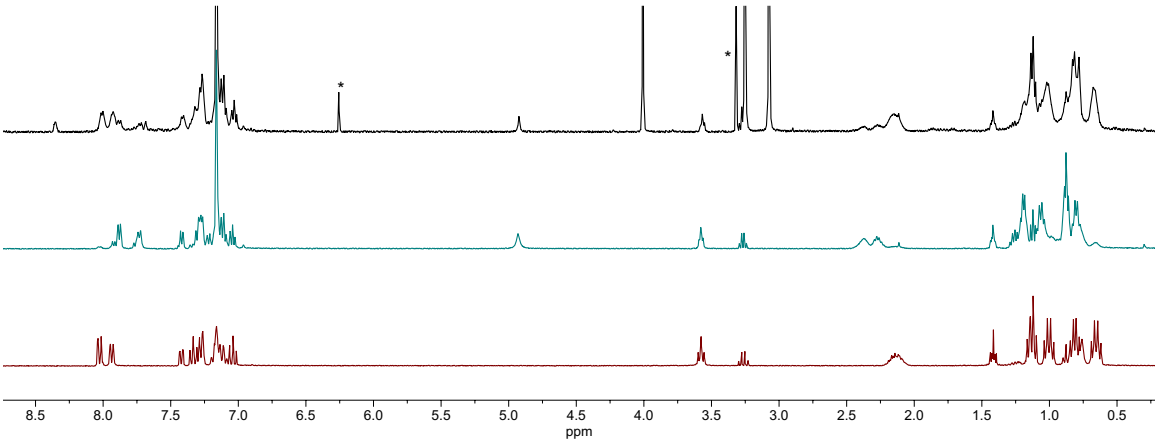

Figure C.1.39. {top} ^{1}H NMR spectrum of the crude mixture upon oxidation of **4.3** in DME, in C_6D_6 (400 MHz, *1,3,5-trimethoxybenzene) {middle} ^{1}H NMR spectrum of **4.4** in C_6D_6 {bottom}^{1}H NMR spectrum of **4.2** in C_6D_6

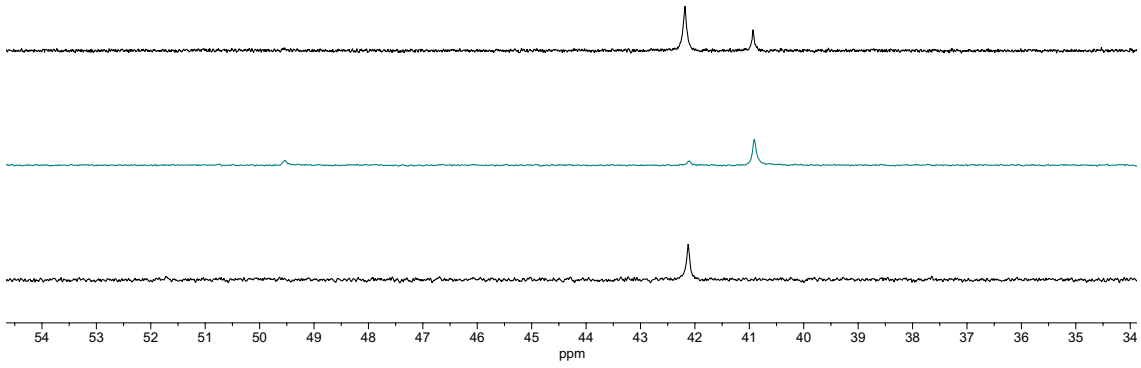

Figure C.1.40. {top} ^{31}P NMR spectrum of the crude mixture upon oxidation of **4.3** in DME, in C_6D_6 (162 MHz) {middle} ^{31}P NMR spectrum of **4.4** in C_6D_6 {bottom} ^{31}P NMR spectrum of **4.2** in C_6D_6

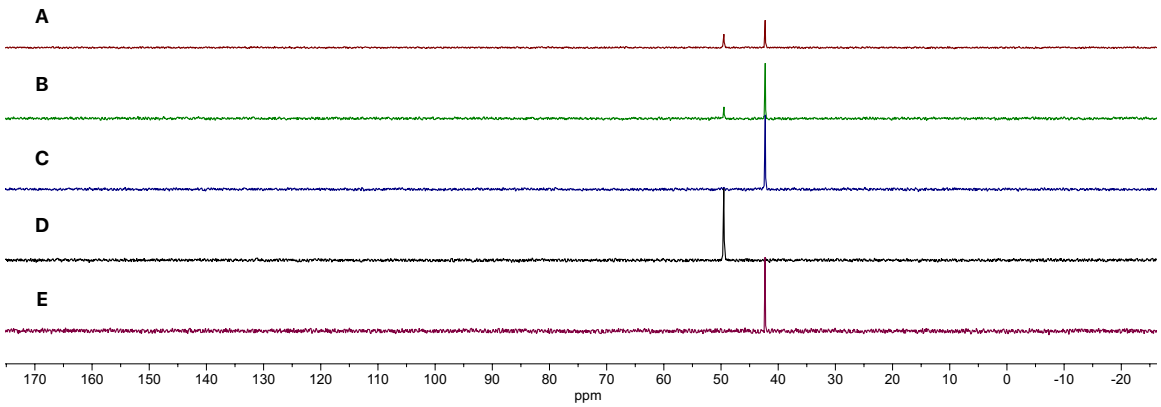

Figure C.1.41. ^{31}P NMR spectra monitoring the conversion of **4.5** to **4.2** in 0.4 M NH_3 in THF (with *ca*. 5% C_6D_6), (A) 30 min after addition (B) 1 h after addition (C) 3 h after addition (121 MHz). Authentic ^{31}P NMR spectra of (D) **4.5** and (E) **4.2** in THF with *ca*. 5% C_6D_6 (162 MHz)

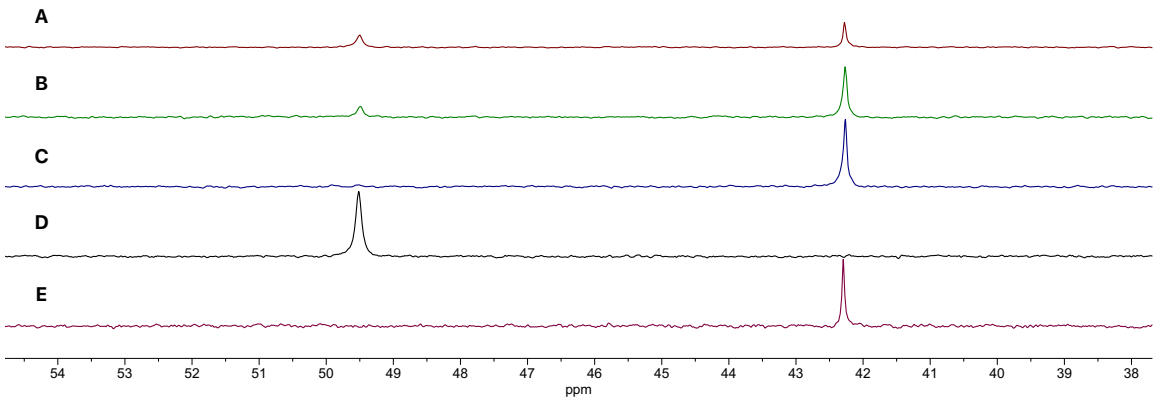

Figure C.1.42. ^{31}P NMR spectra monitoring the conversion of **4.5** to **4.2** in 0.4 M NH_3 in THF (with *ca*. 5% C_6D_6), (A) 30 min after addition (B) 1 h after addition (C) 3 h after addition (121 MHz). Authentic ^{31}P NMR spectra of (D) **4.5** and (E) **4.2** in THF with *ca*. 5% C_6D_6 (162 MHz)

C.2 UV-Visible Spectra

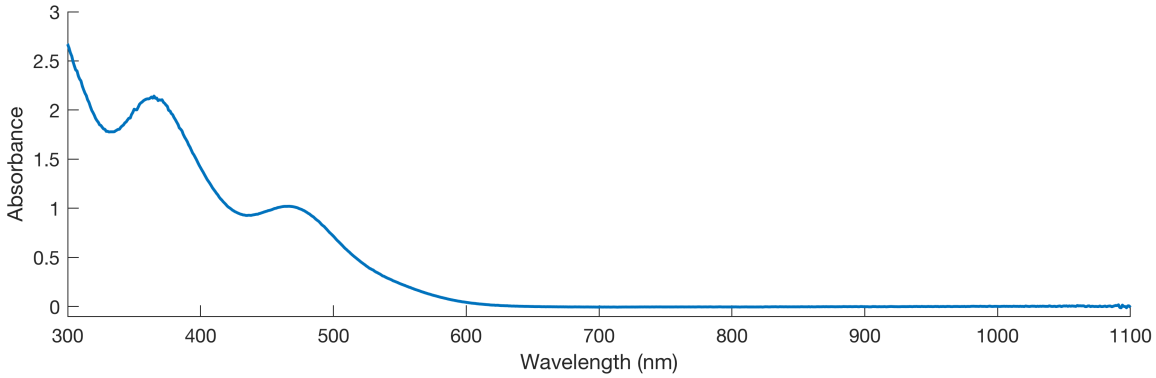

Figure C.2.1. UV-vis spectrum of **4.2** in THF

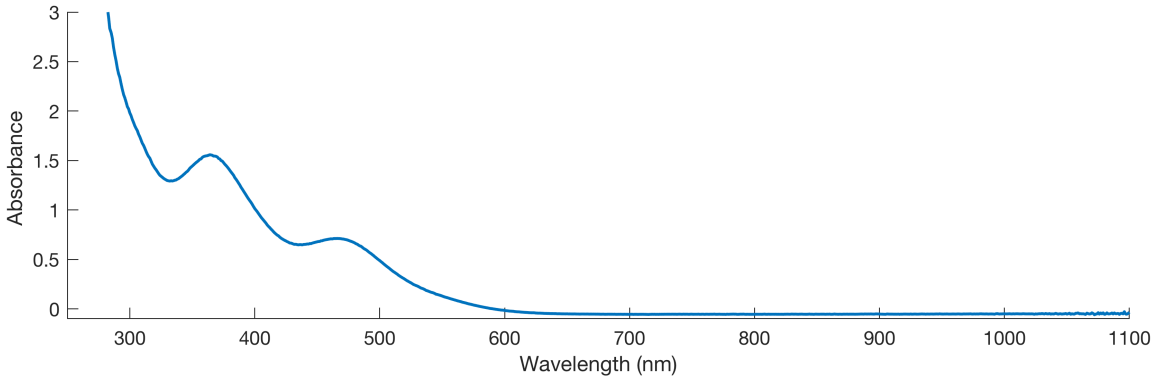

Figure C.2.2. UV-vis spectrum of **4.3** in THF

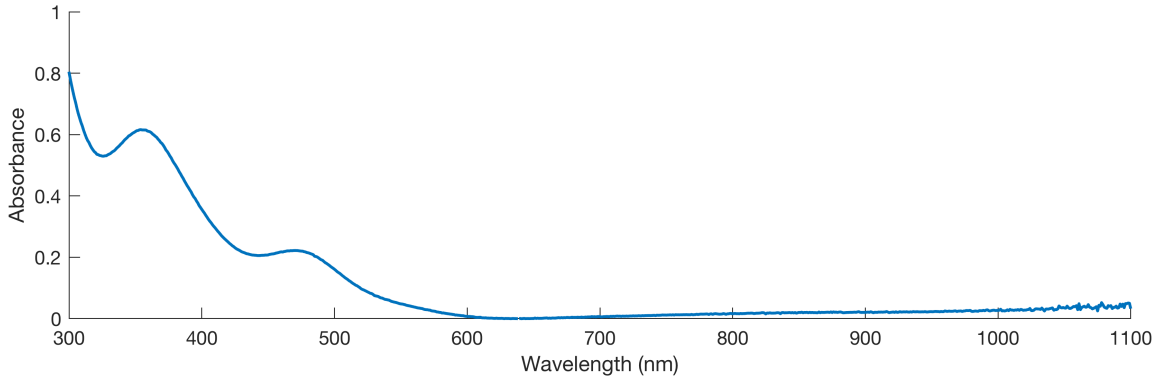

Figure C.2.3. UV-vis spectrum of **4.4** in THF (1 mm cuvette)

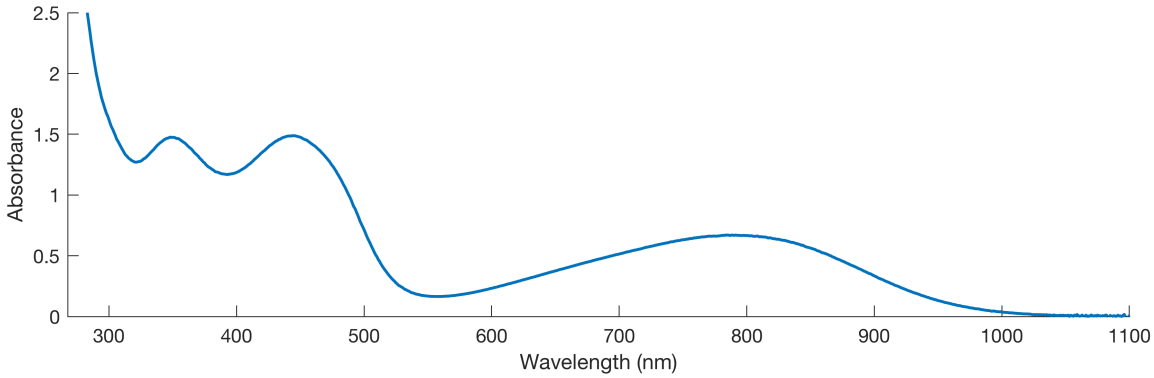

Figure C.2.4. UV-vis spectrum of **4.5** in THF

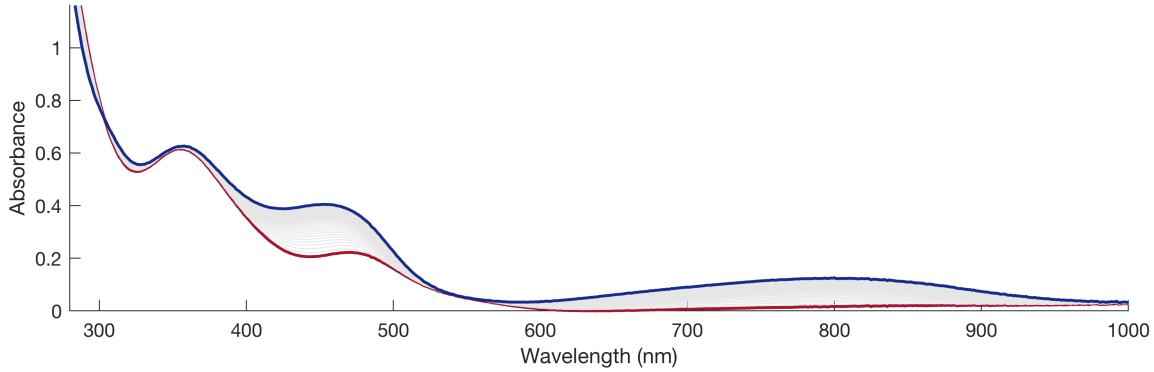

Figure C.2.5. UV-vis spectra monitoring the disproportionation of **4.4** → ½ **4.2** + ½ **4.5** in THF at 25 ºC. Red trace represents the initial spectrum of **4.4**, and the blue trace represents spectrum of the mixture overnight. (1 mm cuvette)

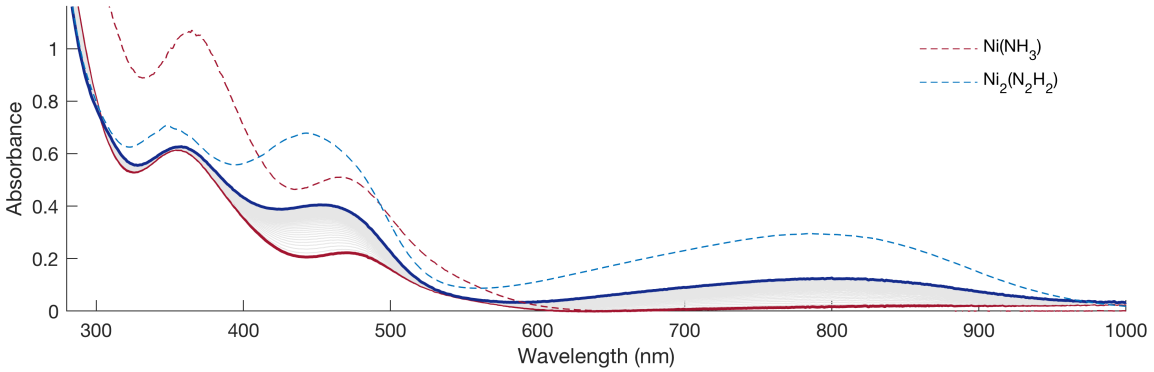

Figure C.2.6. UV-vis spectra monitoring the disproportionation of **4.4** → ½ **4.2** + ½ **4.5** in THF at 25 ºC. Red trace represents the initial spectrum of **4.4**, and the blue trace represents spectrum of the mixture overnight. Dashed spectra are included for reference (**4.2** in dashed red, **4.5** in dashed blue) and are shown at arbitrary absorbance scale relative to the solid spectra).

C.3 IR Spectra

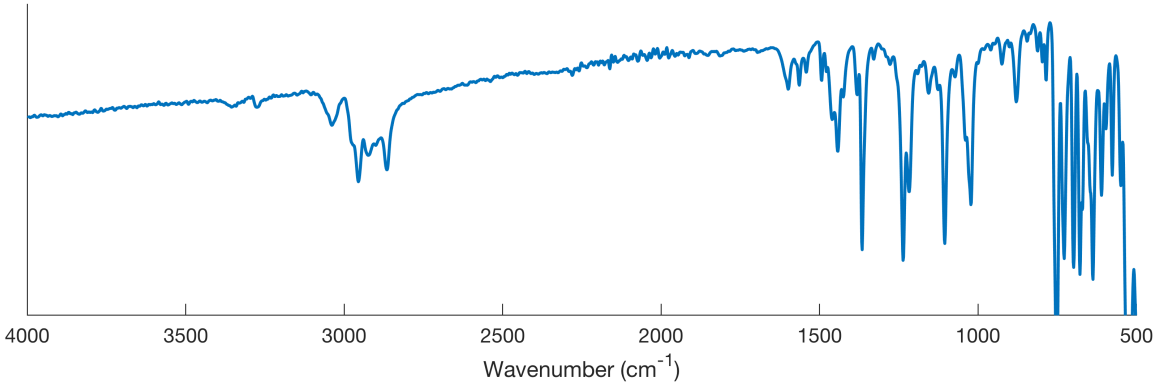

Figure C.3.1. IR spectrum of **4.2** (solid powder sample)

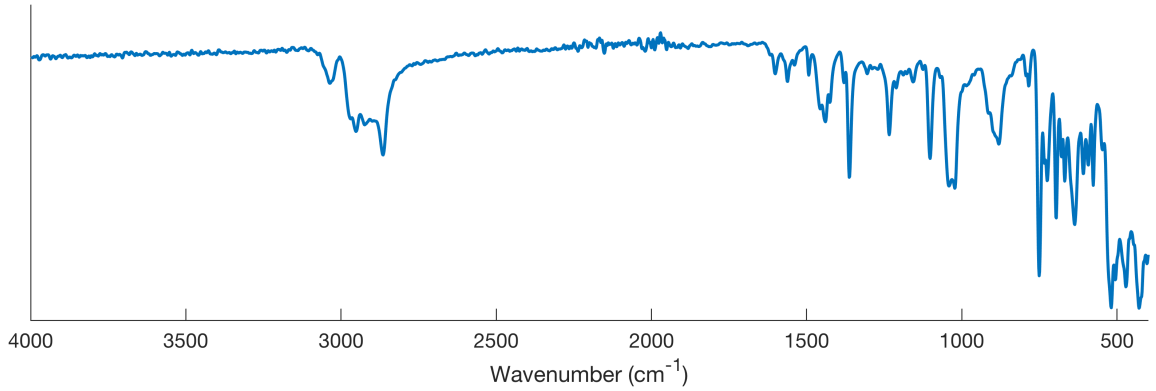

Figure C.3.2. IR spectrum of **4.3** (solid powder sample)

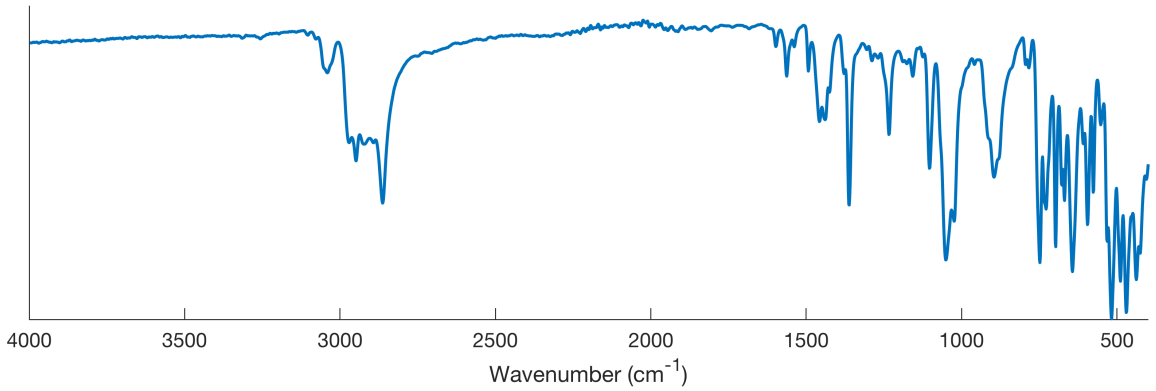

Figure C.3.3. IR spectrum of $(SiP_2S)Ni(NH_2)Na(THF)_3$ (solid powder sample)

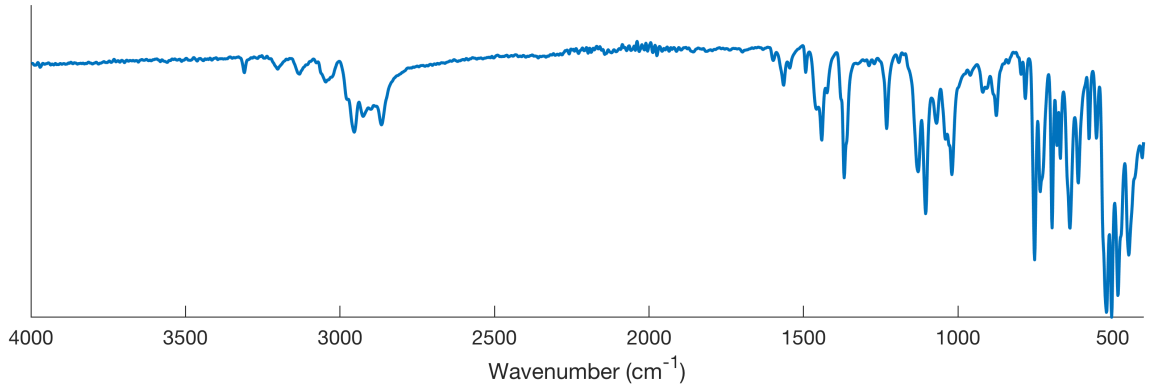

Figure C.3.4. IR spectrum of **4.4** (solid powder sample)

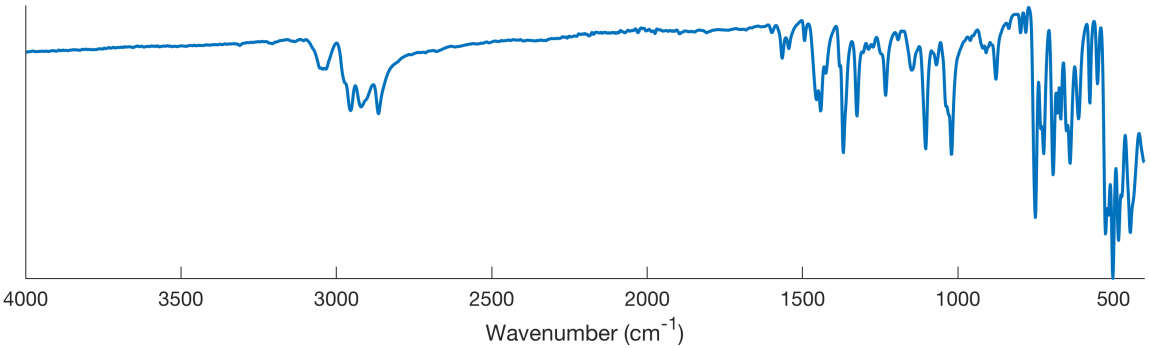

Figure C.3.5. IR spectrum of **4.5** (solid powder sample)

C.4 Cyclic Voltammogram

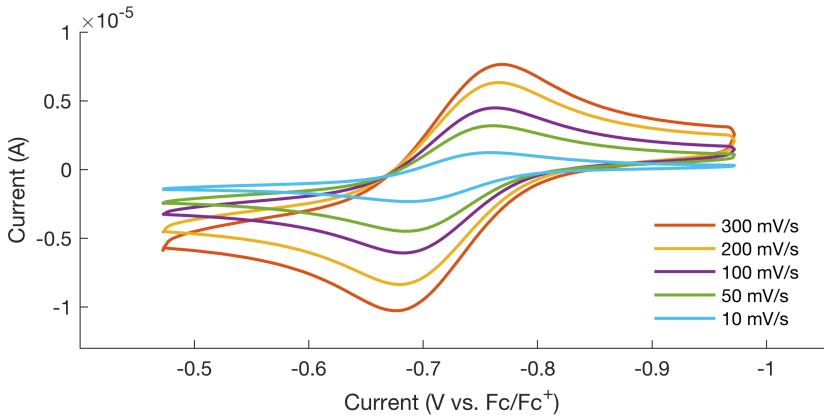

Figure C.4.1. Cyclic voltammograms of **4.3** at various scan rates, depicting the $Ni^{III/II}$ couple at −0.72 V V vs. Fc/Fc^{+} (0.4 M $[NBu_4][PF_6]$ in THF). Data was collected with glassy carbon working, Pt counter, and Ag/Ag^{+} reference electrodes.

C.5 X-ray Diffraction Data

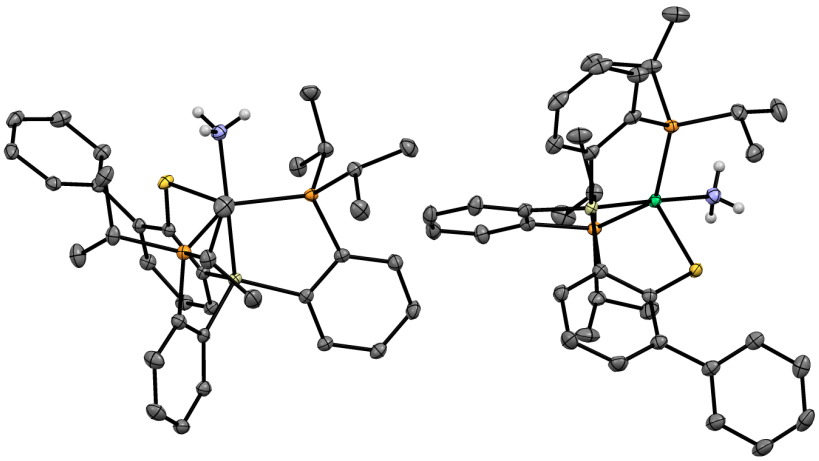

Figure C.5.1. Full asymmetric unit of **4.2**. C–*H* hydrogen atoms omitted; thermal ellipsoids at 50% probability.

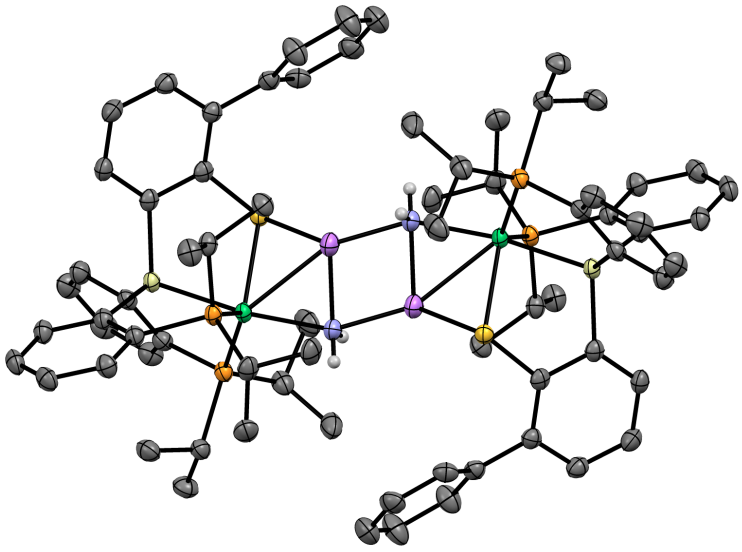

Figure C.5.2. Structure of **4.3** with omission of C–*H* hydrogen atoms, solvent molecules, and disordered components. Thermal ellipsoids at 50% probability.

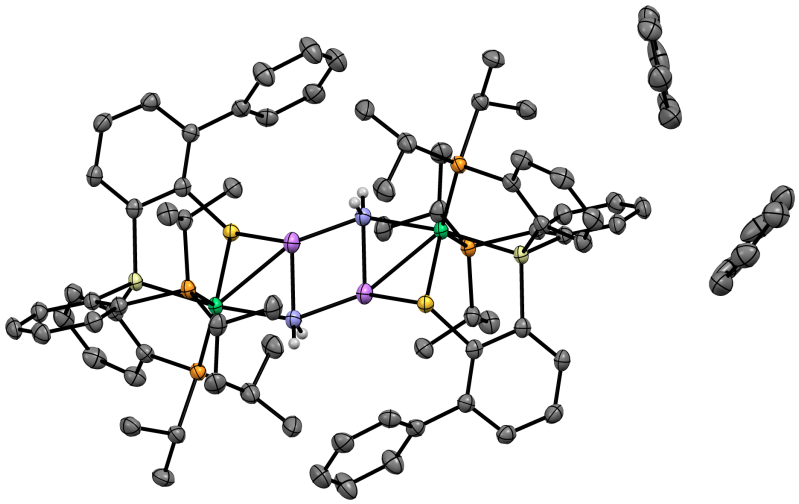

Figure C.5.3. Full asymmetric unit of **4.3** including solvent. C–*H* hydrogen atoms omitted; thermal ellipsoids at 50% probability.

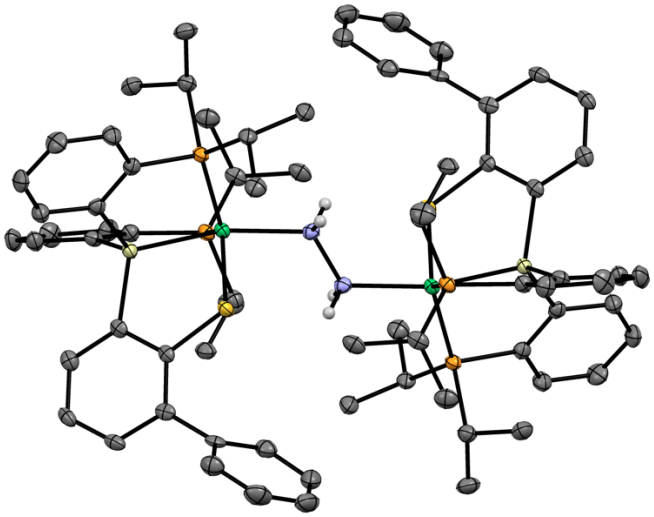

Figure C.5.4. Full asymmetric unit of **4.4** including solvent. C–*H* hydrogen atoms omitted; thermal ellipsoids at 50% probability.

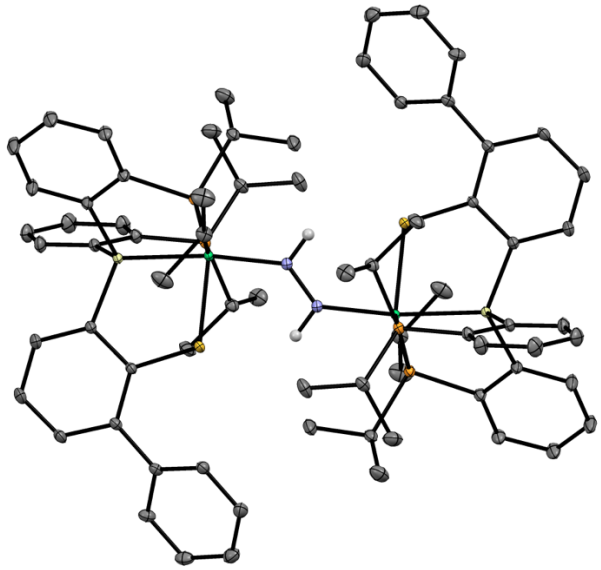

Figure C.5.5. Structure of **4.5** with omission of C–*H* hydrogen atoms, solvent molecules, and disordered components. Thermal ellipsoids at 50% probability.

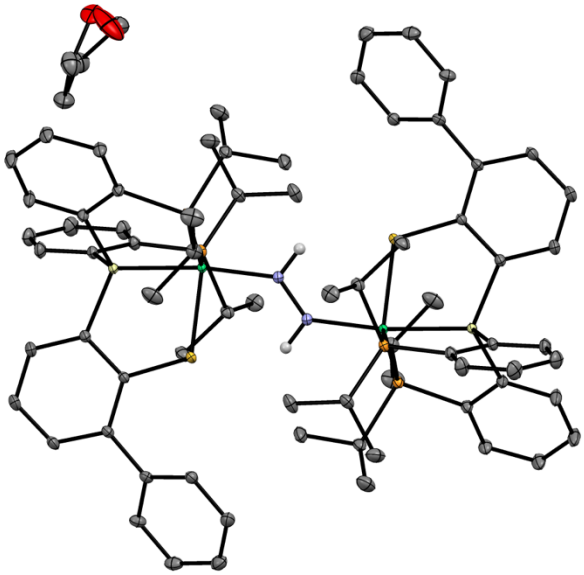

Figure C.5.6. Full asymmetric unit of **4.5** including solvent. C–*H* hydrogen atoms omitted; thermal ellipsoids at 50% probability.

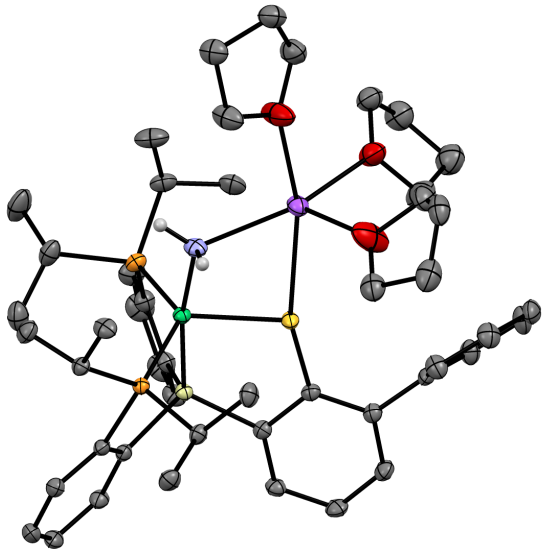

Figure C.5.7. Structure of $(SiP_2S)NiNH_2Na(THF)_3$ with omission of hydrogen atoms and solvent molecules. Thermal ellipsoids at 50% probability.

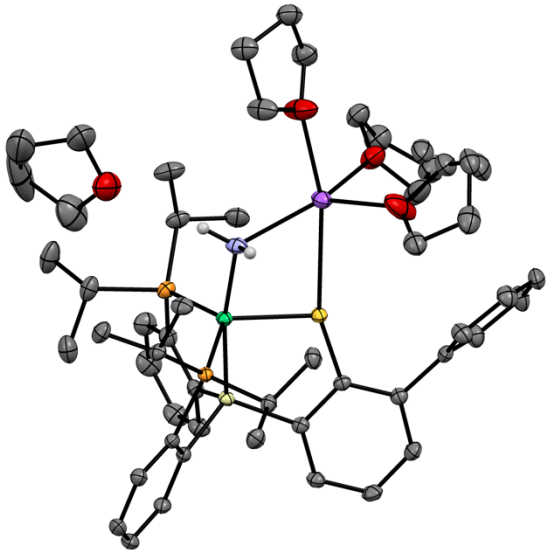

Figure C.5.8. Full asymmetric unit of $(SiP_2S)NiNH_2Na(THF)_3$ including solvent. Hydrogen atoms omitted; thermal ellipsoids at 50% probability.

C.6 Oxidative N−N Coupling from 4.3

Table C.6.1. Single run yields for the generation of **4.4** and **4.2** by oxidation of **4.3**

Entry	4.3 (mg)	$[Cp_2Fe][BAr^F_4]$ (mg)	Solvent	Yield of 4.4 (%)	Yield of 4.2 (%)
a	8	10	DME	42	60
b	8	10	DME	36	65
c	8	10	DME	44	54

A p p e n d i x D

SUPPLEMENTARY INFORMATION FOR CHAPTER 5

D.1 NMR Spectra

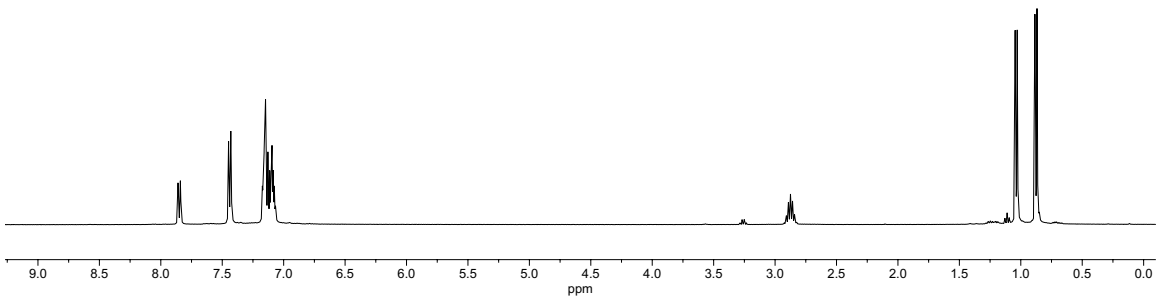

Figure D.1.1. ^{1}H NMR spectrum of **5.3** in C_6D_6 (400 MHz)

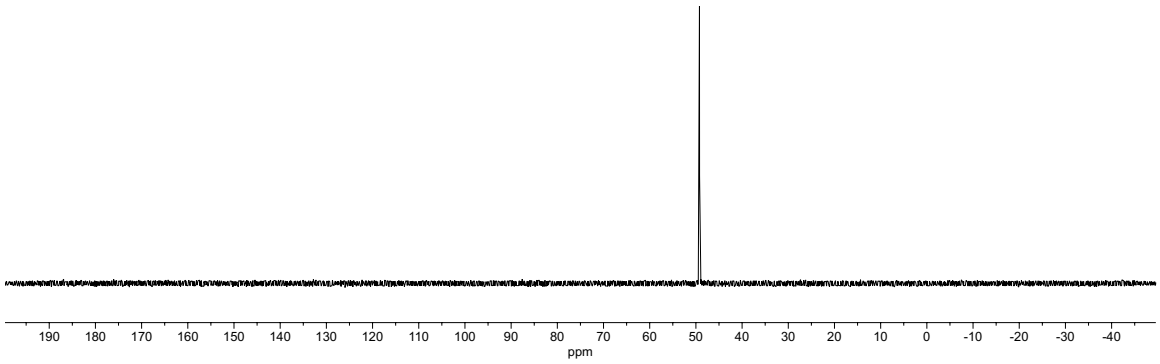

Figure D.1.2. ^{31}P NMR spectrum of **5.3** in C_6D_6 (162 MHz)

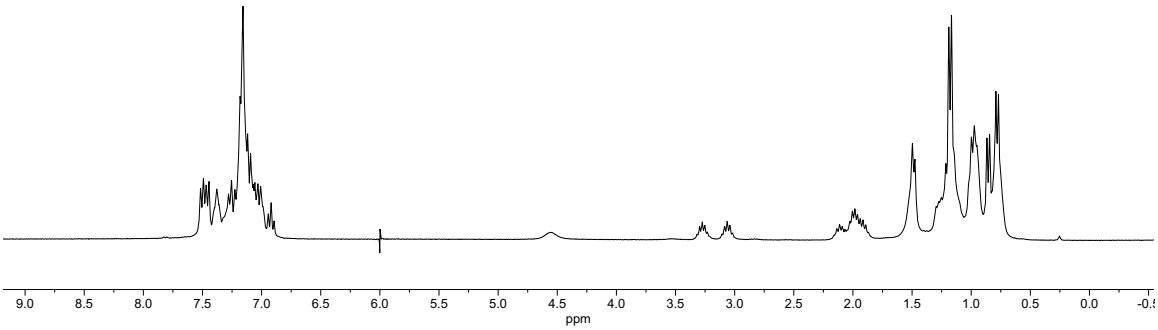

Figure D.1.3. ^{1}H NMR spectrum of **5.4** in C_6D_6 (300 MHz)

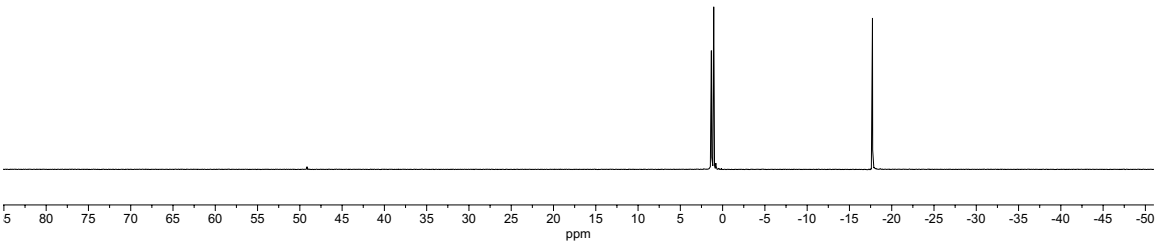

Figure D.1.4. ^{31}P NMR spectrum of **5.4** in C_6D_6 (162 MHz)

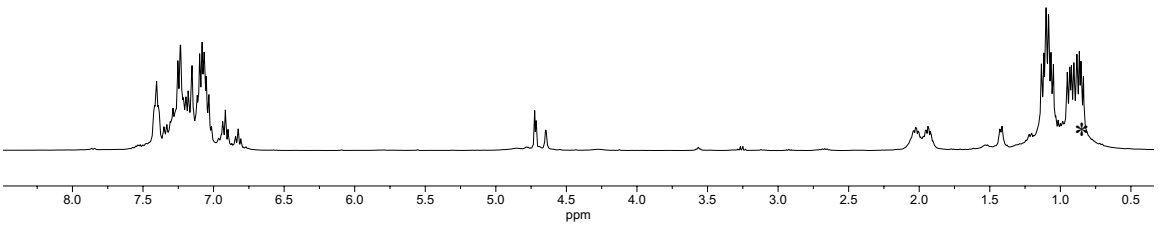

Figure D.1.5. ^{1}H NMR spectrum of **5.6** in C_6D_6 (400 MHz). *impurity

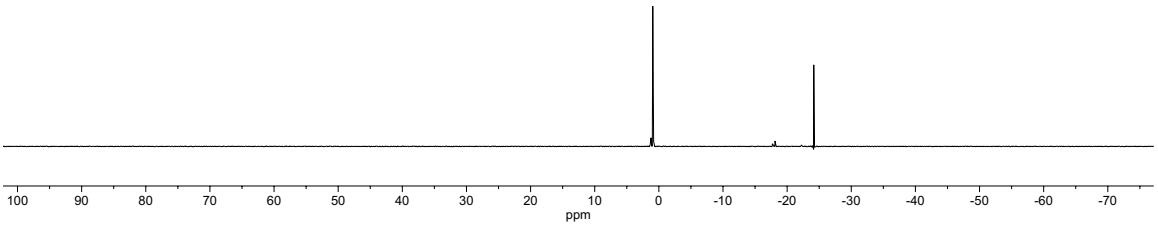

Figure D.1.6. ^{31}P NMR spectrum of **5.6** in C_6D_6 (162 MHz)

D.2 IR Spectra

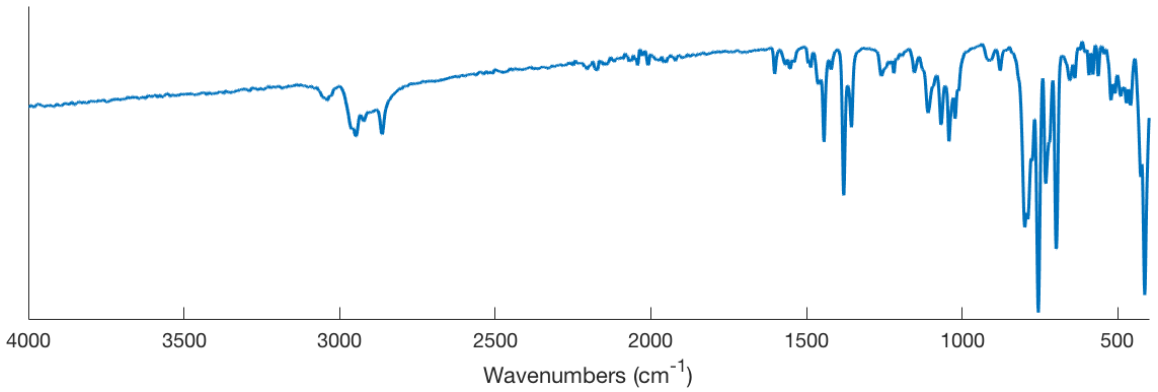

Figure D.2.1. IR spectrum of **5.7** (solid sample)

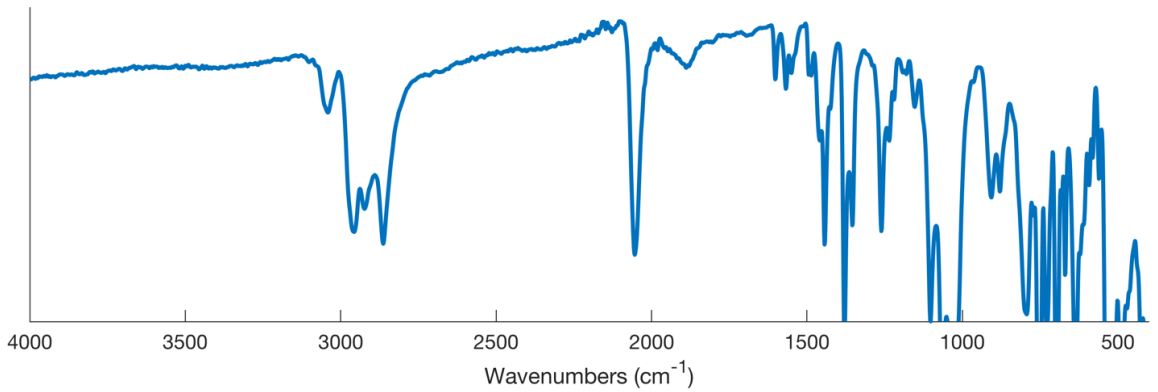

Figure D.2.2. IR spectrum of **5.8** (solid sample)

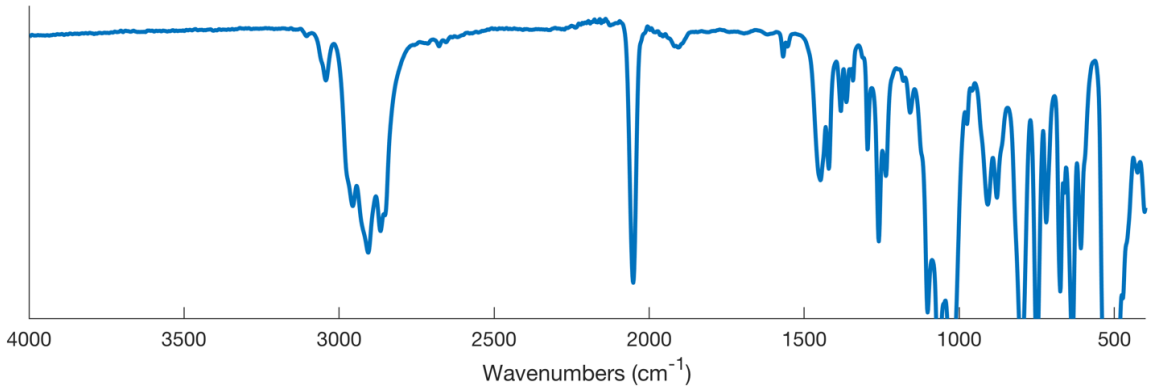

Figure D.2.3. IR spectrum of **5.9** (solid sample)

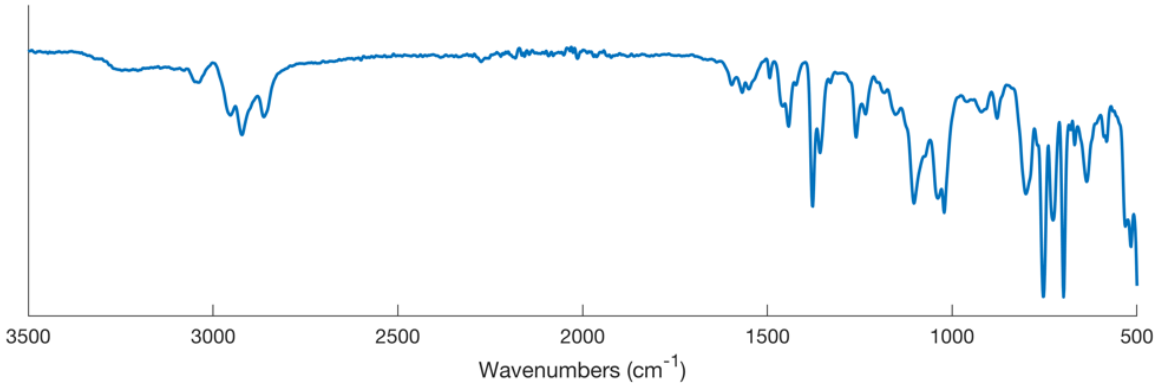

Figure D.2.4. Representative IR spectrum of solids remaining after vacuum transfer of volatiles in a N_2H_4 disproportion catalytic run with **5.8** (solid sample)

D.3 UV-Visible Spectra

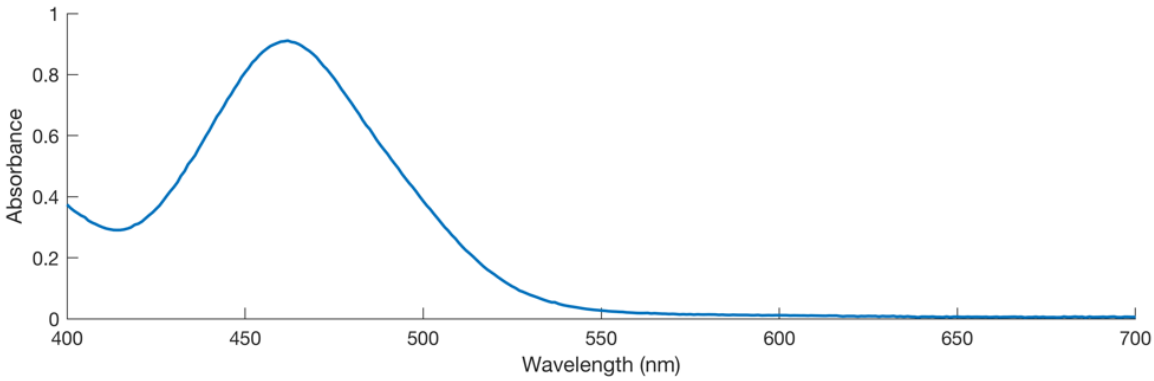

Figure D.3.1. UV-vis spectrum of **5.7** in THF

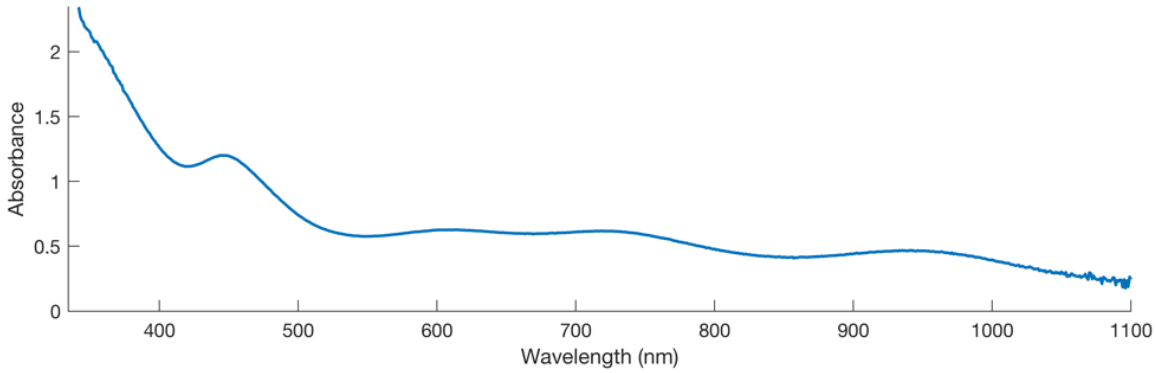

Figure D.3.2. UV-vis spectrum of **5.8** in THF

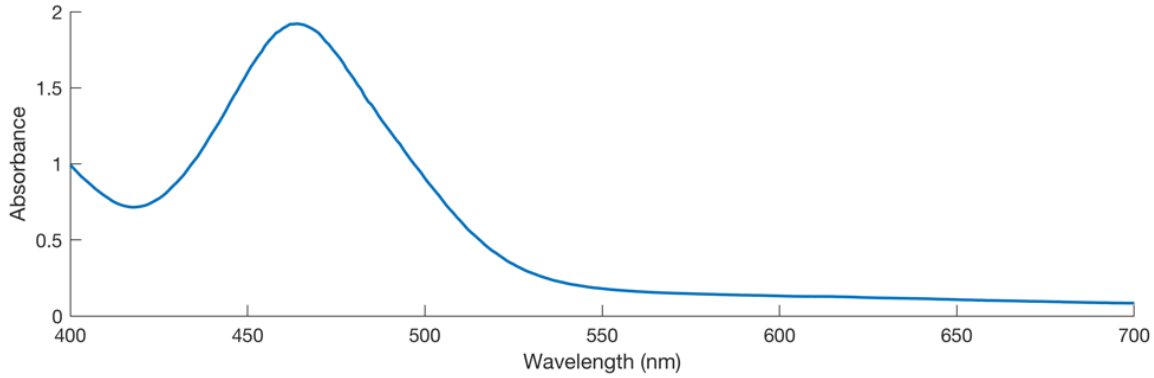

Figure D.3.3. UV-vis spectrum of **5.11** in THF

D.4 X-Ray Diffraction Data

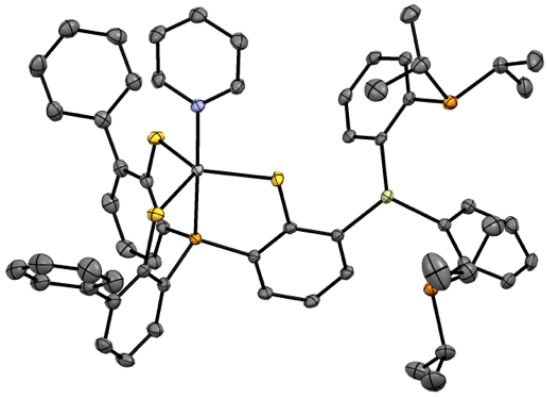

Figure D.4.1. Structure of **5.7** with omission of hydrogen atoms and solvent molecules. Thermal ellipsoids at 50% probability.

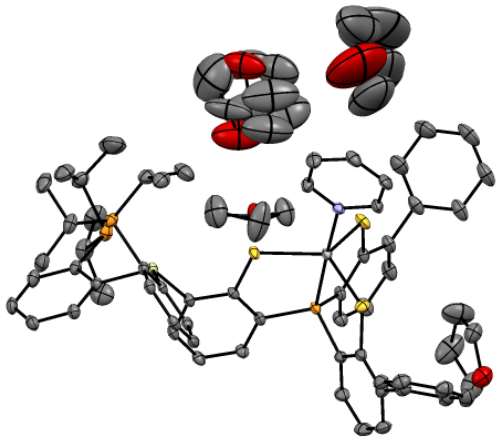

Figure D.4.2. Full asymmetric unit of **5.7** including solvent and disordered components. Hydrogen atoms omitted; thermal ellipsoids at 50% probability.

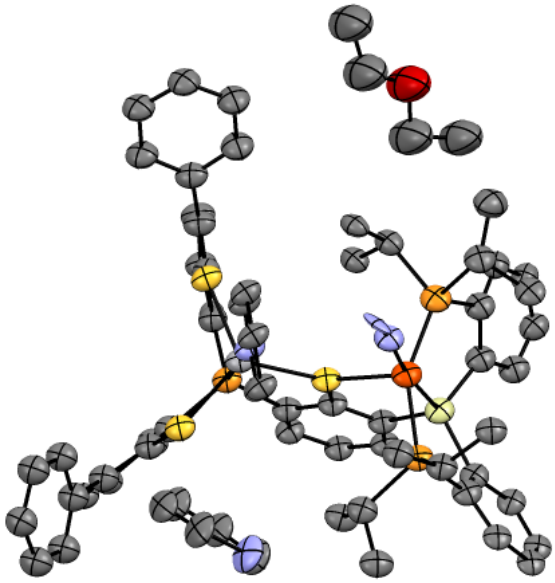

Figure D.4.3. Full asymmetric unit of **5.8** including solvent. Hydrogen atoms omitted; thermal ellipsoids at 50% probability.

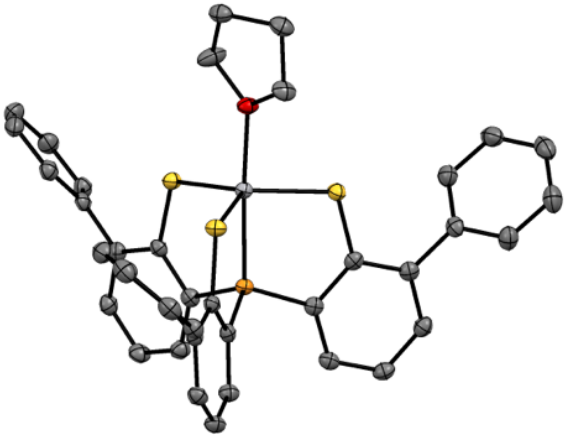

Figure D.4.4. Structure of $^{Ph}PS_3V(THF)$ with omission of hydrogen atoms and solvent molecules. Thermal ellipsoids at 50% probability.

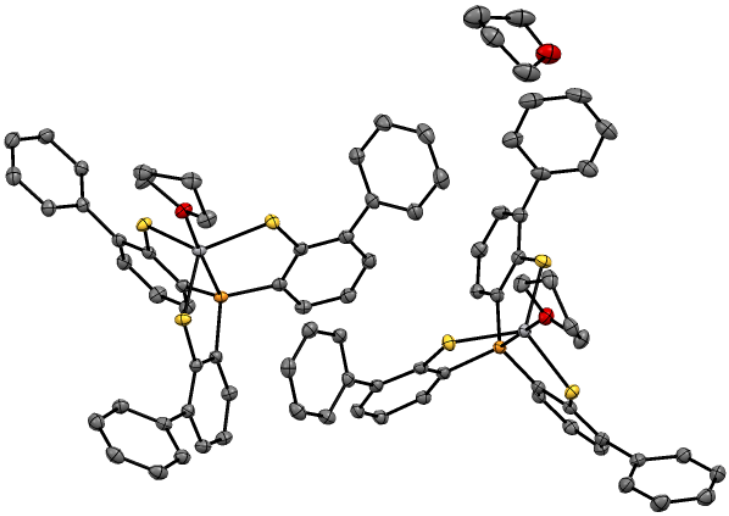

Figure D.4.5. Full asymmetric unit of $^{Ph}PS_3V(THF)$ including solvent. Hydrogen atoms omitted; thermal ellipsoids at 50% probability.

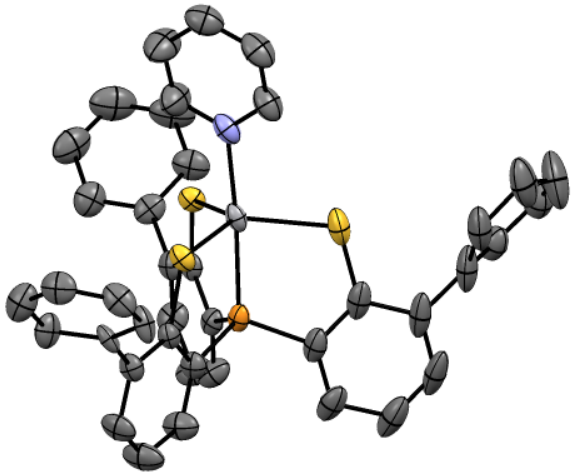

Figure D.4.6. Structure of **5.11** with omission of disordered components and hydrogen atoms. Thermal ellipsoids at 50% probability.

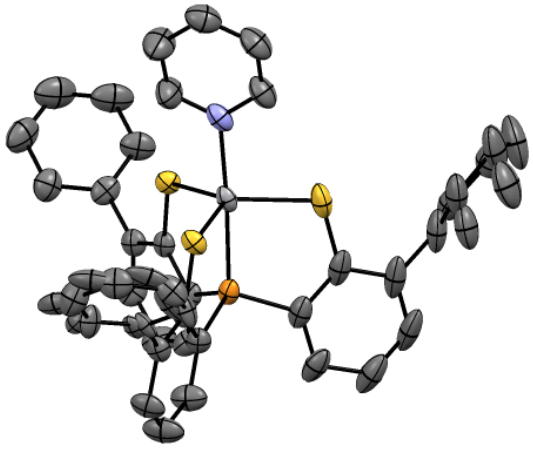

Figure D.4.7. Full asymmetric unit of **5.11** including solvent and disordered components. Hydrogen atoms omitted; thermal ellipsoids at 50% probability.

D.5. Hydrazine Disproportionation Catalysis

Table D.5.1 Single runs from Table 5.1.

Entry	Solvent	Time	N_2H_4 (equiv./5.8)	NH_3 (equiv./5.8)
a	THF	2 h	50	4.0, 5.5
b	Et_2O	2 h	50	9.7, 11
c	Et_2O	12 h	50	41, 50
d	Et_2O	24 h	50	57, 62
e	Et_2O	24 h	100	80, 98
f	Et_2O	48 h	100	102, 124
g[1]	Et_2O	17 d	1440	1014, 1132
S1[*]	Et_2O	12 h	50	46
S2[‡]	Et_2O	12 h	50	42
S3[#]	Et_2O	12 h	50	39

Runs performed at catalyst concentrations of 1 mM in 2.5 mL solvent. [1]Run performed with at 0.1 mM catalyst concentration in 2.5 mL solvent. *Performed in the presence of elemental Hg. ‡Performed in the presence of 0.3 equivalents of PPh_3 per equivalent of **5.8** (1 mM in 2 mL Et_2O). [#] Performed in the presence of 10 equivalents of pyridine per equivalent of **5.8** (1 mM in 2 mL Et_2O).

Table D.5.2 Single runs from Table 5.2.

Entry	Catalyst	NH_3 (equiv./catalyst)
h	**5.9**	0.26, 0.51
i	**5.11**	0.27, 0.13
*j**	**5.9** + **5.11**	0.88, 1.19

Runs performed at catalyst concentrations of 1 mM in 2.5 mL solvent. * [**5.9**] = [**5.11**] = 1 mM

Table D.5.3 Determination of the reaction order of compound **5.8** via method of initial rates

5.8 (mg)	**NH_3 (µmol)**	**ln([5.8]$_0$)[1]**	**ln([NH_3]/t)[1]**
1	3.5, 3.6	−8.0	−7.3
2	5.7, 8.1	−7.3	−6.6
3	12.2, 13.1	−6.9	−6.0
4	16.0, 16.1	−6.6	−5.7

Runs performed with 0.13 mmol N_2H_4 in 2.5 mL THF. Yield of NH_3 determined after 2 h of reaction time. [1]concentrations in M, time in h

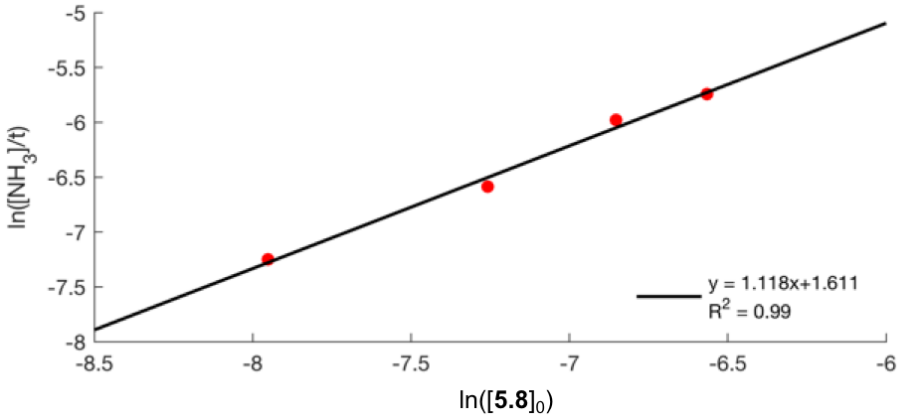

Figure D.5.1. Plot of ln([**5.8**]$_0$) vs. ln(NH_3]/t)

Table D.5.4. Determination of the reaction order on substrate via method of initial rates

[N_2H_4]	**NH_3 (µmol)**	**ln([N_2H_4]$_0$)[1]**	**ln([NH_3]/t)[1]**
0.002	0.23, 0.24	−6.2	−7.3
0.005	0.39, 0.46	−5.3	−6.7
0.010	0.97, 1.4	−4.6	−5.7

Runs performed in 2 mL THF with 1 mM catalyst (a THF solution of substrate is added at 25 °C to a Schlenk tube containing a stirring THF solution of catalyst and immediately sealed). Yield of NH_3 determined after 10 min of reaction time. [1]concentrations in M, time in h

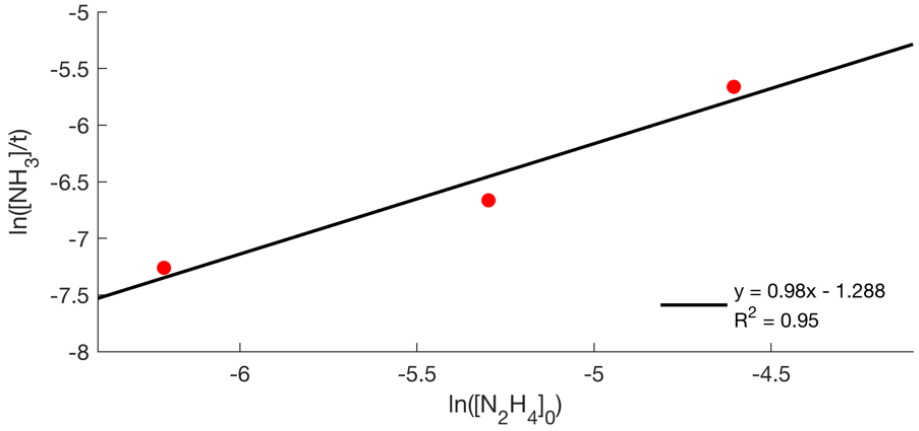

Figure D.5.2. Plot of $\ln([N_2H_4]_0)$ vs. $\ln(NH_3]/t)$

Table D.5.5. Determination of the reaction order on substrate via method of initial rates (saturation kinetics)

$[N_2H_4]$	NH_3 (μmol)	$\ln([N_2H_4]_0)^1$	$\ln([NH_3]/t)^1$
0.025	9.0, 9.6	−3.6	−6.3
0.070	7.9, 8.8	−2.7	−6.4
0.083	8.3, 8.5	−2.5	−6.4

Runs performed in 2.5 mL THF with 1 mM catalyst. Yield of NH_3 determined after 2 h of reaction time. [1]concentrations in M, time in h

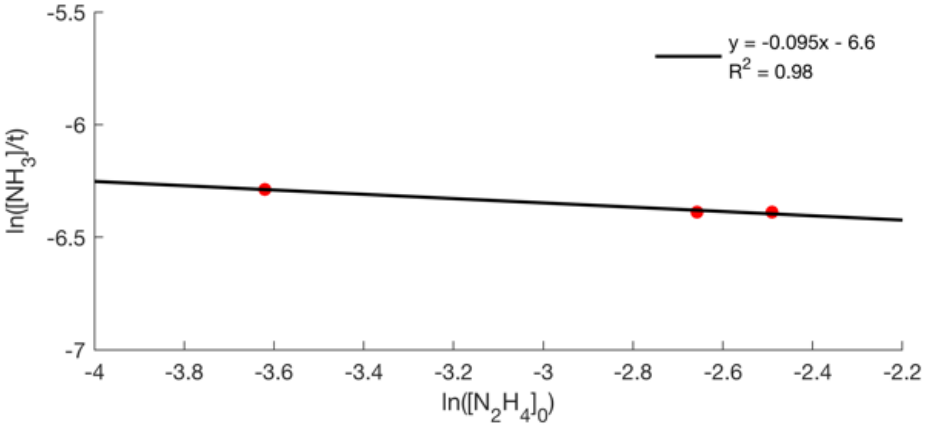

Figure D.5.2. Plot of $\ln([N_2H_4]_0)$ vs. $\ln(NH_3]/t)$ under saturation kinetics